DOTTORATO DI RICERCA
INTERNATIONAL DOCTORATE IN STRUCTURAL BIOLOGY

CICLO XXXIV

COORDINATOR Prof. Lucia Banci

Expression and characterization of human proteins involved in neurological disorders and for biotherapeutic applications

Settore Scientifico Disciplinare CHIM/03

PhD student

Tutor

Dott. Domenico Rizzo

Prof. Marco Fragai

Coordinator

Prof. Lucia Banci

November 2018 – October 2021

This thesis has been approved by the University of Florence, the University of Frankfurt and the Utrecht University

Universiteit Utrecht
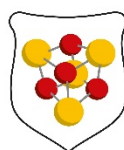
Table of Contents

Preface

In the last years the advancements in molecular biology and in the expression of pharmaceutically relevant recombinant biomolecules have completely changed the perspectives of drug discovery. The present PhD project is focused on the development of new strategies for expression and characterization of human recombinant proteins used to investigate the molecular bases of two neurological diseases and to develop new NMR strategies for the characterization of biomaterials incorporating protein therapeutics.

The first part of the research activity was focused on clarifying important aspects about the role of Aβ-peptides and α-Synuclein in Alzheimer and Parkinson disease, respectively.

The pathogenesis of these disorders generally referred as "proteinopathies" is related to the formation of high molecular weight protein oligomers or aggregates. Kinetic studies of protein aggregation and the structural characterization at atomic details of all the species resulting from protein aggregation are important to clarify the molecular basis of these pathologies and to design new drug discovery campaigns. In this context, nuclear magnetic resonance (NMR) spectroscopy in solution was used to investigate the kinetic of α-Synuclein aggregation. Solid-state Nuclear Magnetic Resonance (SSNMR) spectroscopy is a powerful technique to investigate and characterize non-crystalline samples including protein oligomers, fibrils, biosilica-entrapped proteins, PEGylated and polysaccharide-conjugated proteins and proteins grafted onto nanoparticles. Therefore, SSNMR was used to investigate the structural features of fibrils obtained by mixing Aβ 1-40 and Aβ 1-42 peptides for a better understanding of the variable nature of cross-seeding and for the development of new approaches in Alzheimer prevention and treatment. Finally, it is important to point out that the integration of SSNMR with other techniques can provide a more complete picture of the events involved in the aggregation process.

The last part of my research activity was focused on the development of new NMR strategies for the characterization of protein-based biomaterials and bioinspired composites. The conjugation of therapeutic proteins with synthetic or natural polymers is often used to improve the pharmacokinetic properties (stability, solubility, half-life, immunogenicity, etc.) of biologics and to produce new biomaterials. Several

biomaterials including hydrogels are currently used to replace/support non-functional tissues like those damaged or destroyed by injuries or diseases and in controlled drug release. In particular, protein therapeutics or growth factors can be embedded in biomaterials like hydrogels to modulate the immune response promoting an extensive cell colonization and matrix reabsorption. The preservation of the native folding within the matrix is crucial to maintain the biological/pharmacological activity of the protein. However, the structural characterization of proteins in these heterogeneous materials is still a challenge.

In the present PhD thesis therapeutic protein L-Asparaginase II (ANSII) and the potential drug carrier Transthyretin (TTR) were selected to investigate the use of SSNMR in the characterization of hydrogels incorporating proteins and in the evaluation of the preservation of the higher order structure. Our results show that SSNMR is a powerful methodology also for the characterization of these heterogeneous systems thus opening new perspectives for the design of these innovative materials.

1. Introduction

1.1 Neurodegenerative Diseases

Neurodegenerative diseases are a large group of disorders characterized by progressive loss of neurons associated with deposition of proteins showing altered physicochemical properties in the brain and in peripheral organs. These kinds of pathologies are untreatable and show a progressive degeneration and/or death of nerve cells. Neurons from brain and spinal cord do not regenerate themselves: therefore, when they die, they cannot be replaced. One of the most well-grounded risk factors for developing a neurodegenerative pathology is the increasing of the age and several approved drugs do not seem to stop the progression.[1] Molecular classification of neurodegenerative disease is protein-based. Consequently, this kind of pathologies are classified as "Proteinopathies".[2]

This emphasizes the role of protein-processing systems in the pathogenesis. Therefore, a common link of all these diseases is the presence of deposits of proteins, in a misfolded state, in neurons and other cells or extracellularly. Many factors can trigger protein misfolding: mutations in the gene sequence leading to the production of a protein unable to adopt the native folding, errors on the processes of transcription or translation, failure of chaperone machinery, structural modification produced by environmental changes, mistakes on the post-translational modifications or on protein elimination pathways, such as the ubiquitin-proteasome system and the autophagy-lysosome pathway.[3,4]

Another concept, referred to as prion-like spreading, suggests that the proteins associated with neurodegenerative diseases spread in the nervous system. The template-directed protein misfolding, similarities in cell-to-cell propagation of pathologic proteins, and deposition of proteins that seem to follow anatomic pathways suggest overlap with the pathogenesis of prion diseases.[5]

The clinical presentations are defined by the distinct involvement of functional systems and do not necessarily indicate the molecular pathologic background. Seeding of pathologic proteins and hierarchic involvement of anatomic regions is commonly seen in neurodegenerative diseases. Overlap of neurodegenerative diseases and combinations of different disorders is frequent. Translation of neuropathologic

categories of neurodegenerative diseases into in vivo detectable biomarkers is only partly achieved but intensive research is performed to reach this goal.[1]

The most frequent proteins involved in the pathogenesis of neurodegenerative diseases are β-amyloid[6], prion protein[7], tau[8], α-synuclein, and Fused-in sarcoma (FUS) protein[9]. There are further proteins associated mostly with hereditary disorders such as familial amyloid polyneuropathy.[10]

Disease	Protein featured
Alzheimer's disease	Aβ1-40/42, Tau
Diabetes mellitus type 2	Amylin
Parkinson's disease	α-synuclein
Bovine spongiform encephalopathy	PrP
Fatal Familial Insomnia	PrP
Huntington's Disease	Huntingtin
Medullary carcinoma of the thyroid	Calcitonin
Isolated atrial amyloidosis	Atrial natriuretic factor
Atherosclerosis	Apolipoprotein AI
Rheumatoid arthritis	Serum amyloid A
Aortic medial amyloid	Medin
Prolactinomas	Prolactin
Familial amyloid polyneuropathy	Transthyretin
Dialysis-related amyloidosis	β2M
Amyloid light-chain (AL) amyloidosis	Immunoglobulin light chains
Amyotrophic lateral sclerosis	TDP-43

Table 1 - Amyloid-based neurodegenerative diseases and their hallmarks

1.2 Parkinson Disease and α-Synuclein

Parkinson's disease (PD), the most common neurodegenerative movement disorder, is pathologically characterized by the presence, in selectively vulnerable brain regions, of intracytoplasmic and axonal inclusions, called Lewy bodies (LB) and Lewy neurites, primarily consisting of aggregated α-synuclein (α-syn).[11] Accumulation and formation of insoluble fibrillary α-syn is usually accompanied, both as a cause and a consequence, by the impairment of the autophagy-lysosomal pathways, which represents one of the main routes implicated in the intracellular degradation of α-syn.[12–16] The clinical diagnosis of PD can be very difficult in early stages of the disease,

when the motor and neurological symptoms are still not present, with high risk of misdiagnosis. The long prodromal phase of PD[17] provides the possibility for early therapeutic intervention, once disease-modifying therapies have been developed, but the lack of biomarkers for early diagnosis and monitoring of disease progression represents a major obstacle to the achievement of this goal. CSF levels of total α-syn,[18] oligomeric α-syn,[19] S129-phosphorylated α-syn,[19] DJ-1,[20] Aβ1-42,[20] tau[21] and lysosomal enzymes[13] are promising candidates for PD biomarkers although they have still low specificity and sensitivity for PD and other synucleinopathies. The understanding of the "prion-like" behavior of α-synuclein provided new perspectives for the development of new diagnostic assays. With respect to this, oligomeric and fibrillary aggregates of α-syn are found to spread from cell to cell both through exosomal pathways and by passive diffusion through CSF;[22–24] this evidence makes the detection of misfolded α-syn in CSF a promising strategy for the pre-symptomatic diagnosis of PD.

The α-synuclein encoding gene is SNCA (cytogenetic location: 4q22.1) and its mutations are related to pathological phenotype of autosomal dominant Parkinson disease 1, Parkinson disease 4 and Lewy body dementia. Other two members of Synuclein family are two homologous proteins, β (SNCB) and γ synucleins (SNCC).

Γ-Synuclein, forms fibrils much more slowly than α synuclein, and β synuclein does not form fibrils under typical in vitro or in vivo conditions.[25]

Inside the cellular environment, this protein is involved in the regulation of presynaptic function and in neurotransmitter release (dopamine) and also plays a role in the movement of microtubules and in the binding of fatty acids. [26]

Several factors like post-translational modifications, oxidative stress, fatty acids concentration, proteolysis, phospholipids and metal ions can promote the misfolding of a-syn with the consequent formation of oligomers and amyloid-like fibrils.[27]

A-synuclein is a 14 kDa highly soluble cytosolic protein. It is classified as an intrinsically disordered protein (IDP), as well as Aβ peptides. The term "disordered" indicate a lack of a specific stable three-dimensional structure and the structural disorder in IDPs can be placed in one or more separate regions along the chain, or it may span the entire length of the protein.

The monomer of α-synuclein is composed of three distinct regions: an amphipathic α-helical domain in the N-terminus which mediates binding to phospholipid membranes, a central hydrophobic region, called NAC (non-Aβ component), having the β-sheet

potential, and a C-terminus that is highly negatively charged, and is prone to be unstructured. [28]

Figure 1 - α-synuclein regions. BLUE: N-term domain (1-60), RED: NAC domain (61-95), GREEN: C-term domain (96-140).

1.3   Alzheimer Disease and Aβ-Amyloid

Alzheimer disease (AD) neuropathology is characterized by the extracellular accumulation of Aβ peptide and intracellular aggregation of hyperphosphorylated tau. With the progression of the disease, macroscopic atrophy affects the entorhinal area and hippocampus, amygdala, and associative regions of the neocortex. The deposition of Aβ is first made of diffuse deposits. Amyloid focal deposits constitute the core of the senile plaque which also comprises a corona of tau-positive neurites. Aβ deposits are found successively in the neocortex, the hippocampus, the striatum, the mesencephalon, and finally the cerebellum together with the pontine nuclei (Thal phases).[29]

Aβ is normally synthesized in the brain with a rapid turnover.[30] It is the product of the cleavage of a large transmembrane precursor protein, the amyloid precursor protein or APP, coded by the APP gene on chromosome 21. APP is successively cleaved by β-secretase activity cleaving enzyme (BACE1) and by the γ-secretase complex, in which presenilin (PS) bears the catalytic site. The C-terminus of Aβ is variable, the peptide ending at amino acid 36–43, Aβ 1-40 and Aβ 1-42 being the most abundant.[31] Aβ 1-42 is less soluble than Aβ 1-40 and aggregates spontaneously. Function of Aβ is largely still unknown.

Tau pathology affects in a stereotyped order some specific nuclei of the brain. Loss of synapses is observed in association with tau and Aβ pathology; neuronal loss occurs in the most affected areas. However, the physiopathology of Alzheimer disease remains unknown. Familial cases suggest that Aβ deposition is the initial step, but tau pathology appears early in the course and seems to be better correlated with the symptoms.[29]

DAEFRHDSGYEVHHQKLVFFAEDVGSNKGAIIGLMVGGVV Aβ1-40

DAEFRHDSGYEVHHQKLVFFAEDVGSNKGAIIGLMVGGVVIA Aβ1-42
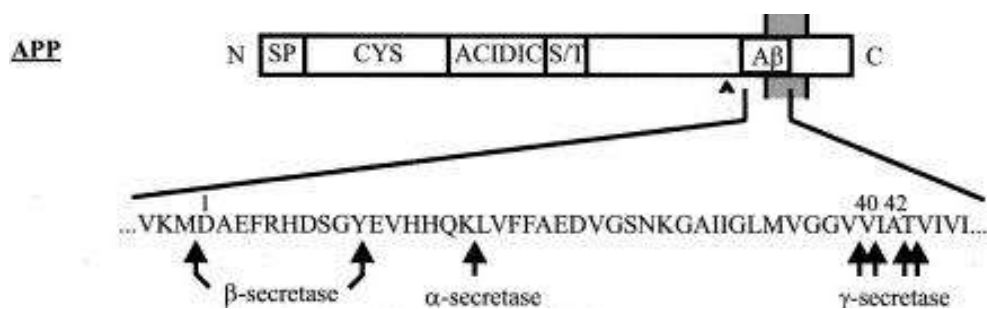
Figure 2 - Amyloid beta peptides

The two major Aβ species are Aβ1-40 and Aβ1-42. Although neurotoxicity can be induced by deposit of Aβ fibrils, recent studies have established close link between the reciprocal ratio of Aβ 1-40 and Aβ 1-42 and the stability of intermediate neurotoxic species. Moreover, Aβ 1-40 and Aβ 1-42 have been found to affect each other's aggregation.[32]

Investigation of the properties of the mixture of Aβ 1-40 and Aβ 1-42, by different research groups, clearly show that these two species interact. In vitro and in vivo studies confirmed that Aβ 1-40 delays Aβ 1-42 aggregation, whereas Aβ 1-42 has an opposite effect.[33]

Aβ 1-42, the most prone to aggregate of Aβ peptides, tends to self-assembly. Once a small but critical concentration of amyloid fibrils has accumulated, the toxic oligomeric species are mainly formed from monomeric peptide molecules through a fibril-catalyzed secondary nucleation reaction, rather than through a classical mechanism of homogeneous primary nucleation.[34] Initially, in the absence of fibrils, all oligomers are generated through primary pathways because secondary nucleation requires the presence of fibrils. Once a critical concentration of amyloid fibrils has formed, however,

secondary nucleation will overtake primary nucleation as the major source of new oligomers and fibrils proliferation.
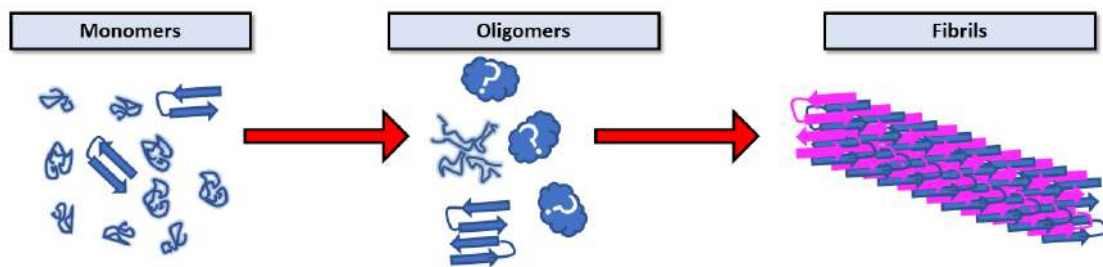

Figure 3 - Aggregate classification for amyloidogenic proteins. Monomers: Native and (generally) unfolded proteins. Oligomers: transient intermediate aggregates, soluble oligomers and protofibrils are known to be the most toxic species among the aggregates of amyloidogenic proteins. Oligomeric intermediates can either have fibrillary β-sheet structure or be in a more globular and amorphous state. Fibrils: last stage of aggregation, fibrils have well characterized cross β-sheet motif. Fibril structure, although characterized by a common cross β-sheet motif, is found be different between different proteins and isoforms of the same proteins (e.g. S-shape structure for Aβ1-42, U-shape structure for Aβ1-40).

The presence of several Aβ peptides differing in length by one or a few amino acids, and the connection between disease progression and both the total Aβ concentration and the Aβ 1-42 fraction motivates studies of co-aggregation and cross-seeding behavior among those peptides. Co-aggregation refers to the formation of mixed fibrils of any size. Cross-seeding is the ability of aggregates of one peptide to promote the conversion of soluble peptides of the other type into growing aggregates. Although there are in literature works that demonstrate that fibril-catalyzed nucleus formation and elongation are highly sequence specific events, even when Aβ 1-40 and Aβ 1-42 interact during primary nucleation,[35] no structure of fibrils including both peptides (mixed fibrils) has been reported so far. There are several works instead in which the Aβ 1-40 and Aβ 1-42 alloforms separately were extensively characterized by SSNMR, and all the Aβ 1-40 species resolved by NMR, share a U-shaped motif [36], while the Aβ 1-42 fibrils structure, which was only recently resolved, has an S-shaped fibrillar species.[37]

In the chapter 3.1 will be reported a work in which the structure of a mixed fibrils (containing Aβ1-42 and Aβ1-40 peptides) is characterized at atomic detail by SSNMR.
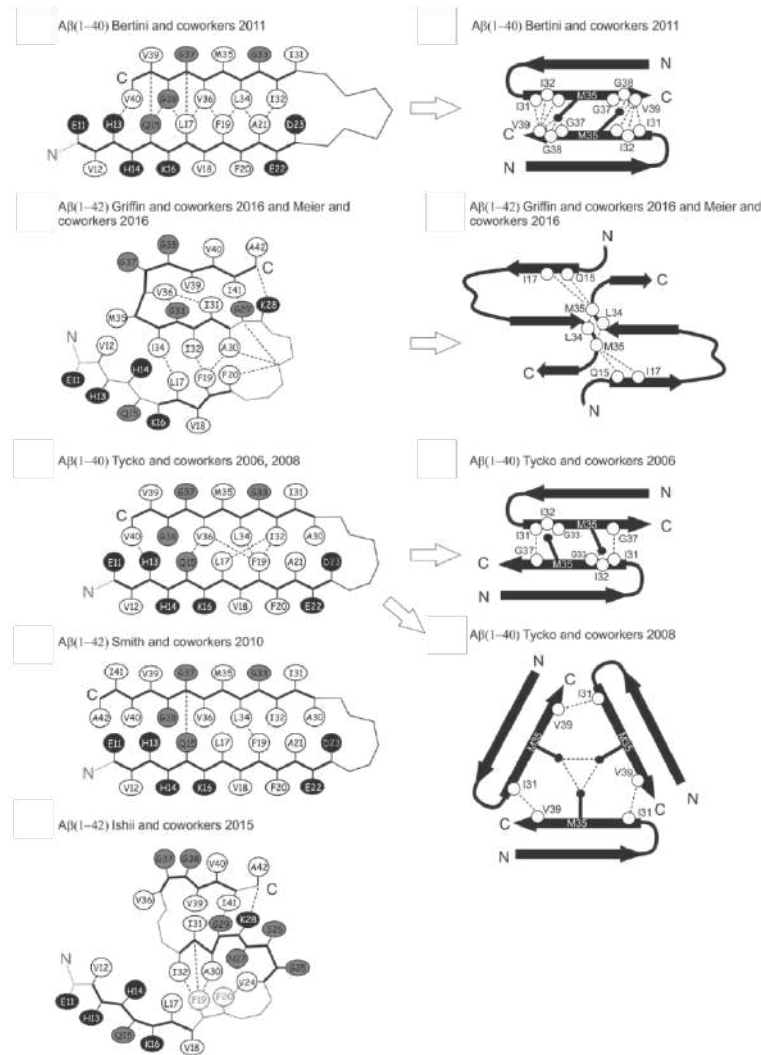
Figure 4 – Aβ 1-40 and Aβ 1-42 alloforms structures by SSNMR. All the Aβ 1-40 species share a U-shaped motif, while the Aβ 1-42 fibrils structure has an S-shaped fibrillar species.

1.4 "Seeding Aggregation Assays" (SAA)

The comprehension of the aggregation mechanism of amyloidogenic proteins has several possible direct applications. The recent development Protein Misfolding Cyclic Amplification (PMCA)[38] and Real-Time Quaking Induced Conversion (RT-QuIC)[39], born for misfolded prion protein (PrPSc) detection in biological fluids of animals and humans, have been recently applied for the detection of prone-to-aggregation α-syn in CSF and brain homogenates.[40–43] These two biophysical assays take advantage on the peculiar aggregation kinetics of prion proteins by amplifying small amounts of aggregates in biological fluids at the expense of recombinant monomeric protein added in solution. The PMCA assay was also applied for the detection of misfolded Aβ1-42 in CSF,[44] for the diagnosis of Alzheimer Disease (AD), but the existence of accurate

and reliable CSF and blood biomarkers for AD[45–47] diagnosis makes the research on new applications of PMCA and RT-QuIC assays more valuable for PD and other synucleinopathies. Furthermore, there are two very recent and interesting studies in this field. The first, of the group of Prof. A. J. Green, which performed a pilot study to evaluate the ability of α-syn RT-QuIC in stratifying PD patients;[48] the second one is a comparative study conducted by the group of Prof. Claudio Soto in collaboration with the group of Prof. A. J. Green in order to validate α-syn PMCA and α-syn RT-QuIC in an independent cohort of patients and control. These studies confirmed the incredible diagnostic potential of these two techniques. The two research groups, considering the similarities of α-syn PMCA and α-syn RT-QuIC agree that the name "*seeding aggregation assays*" (SAA) can group up the two techniques for the future.

The project on PD was born from a collaboration between *CERM* (*Centro Risonanze Magnetiche*) of the *University of Florence* and the *Laboratory of Clinical Neurochemistry* of the *University of Perugia*. The scientists involved in this research have very different academic background (physicians, chemists, biochemists, and physicists) but they work together for the ambitious goal of developing assays, based on PMCA and RT-QuIC techniques, at first for the pre-symptomatic diagnosis of PD, and for identification of compounds able to modulate α-syn aggregation, not only to improve the development of SAAs but may also to indicate novel chaperones able to inhibit the amyloidogenic potential of extracellular α-syn aggregates.
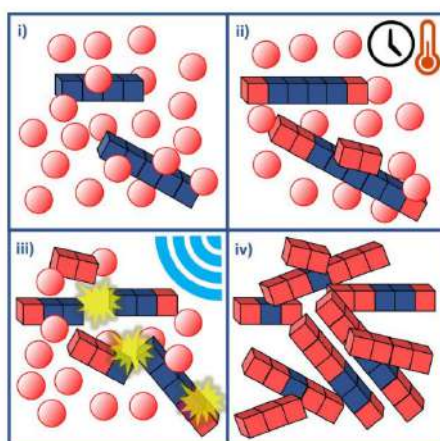
Figure 5 - PMCA assay description. i) monomer (red spheres) is incubated with seeds (blue cubes). ii) Seeds undergo elongation at their extremities and catalyze the formation of new nuclei of polymerization on their surfaces. iii) Sonication or shaking cycles increase the number of points of polymerization. Steps ii) and iii) are repeated several times, depending on the protocol adopted. iv) End point of the procedure in which the initial quantity of protein is exponentially amplified. (Reprint from Paciotti, Silvia et al. "Are We Ready for Detecting α-synuclein Prone to Aggregation in Patients? The Case of "Protein-Misfolding Cyclic Amplification" and "Real-Time Quaking-Induced Conversion" as Diagnostic Tools." Front. Neurol. (2018).)

1.5 Bioprinting and Drug Release

In the last years a very important role has been played by Hydrogels and Nanogels. Injectable hydrogels have gained wider admiration among researchers as they can be used in minimally invasive surgical procedures. Injectable gels completely fill the defect area and have good permeability and hence are promising biomaterials.[49] This technique can be effectively applied to deliver a wide range of bioactive agents, such as drugs, proteins, growth factors, and even living cells. Nanogels (highly cross-linked Nano-sized hydrogels ranges from 20-200 nm) in particular, can be administered through various routes, including oral, pulmonary, nasal, parenteral, intra-ocular etc. Hydrogels and Nanogels have a high degree of drug loading capacity, good permeation capability and tolerability. They release the drug by pH responsive, thermosensitive, volume transition, photochemical internalization and Photoisomerization mechanism. Nanogels can be classified by stimuli responsive or non-responsive behavior and type of linkages present in the network chains of gel structure. They can be used for the treatment of cancer, diabetes, inflammation, and bone regeneration. They are the novel drug delivery systems for both hydrophilic and hydrophobic drugs.[50] Furthermore, 3D Bioprinting technology has been recognized as one of the latest biotechnologies, which is highly used in tissue engineering and regenerative medicine to develop complex artificial tissue and organ structures to mimic native organs and tissues. The bioprinting involves additive deposition of cells-loaded hydrogels in a predetermined structural architecture to regenerate functional and site-specific tissues or organs. This technique integrates hydrogels live cells and controlled printing systems to create complex morphological structures, also in this case Hydrogels and Nanogels has been demonstrated to be perfect materials for the controlled release of therapeutics because of their capacity to embed biologically active agents in their watery environment, high protein-loading capacity, and excellent protein compatibility.[51]

Since they are particularly appealing for protein delivery in the chapter 3.3 it will be described a SS-NMR application for the characterization of pharmaceutically relevant proteins encapsulated in this kind of gel matrices in order to understand if the structures of these enzymes, directly related to their activity, is preserved.

For this purpose, *Escherichia coli* L-asparaginase II (ANSII) and Transthyretin (TTR) were used. ANSII is an enzyme that catalyzes the hydrolysis of L- asparagine to L-aspartic acid with the release of ammonia.
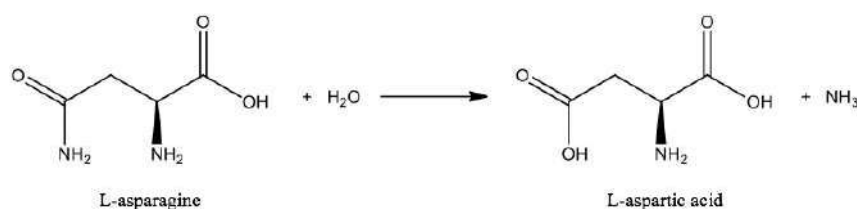

Figure 6 - Hydrolysis reaction of L -Asparagine to L- Aspartic Acid

This enzyme is a complex of four identical subunits, each of them of about 34.6 kDa (326 amino acids). Each subunit consists of two α/β domains connected by a linker. According to the crystal structure the tetramer belongs to the D2 point group and can be considered a dimer of two identical intimate dimers.

Figure 7 - Crystal structure of ANSII (PDB: 3ECA)

The catalytic site sits at the interface of each couple of intimate dimers for a total of four catalytic sites per tetramer. The medical interest for ANSII was born during 1960s when it was found that this enzyme could have effects against lymphoma, leukemia and other malignant neoplasms.[52] In particular, several medical formulations of ANSII are still currently used for the treatment of acute lymphoblastic leukemia (ALL) in children. The antitumor activity of ANSII is correlated to its effect in depletion of L-asparagine. In normal cells circulatory L-asparagine is hydrolyzed into L-asparatic acid which is pumped inside the cell and then reconverted into L-asparagine destined to protein synthesis by the action of asparagine synthase. Tumor cells instead lack

asparagine synthase; thus, they are forced to use directly exogenous L-asparagine for the protein synthesis. However, whether they are treated with ANSII-based drug L-asparagine level is drastically depressed and tumor cells head for apoptosis.[53]
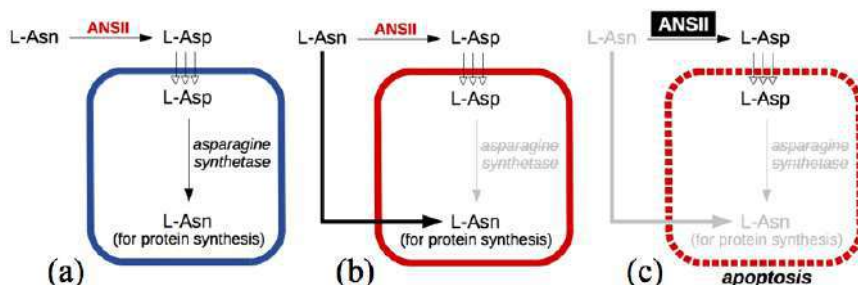

Figure 8 - Schematic representation of the action of ANSII. (a) Health cells (blue circle) use ANSII to covert L-asparagine (L-Asn) into L-aspartic acid (L-Asp) which can be delivered inside the membrane and reconvert to L-Asn by asparagine synthase. (b) Tumor cells (red circle) instead employ directly (bold black arrow) circulatory L-Asn since they lack asparagine synthase. (c) If a ANSII-based drug (black square) is administered, the depletion of circulatory L-Asn (grey font) causes the apoptosis of the cell (dot red circle).

Several medical preparations of ANSII were or are commercially available. Since 1990s, *Pegasparaginase* — a 5 kDa PEG coated ANSII formulation — is mainly used as drug. Its trade name is Oncaspar ® and is sold in UE, USA and Canada as injectable solution. Considering its relevance as biological drug and the quality of the NMR spectra collected in solution and at the solid state, ANSII was chosen as a model.

Transthyretin (TTR) is a plasma protein implicated also in human amyloid diseases. Several small molecules that bind to the thyroxine-binding site of TTR have been shown to stabilize the TTR tetramer and to inhibit amyloid fibril formation of TTR.
TTR amyloid fibrils are found in patients afflicted with familial amyloidotic polyneuropathy (FAP), familial amyloid cardiomyopathy (FAC) and senile systemic amyloidosis (SSA). More than 100 mutations have been shown to induce amyloidosis. The structure of TTR is a homotetrameric β-sheet-rich protein composed of four subunits, termed A, B, C and D. Each subunit is composed of 127 amino acid residues and has eight β-strands designated A−H and a short α-helix termed EF-helix. The TTR tetramer is formed by the association of two dimers (the AB dimer and CD dimer). The dimer−dimer contacts predominantly involve several hydrogen bonds and hydrophobic interactions between residues located in the AB and GH loops. The TTR tetramer contains two funnel-shaped T4-binding sites, each defined by a dimer−dimer interface.[54]
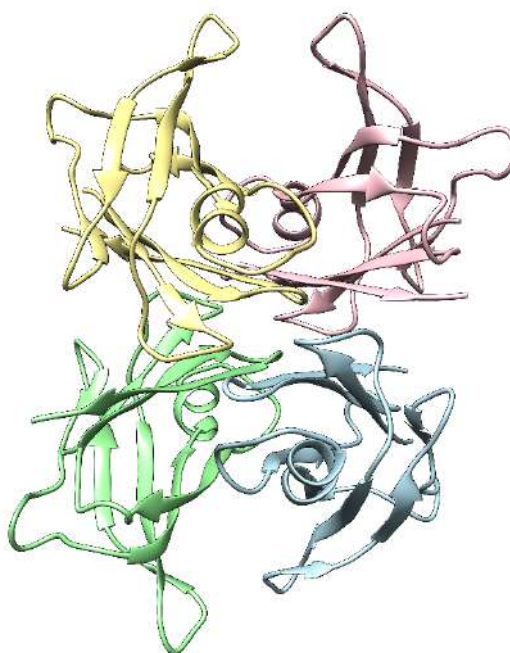
Figure 9 - Crystal structure of *TTR (PDB: 3TCT)*

TTR has a lot of interesting functions, for instance, it is a physiological protein acting as a hormone carrier. It is found in human plasma, where it binds to retinol-binding protein and to thyroxine (T4). TTR is a potential drug carrier and has been recently proposed as a multivalency Fab platform for target clustering.[55] Considering its relevance as potential delivery system and the quality of the NMR spectra collected in solution and at the solid state, TTR was chosen as a model.

2. Materials and Methods

The present chapter describes all the experimental procedures for the production of recombinant Aβ-peptides, A-synuclein, L-Asparaginase II (ANSII), Transthyretin (TTR). These proteins are used to fulfill the aims of my PhD project. Protocols for their expression and purification are reported.

2.1 Recombinant protein expression and purification

The requirement of rapid and economical production of high-quality recombinant proteins, has driven the development of a variety of strategies for achieving high level expression of protein. These strategies involve several aspects such as expression vector design, gene dosage, promoter strength, mRna stability, translation initiation and termination, host design considerations, codon usage, and fermentation factors. The proper selection and manipulation of the expression conditions is essential in obtaining the high yield of protein at low cost.

Several host systems for protein production, including bacteria, yeast, plants, fungi, insect, and mammalian cells have been developed and evaluated. Their choice depends on many factors, including cell growth characteristics, expression levels, intracellular and extracellular expression, posttranslational modifications as well as biological activity of the protein of interest.[56]

For producing many recombinant proteins, *E. coli* is one of the most widely preferred host organisms. The important advantages of this host organism are well recognized: fast growing [57], high cell density is easily attained [58], inexpensive complex media can be used for growth [59], well-characterized genetics, physiology and metabolism has led to the availability of a large number of cloning and expression strains and vectors [60], transformation with foreign DNA can be straightforward and quick and at the end also very easy to scale for fermentation. Furthermore, *E. coli* can also incorporate various labelling types, including stable isotopes for NMR studies [61] (e.g. ^{2}H, ^{13}C, ^{15}N) radiolabels [62] (e.g. ^{3}H, ^{14}C, ^{35}S) and non-natural amino acids (e.g. Se-Met for crystallography). [63]

However, there are disadvantages in the E. coli expression system, especially for producing biopharmaceuticals. These disadvantages include the inability to perform posttranslational modifications found in eukaryotic proteins, since the prokaryotic cells lack the Endoplasmic Reticulum and Golgi Apparatus, which are responsible for these

important processes, low solubility, improper protein folding, inclusion body formation, endotoxin issues, and poor secretion. These drawbacks are being addressed by advances in biotechnology, thus allowing E. coli to remain an attractive protein expression system. Affinity tags have greatly assisted the efficient purification of proteins of interest, whereas solubility tags are still a trial and error experience and the passenger protein can be differentially affected by several fusion tags.[64] Once the expression system is selected, the expression condition should be tested. It is important to take into consideration such factors as culture media composition, temperature, optical density, isopropyl-β-d-1-thiogalactoside (IPTG) inducer concentration, induction time, as well as different E. coli strain possessing different properties. For instance, *E. coli* strain BL21(DE3) and its derivatives are one of the most widely used strains for recombinant protein expression. BL21(DE3) is protease-deficient, lacking Lon protease (cytoplasm) and OmpT protease (outer membrane), it also contains the λDE3 lysogen that carries the gene for T7 RNA polymerase under control of the *lac*UV5 promoter, which can direct high-level expression of cloned genes under control of the T7 promoter. Rosetta (DE3) and Ripl Codon Pluse for gene containing rare codons, Origami (DE3) and Shuffle®T7 for protein containing disulfide bridges and all the pLysS strain that contain a gene for Lysosyme that binds to T7 RNA polymerase and inactivates the enzyme. After the addition of IPTG the expression level of the polymerase will be much higher than that of lysozyme and this will overcome the repression.

Optical density has significant effect. High cell-density culture system suffers from several drawbacks, including limited availability of dissolved oxygen, carbon dioxide levels which can decrease growth rates and stimulate acetate formation. Reduction in the mixing efficiency of the culture and heat generation. Nutrient composition and fermentation variables such as temperature, pH, and other parameters can differentially affect the translation of different mRNAs, proteolytic activity, secretion, and production levels.

The cell can be growth in different types of media: rich media, Luria Bertani (LB), 2xYT, terrific broth, NZY and minimum media (M9).

For expression of isotopically enriched samples, the M9 medium supplied with $^{15}NH_4Cl$ and ^{13}C Glucose is used.

After expression protocol optimization is essential, for the characterization, to obtain high protein purity. The best protein purification strategy is one in which the highest

level of purification is reached in the fewest steps, since each protein purification step usually result in some degree of product loss.

The preliminary step in protein purification is cell lysis. The method of choice of protein extraction depends on how fragile the protein is and how the cells are. Inadequate chosen method can affect the target protein's integrity and activity or expose it to degradative condition. Among many various mechanical, physical or chemical techniques, more frequently used are sonication, repeated freeze-thaw lysis, detergent lysis enzymatic lysis and osmotic lysis.

The subsequent steps of purification procedure involve several chromatographic methods. The three most used techniques in these works were: Ion Exchange Chromatography (IEX), Size Exclusion Chromatography (SEC) and Immobilized Metal Ion Affinity Chromatography (IMAC).

IEX separates proteins with different differences in charge. The separation is based on the reversible interaction between a charged protein and an oppositely charged chromatographic medium. Elution is usually performed by changing pH or Ionic Strenght of the elution buffer in a gradient.

SEC is a chromatographic technique in which molecules are separated by their size or better by their Hydrodynamic Radius. The column matrix is composed of a range of beads with slightly different pore sizes. When the dissolved molecules of various size flow into the column, the large molecules migrate quickly through the column, because they do not penetrate the pores.

IMAC is one of the most used technique. It separates proteins on the basis of reversible interaction between sidechains of specific amino acids and a specific ligand attached to a chromatographic matrix (mainly chelated transition metal ions e.g. Zn^{2+} or Ni^{2+}) Elution is usually performed by using a competitive agent such as imidazole.

2.2 Preparation of human recombinant Aβ-peptides with exogenous methionine

Escherichia coli BL21 (DE3) pLysS were transformed with a pET3a vector cloned with the gene encoding Aβ-peptides (1-40 and 1-42 with exogenous methionine). Fresh transformed cells were resuspended in LB rich medium, and 100-fold diluted in the medium and induced at an OD_{600} value of 0.6–0.8 with 1.2 mM IPTG; after 3-4 h of incubation at 37 °C, the cells were harvested at 7500 rpm (JA-10, Beckman Coulter). Extraction step was performed through sonication for 35 minutes followed by IBs solubilization through a homogenization process with Urea 8 M. Purification was performed via anion exchange chromatography using AKTA FPLC System through the Q-column with linear gradient of NaCl + Urea 8 M buffer (GE Healthcare HiPrep Q HP 5 mL). The last step of purification was a size-exclusion chromatography (SEC) using the preparative column Sephadex 75 HiLoad 16/60 (or 26/60) with 50 mM Ammonium acetate buffer at pH 8.5 as elution buffer.

^{13}C and ^{15}N-labeled Aβ-peptides was expressed in Escherichia coli grown in M9 minimal medium supplemented with ^{15}NH$_4$Cl and ^{13}C Glucose and purified as started for E. coli in LB medium. There are also commercially available and quite expensive enriched media (e.g., ^{2}H,^{13}C,^{15}N -enriched Silantes OD2 medium) which are particularly advantageous for the expression of deuterated labeled protein in terms of simplified cells adaptation process.

Sometimes, however main fraction of the protein is produced in the insoluble fraction known as inclusion bodies (IBs). Although IBs are usually unwanted, they represent still a possibility to obtain the protein, and they are a good alternative in the case of intrinsically disordered proteins (IDPs). In case of structured protein, this problem can be overcome by refolding process. It is a very challenging goal to achieve because each protein can require specific different approach.

When also the refolding trials are unsuccessful, the last choice is to redesign the entire system or to use another expression host.

2.3 Preparation of human recombinant α-synuclein

Escherichia coli BL21 (DE3) Gold were transformed with a pT7-7 vector cloned with the gene encoding α-synuclein. The overnight preculture of transformed cells was diluted 100-fold in LB medium and induced at an OD_{600} value of 0.6–0.8 with 1 mM IPTG; after 5 h of incubation at 37 °C, the cells were harvested at 4000 rpm (JA-10, Beckman Coulter). The extraction was carried out through osmotic shock using 100 mL of the buffer Tris 30 mM, ethylenediaminetetraacetic acid (EDTA) 2 mM, and sucrose 40%, at pH 7.2, according to Shevchik et al.[65] and Huang et al.[66]

The suspension was then ultra-centrifuged at 20 000 rpm (Type 70 Ti rotor, Beckman Coulter) for 25 min, and the pellet was collected and resuspended with 90 mL precooled ultrapure water containing 38 µL of 1 M $MgCl_2$ and then ultra-centrifuged a second time. Supernatants derived from these two centrifugation steps were combined and dialyzed against 4 L of 20 mM Tris/HCl buffer at pH 8.0. The protein was then loaded in the fast protein liquid chromatography system, and anion-exchange chromatography was carried out with 0–50% linear gradient 1 M NaCl (GE Healthcare HiPrep Q HP 16/10 Column). The collected fractions were lyophilized and resuspended in 10 mM Tris/HCl, 1 mM EDTA, and 8 M urea at pH 8.0 for chemical denaturation. To eliminate all of the protein that formed aggregates, two size-exclusion chromatographies (HiLoad 16/600 Superdex 75 pg Column) were performed with 20 mM phosphate and 0.5 mM EDTA at pH 8.0 as the elution buffer. Purified α-synuclein (α-syn) was dialyzed against Milli-Q water and lyophilized in batches for long-term storage. The Roche complete protease inhibitor cocktail was added only during the extraction step in the quantity suggested by the producer. ^{15}N-labeled wild-type α-syn was expressed in Escherichia coli grown in M9 minimal medium supplemented with [15]NH$_4$Cl and purified as started for E. coli in LB medium.

2.4 Preparation of E. coli L-Asparaginase II

E. coli C41(DE3) cells were transformed with pET-21a(+) plasmid encoding ANSII (with the signal peptide). Different culture media, always supplied with 0.1 mg mL^{-1} ampicillin sodium salt, were used for the expression of differently isotopic labelled ANSII and different expression approaches were employed. For the expression of

natural abundance (NA) ANSII, transformed cells were inoculated into 10 mL LB medium. After shaking at 37 °C overnight, the preculture was poured in 1 L LB fresh medium which was let again shake at 37 °C until OD600 nm reached 0.6. The culture was then induced with 750 μM IPTG, shaken at 25 °C overnight and pelleted by centrifugation at 7500 rpm for 15 minutes.

For the expression of [U-^{13}C,^{15}N] ANSII, a Marley-like method was applied. Transformed cells were indeed inoculated in 10 mL LB medium and the preculture was incubated at 37 °C for 8 hours under shaking, then 100-fold scaled up and kept on shaking at 37 °C overnight. The culture was centrifuged at 4000 rpm for 20 minutes at 4 °C, then the harvested pellet was resuspended in 1 L M9 minimal medium, supplied with 2.0 mM MgSO$_4$, 0.2 mM CaCl$_2$, 3.0 g ^{13}C-D-glucose and 1.2 g ^{15}N-ammonium sulphate. After one hour of shaking at 37 °C, the culture was induced with 750 μM IPTG, let shake at 25 °C for 5 hours and pelleted by centrifugation at 7500 rpm for 15 minutes.

Regarding the expression of [U-^{2}H,^{13}C,^{15}N] ANSII, transformed cells were inoculated into 10 mL ^{2}H,^{13}C,^{15}N -enriched Silantes OD2 medium. After shaking at 37 °C overnight, the preculture was scaled up to 1 L of the same enriched medium which was let again shake at 37 °C until OD600 nm reached 0.6. The culture was then induced with 750 μM IPTG, shaken at 25 °C overnight and pelleted by centrifugation at 7500 rpm for 15 minutes. Despite the expression protocol, all samples of ANSII were extracted and purified in the same way. In particular, the cellular pellet was resuspended in 10 mM Tris-HCl, pH 8.0, 15 mM EDTA, 20% w/V sucrose buffer (60 mL per liter of culture). The suspension was stirred at 4 °C for 20 minutes, then centrifuged at 10000 rpm for 30 minutes. The supernatant was discarded, whereas the pellet redissolved in H2O milli-Q (30-60 mL per liter of culture) and incubated at 4 °C for 20 minutes under stirring. The mixture was again centrifuged at 10000 rpm for 30-60 minutes. The pellet was discarded, while the supernatant was treated with solid ammonium sulfate, which was added slowly under stirring at 4 °C until reaching 50% of saturation. The precipitate was collected by centrifugation and then discarded, whereas the supernatant similarly treated with solid ammonium sulfate until reaching 90% of saturation. This time, the supernatant was discarded, while the precipitate was redissolved in a minimal amount of 20 mM Tris-HCl, pH 8.6 buffer. The solution was dialyzed against 4 L of 20 mM Tris-HCl, pH 8.6 buffer, which was refreshed once after a night. ANSII was further purified by anionic exchange chromatography using a

HiPrep 16/10 Q FF column (GE Healthcare) which was preliminary equilibrated with 20 mM Tris-HCl, pH 8.6 buffer. The sample was loaded onto the column at 3 mL min^{-1}. After washing with 3 CV of binding buffer, the protein was eluted with a 0-300 mM NaCl gradient in 15 CV. 5 mL fractions were collected and then checked by Coomassie staining SDS-PAGE gels. Fractions containing the protein were joined and concentrated down to 3 mg mL^{-1}. An additional purification was achieved by size-exclusion chromatography using a HiLoad Superdex 75 pg column (GE Healthcare). The protein was eluted in 150 mM NaPi, pH 7.5 buffer. Fractions of pure protein were joined, and the solution stored at 4°C.

2.5   Preparation of human recombinant Transthyretin

Escherichia coli BL21(DE3) RIPL PLysS cells were transformed with pET-28a(+) plasmid encoding TTR gene. The cells were cultured in LB Medium containing 0.1 mg/mL of Kanamycin, grown at 37 °C, until OD_{600} reached 0.6–0.8, then induced with 1 mM IPTG. They were further grown at 37 °C overnight and then harvested by centrifugation at 6500 rpm (JA-10 Beckman Coulter) for 15 min at 4 °C. The pellet was suspended in 20 mM Tris-HCl, pH 8.5 (60 mL per liter of culture) and sonicated at 4 °C for 40 min. The suspension was centrifuged at 40,000 rpm (F15-6x100y Thermo Scientific) for 40 min and the pellet discarded. TTR was purified by anionic-exchange chromatography using a HiPrep Q FF 16/10 column (GE Healthcare Life Science). The protein was eluted in 20 mM Tris-HCl buffer at pH 8.6 with a linear 0–1 M NaCl gradient. Fractions containing pure TTR were identified by Coomassie staining SDS-PAGE gels, then joined and purified by Size Exclusion Chromatography using HiLoad Superdex 26/60 75pg in 50 mM phosphate buffer at pH 7.5. ^{15}N-labeled wild-type TTR was expressed in Escherichia coli grown in M9 minimal medium supplemented with $^{15}NH_4Cl$ and purified as started for E. coli in LB medium.

2.6   UV-visible spectroscopy (UV-Vis)

UV-visible spectroscopy (UV-Vis) is a technique that measure the absorption of electromagnetic radiation by molecules in the ultraviolet-visible region. In this region of the electromagnetic spectrum, molecules undergo electronic transition.

UV-vis spectroscopy allows for following ligand-binding interaction, enzyme catalysis, conformation transition and is commonly used as a tool to quantify the concentration of proteins and nucleic acids. Protein concentration can be determined by the absorption around 280 nm (most of the proteins contain aromatic residues – tryptophan, tyrosine and phenylalanine), using the Beer-Lamber law reported here:

$$A = e\ c\ l$$

In which **e** is the extinction coefficient **c** is the concentration **l** is the optical length.

2.7 Fluorescence spectroscopy

Fluorescence spectroscopy is a common technique used in studies of the structure and dynamics of macromolecules, which allows a real-time observation of the dynamics of intact biological system with an unprecedented resolution. In fluorescence spectroscopy, the molecule is first excited, by absorbing a photon, from its ground electronic state to one of the various excited electronic states. This higher energy state is unstable, and when the molecule returns to the ground state again a photon with a different wavelength is emitted and can be measure.[67]

Fluorescent studies provide several information about physical and physicochemical properties of proteins, as well as their intermolecular interactions and conformational changes. In addition, fluorescence spectroscopy can be used to study those structural and dynamics properties of protein which are directly related to such biological functions as specific binding, biocatalysis, membrane transport, and muscular motility. However, the use of Fluorescence spectroscopy is only possible when the biologically active compounds contain in their structure a fluorophore.

Fluorescent proteins contain three aromatic amino acid residues (tryptophan, tyrosine and phenylalanine) which may contribute to their intrinsic fluorescence when are excited by UV light. The most important is the presence of tryptophan, which has much stronger fluorescence and higher quantum yield then the other two aromatic amino acids.

In this thesis work fluorescence spectroscopy was used to monitor the formation of aggregates of α-synuclein and amyloids. In vitro, the amyloid fibrils are easily and readily detected by using benzothiazole salt Thioflavin T (ThT), a commonly used

probe to monitor their formation. In particular, the binding of ThT to amyloid fibrils, induces a shift in excitation maximum (385 nm to 450 nm) and emission maximum (445 nm to 482 nm), as is shown in the spectrum in the Figure 10.
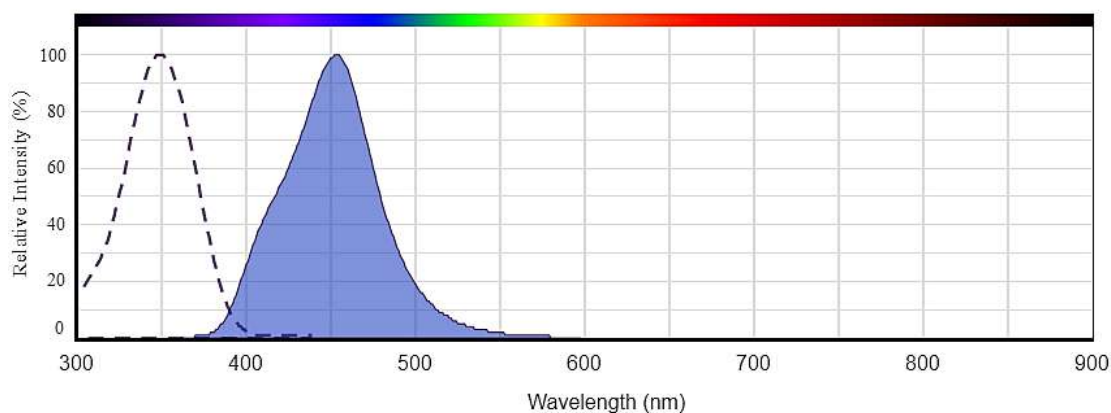

Figure 10 - Excitation/emission spectrum of the fluorophore ThT (Reprint from AAT Bioquest's interactive Spectrum Viewer tool)

The mechanism of ThT strong fluorescence signal at 482 nm has been associated with the rotational immobilization of the central C–C bond connecting the benzothiazole and aniline rings (Figure 11). The target sites of ThT-fibrils interaction are the side chain channels along the long axis of amyloid filaments and the minimal binding site on the fiber surface has been suggested to extend across three or four consecutive β-strands. The reagent binds rapidly and specifically to the anti-parallel beta-sheet fibrils but does not bind to monomer or oligomeric intermediates. In addition, the binding of ThT does not interfere with the aggregation of beta-amyloid peptide into amyloid fibrils.
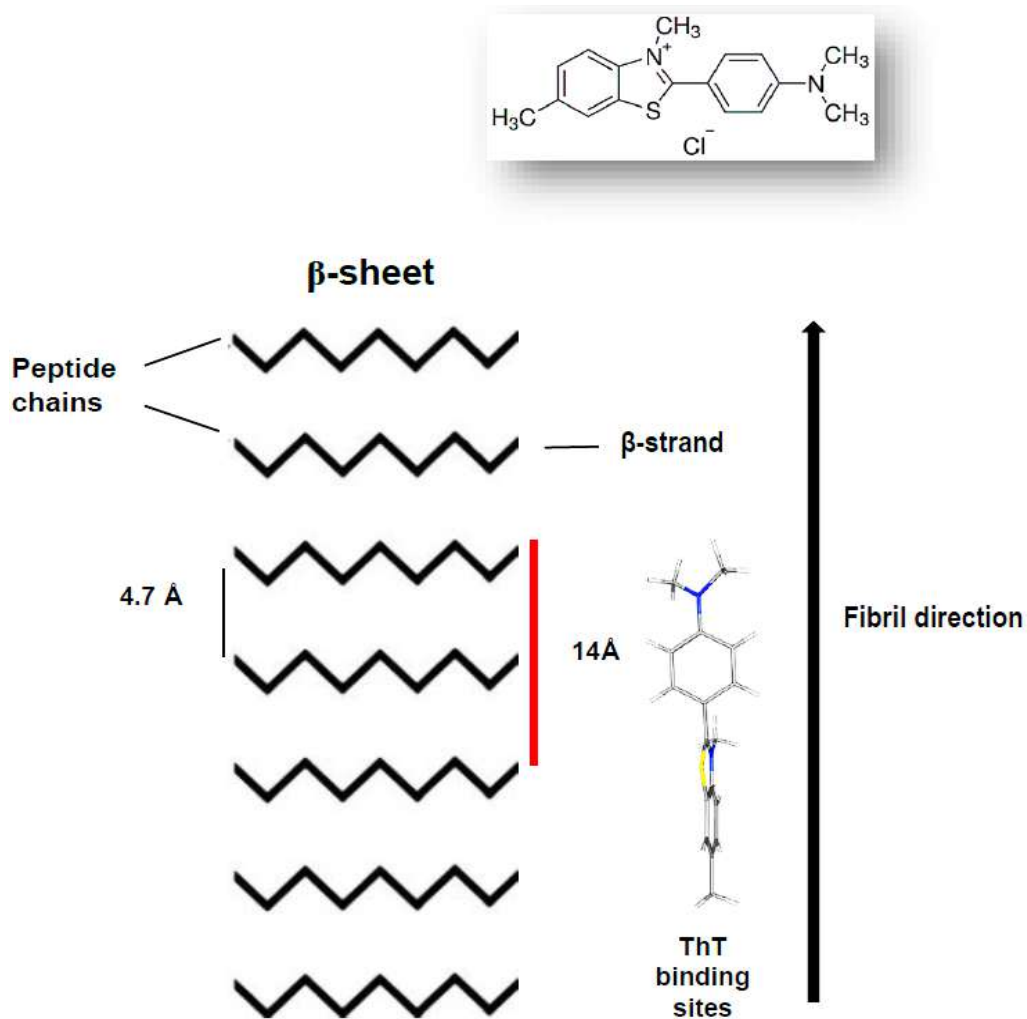
**Figure 11 -** Schematic illustration of Thioflavin T oriented with its long axis parallel to the long axis of the fibril. The minimal binding site on the fiber surface is extended across three consecutive β-strands (14 Å). (Reprint from Groenning, M. Binding mode of Thioflavin T and other molecular probes in the context of amyloid fibrils—current status. *J Chem Biol* 3, 1–18 (2010). https://doi.org/10.1007/s12154-009-0027-5)

2.8   Transmission Electron Microscopy (TEM)

Transmission electron microscopy (TEM) is a microscopy technique in which a beam of electrons is transmitted through an ultra-thin specimen of interest, interacting with the specimen as it passes through. An image is formed from the interaction of the electrons transmitted through the specimen. Once the electrons pass the anode, they are focused by condenser lens onto the sample grid. The sample grid is usually a copper mesh grid with a support film. Before TEM analysis, specimen of interest is adsorbed to this film and typically stained using a heavy metal salt which have high atomic number capable of scattering electrons.

The TEM reveals levels of detail and complexity inaccessible by light microscopy because it uses a focused beam of high energy electrons and allows detailed micro-structural examination through high-resolution. It is used to investigate the morphology, examine the structure, composition, and properties of specimens in submicron detail.

In this thesis work was used to characterize the morphology and molecular architecture of Amyloid peptides and Alfa-Synuclein fibrils and prefibrillar aggregates.

2.9   Atomic Force Microscopy (AFM)

Atomic Force Microscopy (AFM) is the most common of the Scanning Probe Microscopy (SPM) techniques, diffusely applied in a wide range of research as well as industrial fields. The surface is probed through a sharp tip, located at the free end of a cantilever that is 100 to 400 µm long. This tip is some microns long, with a curvature at the very end that is often less than 10 nm; high force sensitivities (between 10^{-7} and 10^{-12} N) make possible the measurement of a single, chemical bond-breaking force. Having an appropriately sized tip is important for acquiring real surface features and atomic resolutions, but advancements in piezoelectric transducers (PZT) are responsible for enabling SPMs to probe a surface with sub-Ångstrom precision. As the tip is scanned over the sample, or the sample is scanned under the tip, forces between the tip and the sample surface cause spatial deflections and oscillations of the cantilever. The key information gathered in AFM comes with

measuring those deflections, quantified by means of an optical lever system, coupled with position sensitive a photodiode.

2.10 SSNMR spectroscopy

NMR spectroscopy is a technique based on the interaction of the nuclear spin with the electromagnetic radiation, in the presence of an external magnetic field. Nowadays solution and solid-state NMR (SSNMR), are powerful tools to characterize the structure, dynamics, and interactions of biomolecules. Solution NMR is the most common tool for structure determination and SSNMR is in continue development in terms of sample preparation, device optimization and theoretical background.

SSNMR is one of the best techniques for obtaining atomic resolution structures of amyloid fibrils, large protein complexes and bioconjugates.

In this thesis work SSNMR was applied to detailed structural characterization of fibrillar assemblies, evaluation of the maintenance of High Order Structure (HOS) of protein encapsulated in hydrogels. In these works, a method defined as sedimented solutes NMR (SedNMR) was applied. In this method, experiments are used to observe proteins that are sedimented from solution using an ultra-centrifugal field.[68]

To immobilize macromolecules and make them amenable for SedNMR studies, sedimentation through in situ ultracentrifugation, by magic angle spinning (MAS) was performed.[69]

This application is possible on several systems with high molecular weight that are large enough to sediment and thus become visible by SSNMR.[70]

3. Results and Discussion

3.1 Mixing Aβ1-40 and Aβ1-42 peptides generates unique amyloid fibrils

The aim of this work is to characterize the structure of the mixed fibrils (containing Aβ1-42 and Aβ1-40 peptides) at atomic detail. My contribution to this project was to express and purify Aβ1-42 and Aβ1-40 monomers and to generate fibrils by mixing the isotopically enriched peptides in an equimolar ratio. Aβ peptides have been expressed through different labeling schemes to confirm the observations previously hypothesized in our lab during the past years. To investigate the arrangement of the fibrils obtained by mixing Aβ1-40 and Aβ1-42 peptides, equimolar solutions of the two proteins were mixed and the resulting fibrils investigated by Solid-state NMR Spectroscopy (SSNMR). I was involved in the production of mixed fibrils using specific labeling schemes to record SSNMR experiments to demonstrate the interleaved arrangement of Aβ1-40 and Aβ1-42 peptides along the fibril axis. In particular, these labeling schemes are:

- ^{15}N-uniformly enriched Aβ1-42/ ^{13}C-uniformly enriched Aβ1-40.
- ^{15}N-uniformly enriched Aβ1-42/ natural isotopic abundance Aβ1-40 (control sample).
- ^{15}N-uniformly enriched Aβ1-40/ natural isotopic abundance Aβ1-42 (control sample)

In our experimental conditions, under vigorous agitation (aimed at favoring the establishment of a thermodynamic equilibrium of Aβ1-40 and Aβ1-42), a very stable and homogeneous interlaced 1:1 assembly was formed. The characterization of mixed Aβ fibrils has been carried out by acquiring High-Resolution SS-NMR Spectra in combination with microscopy (AFM and TEM).

Check for updates

Mixing Aβ(1−40) and Aβ(1−42) peptides generates unique amyloid fibrils†

Linda Cerofolini, [a] Enrico Ravera, [ab] Sara Bologna, [ab] Thomas Wiglenda, [c] Annett Böddrich, [c] Bettina Purfürst, [d] Iryna Benilova, ‡[e] Magdalena Korsak,§[f] Gianluca Gallo, ¶[ab] Domenico Rizzo, [ab] Leonardo Gonnelli, [ab] Marco Fragai, [ab] Bart De Strooper, *[eg] Erich E. Wanker *[c] and Claudio Luchinat *[abf]

Recent structural studies show distinct morphologies for the fibrils of Aβ(1−42) and Aβ(1−40), which are believed not to co-fibrillize. We describe here a novel, structurally-uniform 1:1 mixed fibrillar species, which differs from both pure fibrils. It forms preferentially even when Aβ(1−42):Aβ(1−40) peptides are mixed in a non-stoichiometric ratio.

Among the major unknowns in Alzheimer's disease research are the mechanisms by which different Aβ(1−42) and/or Aβ(1−40) aggregate species cause toxicity in mammalian cells. Most biophysical studies on Aβ peptides reported in the literature only deal with the behavior of a single alloform of the peptide, and do not consider the many Aβ peptides that coexist *in vivo*.[1–6] However, it has been widely demonstrated that increasing amounts of Aβ(1−42) relative to Aβ(1−40) speed up the aggregation kinetics and also alter the pattern of spontaneously formed oligomeric species,[7–11] which are considered the main toxic

species.[12–14] The rate of formation of these species is markedly different between the two main isoforms.[15,16]

Kuperstein *et al.* have previously reported that all mixtures of Aβ(1−42) and Aβ(1−40) peptides with ratios higher than 3:7 are equally prone to aggregation, and show a similar lag-phase.[10] Based on this observation, it was concluded that toxicity results from an increase of the Aβ(1−42)/Aβ(1−40) ratio,[10] suggesting that the properties of mixture do not match the sum of the properties of the two individual components, therefore implying the formation of mixed species. The formation of mixed intermediate species has been proposed,[17] and can be considered the result of the diverse conversion and aggregation pathways of these peptides.[15,18,19] However, it is widely believed that Aβ(1−42) and Aβ(1−40) do not co-fibrillize.[17] Whether the two alloforms interplay or act separately instead is an important question, as this has implications for the propagation of fibrillar seeds in the brain.[20,21]

We have prepared fibrils in the same experimental conditions as those previously used to obtain well-shaped fibrils of pure Aβ(1−40),[22] using a 1:1 ratio of the two isoforms (Fig. S1 and S2, ESI†). A new single species is spontaneously formed. The mixtures before fibrillization show a marked toxicity to cultured neurons (see for the characterization Fig. S3, ESI†). When a 3:7 Aβ(1−42):Aβ(1−40) ratio (previously found to be the most toxic mixture[10]) is used, the same single species is observed, but with the excess Aβ(1−40) simultaneously forming the same pure fibrillar species previously characterized by Bertini *et al.*[22] (Fig. S4, ESI†). No cross-peaks among the two species are observable. The ratio between the two species has been estimated from the intensity of the signals in the 2D ^{13}C–^{13}C correlation spectra and found to be approximately 4:3, in line with the expectation (see ESI†).‖

We have acquired solid-state NMR spectra on two samples of the species obtained at the 1:1 ratio with either one of the peptides uniformly ^{13}C–^{15}N labeled. The spectra of the labeled Aβ(1−42) and the Aβ(1−40) components in the two 1:1 mixed samples are superimposable (Fig. 1). The spectra of the Aβ(1−42)

a Magnetic Resonance Center (CERM), University of Florence and Interuniversity Consortium for Magnetic Resonance of Metalloproteins (CIRMMP), Via L. Sacconi 6, 50019, Sesto Fiorentino (FI), Italy.
E-mail: claudioluchinat@cerm.unifi.it
b Department of Chemistry "Ugo Schiff", University of Florence, Via della Lastruccia 3, 50019, Sesto Fiorentino (FI), Italy
c Neuroproteomics, Max Delbrück Center for Molecular Medicine, Robert-Roessle-Strasse 10, 13125 Berlin, Germany. E-mail: ewanker@mdc-berlin.de
d Core Facility Electron Microscopy, Max-Delbrück Center for Molecular Medicine, Robert-Roessle-Strasse 10, 13125 Berlin, Germany
e VIB Center for Brain and Disease Research, Herestraat 49, 3000 Leuven, Belgium
f Giotto Biotech S.R.L., Via Madonna del Piano 6, 50019 Sesto Fiorentino (FI), Italy
g KULeuven, Department of Neurology, Herestraat 49, 3000 Leuven, Belgium.
E-mail: bart.destrooper@kuleuven.vib.be
† Electronic supplementary information (ESI) available. See DOI: 10.1039/d0cc02463e
‡ Current address: MRC Prion Unit at UCL, Institute of Prion diseases, Courtauld building, 33 Cleveland Street, London W1W7FF, UK.
§ Current address: Roche Polska Sp. zo. o. Domaniewska 28, 02-672 Warszawa, Poland.
¶ Current address: Fresenius Kabi, Via Camagri 41, Verona, Italy.

Communication
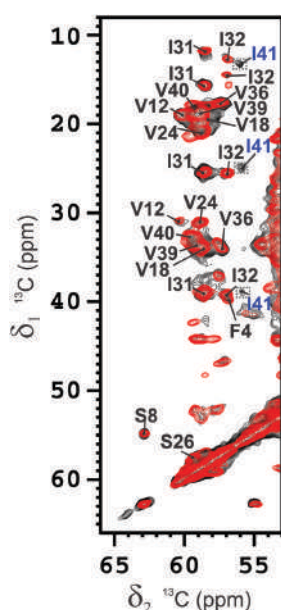
Fig. 1 Section of the overlaid 2D ^{13}C–^{13}C-correlation spectra of the Aβ(1–42) component (black) and of the Aβ(1–40) component (red) in the 1 : 1 Aβ(1–42) : Aβ(1–40) mixed fibrils. Mixing time = 100 ms. Magnetic field: 700 MHz (16.4 T), dimension of rotor: 3.2 mm (∼14 mg of fibrils), 12 kHz spinning, 100 kHz ^{1}H decoupling, T = 283 K. The resonances are assigned as indicated. The crosspeaks corresponding to I41 are magnified by a factor 2.

Scheme 1 Topologies of monomer and the interprotofilament interface identified in the present work and in previously studied pure Aβ(1–40).[22] The dashed/dotted lines represent unambiguous experimental restraints used to derive the corresponding topology. In the schematic description of the monomer, the hydrophobic, acidic/basic, and other types of residues are shown in white, black, and gray, respectively. The filled black circles represent the C_ε of the Met35 residue. Other residues included in SS-NMR-observed structural restraints for linking the protofilaments are shown as hollow circles.

component show some extra peaks (particularly for S8 and G9), suggesting that the Aβ(1–42) may be more rigid than the Aβ(1–40) in the N-terminal loop, as well as a few minor peaks attributable to other species, possibly linked to a slight imbalance in the concentration of the two isoforms. When assigned[23,24] (Fig. S6 and S7, ESI†), the spectra yield the same intra- and intermolecular contacts, showing that the conformation of the two peptides is identical. Signals correlating the side chains of Leu17 with Leu34/Val36, Phe19 with Gly33/Leu34, Ala21 with Ile32, and His13 with Val40 were detected and assigned unambiguously on the ^{13}C–^{13}C correlation[25] spectra at different mixing times on both samples (see Table S1, ESI†). These contacts are only consistent with a U-shaped conformation of the monomer typical of Aβ(1–40) and not with the characteristic S-shaped conformation of Aβ(1–42) (Scheme S1, ESI†).

When the unambiguous contacts are reported on the topology of the monomer, it is clear that in the β-arch the reciprocal packing of the two β-strands ($β_1$ and $β_2$) (Fig. S8A, ESI†), is different from that of pure Aβ(1–40) obtained in the same conditions[22] (Fig. S8B, ESI,† and Scheme 1) and, instead, resembles that reported for fibrils of pure Aβ(1–40) or Aβ(1–42) obtained under different conditions by Tycko and Smith and coworkers[2,26,27] (Scheme S1, see ESI,† for the details of structure

calculations), and has also the same register of the highly toxic oligomers stabilized by an intramolecular disulfide bond between residues 21 and 30, mutated to cysteine.[28]

As previously observed,[22] Lys28 is exposed to the solvent and not involved in the formation of salt-bridges.[29–32] The analysis of the cross-peaks in the ^{13}C–^{13}C correlation spectra supports the presence of a parallel arrangement of the protein molecules along the β-spine. No cross-peaks correlating the N-terminus and C-terminus of $β_1$ or $β_2$ strands have been observed in the spectrum of either sample. This indicates that the β-strand-turn-β-strand motif is organized in parallel cross-β sheets as reported in the literature for mature fibrils of Aβ(1–40).[2,22,26,27,33,34] This model is further supported by the presence of a single pattern of signals for each residue in the SS-NMR spectra. For symmetry considerations, this is consistent only with the presence of a parallel in-registry β-spine.[35] Each of the β-spines constituting the sides of the cross-β sheet arrangement is called "protofilament" for simplicity.

More specifically, the $β_1$–$β_2$ arrangement of the 1–40 filaments of both Aβ(1–40) and Aβ(1–42) are identical in the mixed fibrils.

31

Fig. 3 Structural model of Aβ(1−40)/Aβ(1−42) interlaced mixed fibrils. The Aβ(1−42) polypeptide is colored in magenta while the Aβ(1−40) polypeptide in blue.
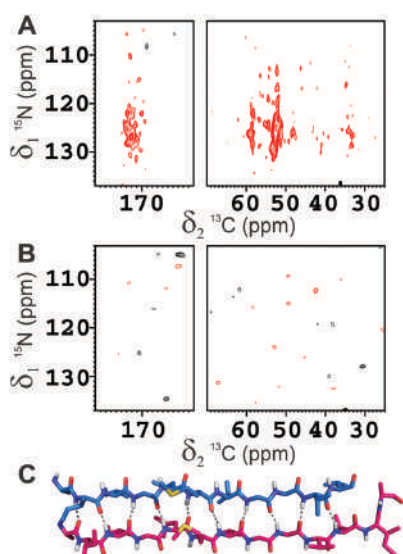

Fig. 2 2D ^{15}N–^{13}C hNhhC spectra of the Aβ(1−42) : Aβ(1−40) mixed fibrils in the 1 : 1 molar ratio, where (A) Aβ(1−42) is ^{15}N-enriched and Aβ(1−40) is ^{13}C-enriched, (B) Aβ(1−42) is ^{15}N-enriched and Aβ(1−40) is in natural abundance. Magnetic field: 800 MHz (19 T, 201.2 MHz ^{13}C Larmor frequency), dimension of rotor: 3.2 mm, 16 kHz spinning, 80 kHz ^{1}H decoupling; number of scans: 2048. The strong cross peaks in the carbonyl and C_α regions in (A) and the total absence of signals in (B) clearly demonstrates that the transfer in (A) is occurring between the two alloforms. (C) The H-bonds pattern of Aβ(1−42) interlaced with Aβ(1−40) in the β-spine is displayed.

Homogeneous protofilaments of either Aβ(1−40) or Aβ(1−42) can be excluded by the presence in the spectra of cross-peaks between N-terminus and C-terminus of the β_2 strand, which would not be present if all the labeled peptide molecules were in the same protofibril (Fig. S9 and S10, ESI†). We are thus left with the possibility of an interlaced arrangement. To further prove this, fibrils from 1 : 1 mixtures of ^{15}N-enriched Aβ(1−42) and ^{13}C-enriched Aβ(1−40) were prepared, in such a way as to have NMR signals only if ^{15}N and ^{13}C nuclei are in close proximity. In particular, a two-dimensional nitrogen-carbon correlation experiment, 2D ^{15}N–^{13}C hNhhC[36] shows good signal intensity in several parts of the spectrum and particularly in the NH-carbonyl region, thus demonstrating direct, short range contacts between Aβ(1−40) and Aβ(1−42) filaments (Fig. 2), further confirmed by a 1D TEDOR experiment (Fig. S11, ESI†).[37] These data demonstrate beyond any doubt that Aβ(1−40) and Aβ(1−42) can co-fibrillize in a 1 : 1 ratio to form an interlaced fibril (Fig. 3 and Fig. S12, ESI†).

The heterogeneity observed in the SS-NMR spectra of pure Aβ(1−42) under the present conditions may reflect the endpoint of a fast aggregation reaction, which is instead prevented by the formation of a 1 : 1 product when Aβ(1−40) and Aβ(1−42) are present simultaneously in solution and which also favors a
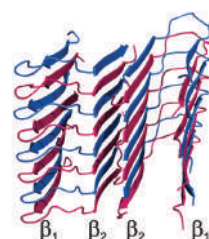
conformation with the turn at positions G25 and S26 over the one with the turn at positions E22 and D23, which are putatively involved in the toxicity of early aggregates.[38,39] In the present interlaced fibrils, the observed U-shape register ideally accommodates the requirements of both filaments, and is likely to provide an extra stabilization by preventing the steric clashes potentially caused by Ile41 and Ala42 because these two residues are alternatively present and absent in the interlaced fibrils. The buried surface area is maximum for the mixture in this arrangement, see Table S5 (ESI†).

The present observation that a single fibrillary species is obtained from mixtures of Aβ(1−42) and Aβ(1−40) indicates that the interplay between the two alloforms may contribute to extend the number of possible polymorphs formed by these peptides, increasing the complexity of the structural landscape of the amyloid aggregates, which may correspond to phenotypic differences.[40] We expect that the availability of a structural model for this mixed-species will be useful for a better understanding of the variable nature of cross-seeding,[29,41,42] as well as in the development of potential drugs.[43,44]

32

Conflicts of interest

There are no conflicts to declare.

Notes and references

‖ Structures formed by a molar excess of Aβ(1–42) were not analyzed, but Aβ(1–42) by itself yields a strongly heterogeneous mixture under the present conditions (Fig. S5, ESI†).

1 R. Tycko, *Protein Sci.*, 2014, **23**, 1528–1539.
2 A. K. Paravastu, R. D. Leapman, W.-M. Yau and R. Tycko, *Proc. Natl. Acad. Sci. U. S. A.*, 2008, **105**, 18349–18354.
3 Y. Qi-Takahara, M. Morishima-Kawashima, Y. Tanimura, G. Dolios, N. Hirotani, Y. Horikoshi, F. Kametani, M. Maeda, T. C. Saido, R. Wang and Y. Ihara, *J. Neurosci.*, 2005, **25**, 436–445.
4 D. M. Bolduc, D. R. Montagna, M. C. Seghers, M. S. Wolfe and D. J. Selkoe, *eLife*, 2016, **5**, e17578.
5 J.-P. Colletier, A. Laganowsky, M. Landau, M. Zhao, A. B. Soriaga, L. Goldschmidt, D. Flot, D. Cascio, M. R. Sawaya and D. Eisenberg, *Proc. Natl. Acad. Sci. U. S. A.*, 2011, **108**, 16938–16943.
6 D. M. Bolduc and M. S. Wolfe, *Proc. Natl. Acad. Sci. U. S. A.*, 2014, **111**, 14643–14644.
7 Y. Yoshiike, D.-H. Chui, T. Akagi, N. Tanaka and A. Takashima, *J. Biol. Chem.*, 2003, **278**, 23648–23655.
8 A. Jan, O. Gokce, R. Luthi-Carter and H. A. Lashuel, *J. Biol. Chem.*, 2008, **283**, 28176–28189.
9 A. Jan, D. M. Hartley and H. A. Lashuel, *Nat. Protocols*, 2010, **5**, 1186–1209.
10 I. Kuperstein, K. Broersen, I. Benilova, J. Rozenski, W. Jonckheere, M. Debulpaep, A. Vandersteen, I. Segers-Nolten, K. Van Der Werf, V. Subramaniam, D. Braeken, G. Callewaert, C. Bartic, R. D'Hooge, I. C. Martins, F. Rousseau, J. Schymkowitz and B. De Strooper, *EMBO J.*, 2010, **29**, 3408–3420.
11 K. Pauwels, T. L. Williams, K. L. Morris, W. Jonckheere, A. Vandersteen, G. Kelly, J. Schymkowitz, F. Rousseau, A. Pastore, L. C. Serpell and K. Broersen, *J. Biol. Chem.*, 2012, **287**, 5650–5660.
12 B. R. Sahoo, S. J. Cox and A. Ramamoorthy, *Chem. Commun.*, 2020, **56**, 4627–4639.
13 D. M. Walsh, I. Klyubin, J. V. Fadeeva, W. K. Cullen, R. Anwyl, M. S. Wolfe, M. J. Rowan and D. J. Selkoe, *Nature*, 2002, **416**, 535–539.
14 K. Ono, *Neurochem. Int.*, 2018, **119**, 57–70.
15 G. Bellomo, S. Bologna, L. Gonnelli, E. Ravera, M. Fragai, M. Lelli and C. Luchinat, *Chem. Commun.*, 2018, **54**, 7601–7604.
16 T. C. T. Michaels, A. Šarić, S. Curk, K. Bernfur, P. Arosio, G. Meisl, A. J. Dear, S. I. A. Cohen, C. M. Dobson, M. Vendruscolo, S. Linse and T. P. J. Knowles, *Nat. Chem.*, 2020, **12**, 445–451.
17 R. Cukalevski, X. Yang, G. Meisl, U. Weininger, K. Bernfur, B. Frohm, T. P. J. Knowles and S. Linse, *Chem. Sci.*, 2015, **6**, 4215–4233.
18 Y. Lin, B. R. Sahoo, D. Ozawa, M. Kinoshita, J. Kang, M. H. Lim, M. Okumura, Y. H. Huh, E. Moon, J. H. Jang, H.-J. Lee, K.-Y. Ryu, S. Ham, H.-S. Won, K-S. Ryu, T. Sugiki, J. K. Bang, H.-S. Hoe, T. Fujiwara, A. Ramamoorthy and Y.-H. Lee, *ACS Nano*, 2019, **13**, 8766–8783.
19 I. Bertini, G. Gallo, M. Korsak, C. Luchinat, J. Mao and E. Ravera, *ChemBioChem*, 2013, **14**, 1891–1897.
20 R. Tycko, *Nature*, 2016, **537**, 492–493.
21 M. Jucker and L. C. Walker, *Nat. Neurosci.*, 2018, **21**, 1341–1349.
22 I. Bertini, L. Gonnelli, C. Luchinat, J. Mao and A. Nesi, *J. Am. Chem. Soc.*, 2011, **133**, 16013–16022.
23 A. Schuetz, C. Wasmer, B. Habenstein, R. Verel, J. Greenwald, R. Riek, A. Böckmann and B. H. Meier, *ChemBioChem*, 2010, **11**, 1543–1551.
24 S. Sun, Y. Han, S. Paramasivam, S. Yan, A. E. Siglin, J. C. Williams, I.-J. L. Byeon, J. Ahn, A. M. Gronenborn and T. Polenova, in *Protein NMR Techniques*, ed. A. Shekhtman and D. S. Burz, Humana Press, Totowa, NJ, 2012, pp. 303–331.
25 B. Hu, O. Lafon, J. Trébosc, Q. Chen and J.-P. Amoureux, *J. Magn. Reson.*, 2011, **212**, 320–329.
26 A. T. Petkova, W.-M. Yau and R. Tycko, *Biochemistry*, 2006, **45**, 498–512.
27 M. Ahmed, J. Davis, D. Aucoin, T. Sato, S. Ahuja, S. Aimoto, J. I. Elliott, W. E. Van Nostrand and S. O. Smith, *Nat. Struct. Mol. Biol.*, 2010, **17**, 561–567.
28 A. Sandberg, L. M. Luheshi, S. Söllvander, T. P. de Barros, B. Macao, T. P. J. Knowles, H. Biverstål, C. Lendel, F. Ekholm-Petterson, A. Dubnovitsky, L. Lannfelt, C. M. Dobson and T. Härd, *Proc. Natl. Acad. Sci. U. S. A.*, 2010, **107**, 15595–15600.
29 Y. Xiao, B. Ma, D. McElheny, S. Parthasarathy, F. Long, M. Hoshi, R. Nussinov and Y. Ishii, *Nat. Struct. Mol. Biol.*, 2015, **22**, 499–505.
30 M. T. Colvin, R. Silvers, Q. Z. Ni, T. V. Can, I. Sergeyev, M. Rosay, K. J. Donovan, B. Michael, J. Wall, S. Linse and R. G. Griffin, *J. Am. Chem. Soc.*, 2016, **138**, 9663–9674.
31 J.-X. Lu, W. Qiang, W.-M. Yau, C. D. Schwieters, S. C. Meredith and R. Tycko, *Cell*, 2013, **154**, 1257–1268.
32 A. T. Petkova, R. D. Leapman, Z. Guo, W.-M. Yau, M. P. Mattson and R. Tycko, *Science*, 2005, **307**, 262–265.
33 A. T. Petkova, Y. Ishii, J. J. Balbach, O. N. Antzutkin, R. D. Leapman, F. Delaglio and R. Tycko, *Proc. Natl. Acad. Sci. U. S. A.*, 2002, **99**, 16742–16747.
34 W. Qiang, W.-M. Yau, Y. Luo, M. P. Mattson and R. Tycko, *Proc. Natl. Acad. Sci. U. S. A.*, 2012, **109**, 4443–4448.
35 J. T. Nielsen, M. Bjerring, M. D. Jeppesen, R. O. Pedersen, J. M. Pedersen, K. L. Hein, T. Vosegaard, T. Skrydstrup, D. E. Otzen and N. C. Nielsen, *Angew. Chem., Int. Ed.*, 2009, **48**, 2118–2121.
36 A. Lange, S. Becker, K. Seidel, K. Giller, O. Pongs and M. Baldus, *Angew. Chem., Int. Ed.*, 2005, **44**, 2089–2092.
37 C. P. Jaroniec, C. Filip and R. G. Griffin, *J. Am. Chem. Soc.*, 2002, **124**, 10728–10742.
38 Y. Matsushima, R. C. Yanagita and K. Irie, *Chem. Commun.*, 2020, **56**, 4118–4121.
39 A. R. Foley, H.-W. Lee and J. A. Raskatov, *J. Org. Chem.*, 2020, **85**, 1385–1391.
40 J. Stöhr, C. Condello, J. C. Watts, L. Bloch, A. Oehler, M. Nick, S. J. DeArmond, K. Giles, W. F. DeGrado and S. B. Prusiner, *Proc. Natl. Acad. Sci. U. S. A.*, 2014, **111**, 10329–10334.
41 M. Törnquist, R. Cukalevski, U. Weininger, G. Meisl, T. P. J. Knowles, T. Leiding, A. Malmendal, M. Akke and S. Linse, *Proc. Natl. Acad. Sci. U. S. A.*, 2020, **117**(21), 11265–11273.
42 J. Tran, D. Chang, F. Hsu, H. Wang and Z. Guo, *FEBS Lett.*, 2017, **591**, 177–185.
43 M. Zhang, J. Zheng, R. Nussinov and B. Ma, *Antibodies*, 2018, **7**(3), 25.
44 J. Zhao, R. Nussinov and B. Ma, *J. Biol. Chem.*, 2017, **292**, 18325–18343.

SUPPORTING INFORMATION

Mixing Aβ(1-40) and Aβ(1-42) peptides generates unique amyloid fibrils

Linda Cerofolini[a], Enrico Ravera[a,b], Sara Bologna[a,b], Thomas Wiglenda[c], Annett Böddrich[c], Bettina Purfürst[d], Iryna Benilova[e,§], Magdalena Korsak[f,l], Gianluca Gallo[a,b,#], Domenico Rizzo[a,b], Leonardo Gonnelli[a,b], Marco Fragai[a,b], Bart De Strooper*[e,g], Erich E. Wanker*[c], Claudio Luchinat*[a,b,f]

a. Magnetic Resonance Center (CERM), University of Florence and Interuniversity Consortium for Magnetic Resonance of Metalloproteins (CIRMMP), Via L. Sacconi 6, 50019, Sesto Fiorentino (FI), Italy

b. Department of Chemistry "Ugo Schiff", University of Florence, Via della Lastruccia 3, 50019, Sesto Fiorentino (FI), Italy

c. Neuroproteomics, Max Delbrück Center for Molecular Medicine, Robert-Roessle-Strasse 10, 13125 Berlin, Germany

d. Core facility electron microscopy, Max-Delbrück Center for Molecular Medicine, Robert-Roessle-Strasse 10, 13125 Berlin, Germany

e. VIB Center for Brain and Disease research, Herestraat 49, 3000 Leuven, Belgium

f. Giotto Biotech S.R.L., Via Madonna del Piano 6, 50019 Sesto Fiorentino (FI), Italy.

g. KULeuven, Department of Neurology, Herestraat 49, 3000 Leuven, Belgium

§Current address: MRC Prion Unit at UCL, Institute of Prion diseases, Courtauld building, 33 Cleveland Street, London W1W7FF, UK.

lCurrent address: Roche Polska Sp. zo. o. Domaniewska 28, 02-672 Warszawa, Poland.

§§ Current address: Fresenius Kabi, Via Camagri 41, Verona, Italy.

* To whom correspondence may be addressed. Email: claudioluchinat@cerm.unifi.it, ewanker@mdc-berlin.de, bart.destrooper@cme.vib-kuleuven.be.

S1
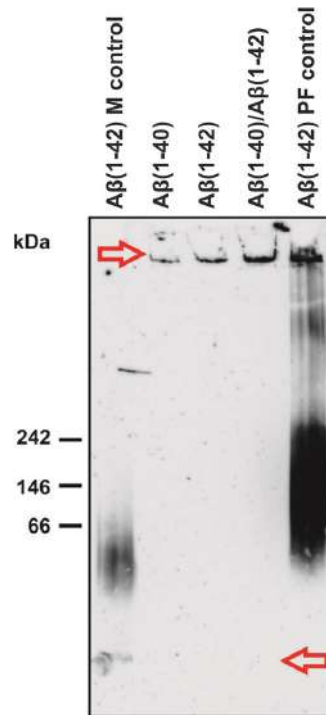
Figure S1. Native polyacrylamide gel electrophoresis of mature fibrils showing no sign of smaller aggregates; Arrows indicate high molecular weight aggregates (top) and monomers (bottom), respectively. The abbreviation PF stand for protofibrils, M for monomers. The prepared amyloid fibrils are detectable in the gel pockets, while monomers or smaller protofibrillar Aβ(1-42) oligomers, which were used as controls, can enter the separating gel. This indicates that all three aggregate preparations contain large, relatively stable structures that cannot be dissociated with native polyacrylamide gels.

S2
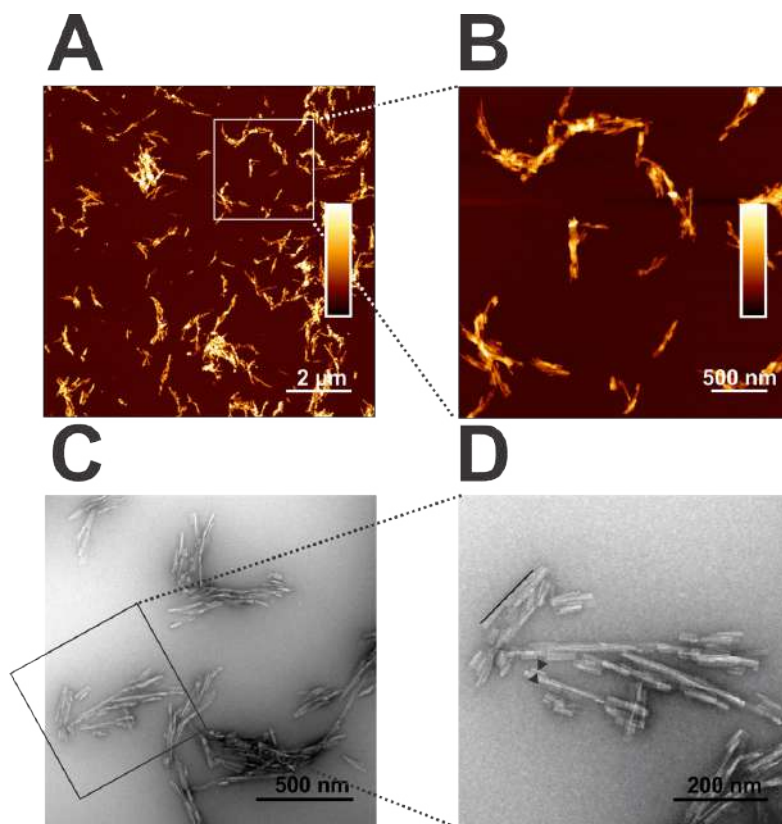
Figure S2. Analysis of 1:1 Aβ(1-42):Aβ(1-40) mixed fibrils by AFM (A, B) and TEM (C, D). B) and D) show a detail from A and C in higher magnification (see frames). A) and B) color gradient: 0-40 nm height. D) The line and the arrowheads illustrate how the length and breadth of fibrils were determined. Under the fibrillization conditions used in the present work the resulting fibrils appear short and highly associated in flat bundles, which do not disassemble to isolated fibrils upon sonication (data not shown). For length determination 592 fibrils have been measured which show an average length of 106.61 nm (SD = 54.75). For breadth determination 244 fibrils have been analyzed which show an average breadth of 3.25 nm (SD = 0.67).

S3

36
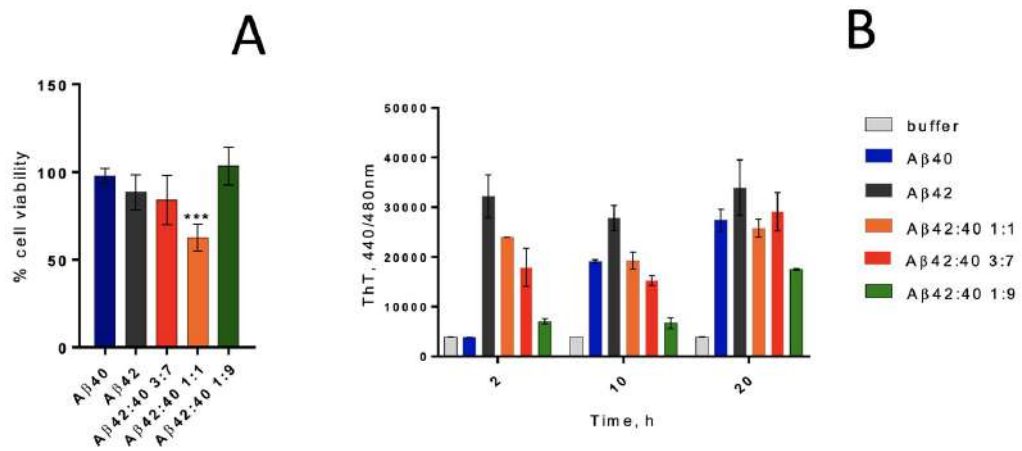
Figure S3. (A) Viability of primary hippocampal mouse neurons in a Cell-Titer blue assay after 72 h treatment with 10 μM of pre-aggregated pure Aβ(1-40), pure Aβ(1-42), and mixture of Aβ(1-42):Aβ(1-40) peptides in different ratios. In this assay only the 1:1 Aβ(1-42):Aβ(1-40) preparations induce a significant reduction of cell viability of about 30 % (Mean±St.Dev.,***p<0.001, 2-tailed unpaired t-test, comparison to untreated cells, n=3-4). All other preparations did not significantly reduce cell viability, indicating that they are less toxic than the 1:1 Aβ(1-42):Aβ(1-40) preparations. Note that non-aggregated and aggregated Aβ preparations at a concentration below 10 μM did not show any cytotoxicity under the same conditions. (B) Presence of fibrillar (Thioflavin-T reactive) species in the samples at different incubation times. Mean±St.Dev., ThT concentration 12 μM (*vide infra*).

S4
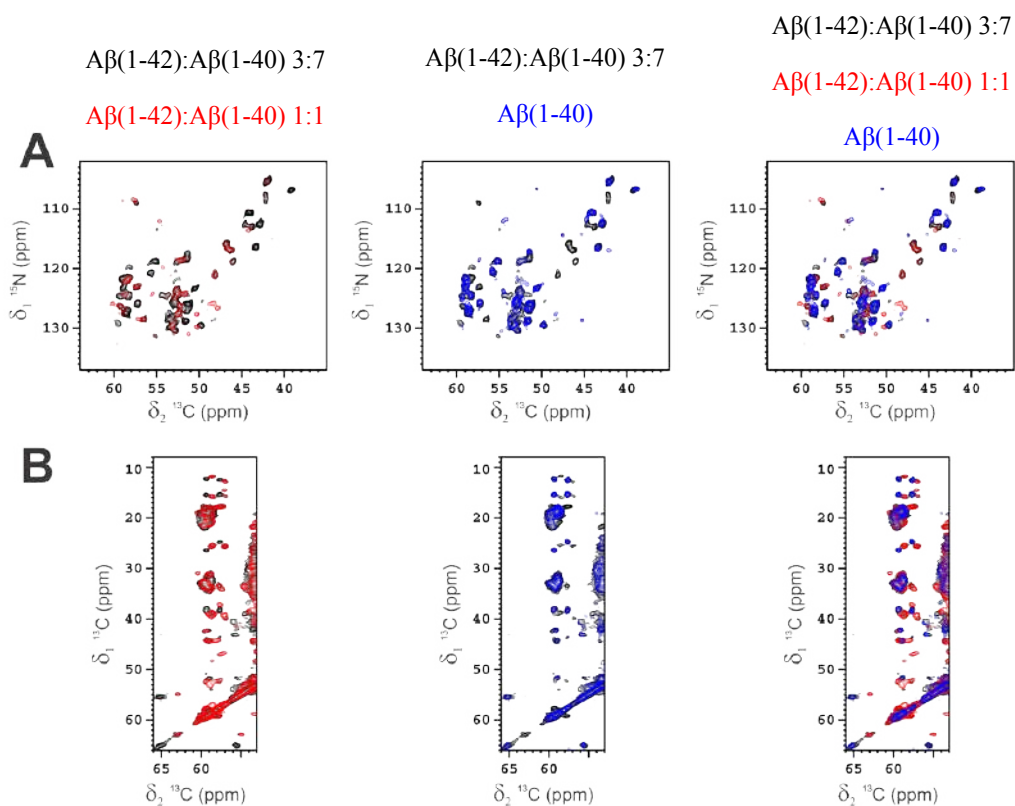
Figure S4. A) 2D ^{15}N-^{13}C NCA spectra of the Aβ(1-42):Aβ(1-40) mixed fibrils in the 3:7 molar ratio (black) overlaid with the 2D ^{15}N-^{13}C NCA spectra of Aβ(1-42):Aβ(1-40) mixed fibrils in the 1:1 molar ratio (red) and with fibrils of pure Aβ(1-40) (blue). Magnetic field: 700 MHz (16.4 T), dimension of rotor: 3.2 mm (~10-14 mg of fibrils), 14 kHz spinning, 100 kHz ^{1}H decoupling. B) 2D ^{13}C-^{13}C correlation spectra (in the region of the Cα of the isoleucine residues) of the Aβ(1-42):Aβ(1-40) mixed fibrils in the 3:7 molar ratio (black) overlaid with the 2D ^{13}C-^{13}C correlation spectrum of Aβ(1-42):Aβ(1-40) mixed fibrils in the 1:1 molar ratio (red) and with 2D ^{13}C-^{13}C-correlation spectrum of fibrils of pure Aβ(1-40) (blue). Magnetic field: 700 MHz (16.4 T), dimension of rotor: 3.2 mm (~10-14 mg of fibrils), 12 kHz spinning, 100 kHz ^{1}H decoupling.

S5

38
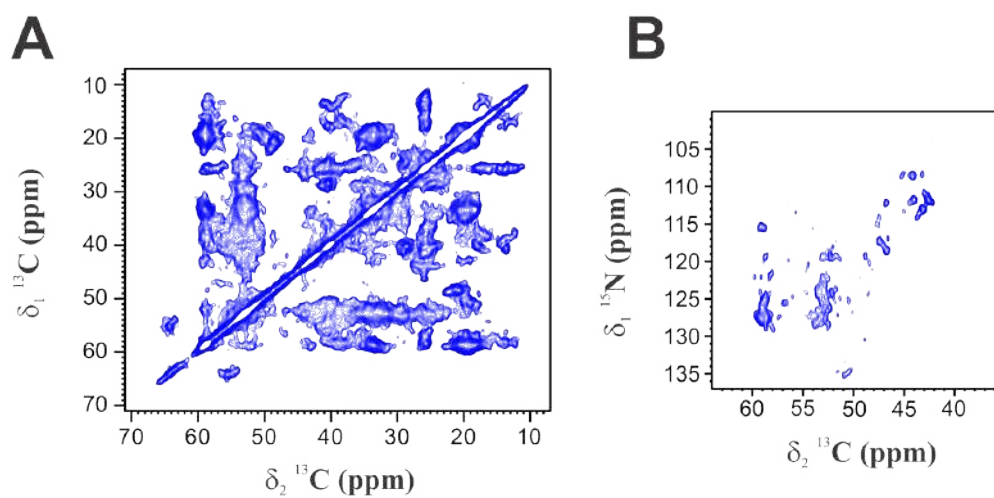
Figure S5. A) 2D ^{13}C-^{13}C correlation spectrum of the Aβ(1-42) aggregates. Magnetic field: 700 MHz (16.4 T), dimension of rotor: 3.2 mm (~10-14 mg of aggregates), 12 kHz spinning, 100 kHz ^{1}H decoupling; B) 2D ^{15}N-^{13}C NCA spectrum of the Aβ(1-42). Magnetic field: 700 MHz (16.4 T), dimension of rotor: 3.2 mm (~10-14 mg of aggregates), 14 kHz spinning, 100 kHz ^{1}H decoupling.
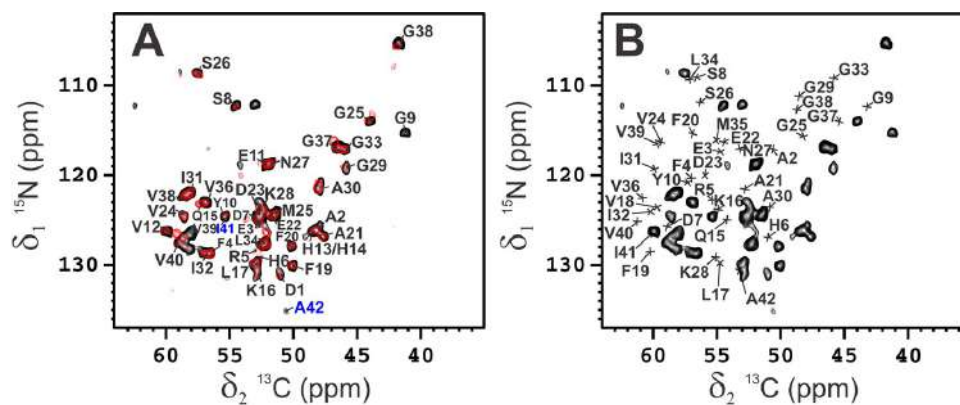
Figure S6. (A) 2D ^{15}N-^{13}C NCA spectrum of the Aβ(1-42) component (black) overlaid with the 2D ^{15}N-^{13}C NCA spectrum of the Aβ(1-40) component (red) in the 1:1 Aβ(1-42):Aβ(1-40) mixed fibrils; the full assignment of the spectrum is shown. (B) 2D ^{15}N-^{13}C NCA spectrum of the Aβ(1-42) component (black), with the assignments of the S-shaped fibrils [1].
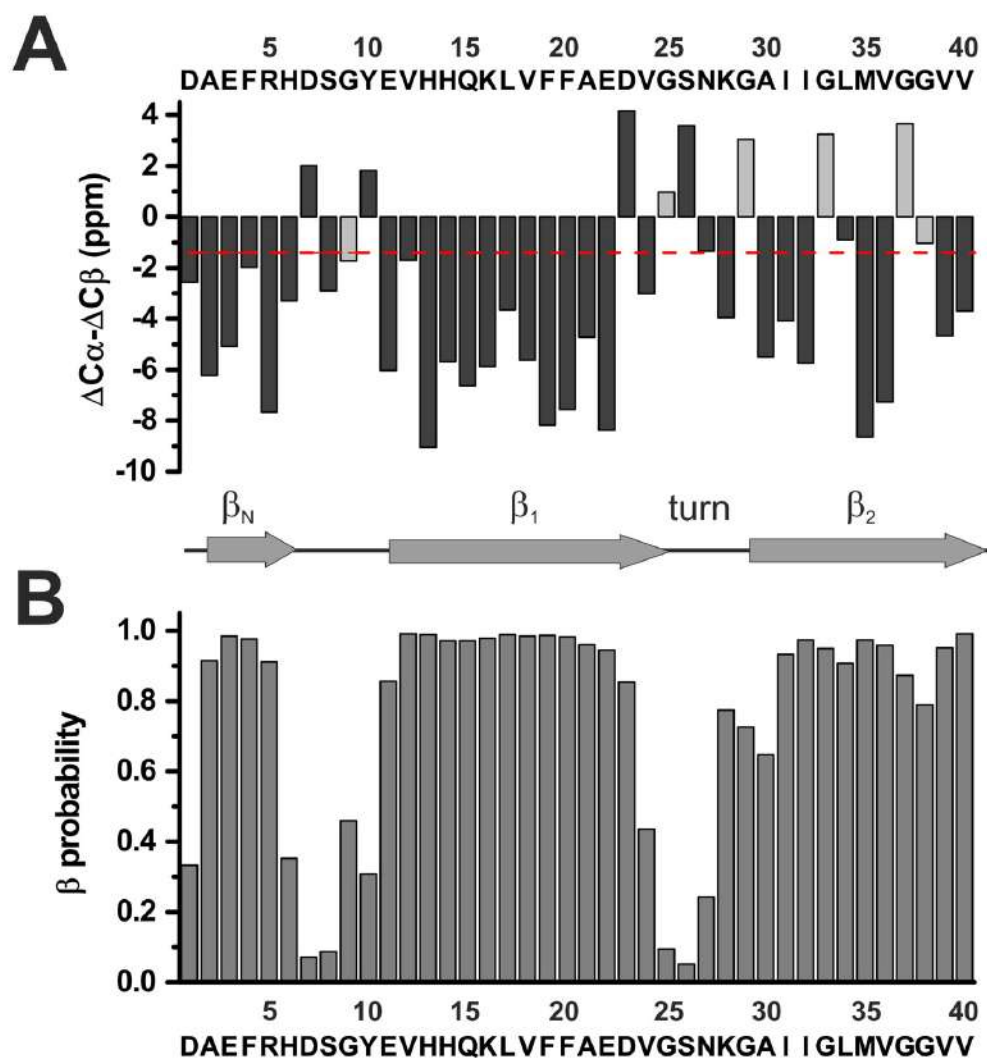
Figure S7. Secondary structural analysis of Aβ(1-42):Aβ(1-40) mixed fibrils (1:1 ratio). Chemical shift differences with respect to the corresponding random coil values (panel A) and residue specific β-probabilities predicted by TALOS+ (panel B) are displayed. In panel A the red line indicates the cutoff of -1.4 ppm and the ΔδCα shifts for the glycines are displayed in light-grey.

Table S1. Long-range intramolecular contacts between β_1- and β_2-strands observed and used for deriving the structural models of Aβ(1-42):Aβ(1-40) mixed fibrils in the present work.

Number	Contacts	Source spectra
1	H13 Cε_1 - V40 Cβ	DARR (300 ms)
2	H13 Cγ - V40 Cγ_2	DARR (300 ms)
3	H13 Cγ - V40 Cβ	DARR (300 ms)
4	L17 Cβ - L34 Cδ_2	DARR (100 ms)
5	L17 Cβ - L34 Cδ_1	DARR (100 ms)
6	L17 Cβ - L34 Cβ	DARR (100 ms)
7	L17 Cδ_1 - V36 Cγ_1	DARR (100 ms)
8	L17 N - L34 Cδ_2	PAIN(10ms)
9	L17 N - L34 Cδ_1	PAIN(10 ms)
10	F19 Cδ_1 - L34 Cδ_2	DARR (200 ms)
11	F19 Cβ - G33 Cα	DARR (100 ms)
12	A21 Cα - I32 Cγ_2	DARR (300 ms)
13	A21 Cβ - I32 Cγ_1	DARR (100 ms)
14	A21 Cβ - I32 Cβ	DARR (300 ms)
15	D23 Cβ - A30 Cβ	DARR (100 ms)

S9
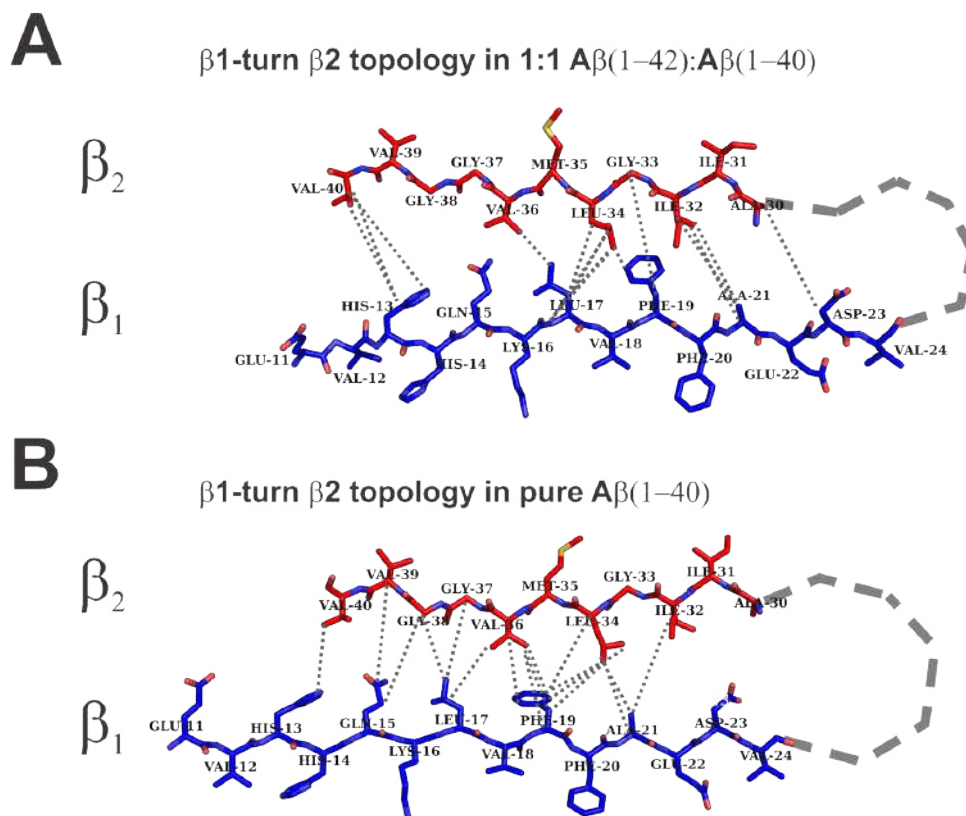
Figure S8. Folding of the monomeric Aβ(1-40) peptide in the model of 1:1 Aβ(1-42):Aβ(1-40) mixed fibrils (A) and in the model obtained for the fibrils of pure Aβ(1-40) [2] (B). It is clear that, in the current conformation of the β–arch, the contacts indicate a reciprocal packing of the two β-strands (β$_1$ and β$_2$) (A), which is different from that previously calculated for the fibrils of pure Aβ(1-40) [2] (B), but is consistent with the contacts observed in reference [10].

Table S2. Long-range intermolecular contacts between two β_2-strands observed and used for deriving the structural models of Aβ(1-42):Aβ(1-40) mixed fibrils in present work. The contacts of the side chains of Ile31 with Gly38/Val39/Val40, and of Met35 with Gly38/Val39, indicate the presence of a head-to-tail antiparallel association of two β_2-strands of different monomers. These experimental restraints are in agreement with a two-fold rotational symmetry (also reported for the co-aligned homo-zipper model [3]) and with the parallel registry of the protofilament.

Number	Contacts	Source spectra
1	M35 Cε - V39 Cβ	DARR (200 ms)
2	M35 Cβ - G38 Cα	PDSD (400 ms)
3	I31 Cδ_1 - G38 Cα	PDSD (400 ms)
4	I31 Cγ_2 - G38 Cα	PDSD (400 ms)
5	I31 Cβ - V39 Cγ_1	DARR (200 ms)
6	I31 Cδ_1 - V39 Cγ_2	DARR (200 ms)
7	I31 Cγ_2 - V39 C	DARR (100 ms)
8	I31 Cγ_2 - V39 Cβ	DARR (200 ms)
9	I31 Cγ_2 - V39 Cγ_2	DARR (100 ms)
10	I31 Cγ_2 - V40 Cγ_1	DARR (200 ms)

Figure S9. Lateral packing of two different protofilaments in the model of 1:1 Aβ(1-42):Aβ(1-40) mixed fibrils (A) and in the model of the fibrils of pure Aβ(1-40) [2] (B), calculated implementing long-range distance restraints in HADDOCK [4]. The contacts and the generated model (A) are similar, but not identical, to those of the pure Aβ(1-40) (B) [2]. In particular, the contacts Ile32-Val39, Gly33-Val39 and Met35-Gly37 are not observed in the mixed fibrils, while the additional contact between Ile31 and Val40 is observed because of the higher rigidity of Val40.

S12

Scheme S1. Different β-strand zippers in various SS-NMR-derived structural models of Aβ fibrils. The topologies of the β₁-turn-β₂ motif identified in the present work (A) and in other previously

studied Aβ(1-40) fibrils (B, D) [2,5–7] and Aβ(1-42) fibrils (C, E, F) [8–10] are shown in the left column. The dashed/dotted lines represent unambiguous experimental restraints used to derive the corresponding topology. In the schematic description of distinct structures of the U-shaped motif, the hydrophobic, acidic/basic, and other types of residues are shown in white, black, and gray, respectively. The topologies of the interprotofilament interface (β_2-β_2 zippers) in the fibrils determined in the present work (G) and proposed in previous studies (H, I, J, K) [2,5,6] are shown in the right column. The dashed lines represent unambiguous experimental restraints used to derive the corresponding topology. The filled black circles represent the Cε of the Met35 residue. Other residues included in SS-NMR-observed structural restraints for linking the two β_2-strands are shown as hollow circles. Residues Ile41 and Ala42, in the present model of the mixed fibrils, are indicated with dashed circles to stress that both Aβ(1-40) and Aβ(1-42) share the same arrangement.
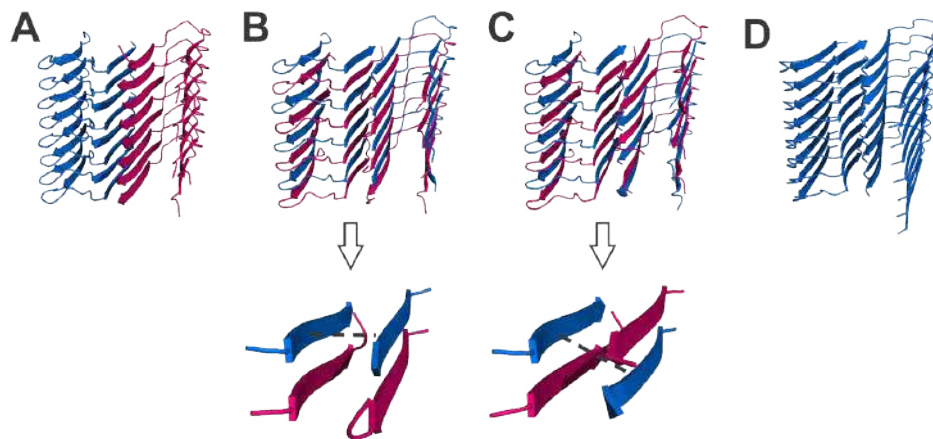
Figure S10. Possible reciprocal packing modes of Aβ(1-40) and Aβ(1-42) peptides along the fibril axis generated and scored by HADDOCK 2.2 [4]: homogeneous protofilaments (all composed of either Aβ(1-40) or Aβ(1-42) peptides) that form a mixed cross-β structure (model A); interlaced protofilaments that form a paired (model B), or staggered (model C) cross-β structure. The Aβ(1-42) polypeptide is colored magenta and the Aβ(1-40) polypeptide in blue. The model of pure Aβ(1-40) fibrils is also displayed (panel D).[2] Model A is excluded by the presence of cross-peaks between the N-terminus and C-terminus of the β₂ strand. Arrangements B and C are very similar and equally possible (see Table S3).
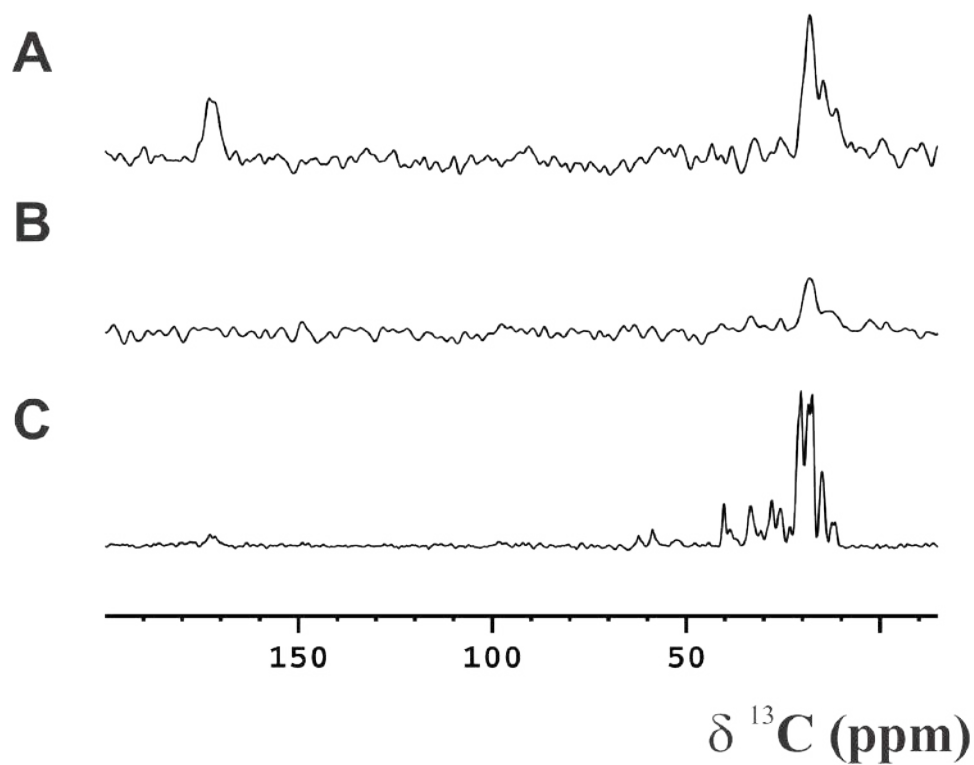
Figure S11. 1D zTEDOR spectra of the Aβ(1-42):Aβ(1-40) mixed fibrils in the 1:1 molar ratio, where A) Aβ(1-42) is ^{15}N-enriched and Aβ(1-40) is ^{13}C-enriched and B) Aβ(1-42) is ^{15}N-enriched and Aβ(1-40) is in natural abundance, and C) Aβ(1-42) is in natural abundance and Aβ(1-40) is ^{15}N-^{13}C-enriched. Magnetic field: 800 MHz (19 T, 201.2 MHz ^{13}C Larmor frequency), dimension of rotor: 3.2 mm, 16 kHz spinning, 80 kHz ^{1}H decoupling. The number of scans was tuned according to the sample amount (10240, for sample A and C, and 40960 for sample B). The signal of the backbone carbonyls appears only in (A), whereas it is absent in (B), confirming an interlaced arrangement. The spectrum (C) shows relatively lower intensity in the carbonyl region because the coupling across the hydrogen bond is masked by other intra-filament couplings.
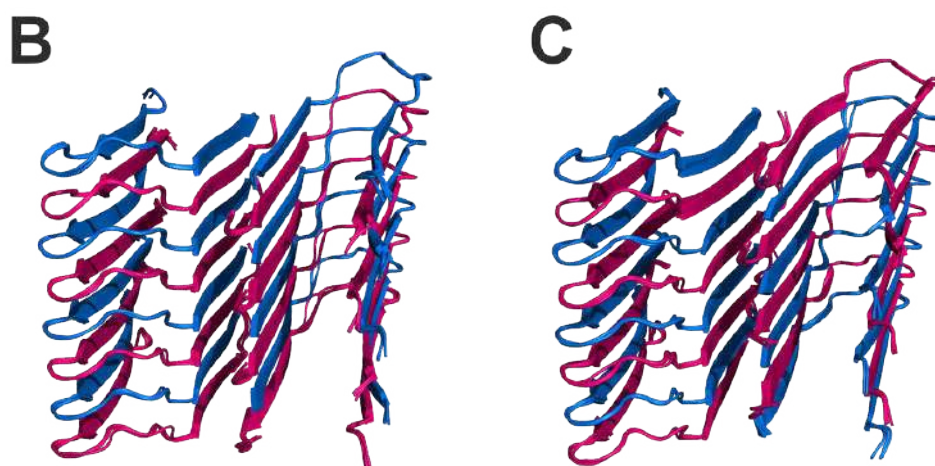
Figure S12. Family of the best four structures corresponding to model B (left) and model C (right), obtained with an experimental restraint-driven calculation with HADDOCK 2.2. Two identical interlaced Aβ(1-40)/Aβ(1-42) protofilaments (left) and two different interlaced protofilaments, Aβ(1-40)/Aβ(1-42) and Aβ(1-42)/Aβ(1-40) (right) have been considered, respectively, in the calculations. The HADDOCK-scores for the models of the two families are not very different, although somewhat more favorable for the right-hand model (Table S3), so that firm conclusions for one or the other model cannot be drawn.

Table S3. HADDOCK statistics evaluated on the 200 water refined models. The reported data are related to the best four structures of the clusters with the lowest HADDOCK-scores. The packing density and number of cavities have been evaluated using the Voronoia plugin in Pymol [11].

	Model B	**Model C**
HADDOCK-Score	-353 ± 5	-267 ± 2
HADDOCK-Score (without E_{AIR})	-394 ± 5	-299 ± 2
N° of structures of the cluster	199	200
RMSD	0.3 ± 0.2	0.3 ± 0.2
Desolvation Energy	-185 ± 4	-150 ± 5
Buried surface area (BSA)	4862 ± 33	4686 ± 21
Ambiguous interaction restraint energy (E_{AIR})	418 ± 23	321 ± 8
Average packing density	0.81 ± 0.01	0.82 ± 0.01
Number of cavities	22 ± 4	29 ± 5

Table S4. HADDOCK statistics evaluated on the water refined models of model B, fibrils of pure Aβ(1-40) and fibrils of pure Aβ(1-42) in the S-shaped conformation after HADDOCK minimization. The reported data are related to the best four structures of the clusters with the lowest HADDOCK-scores.

	Model B	**Aβ(1-40)** [2]	**Aβ(1-42)** [12] **S-shaped conformation**
HADDOCK-Score	-353 ± 5	-322 ± 3	-407 ± 0.4
HADDOCK-Score (without E_{AIR})	-394 ± 5	-326 ± 3	-408 ± 0.4
RMSD	0.3 ± 0.2	0.2 ± 0.1	0.2 ± 0.1
Desolvation Energy	-185 ± 4	-135 ± 4	-104 ± 5
Buried surface area (BSA)	4862 ± 33	4073 ± 30	5617 ± 71
Ambiguous interaction restraint energy (E_{AIR})	418 ± 23	38 ± 4	15 ± 2

Table S5. HADDOCK statistics evaluated on 20 water refined models. The reported data are related to the best four structures. The calculations were performed on the HADDOCK2.2 web-server using the *refinement* interface. The models that were refined derived from calculations where the last residues of Aβ(1-42) were left free without the imposition of β-strand restraints.

	Aβ(1-40) monomer conformation of Bertini et al. 2011	Aβ(1-40) monomer conformation of current work	Aβ(1-42) monomer conformation of Bertini et al. 2011	Aβ(1-42) monomer conformation of current work	Aβ(1-40)/ Aβ(1-42) monomer conformation of current work
HADDOCK-Score	-238 ± 3	-205 ± 2	-204 ± 3	-235 ± 3	-266 ± 1
N° of structures of the cluster	20	20	20	20	20
RMSD	0.3 ± 0.2	0.3 ± 0.2	0.3 ± 0.2	0.3 ± 0.2	0.3 ± 0.2
Desolvation Energy	-57 ± 1	-37 ± 1	-49 ± 6	-68 ± 5	-58 ± 1
Buried surface area (BSA)	4072 ± 29	3979 ± 22	4703 ± 56	4661 ± 40	4888 ± 37
Ambiguous interaction restraint energy (E_{AIR})	7 ± 2	19 ± 2	7 ± 2	18 ± 4	21 ± 1

Methods

Expression, purification, and sample preparation of Aβ(1-42):Aβ(1-40) mixed fibrils

The cDNAs encoding the Aβ(1-40) and Aβ(1-42) polypeptides were cloned in the pET3a vector using the NdeI and BamHI restriction enzymes. The peptides were expressed in the BL21 (DE3)pLys *E. coli* strain.

The peptides were purified as reported in the literature [2,13–16] with the modification of using a combination of anion-exchange and size exclusion chromatography. All the manipulations were performed at slightly alkaline pH in order to avoid the formation of structural contaminants produced by isoelectric precipitation. The inclusion bodies were first solubilized with 8 M urea and then purified by ion exchange chromatography performed in batch. All the obtained fractions of the diluted proteins were concentrated to a final volume using an Amicon device. The next step of purification was gel filtration, which was performed using the preparative column Sephadex 75 HiLoad 26/60 with 50 mM $(NH_4)OAc$ pH 8.5 as a buffer. The obtained fractions were collected together and concentrated. During all the purification steps, the protein purity was analysed by SDS-PAGE, whereas the protein concentration was estimated spectrophotometrically.

Both Aβ(1-42) and Aβ(1-40) bear the exogenous N-terminal Met0 due to the introduction of a translation start codon that has been shown previously to not significantly influence aggregation or toxicity of Aβ aggregates [16,17]. Both peptides were expressed using the Marley method [18], and purified as reported in literature [2,13–16] but using a combination of anion-exchange and size exclusion chromatography [2]. These two-steps of purification allowed us to obtain highly pure products with the yield in the range of 10 mg for Aβ(1-40) and 5-10 mg for Aβ(1-42) per liter of culture [19–21].

The fibrils for SS-NMR studies were produced as described by Bertini et al. [2]. Some samples were obtained by mixing ^{13}C, ^{15}N-uniformly enriched Aβ(1-40) polypeptide with Aβ(1-42) in natural isotopic abundance. Solutions containing Aβ(1-42) and Aβ(1-40) (total concentration of 100 μM) in 50 mM ammonium acetate (pH 8.5) were incubated at 310 K under agitation (950 rpm) for 5 weeks. The 3:7 mixture sample was prepared using 30 μM and 70 μM of Aβ(1-42) and Aβ(1-40) respectively, while the 1:1 sample was produced using the same concentration (50 μM) of both proteins. The 3:7 sample spontaneously resulted in two species (see main text), one of which corresponds to the previously characterized pure Aβ(1-40), and the other is a different species. Assuming that all the available Aβ(1-42) 30 μM formed fibrils with a stoichiometric amount of Aβ(1-40), 40 μM of Aβ(1-40) are free to form pure fibrils that, having a symmetric dimer as basic unit, contribute to 4/3 times the signal intensity of the other species, in line with the experimental

observation. Fibrils were collected by ultracentrifugation at 60,000 rpm and 277 K for 24 h. The pellet was washed with fresh and cold ultrapure water (Millipore) for three times (1 mL per time). About 14 mg of wet material were packed into a 3.2 mm ZrO_2 magic angle spinning (MAS) rotor at 277 K using an ultracentrifugal device (GiottoBiotech) [22,23]. The fibril samples were kept fully hydrated during all steps.

An equimolar mixture of ^{13}C, ^{15}N-uniformly enriched Aβ(1-42) polypeptide (50 μM) and Aβ(1:40) polypeptide (50 μM) in natural isotopic abundance was prepared using the same protocol.

^{13}C, ^{15}N-uniformly enriched Aβ(1-42) fibrils were also grown, incubating the Aβ(1-42) polypeptide at the concentration of 20 μM to slow down the oligomerization process.

Equimolar mixtures of Aβ(1-42) and Aβ(1-40) polypeptides with different labeling schemes [^{15}N-uniformly enriched Aβ(1-42)/^{13}C-uniformly enriched Aβ(1-40) and ^{15}N-uniformly enriched Aβ(1-42)/natural isotopic abundance Aβ(1-40)] were also prepared following the same protocol.

Preparation of Aβ(1-42) monomer solutions and Aβ(1-42) protofibrillar aggregates

Synthetic Aβ(1-42) peptide produced by Bachem (Bubendorf, Schwitzerland) was dissolved in 1,1,1,3,3,3-Hexafluoro-2-propanol (HFIP) for three days, aliquoted and then lyophilized. Monomeric Aβ(1-42) solutions were prepared by dissolving peptides in 10 mM NaOH, sonication for 5 min and dilution to the final concentration in low salt buffer (LSB, 1.9 mM KH_2PO_4, 8.1 mM K_2HPO_4, 10 mM NaCl, pH 7.4). Synthetic Aβ(1-42) peptide produced by the laboratory of Dr. Volkmar-Engert (Institute for Medical Immunology, Charité, Berlin, Germany) was dissolved in HFIP overnight, sonicated for 30 min, aliquoted and then lyophilized. HFIP-treated peptide was dissolved in 100 mM NaOH, sonicated for 5 min and diluted in LSB to a final concentration of 200 μM. The solution was incubated for 6 h in an Eppendorf Thermomixer (Wesseling-Berzdorf, Germany) at 310 K and 300 rpm. The protofibrillar aggregate species was aliquoted and stored at 193 K.

Separation of Aβ(1-42) aggregates by native gels.

Aβ aggregates or monomers (4.5 µL, 10 µM) were diluted with NativePAGE 4x sample buffer (2.5 µL, Invitogen/Thermo Scientific, Dreieich, Germany) and LSB. Samples were loaded onto a Novex Bis-Tris 4-16% gel (Invitogen/Thermo Scientific, Dreieich, Germany) and separated. Aggregates were transferred to a nitrocellulose membrane (GE Healthcare, Freiburg, Germany) and visualized using the 6E10 antibody (BioLegend, San Diego, US) and a mouse anti-POD detection antibody (Sigma, Taufkirchen, Germany). Secondary antibody binding was detected by

chemiluminescence using ChemiGlow West Substrate (Alpha Innotech, Kasendorf, Germany); luminescence was measured using a FujiFilm LAS-3000 imager (Fuji, Kleve, Germany).

Microscopic characterization

For the AFM measurements of Aβ(1-42):Aβ(1-40) mixed fibrils, sheet mica (Glimmer V3; Plano, Wetzlar, Germany) was glued to a microscope slide and samples (20 μL) were adsorbed for 10 min onto the freshly cleaved mica, washed with freshly filtered deionized water (4×30 μL) and dried overnight. Dry AFM images were recorded on a Nanowizard II/Zeiss Axiovert setup (JPK, Germany) using intermittent contact mode and PPP-NCHAuD probes (NANOSENSORS™, Neuchâtel, Switzerland).

For the TEM measurement, samples of Aβ(1-42):Aβ(1-40) mixed fibrils were adsorbed onto formvar-carbon coated grids, stained with 5 % of uranyl acetate, and analyzed with a Morgagni electron microscope (Thermo Fisher), and a Morada camera. Pictures were taken and analyzed with the iTEM software (EMSIS GmbH, Münster, Germany).

Cell viability assay

Primary hippocampal neurons were prepared from trypsinized brains of 17-days old C57/Bl6 mouse embryos, and plated out in minimal essential medium (Invitrogen, catalogue no. 31095-029) supplemented with horse serum, penicillin, and streptomycin (PenStrep, Invitrogen, catalogue no. 15140-122). 4 h after plating, medium was replaced with Neurobasal medium (NB, Invitrogen, catalogue no. 21103-049) supplemented with B27 (Invitrogen, catalogue no. 17504-044), and PenStrep. Neurons were grown in B27-supplemented Neurobasal medium for 10 days, and then were treated with 10 μM of pre-aggregated Aβ(1-40), Aβ(1-42) and a mixture thereof (Fig. S3 A). Pre-aggregation was obtained from recombinant monomers incubated at the concentration of 100 μM in Tris-EDTA buffer (50 mM Tris, 1 mM EDTA, pH 7.4) for 2 h at room temperature. At this stage, Aβ(1-42) and preparations Aβ(1-42):Aβ(1-40) 1:1 and 3:7 demonstrated a pronounced Thioflavin T (ThT) incorporation whilst Aβ(1-40) and Aβ(1-42):Aβ(1-40) 1:9 still had a very low content of aggregates (Figure S3 B). Aβ(1-40) aggregation was detectable at 10 h and 20 h of incubation, and aggregation of Aβ(1-42):Aβ(1-40) 1:9 increased at 20 h of incubation (Figure S3 B). After 72 h treatment, 10 μL Cell-Titer-Blue dye (Promega) was added to 200 μL of the culture medium on the cells. After 3 h, the fluorescence intensity of the samples was measured at an excitation wavelength of 560 nm and an emission wavelength of 590 nm. Data was normalized to untreated cells (100%) and presented as Mean±St.Dev.; statistical significance is indicated by *** (Figure S3 A), $p < 0.001$, 2-tailed unpaired t-test (comparison to untreated cells), n=3-4.

NMR measurements

[15]N-^{13}C NCA and NCO (2D), NCACX, NCOCX, NCACB, N(CO)CACB and CANCO (3D) experiments were performed either on a Bruker Avance III 850 MHz wide-bore spectrometer (20.0 T, 213.7 MHz [13]C Larmor frequency), or on a Bruker Avance II 700 MHz wide-bore spectrometer (16.4 T, 176.1 MHz [13]C Larmor frequency) using 3.2 mm DVT MAS probeheads in triple-resonance mode. MAS frequency ($\omega_r/2\pi$) was set to 17.0, 14.0 or 12.0 kHz ($\pm$ 2 Hz) depending on the experiment. The NCA, NCO, NCACX, NCOCX, NCACB, N(CO)CACB and CANCO experiments were carried out using the pulse sequences reported in the literature [24,25]. At 700 MHz NC transfers were achieved by optimal-control derived pulses [26]. Backwards CN transfer was achieved with a time-reversal of the same optimal-control pulses. The amount of material used to fill the rotor was ~ 10-14 mg; NCA and NCO experiments were acquired using 256 and 128 scans, respectively, with an acquisition time on t1 dimension of 9 ms, and a recycle delay of 1.8 sec; NCACX and NCOCX experiments were acquired using 64 and 32 scans, respectively, with an acquisition time of 7 ms on t1 dimension and of 6 ms on t2 dimension, and a recycle delay of 1.9 sec; NCACB and N(CO)CACB experiments were acquired using 64 and 144 scans, respectively, with an acquisition time of 5 ms on t1 dimension and of 4 ms on t2 dimension, and a recycle delay of 1.9 sec; CANCO experiment was acquired using 64 scans, with acquisition time of 5 ms on t1 dimension and of 6 ms on t2 dimension, and recycle delay of 2 sec.

2D [13]C-^{13}C proton-driven spin diffusion (PDSD) [27], dipolar-assisted rotational resonance (DARR) [27,28] and Second-order Hamiltonian among Analogous Nuclei Generated by Hetero-nuclear Assistance Irradiation (SHANGHAI) [29] correlation spectra with different mixing times (15 to 800 ms) were recorded on the 700 MHz instrument. For these experiments, the MAS frequency was stabilized at 12 kHz ($\pm$ 2 Hz). SHANGHAI was included, with respect to the characterization reported in [2], because it warrants a more homogeneous transfer throughout signals at different frequencies at high field and moderate spinning rates. The [13]C-^{13}C correlation spectra were acquired using increasing number of scans with increasing mixing time (from 32 scans for shorter mixing times up to 96 scans for longer mixing times). For the sample of the 1:1 mixture of Aβ(1-42): Aβ(1-40) were Aβ(1-42) is [13]C-^{15}N isotopically enriched higher number of scans were employed since the amount of material was smaller (~8-10 mg; number of scan from 128 to 256). The acquisition time on t1 dimension was 8 ms and the recycle delay 1.9 sec.

Bidimensional (2D [15]N-[13]C hNhhC, 500 μs HH mixing time) and monodimensional (zTEDOR, 10 ms mixing time) nitrogen and carbon correlation spectra were recorded on a Bruker AvanceIII spectrometer operating at 800 MHz (19 T, 201.2 MHz [13]C Larmor frequency) equipped with Bruker 3.2 mm Efree NCH probe-head. The spectra were recorded at 16 kHz ($\pm$ 2 Hz) MAS

frequency; the number of scans was 2048 for the bidimensional (10 ms of acquisition time on t1 dimension) and 10240 or 40960 (according to the fibril amount) for the monodimensional experiments, respectively; the recycle delay was 3 sec.

In all cases, ^{1}H decoupling was applied at 80-100 kHz (optimized on the basis of the [13]C' echo lifetime [30]) using sw$_f$TPPM [31–33]. During the experiments, the sample was cooled by a dry, cold air flow (> 935 L/h), and the effective sample temperature was estimated to be ∼283 K [23].

Spectra were analyzed by the program CARA (Computer Aided Resonance Assignment, ETH Zurich) [34].

SS-NMR data analysis and structural modeling.

Sequential assignment of the new species present in the Aβ(1-42):Aβ(1-40) mixed fibrils, where either Aβ(1-40) or Aβ(1-42) was ^{13}C, ^{15}N-uniformly enriched, was performed using the same procedure for both samples, starting from the identification of the residues 31Ile-32Ile. These two consecutive residues can be identified following the signals of the two sidechains, which can be easily distinguished in the 2D [13]C-^{13}C correlation spectra. Starting from these residues, the sequential assignment was obtained by analyzing the 3D [15]N-^{13}C spectra according to the procedure reported by Bertini et al. [2]. The assignment is deposited in the BMRB with ID 34455). The secondary structure was predicted by TALOS+ [35] using the chemical shifts of the N, C, Cα and Cβ.

For model building, the length of the β$_1$ and β$_2$ strands was based on the secondary structure predicted by TALOS+. The β$_1$- and β$_2$-strands were then docked to one another by HADDOCK [4] using all the experimental long-range β$_1$-β$_2$ restraints. HADDOCK calculations were performed on the WeNMR GRID (http://www.wenmr.eu/, Guru interface, see supporting information for details).

The β-sheets were then generated by duplicating the β$_1$ and β$_2$ strands along the direction of the backbone N-H and C=O bonds with PYMOL, using the inter-strand distance of 4.8 Å [36], typical of the parallel register. Eight β-strands for each β$_1$ and β$_2$ sheets were generated, considering for the β$_2$-sheet an interlaced arrangement of the Aβ(1-40) and Aβ(1-42) monomers.

The turn regions were randomly generated using MODELLER [37] and the final one was selected from the resulting pool of 50 structures.

The inter-protofilament structural models were generated by docking calculations starting from two β$_2$-sheets belonging to two different protofilaments and imposing non-crystallographic symmetry restraints between the two β$_2$-sheets.

During HADDOCK calculations, first the β$_1$- and β$_2$-strands were docked to one another, using all the experimental long-range β$_1$-β$_2$ restraints of β$_1$- and β$_2$-strands. The lower distance

cutoff was set to 3.0 Å, and the upper to 6.0 Å for the shorter mixing times (100 and 200 ms) and to 7.5-8.0 Å for longer mixing (300 and 400 ms). The charges on the N- and C-termini of the β_1-strands and on the N-termini of the β_2-strands were not included in the calculations in order to prevent electrostatic interactions, which do not exist when the two β-strands are linked by a turn region. The histidine protonation states were automatically determined by the Molprobity module embedded in the HADDOCK server. During the rigid docking calculations, 1000 structures were generated, then the best 200 structures were selected for the semi-rigid simulated annealing in torsion angle space, and finally refined in Cartesian space with explicit solvent.

The structural models were then generated by implementing in the calculations all the observed intermolecular β_2-β_2 long-range contacts and inter-strand distance restraints. All the restraints were duplicated symmetrically between the two β_2-sheets using the same protocol used for structural calculations of symmetric protein dimers. Since these long-range distance restraints could be identified only using long mixing times, the upper distance cutoffs in the HADDOCK calculation was set to 8.0 Å. Semi-flexible refinement was enabled on both β_2-sheets.

The family of structures obtained for the mixed Aβ(1-42) and Aβ(1-40) fibrils have been deposited in the protein data bank (model B, PDB ID: 6TI6 and model C, PDB ID:6TI7), together with the structure of the pure Aβ(1-40) fibrils previously reported by Bertini and co-workers (model D, PDB ID: 6TI5, BMRB ID: 34454) [2].

References:

1   F. Ravotti, M. A. Wälti, P. Güntert, R. Riek, A. Böckmann and B. H. Meier, *Biomol. NMR Assign.*, 2016, **10**, 269–276.

2   I. Bertini, L. Gonnelli, C. Luchinat, J. Mao and A. Nesi, *J. Am. Chem. Soc.*, 2011, **133**, 16013–16022.

3   J. T. Nielsen, M. Bjerring, M. D. Jeppesen, R. O. Pedersen, J. M. Pedersen, K. L. Hein, T. Vosegaard, T. Skrydstrup, D. E. Otzen and N. C. Nielsen, *Angew. Chem. Int. Ed Engl.*, 2009, **48**, 2118–2121.

4   S. J. de Vries, M. van Dijk and A. M. J. J. Bonvin, *Nat. Protoc.*, 2010, **5**, 883–897.

5   A. T. Petkova, W.-M. Yau and R. Tycko, *Biochemistry*, 2006, **45**, 498–512.

6   A. K. Paravastu, R. D. Leapman, W.-M. Yau and R. Tycko, *Proc. Natl. Acad. Sci.*, 2008, **105**, 18349–18354.

7   M. Ahmed, J. Davis, D. Aucoin, T. Sato, S. Ahuja, S. Aimoto, J. I. Elliott, W. E. Van Nostrand and S. O. Smith, *Nat. Struct. Mol. Biol.*, 2010, **17**, 561–567.

8   Y. Xiao, B. Ma, D. McElheny, S. Parthasarathy, F. Long, M. Hoshi, R. Nussinov and Y. Ishii, *Nat. Struct. Mol. Biol.*, 2015, **22**, 499–505.

9   M. T. Colvin, R. Silvers, Q. Z. Ni, T. V. Can, I. Sergeyev, M. Rosay, K. J. Donovan, B. Michael, J. Wall, S. Linse and R. G. Griffin, *J. Am. Chem. Soc.*, 2016, **138**, 9663–9674.

10 M. A. Wälti, F. Ravotti, H. Arai, C. G. Glabe, J. S. Wall, A. Böckmann, P. Güntert, B. H. Meier and R. Riek, *Proc. Natl. Acad. Sci. U. S. A.*, 2016, **113**, E4976-4984.

11 K. Rother, P. W. Hildebrand, A. Goede, B. Gruening and R. Preissner, *Nucleic Acids Res.*, 2009, **37**, D393-395.

12 M. T. Colvin, R. Silvers, Q. Z. Ni, T. V. Can, I. V. Sergeyev, M. Rosay, K. J. Donovan, B. Michael, J. S. Wall, S. Linse and R. G. Griffin, *J. Am. Chem. Soc.*, , DOI:10.1021/jacs.6b05129.

13 E. Hellstrand, B. Boland, D. M. Walsh and S. Linse, *ACS Chem. Neurosci.*, 2009, **1**, 13–18.

14 A. Jan, O. Gokce, R. Luthi-Carter and H. A. Lashuel, *J. Biol. Chem.*, 2008, **283**, 28176–28189.

15 D. M. Walsh, D. M. Hartley, Y. Kusumoto, Y. Fezoui, M. M. Condron, A. Lomakin, G. B. Benedek, D. J. Selkoe and D. B. Teplow, *J. Biol. Chem.*, 1999, **274**, 25945–25952.

16 D. M. Walsh, E. Thulin, A. M. Minogue, N. Gustavsson, E. Pang, D. B. Teplow and S. Linse, *FEBS J.*, 2009, **276**, 1266–1281.

17 O. Szczepankiewicz, B. Linse, G. Meisl, E. Thulin, B. Frohm, C. Sala Frigerio, M. T. Colvin, A. C. Jacavone, R. G. Griffin, T. Knowles, D. M. Walsh and S. Linse, *J. Am. Chem. Soc.*, 2015, **137**, 14673–14685.

18 J. Marley, M. Lu and C. Bracken, *J. Biomol. NMR*, 2001, **20**, 71–75.

19 J. R. Brender, A. Ghosh, S. A. Kotler, J. Krishnamoorthy, S. Bera, V. Morris, T. B. Sil, K. Garai, B. Reif, A. Bhunia and A. Ramamoorthy, *Chem. Commun. Camb. Engl.*, 2019, **55**, 4483–4486.

20 B. R. Sahoo, M. E. Bekier, Z. Liu, V. Kocman, A. K. Stoddard, G. M. Anantharamaiah, J. Nowick, C. A. Fierke, Y. Wang and A. Ramamoorthy, *J. Mol. Biol.*, 2020, **432**, 1020–1034.

21 S. Yoo, S. Zhang, A. G. Kreutzer and J. S. Nowick, *Biochemistry*, 2018, **57**, 3861–3866.

22 I. Bertini, F. Engelke, L. Gonnelli, B. Knott, C. Luchinat, D. Osen and E. Ravera, *J. Biomol. NMR*, 2012, **54**, 123–127.

23 A. Böckmann, C. Gardiennet, R. Verel, A. Hunkeler, A. Loquet, G. Pintacuda, L. Emsley, B. H. Meier and A. Lesage, *J. Biomol. NMR*, 2009, **45**, 319–327.

24 A. Schuetz, C. Wasmer, B. Habenstein, R. Verel, J. Greenwald, R. Riek, A. Böckmann and B. H. Meier, *ChemBioChem*, 2010, **11**, 1543–1551.

25 S. Sun, Y. Han, S. Paramasivam, S. Yan, A. E. Siglin, J. C. Williams, I.-J. L. Byeon, J. Ahn, A. M. Gronenborn and T. Polenova, in *Protein NMR Techniques*, eds. A. Shekhtman and D. S. Burz, Humana Press, Totowa, NJ, 2012, pp. 303–331.

26 N. M. Loening, M. Bjerring, N. C. Nielsen and H. Oschkinat, *J. Magn. Reson. San Diego Calif 1997*, 2012, **214**, 81–90.

27 K. Takegoshi, S. Nakamura and T. Terao, *J. Chem. Phys.*, 2003, **118**, 2325–2341.

28 K. Takegoshi, S. Nakamura and T. Terao, *Chem. Phys. Lett.*, 2001, **344**, 631–637.

29 B. Hu, O. Lafon, J. Trébosc, Q. Chen and J.-P. Amoureux, *J. Magn. Reson.*, 2011, **212**, 320–329.

30 W. P. Rothwell and J. S. Waugh, *J. Chem. Phys.*, 1981, **74**, 2721–2732.

31 R. S. Thakur, N. D. Kurur and P. K. Madhu, *Chem. Phys. Lett.*, 2006, **426**, 459–463.

32 R. S. Thakur, N. D. Kurur and P. K. Madhu, *Magn. Reson. Chem. MRC*, 2008, **46**, 166–169.

33 R. S. Thakur, N. D. Kurur and P. K. Madhu, *J. Magn. Reson. San Diego Calif 1997*, 2008, **193**, 77–88.

34 R. Keller, *The Computer Aided Resonance Assignment Tutorial (CARA)*, CANTINA Verlag, Goldau. Switzerland, 2004.

35 Y. Shen, F. Delaglio, G. Cornilescu and A. Bax, *J. Biomol. NMR*, 2009, **44**, 213–223.

36 D. A. Kirschner, C. Abraham and D. J. Selkoe, *Proc. Natl. Acad. Sci. U. S. A.*, 1986, **83**, 503–507.

37 A. Fiser and A. Šali, in *Methods in Enzymology*, ed. Jr. and R. M. S. Charles W. Carter, Academic Press, 2003, vol. Volume 374, pp. 461–491.

3.2 Evaluation of the Higher Order Structure of biotherapeutics embedded in hydrogels for bioprinting and drug release

The aim of this work is to characterize, by SS-NMR, pharmaceutically relevant proteins encapsulated in two different type of hydrogel matrices in order to understand if the structures of these biomolecules, directly related to their activity, is preserved. For this purpose, my contribution to this project was:

- Expression and Characterization of recombinant [U-^{13}C,^{15}N] *Escherichia coli* L-asparaginase II (ANSII)
- Expression and Characterization of recombinant [U-^{13}C,^{15}N] Human Transthyretin (TTR)
- Preparation of Hydrogel Matrices
- Encapsulation in the Hydrogel Matrices
- Preparation of SSNMR Sample

Evaluation of the Higher Order Structure of Biotherapeutics Embedded in Hydrogels for Bioprinting and Drug Release

Domenico Rizzo, Linda Cerofolini, Anna Pérez-Ràfols, Stefano Giuntini, Fabio Baroni, Enrico Ravera, Claudio Luchinat, and Marco Fragai*

Cite This: https://doi.org/10.1021/acs.analchem.1c01850

Read Online

ACCESS | Metrics & More | Article Recommendations | Supporting Information

ABSTRACT: Biocompatible hydrogels for tissue regeneration/replacement and drug release with specific architectures can be obtained by three-dimensional bioprinting techniques. The preservation of the higher order structure of the proteins embedded in the hydrogels as drugs or modulators is critical for their biological activity. Solution nuclear magnetic resonance (NMR) experiments are currently used to investigate the higher order structure of biotherapeutics in comparability, similarity, and stability studies. However, the size of pores in the gel, protein–matrix interactions, and the size of the embedded proteins often prevent the use of this methodology. The recent advancements of solid-state NMR allow for the comparison of the higher order structure of the matrix-embedded and free isotopically enriched proteins, allowing for the evaluation of the functionality of the material in several steps of hydrogel development. Moreover, the structural information at atomic detail on the matrix–protein interactions paves the way for a structure-based design of these biomaterials.
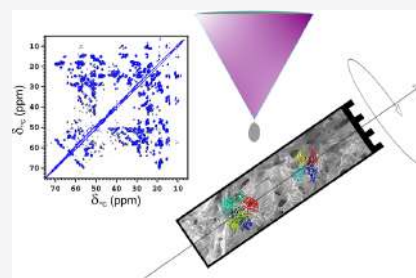
INTRODUCTION

The continuous development of new biocompatible materials is opening new frontiers in medicine and new biotechnological opportunities. Several biomaterials are currently used to replace/support non-functional tissues like those damaged or destroyed by injuries or diseases and in controlled drug release. Materials for tissue regeneration are designed to provide mechanical support to the surrounding tissue, to stimulate cell growth, and to modulate the immune response promoting an extensive cell colonization and matrix reabsorption.[1,2] Composite scaffolds with a highly resolved architecture, incorporating proteins and seeding cells, can be obtained by three-dimensional (3D) bioprinting techniques starting from biocompatible hydrogels like those formed by hyaluronic acid[3–7] or mixtures of alginate and gelatine.[6,8–13] In this context, there is an increasing interest in loading proteins on hydrogels as drugs or modulators of the biological activity.[14–25] The biological function of a protein is strictly related to its native folding, and the preservation of the higher order structure (HOS) in the composite biomaterial is crucial for its therapeutic function. Actually, the interaction of the protein with the matrix components can alter the protein structure leading to a loss of activity and immunological effects.

Several biophysical methodologies, such as attenuated total reflectance Fourier-transformed infrared and fluorescence spectroscopy, circular dichroism, and differential scanning calorimetry, are usually used to characterize the protein

component in heterogeneous materials.[26–28] However, these analytical methods measure different aspects of the structure, either directly or indirectly, and are often not sensitive enough to small, local changes in the protein fold. Nuclear magnetic resonance (NMR) and mass spectrometry are well-established techniques to investigate the preservation of the HOS of biologics in solution.[29–39] Solution NMR has been used previously on small proteins and peptides embedded in hydrogels to investigate the folding state in a confined environment[40] and for the structural characterization through residual dipolar couplings, since hydrogels behave as anisotropic external alignment media.[41–43] However, when the size of the pores in the gels is too small or strong interactions between the gel matrix and the cargo protein take place, the rotational correlation time of the protein in solution increases and makes solution NMR ineffective in the analysis of the protein structure at the atomic level.

Recently, solid-state NMR has emerged as a tool to characterize the protein component and to reveal protein–matrix interactions in heterogeneous materials. In this respect,

the use of solid-state NMR has been described to characterize noncrystalline large protein assemblies,[44−50] biomaterials,[51,52] bioinspired silica matrix embedding enzymes,[53−58] conjugated proteins,[59−62] protein-grafted nanoparticles,[63] and vaccines.[64−66] Here, we prove that solid-state NMR provides detailed information on the preservation of the HOS of proteins embedded into two popular matrices used for 3D bioprinting.

The therapeutic protein *E. coli* asparaginase-II (ANSII), clinically used against acute lymphoblastic leukemia, has recently shown its activity also against solid tumor when administered in long half-life formulations that reduce immunological adverse reactions.[67]

Human transthyretin (TTR) is a physiological protein acting as a hormone carrier.[68,69] Although some genetic variants of TTR lead to a systemic amyloidosis called familial amyloid polyneuropathy,[70] TTR is a potential drug carrier and has been recently proposed as a multivalency Fab platform for target clustering.[71]

Therefore, these two proteins are suitable models to investigate how the matrices used for 3D bioprinting interplay with embedded proteins and are used here to prove the potential of solid-state NMR (SSNMR) in the characterization of the protein components during the design of these composite hydrogels.

■ EXPERIMENTAL SECTION

Sample Preparation and NMR Measurements. [U-^{13}C-^{15}N] ANSII was expressed and purified as previously described.[59,61−64] The expression and purification protocol of [U-^{13}C-^{15}N] TTR is reported in the Supporting Information. All the hydrogels embedding the selected proteins (ANSII and TTR) were directly generated in Bruker 3.2 mm thin-walls zirconia rotors with bottom and top caps, starting from the dried materials prepared by using the different procedures described below.

The sample of [U-^{13}C-^{15}N] ANSII encapsulated in the alginate/gelatine hydrogel was prepared by incorporating the freeze-dried protein (4 mg) into a mixture of 1:1 alginate/gelatine powders (5 mg) and then by rehydrating the dried mixture within the rotor.[72] A different procedure was used to prepare the sample of [U-^{13}C-^{15}N] TTR encapsulated in the alginate/gelatine hydrogel. The dry mixture containing TTR was prepared by lyophilizing a solution containing all the components (6 mg of protein and 5 mg of the 1:1 alginate/gelatine mixture). In both cases, the dried material was packed in the rotor and hydrated with MilliQ H$_2$O to reach a final concentration of ∼5−7% w/w for alginate and gelatine. Finally, a concentrated solution of CaCl$_2$ (to reach a concentration of 100 mM in the rotor) was added to cross-link the hydrogel materials within the rotor.[73,74]

A sample of [U-^{13}C-^{15}N] TTR protein encapsulated in the alginate/gelatine hydrogel was also analyzed by solution NMR. The gel was prepared by dissolving a mixture of alginate and gelatine (∼7% w/w) in 600 µL of a solution of TTR (100 µM in 50 mM MES, pH 6.5, 100 mM NaCl, 5 mM DTT). Then, the material was transferred in a 5 mm tube and cross-linked by adding a concentrated solution of CaCl$_2$ (to reach a concentration of 100 mM) in the NMR tube. The 2D ^{1}H-^{15}N TROSY-HSQC spectrum recorded on the encapsulated protein was superimposed with that of TTR collected in solution (see Figure S1).

The hyaluronic acid hydrogels encapsulating the selected proteins ([U-^{13}C-^{15}N] ANSII or TTR) were prepared by packing the rotor with consecutive layers of the freeze-dried protein (∼4−6 mg) and freeze-dried hyaluronic acid (Jonexa, 7−9 mg), which had been previously dialyzed against MilliQ H$_2$O to remove the excess of salts. The material was finally rehydrated with MilliQ H$_2$O (from 10 to 20 µL). Sample homogeneity was obtained after rotor spinning and supported by the quality of the spectra that suggests the presence of a protein experiencing a single environment.

Samples of freeze-dried proteins were prepared as reference. The free proteins (∼20 and 25 mg of ANSII and TTR, respectively) were freeze-dried in the presence of PEG1000 (4 and 2.5 mg for ANSII and TTR, respectively); the materials were packed into a Bruker 3.2 mm zirconia rotor and rehydrated with MilliQ H$_2$O (∼9 and 16 µL for ANSII and TTR, respectively). CaCl$_2$ was not present in the samples of rehydrated freeze-dried proteins.
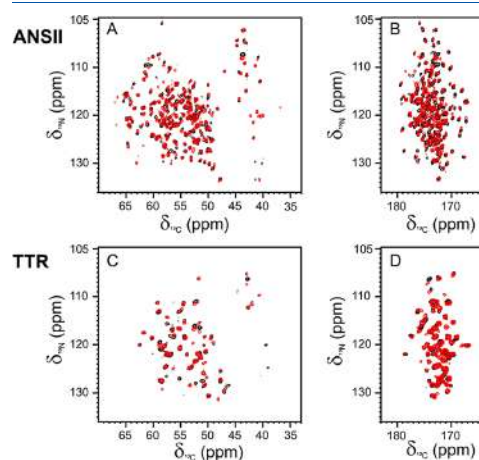
Figure 1. (A, C) 2D ^{15}N ^{13}C NCA and (B, D) NCO spectra of ANSII-HA (red, top) and TTR-HA (red, bottom) superimposed with NCA and NCO of the rehydrated freeze-dried reference proteins (black). The spectra were acquired at ∼290 K, MAS 14 kHz and 800 MHz.

Silicon plugs (courtesy of Bruker Biospin) placed below the turbine cap were used to close the rotor and preserve hydration.

SSNMR experiments were recorded on a Bruker Avance III spectrometer operating at 800 MHz (18.8 T, 201.2 MHz ^{13}C Larmor frequency) equipped with a Bruker 3.2 mm Efree NCH probe-head. The spectra were recorded at 14 kHz MAS frequency, and the sample temperature was kept at ∼290 K. The sample of the alginate/gelatine hydrogel encapsulating TTR was also investigated at a higher spinning frequency (16 and 20 kHz).

Standard ^{13}C-detected SSNMR spectra (2D ^{15}N-^{13}C NCA, ^{15}N-^{13}C NCO, and ^{13}C-^{13}C DARR, mixing time 50 ms) were acquired on all the samples (except for TTR encapsulated in the alginate/gelatine hydrogel) using the pulse sequences reported in the literature.[75] 2D ^{13}C-^{13}C CORDxy4[76] was instead recorded for the sample of the alginate/gelatine
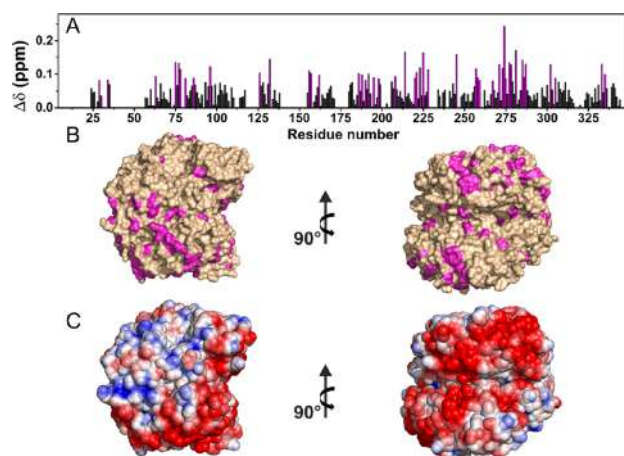
Figure 2. (A) Chemical shift perturbations (CSPs) of ANSII-HA with respect to rehydrated freeze-dried ANSII, evaluated according to the formula $\Delta\delta = \frac{1}{2}\sqrt{(\Delta\delta_{C\alpha}/2)^2 + (\Delta\delta_N/5)^2}$. The residues experiencing the largest variations have been highlighted in magenta. (B) CSP mapping on the protein surface (PDB code: 3ECA) with the region with the largest perturbation in magenta. (C) Electrostatic potential generated by APBS plugin in PyMOL on 3ECA with blue and red representing the regions of positive and negative electrostatic potential, respectively.
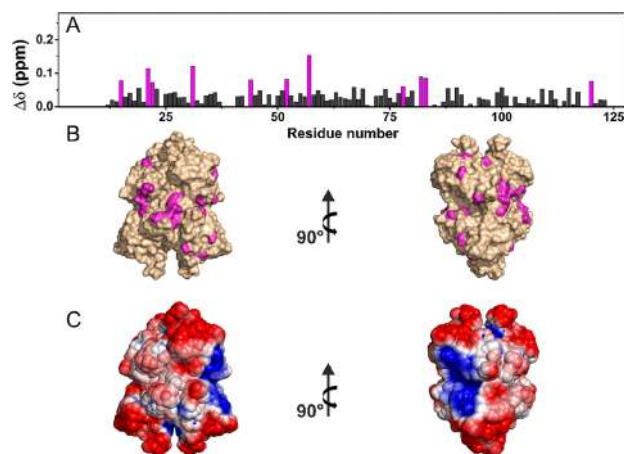
Figure 3. (A) Chemical shift perturbations (CSPs) of TTR-HA with respect to rehydrated freeze-dried TTR, evaluated according to the formula $\Delta\delta = \frac{1}{2}\sqrt{(\Delta\delta_{C\alpha}/2)^2 + (\Delta\delta_N/5)^2}$. The residues experiencing the largest variations have been highlighted in magenta. (B) CSP mapping on the protein surface (PDB code: 1BMZ) with the region with the largest perturbation in magenta. (C) Electrostatic potential generated by APBS plugin in PyMOL on 1BMZ with blue and red representing the regions of positive and negative electrostatic potential, respectively.

hydrogel encapsulating TTR at a higher frequency speed (20 kHz), to favor the protein sedimentation.

All the spectra were processed with the Bruker TopSpin 3.2 software package and analyzed with the program CARA.[77]

■ RESULTS AND DISCUSSION

Analysis of the Preservation of the HOS of the Proteins Encapsulated in the Hyaluronic Acid Hydrogel by SSNMR. The selected proteins (ANSII and TTR)

encapsulated in the hyaluronic acid hydrogel (ANSII-HA and TTR-HA, respectively) were first analyzed by SSNMR. The 1D {^{1}H}-^{13}C cross polarization spectra of ANSII-HA and TTR-HA show well-resolved and sharp signals with quality comparable with that of the spectra of the rehydrated freeze-dried materials (Figure S2).

Despite the limited concentration of the embedded proteins in the hydrogel, the 2D amide-carbon alpha (2D ^{15}N ^{13}C NCA) and amide-carbonyl (2D ^{15}N ^{13}C NCO) correlation spectra of ANSII-HA (Figure 1A,B) and TTR-HA (Figure
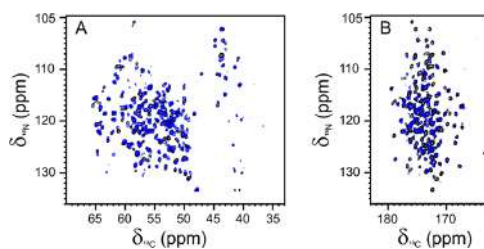
**Figure 4.** (A) 2D ^{15}N ^{13}C NCA and (B) NCO spectra of ANSII-AG (blue) superimposed with the NCA and NCO of the rehydrated freeze-dried reference protein (black). The spectra were acquired at ~290 K, MAS 14 kHz and 800 MHz.

1C,D) are of high quality and comparable, for the number of cross-peaks detected, with those of rehydrated freeze-dried proteins. For both proteins embedded in the hyaluronic acid matrix, the matching of the resonances of the 2D-NMR spectral fingerprints with those of their own reference allows us to assess the preservation of the HOS after encapsulation in the matrix.

The assignment of the 2D ^{15}N ^{13}C NCA and NCO spectra of ANSII-HA and TTR-HA was easily obtained by comparison with the 2D ^{15}N ^{13}C NCA and NCO collected for the rehydrated freeze-dried proteins and also using the information from the 2D ^{13}C-^{13}C correlation spectrum (dipolar assisted rotational resonance, DARR) acquired for ANSII-HA and TTR-HA. The analyses of the chemical shift perturbation (CSP) of the NCA spectra of the proteins embedded in the hyaluronic acid hydrogels, with respect to the NCA of the corresponding rehydrated freeze-dried references, are reported in Figures 2 and 3. Most CSP values were less than 0.1 ppm for ANSII-HA and even lower for TTR-HA. The analysis of the

CSPs shows that for ANSII-HA, hydrophobic (Ala, Val, Ile, Tyr, and Phe) and neutral polar (Thr, Ser, Asn, and Gln) residues experience the largest effects (Figure 2). Minimal CSPs were observed in TTR-HA protein where the largest effects again involve hydrophobic residues and neutral polar surface patches (Figure 3).

Analysis of the Preservation of the HOS of the Proteins Encapsulated in the Alginate/Gelatine Hydrogel by SSNMR. The same analysis was also performed on the alginate/gelatine hydrogels encapsulating ANSII and TTR, respectively (ANSII-AG and TTR-AG). The 1D {^1H}-^{13}C cross polarization spectra of ANSII-AG and TTR-AG show the same spreading of the resonances of the corresponding rehydrated freeze-dried analogue. However, in particular for TTR-AG, the signals feature broader lines than in the rehydrated freeze-dried protein (Figure S2).

The NCA and NCO correlation spectra collected for ANSII-AG (Figure 4) are still of high quality and comparable, for the number of cross-peaks detected, with those collected on rehydrated freeze-dried ANSII. On the contrary, for TTR-AG, the fast decay of the NMR signal does not allow us to collect high quality and well-resolved 2D spectra. However, by increasing the spinning rate up to 16 and 20 kHz, the signals become sharper and increase in intensity (Figure S3), indicating a more efficient protein immobilization. Therefore, it was possible to acquire a 2D ^{13}C-^{13}C correlation spectrum at 20 kHz, which allowed us to assess the folding state of the protein in the hydrogel and, after comparison with that acquired for the rehydrated freeze-dried reference (Figure S4), confirm the preservation of the HOS after encapsulation. The structural analysis of TTR encapsulated in the alginate/gelatine matrix was also attempted using solution NMR. However, all the signals, but the N- and C-termini (Thr3-Ser8; Lys126-Glu127), are broadened beyond detection (Figure S1).
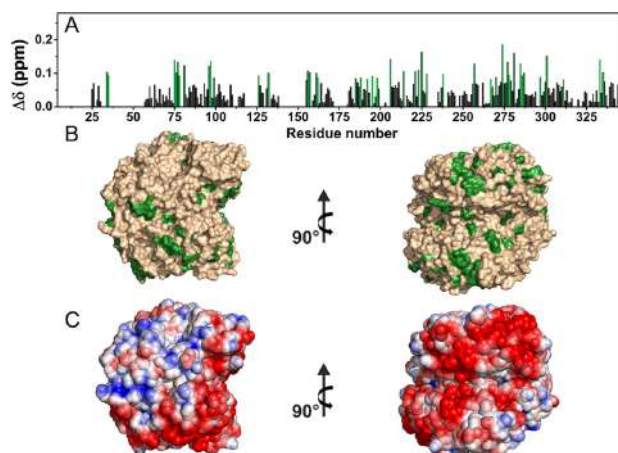
Figure 5. (A) Chemical shift perturbations (CSPs) of ANSII-AG with respect to rehydrated freeze-dried ANSII, evaluated according to the formula $\Delta\delta = \frac{1}{2}\sqrt{(\Delta\delta_{C\alpha}/2)^2 + (\Delta\delta_N/5)^2}$. The residues experiencing the largest variations have been highlighted in green. (B) CSP mapping on the protein surface (PDB code: 3ECA) with the region with the largest perturbation in green. (C) Electrostatic potential generated by APBS plugin in PyMOL on 3ECA with blue and red representing the regions of positive and negative electrostatic potential, respectively.

The assignment of the ANSII-AG spectra could be easily obtained by comparison with the spectra collected for the rehydrated freeze-dried protein and complemented with the information from the 2D ^{13}C-^{13}C correlation spectrum acquired for ANSII-AG. The analysis of the CSP of the NCA spectrum of ANSII-AG with respect to the NCA of the rehydrated freeze-dried reference is reported in Figure 5.

The analysis of the CSPs shows that also for ANSII-AG, hydrophobic (Ala, Val, Ile, Tyr, and Phe) and neutral polar (Thr, Ser, Ans, and Gln) residues experience the largest effects. In particular, many threonine residues are affected by significant CSP, thus suggesting a possible interaction of these surface residues with the hydroxyl groups of alginate in the hydrogel.

Collectively, the good superimposition of the spectra and the small CSPs observed for the two proteins prove the preservation of their native HOS, thus providing the first fundamental information on the investigated biomaterial. Additional information on protein—matrix interactions is obtained from the line broadening of the signals in the spectra. For TTR, the large line broadening, its dependence from the spinning rate, and the small CSPs suggest a weaker protein—matrix interaction with respect to ANSII protein, although the different molecular weights may also play a role. The different behavior is probably related to the different sizes of the proteins and to the physical—chemical properties of the surface due to the different amino acid compositions. In this respect, the observation that hydrophobic and polar neutral amino acids on the protein surface experience the largest effects provides a way to design possible chemical modifications of the matrix in order to tune the protein—matrix interactions and the properties of the resulting biomaterial.[78−82]

CONCLUSIONS

In summary, we demonstrate that 2D-SSNMR spectra can be exploited to assess the preservation of HOS of proteins when embedded in matrices used for 3D bioprinting and drug release. This analytical method can be integrated in the pipeline for the development of new composite hydrogels bearing biotherapeutics. In particular, when the assignment is available, the analysis of the residues experiencing chemical shift variations can provide information for a quality by design approach of these innovative biomaterials.

ASSOCIATED CONTENT

(SI) Supporting Information

The Supporting Information is available free of charge at https://pubs.acs.org/doi/10.1021/acs.analchem.1c01850.

Protocols for the expression and purification of isotopically enriched E. coli asparaginase-II (ANSII) and human transthyretin (TTR) and figures showing additional spectra of E. coli asparaginase-II (ANSII) and human transthyretin (TTR) (PDF)

AUTHOR INFORMATION

Corresponding Author

Marco Fragai − *Magnetic Resonance Center (CERM), University of Florence, and Consorzio Interuniversitario Risonanze Magnetiche di Metalloproteine (CIRMMP), Sesto Fiorentino 50019, Italy; Department of Chemistry "Ugo Schiff", University of Florence, Sesto Fiorentino 50019, Italy;* orcid.org/0000-0002-8440-1690; Phone: +39 055 4574261; Email: fragai@cerm.unifi.it

Authors

Domenico Rizzo − *Magnetic Resonance Center (CERM), University of Florence, and Consorzio Interuniversitario Risonanze Magnetiche di Metalloproteine (CIRMMP), Sesto Fiorentino 50019, Italy; Department of Chemistry "Ugo Schiff", University of Florence, Sesto Fiorentino 50019, Italy*

Linda Cerofolini − *Magnetic Resonance Center (CERM), University of Florence, and Consorzio Interuniversitario Risonanze Magnetiche di Metalloproteine (CIRMMP), Sesto Fiorentino 50019, Italy*

Anna Pérez-Ràfols − *Department of Chemistry "Ugo Schiff", University of Florence, Sesto Fiorentino 50019, Italy; Giotto Biotech, S.R.L, Sesto Fiorentino, Florence 50019, Italy*

Stefano Giuntini − *Magnetic Resonance Center (CERM), University of Florence, and Consorzio Interuniversitario Risonanze Magnetiche di Metalloproteine (CIRMMP), Sesto Fiorentino 50019, Italy; Department of Chemistry "Ugo Schiff", University of Florence, Sesto Fiorentino 50019, Italy*

Fabio Baroni − *Analytical Development Biotech Department, Merck Serono S.p.a, Merck KGaA, Guidonia, Rome 00012, Italy*

Enrico Ravera − *Magnetic Resonance Center (CERM), University of Florence, and Consorzio Interuniversitario Risonanze Magnetiche di Metalloproteine (CIRMMP), Sesto Fiorentino 50019, Italy; Department of Chemistry "Ugo Schiff", University of Florence, Sesto Fiorentino 50019, Italy;* orcid.org/0000-0001-7708-9208

Claudio Luchinat − *Magnetic Resonance Center (CERM), University of Florence, and Consorzio Interuniversitario Risonanze Magnetiche di Metalloproteine (CIRMMP), Sesto Fiorentino 50019, Italy; Department of Chemistry "Ugo Schiff", University of Florence, Sesto Fiorentino 50019, Italy*

Complete contact information is available at:
https://pubs.acs.org/10.1021/acs.analchem.1c01850

Author Contributions

The manuscript was written through contributions of all authors. All authors have given approval to the final version of the manuscript.

Notes

The authors declare no competing financial interest.

■ REFERENCES

(1) Gaharwar, A. K.; Singh, I.; Khademhosseini, A. *Nat. Rev. Mater.* **2020**, *5*, 686−705.
(2) Gu, L.; Mooney, D. J. *Nat. Rev. Cancer* **2016**, *16*, 56−66.
(3) Suri, S.; Han, L.-H.; Zhang, W.; Singh, A.; Chen, S.; Schmidt, C. E. *Biomed. Microdevices* **2011**, *13*, 983−993.
(4) Noh, I.; Kim, N.; Tran, H. N.; Lee, J.; Lee, C. *Biomater. Res.* **2019**, *23*, 3.
(5) Wei, Y.-T.; He, Y.; Xu, C.-L.; Wang, Y.; Liu, B.-F.; Wang, X.-M.; Sun, X.-D.; Cui, F.-Z.; Xu, Q.-Y. *J. Biomed. Mater. Res. B Appl. Biomater.* **2010**, *95B*, 110−117.
(6) Antich, C.; de Vicente, J.; Jiménez, G.; Chocarro, C.; Carrillo, E.; Montañez, E.; Gálvez-Martín, P.; Marchal, J. A. *Acta Biomater.* **2020**, *106*, 114−123.
(7) Skardal, A.; Zhang, J.; Prestwich, G. D. *Biomaterials* **2010**, *31*, 6173−6181.
(8) Chung, J. H. Y.; Naficy, S.; Yue, Z.; Kapsa, R.; Quigley, A.; Moulton, S. E.; Wallace, G. G. *Biomater. Sci.* **2013**, *1*, 763−773.
(9) Wu, Z.; Su, X.; Xu, Y.; Kong, B.; Sun, W.; Mi, S. *Sci. Rep.* **2016**, *6*, 24474.
(10) Poldervaart, M. T.; Wang, H.; van der Stok, J.; Weinans, H.; Leeuwenburgh, S. C. G.; Öner, F. C.; Dhert, W. J. A.; Alblas, J. *PLoS One* **2013**, *8*, No. e72610.
(11) Duan, B.; Hockaday, L. A.; Kang, K. H.; Butcher, J. T. *J. Biomed. Mater. Res. A* **2013**, *101A*, 1255−1264.
(12) Giuseppe, M. D.; Law, N.; Webb, B.; Macrae, R. A.; Liew, L. J.; Sercombe, T. B.; Dilley, R. J.; Doyle, B. J. *J. Mech. Behav. Biomed. Mater.* **2018**, *79*, 150−157.
(13) Jia, W.; Gungor-Ozkerim, P. S.; Zhang, Y. S.; Yue, K.; Zhu, K.; Liu, W.; Pi, Q.; Byambaa, B.; Dokmeci, M. R.; Shin, S. R.; Khademhosseini, A. *Biomaterials* **2016**, *106*, 58−68.
(14) Buwalda, S. J.; Vermonden, T.; Hennink, W. E. *Biomacromolecules* **2017**, *18*, 316−330.
(15) Chen, J.; Ouyang, J.; Chen, Q.; Deng, C.; Meng, F.; Zhang, J.; Cheng, R.; Lan, Q.; Zhong, Z. *ACS Appl. Mater. Interfaces* **2017**, *9*, 24140−24147.
(16) Zhu, Q.; Chen, X.; Xu, X.; Zhang, Y.; Zhang, C.; Mo, R. *Adv. Funct. Mater.* **2018**, *28*, No. 1707371.
(17) Wawrzyńska, E.; Kubies, D. *Physiol. Res.* **2018**, S319−S334.
(18) Iqbal, S.; Blenner, M.; Alexander-Bryant, A.; Larsen, J. *Biomacromolecules* **2020**, *21*, 1327−1350.
(19) Shigemitsu, H.; Kubota, R.; Nakamura, K.; Matsuzaki, T.; Minami, S.; Aoyama, T.; Urayama, K.; Hamachi, I. *Nat. Commun.* **2020**, *11*, 3859.
(20) Lau, C. M. L.; Jahanmir, G.; Yu, Y.; Chau, Y. *J. Controlled Release* **2021**, *335*, 75−85.
(21) Tae, H.; Lee, S.; Ki, C. S. *J. Ind. Eng. Chem.* **2019**, *75*, 69−76.
(22) Chang, D.; Park, K.; Famili, A. *Drug Discovery Today* **2019**, *24*, 1470−1482.
(23) Ziegler, C. E.; Graf, M.; Beck, S.; Goepferich, A. M. *Eur. Polym. J.* **2021**, *147*, No. 110286.
(24) Gombotz, W. R.; Wee, S. F. *Adv. Drug Delivery Rev.* **2012**, *64*, 194−205.
(25) Vermonden, T.; Censi, R.; Hennink, W. E. *Chem. Rev.* **2012**, *112*, 2853−2888.
(26) Kumar, S.; Koh, J. *Int. J. Mol. Sci.* **2012**, *13*, 6102−6116.
(27) Dong, A.; Jones, L. S.; Kerwin, B. A.; Krishnan, S.; Carpenter, J. F. *Anal. Biochem.* **2006**, *351*, 282−289.
(28) Kirkitadze, M.; Sinha, A.; Hu, J.; Williams, W.; Cates, G. *Procedia Vaccinol.* **2009**, *1*, 135−139.
(29) Arbogast, L. W.; Brinson, R. G.; Marino, J. P. *Anal. Chem.* **2015**, *87*, 3556−3561.
(30) Brinson, R. G.; Marino, J. P.; Delaglio, F.; Arbogast, L. W.; Evans, R. M.; Kearsley, A.; Gingras, G.; Ghasriani, H.; Aubin, Y.;

Pierens, G. K.; Jia, X.; Mobli, M.; Grant, H. G.; Keizer, D. W.; Schweimer, K.; Ståhle, J.; Widmalm, G.; Zartler, E. R.; Lawrence, C. W.; Reardon, P. N.; Cort, J. R.; Xu, P.; Ni, F.; Yanaka, S.; Kato, K.; Parnham, S. R.; Tsao, D.; Blomgren, A.; Rundlöf, T.; Trieloff, N.; Schmieder, P.; Ross, A.; Skidmore, K.; Chen, K.; Keire, D.; Freedberg, D. I.; Suter-Stahel, T.; Wider, G.; Ilc, G.; Plavec, J.; Bradley, S. A.; Baldisseri, D. M.; Sforça, M. L.; de Zeri, A. C. M.; Wei, J. Y.; Szabo, C. M.; Amezcua, C. A.; Jordan, J. B.; Wikström, M. *mAbs* **2019**, *11*, 94−105.
(31) Jones, L. M.; Zhang, H.; Cui, W.; Kumar, S.; Sperry, J. B.; Carroll, J. A.; Gross, M. L. *J. Am. Soc. Mass Spectrom.* **2013**, *24*, 835−845.
(32) Pan, L. Y.; Salas-Solano, O.; Valliere-Douglass, J. F. *Anal. Chem.* **2014**, *86*, 2657−2664.
(33) Ehkirch, A.; Hernandez-Alba, O.; Colas, O.; Beck, A.; Guillarme, D.; Cianférani, S. *J. Chromatogr. B Analyt. Technol. Biomed. Life Sci.* **2018**, *1086*, 176−183.
(34) Brinson, R. G.; Ghasriani, H.; Hodgson, D. J.; Adams, K. M.; McEwen, I.; Freedberg, D. I.; Chen, K.; Keire, D. A.; Aubin, Y.; Marino, J. P. *J. Pharm. Biomed. Anal.* **2017**, *141*, 229−233.
(35) Ghasriani, H.; Hodgson, D. J.; Brinson, R. G.; McEwen, I.; Buhse, L. F.; Kozlowski, S.; Marino, J. P.; Aubin, Y.; Keire, D. A. *Nat. Biotechnol.* **2016**, *34*, 139−141.
(36) Arbogast, L. W.; Brinson, R. G.; Formolo, T.; Hoopes, J. T.; Marino, J. P. *Pharm. Res.* **2016**, *33*, 462−475.
(37) Arbogast, L. W.; Delaglio, F.; Tolman, J. R.; Marino, J. P. *J. Biomol. NMR* **2018**, *72*, 149−161.
(38) Arbogast, L. W.; Delaglio, F.; Brinson, R. G.; Marino, J. P. *Curr. Protoc. Protein Sci.* **2020**, *100*, No. e105.
(39) Wu, K.; Luo, J.; Zeng, Q.; Dong, X.; Chen, J.; Zhan, C.; Chen, Z.; Lin, Y. *Anal. Chem.* **2021**, *93*, 1377−1382.
(40) Pastore, A.; Salvadori, S.; Temussi, P. A. *J. Pept. Sci.* **2007**, *13*, 342−347.
(41) Sass, H.-J.; Musco, G.; Stahl, S. J.; Wingfield, P. T.; Grzesiek, S. *J. Biomol. NMR* **2000**, *18*, 303−309.
(42) Barrientos, L. G.; Dolan, C.; Gronenborn, A. M. *J. Biomol. NMR* **2000**, *16*, 329−337.
(43) Tycko, R.; Blanco, F. J.; Ishii, Y. *J. Am. Chem. Soc.* **2000**, *122*, 9340−9341.
(44) Lecoq, L.; Fogeron, M.-L.; Meier, B. H.; Nassal, M.; Böckmann, A. Solid-State NMR for Studying the Structure and Dynamics of Viral Assemblies. *Viruses* **2020**, *12* (), DOI: 10.3390/v12101069.
(45) Wiegand, T.; Lacabanne, D.; Torosyan, A.; Boudet, J.; Cadalbert, R.; Allain, F. H.-T.; Meier, B. H.; Böckmann, A. *Front. Mol. Biosci.* **2020**, *7*, 17.
(46) Hassan, A.; Quinn, C. M.; Struppe, J.; Sergeyev, I. V.; Zhang, C.; Guo, C.; Runge, B.; Theint, T.; Dao, H. H.; Jaroniec, C. P.; Berbon, M.; Lends, A.; Habenstein, B.; Loquet, A.; Kuemmerle, R.; Perrone, B.; Gronenborn, A. M.; Polenova, T. *J. Magn. Reson.* **2020**, *311*, No. 106680.
(47) Lu, M.; Russell, R. W.; Bryer, A. J.; Quinn, C. M.; Hou, G.; Zhang, H.; Schwieters, C. D.; Perilla, J. R.; Gronenborn, A. M.; Polenova, T. *Nat. Struct. Mol. Biol.* **2020**, *27*, 863−869.
(48) Eddy, M. T.; Yu, T.-Y.; Wagner, G.; Griffin, R. G. *J. Biomol. NMR* **2019**, *73*, 451−460.
(49) Gupta, R.; Zhang, H.; Lu, M.; Hou, G.; Caporini, M.; Rosay, M.; Maas, W.; Struppe, J.; Ahn, J.; Byeon, I.-J. L.; Oschkinat, H.; Jaudzems, K.; Barbet-Massin, E.; Emsley, L.; Pintacuda, G.; Lesage, A.; Gronenborn, A. M.; Polenova, T. *J. Phys. Chem. B* **2019**, *123*, 5048−5058.
(50) le Paige, U. B.; Xiang, S.; Hendrix, M. M. R. M.; Zhang, Y.; Folkers, G. E.; Weingarth, M.; Bonvin, A. M. J. J.; Kutateladze, T. G.; Voets, I. K.; Baldus, M.; van Ingen, H. *Magn. Reson.* **2021**, *2*, 187−202.
(51) Mroue, K. H.; MacKinnon, N.; Xu, J.; Zhu, P.; McNerny, E.; Kohn, D. H.; Morris, M. D.; Ramamoorthy, A. *J. Phys. Chem. B* **2012**, *116*, 11656−11661.

68

(52) Azaïs, T.; Von Euw, S.; Ajili, W.; Auzoux-Bordenave, S.; Bertani, P.; Gajan, D.; Emsley, L.; Nassif, N.; Lesage, A. *Solid State Nucl. Magn. Reson.* **2019**, *102*, 2−11.

(53) Cerofolini, L.; Giuntini, S.; Louka, A.; Ravera, E.; Fragai, M.; Luchinat, C. *J. Phys. Chem. B* **2017**, *121*, 8094−8101.

(54) Louka, A.; Matlahov, I.; Giuntini, S.; Cerofolini, L.; Cavallo, A.; Pillozzi, S.; Ravera, E.; Fragai, M.; Arcangeli, A.; Ramamoorthy, A.; Goobes, G.; Luchinat, C. *Phys. Chem. Chem. Phys.* **2018**, *20*, 12719−12726.

(55) Ravera, E.; Cerofolini, L.; Martelli, T.; Louka, A.; Fragai, M.; Luchinat, C. *Sci. Rep.* **2016**, *6*, 27851.

(56) Martelli, T.; Ravera, E.; Louka, A.; Cerofolini, L.; Hafner, M.; Fragai, M.; Becker, C. F. W.; Luchinat, C. *Chemistry* **2016**, *22*, 425−432.

(57) Fragai, M.; Luchinat, C.; Martelli, T.; Ravera, E.; Sagi, I.; Solomonov, I.; Udi, Y. *Chem. Commun.* **2014**, *50*, 421−423.

(58) Ravera, E.; Schubeis, T.; Martelli, T.; Fragai, M.; Parigi, G.; Luchinat, C. *J. Magn. Reson.* **2015**, *253*, 60−70.

(59) Cerofolini, L.; Giuntini, S.; Carlon, A.; Ravera, E.; Calderone, V.; Fragai, M.; Parigi, G.; Luchinat, C. *Chem. − Eur. J.* **2019**, *25*, 1984−1991.

(60) Cerofolini, L.; Fragai, M.; Ravera, E.; Diebolder, C. A.; Renault, L.; Calderone, V. *Biomolecules* **2019**, *9*, 370.

(61) Giuntini, S.; Balducci, E.; Cerofolini, L.; Ravera, E.; Fragai, M.; Berti, F.; Luchinat, C. *Angew. Chem., Int. Ed.* **2017**, *56*, 14997−15001.

(62) Ravera, E.; Ciambellotti, S.; Cerofolini, L.; Martelli, T.; Kozyreva, T.; Bernacchioni, C.; Giuntini, S.; Fragai, M.; Turano, P.; Luchinat, C. *Angew. Chem. Int. Ed. Engl.* **2016**, *55*, 2446−2449.

(63) Giuntini, S.; Cerofolini, L.; Ravera, E.; Fragai, M.; Luchinat, C. *Sci. Rep.* **2017**, *7*, 17934.

(64) Cerofolini, L.; Giuntini, S.; Ravera, E.; Luchinat, C.; Berti, F.; Fragai, M. *npj Vaccines* **2019**, *4*, 20.

(65) Viger-Gravel, J.; Paruzzo, F. M.; Cazaux, C.; Jabbour, R.; Leleu, A.; Canini, F.; Florian, P.; Ronzon, F.; Gajan, D.; Lesage, A. *Chemistry* **2020**, *26*, 8976−8982.

(66) Jaudzems, K.; Kirsteina, A.; Schubeis, T.; Casano, G.; Ouari, O.; Bogans, J.; Kazaks, A.; Tars, K.; Lesage, A.; Pintacuda, G. *Angew. Chem. Int. Ed. Engl.* **2021**, *60*, 12847.

(67) Wang, H.; Wang, L.; Li, C.; Wuxiao, Z.; Chen, G.; Luo, W.; Lu, Y. *Oncologist* **2020**, *25*, e1725−e1731.

(68) Herbert, J.; Wilcox, J. N.; Pham, K.-T. C.; Fremeau, R. T.; Zeviani, M.; Dwork, A.; Soprano, D. R.; Makover, A.; Goodman, D. S.; Zimmerman, E. A.; Roberts, J. L.; Schon, E. A. *Neurology* **1986**, *36*, 900−900.

(69) Hamilton, J. A.; Benson, M. D. *Cell. Mol. Life Sci.* **2001**, *58*, 1491−1521.

(70) Connors, L. H.; Lim, A.; Prokaeva, T.; Roskens, V. A.; Costello, C. E. *Amyloid* **2003**, *10*, 160−184.

(71) Walker, K. W.; Foltz, I. N.; Wang, T.; Salimi-Moosavi, H.; Bailis, J. M.; Lee, F.; An, P.; Smith, S.; Bruno, R.; Wang, Z. *J. Biol. Chem.* **2020**, *295*, 10446−10455.

(72) Fragai, M.; Luchinat, C.; Parigi, G.; Ravera, E. *J. Biomol. NMR* **2013**, *57*, 155−166.

(73) Sarker, B.; Papageorgiou, D. G.; Silva, R.; Zehnder, T.; Gul-E-Noor, F.; Bertmer, M.; Kaschta, J.; Chrissafis, K.; Detsch, R.; Boccaccini, A. R. *J. Mater. Chem. B* **2014**, *2*, 1470−1482.

(74) Wang, Q.-Q.; Liu, Y.; Zhang, C.-J.; Zhang, C.; Zhu, P. *Mater. Sci. Eng. C Mater. Biol. Appl.* **2019**, *99*, 1469−1476.

(75) Schuetz, A.; Wasmer, C.; Habenstein, B.; Verel, R.; Greenwald, J.; Riek, R.; Böckmann, A.; Meier, B. H. *ChemBioChem* **2010**, *11*, 1543−1551.

(76) Lu, X.; Guo, C.; Hou, G.; Polenova, T. *J. Biomol. NMR* **2015**, *61*, 7−20.

(77) Keller, R. The Computer Aided Resonance Assignment Tutorial (CARA); *The CARA/Lua Programmers Manual. DATONAL AG.*; CANTINA Verlag: Goldau. Switzerland, 2004.

(78) Leach, J. B.; Schmidt, C. E. *Biomaterials* **2005**, *26*, 125−135.

(79) Jia, J.; Richards, D. J.; Pollard, S.; Tan, Y.; Rodriguez, J.; Visconti, R. P.; Trusk, T. C.; Yost, M. J.; Yao, H.; Markwald, R. R.; Mei, Y. *Acta Biomater.* **2014**, *10*, 4323−4331.

(80) Ouyang, L.; Yao, R.; Zhao, Y.; Sun, W. *Biofabrication* **2016**, *8*, No. 035020.

(81) Gao, T.; Gillispie, G. J.; Copus, J. S.; Pr, A. K.; Seol, Y.-J.; Atala, A.; Yoo, J. J.; Lee, S. J. *Biofabrication* **2018**, *10*, No. 034106.

(82) Liao, Y.-H.; Jones, S. A.; Forbes, B.; Martin, G. P.; Brown, M. B. *Drug Delivery* **2005**, *12*, 327−342.

69

Supporting Information

Evaluation of the Higher Order Structure of biotherapeutics embedded in hydrogels for bioprinting and drug release

Domenico Rizzo[1,2], Linda Cerofolini[1], Anna Pérez-Ràfols[2,3], Stefano Giuntini[1,2], Fabio Baroni[4], Enrico Ravera[1,2], Claudio Luchinat[1,2], Marco Fragai[*1,2]

1. Magnetic Resonance Center (CERM), University of Florence, and Consorzio Interuniversitario Risonanze Magnetiche di Metalloproteine (CIRMMP) Via L. Sacconi 6, 50019 Sesto Fiorentino, Italy
2. Department of Chemistry "Ugo Schiff", University of Florence, Via della Lastruccia 3, 50019, Sesto Fiorentino, Italy
3. Giotto Biotech, S.R.L, Via Madonna del piano 6, 50019, Sesto Fiorentino (FI), Italy
4. Analytical Development Biotech Department, Merck Serono S.p.a, Guidonia, RM, Italy; an affiliate of Merck KGaA

*Corresponding author; Phone: +39 055 4574261; E-mail: fragai@cerm.unifi.it

Table of Contents

Expression and purification of uniformly isotopically enriched ANSII [U-^{13}C-^{15}N]. Escherichia coli C41(DE3) cells were transformed with pET-21a(+) plasmid encoding ANSII gene. The cells were cultured in ^{13}C-, ^{15}N-enriched minimal medium (M9) containing 0.1 mg/mL of ampicillin, and grown at 310 K until OD_{600} reached 0.6–0.8. Then, the cells were induced with 1 mM isopropyl β-D-1-thiogalactopyranoside and further grown at 310 K overnight. Finally, they were harvested by centrifugation at 6500 rpm (JA-10 Beckman Coulter) for 15 min at 277 K. The pellet obtained from 1 liter of culture was suspended in 60 mL of 10 mM Tris-HCl buffer, at pH 8.0, with 15 mM EDTA, 20% sucrose and incubated at 277 K for 20 min, under magnetic stirring. The suspension was centrifuged at 10,000 rpm (F15-6x100y Thermo Scientific) for 30 min, and the supernatant discarded. The recovered pellet was re-suspended in H_2O milli-Q and newly incubated with the Tris-HCl buffer solution at 277 K for 20 min under magnetic stirring. Again, the suspension was centrifuged at 10,000 rpm (F15-6x100y Thermo Scientific) for 30 min. The pellet was discarded, whereas the supernatant was treated with ammonium sulfate. Still under magnetic stirring, aliquots of solid ammonium sulfate were added up to 50% saturation. Then, the precipitate was removed by centrifugation, and ammonium sulfate added again up to 90% saturation to trigger the precipitation of ANSII, which was recovered by centrifugation. The precipitated ANSII was re-dissolved in a minimal amount of 20 mM Tris-HCl buffer at pH 8.6 and dialyzed extensively against the same buffer. ANSII was purified by anionic-exchange chromatography using a HiPrep Q FF 16/10 column (GE Healthcare Life Science). The protein was eluted in 20 mM Tris-HCl buffer at pH 8.6 with a linear 0–1 M NaCl gradient. Fractions containing pure ANSII were identified by Coomassie staining SDS-PAGE gels, then joined and dialyzed extensively against 0.5 mM Tris-HCl buffer at pH 7.5. Aliquots of 0.5 mL, each containing 1 mg of protein, were freeze-dried to be used for SSNMR analysis.

Expression and purification of uniformly isotopically enriched TTR [U-^{13}C-^{15}N]. Escherichia coli BL21(DE3) RIPL pLysS cells were transformed with pET-28a(+) plasmid encoding TTR gene. The cells were cultured in ^{13}C-, ^{15}N-enriched minimal medium (M9) containing 0.1 mg/mL of kanamycin, grown at 310 K, until OD_{600} reached 0.6–0.8 and then induced with 1 mM isopropyl β-D-1-thiogalactopyranoside. The cells were further grown at 310 K overnight and then harvested by centrifugation at 6500 rpm (JA-10 Beckman Coulter) for 15 min at 277 K. The pellet was suspended in 20 mM Tris-HCl at pH 8.5 (60 mL per liter of culture) and sonicated at 277 K for 40 min. The suspension was centrifuged at 40,000 rpm (F15-6x100y Thermo Scientific) for 40 min and the pellet discarded. The protein was purified by anionic-exchange chromatography using a HiPrep Q FF 16/10 column (GE Healthcare Life Science). The protein was eluted in 20 mM Tris-HCl buffer at pH 8.6 with a linear 0–1 M NaCl gradient. Fractions containing pure TTR were identified by Coomassie

staining SDS-PAGE gels, then joined and purified by Size Exclusion Chromatography using HiLoad Superdex 26/60 75pg in 50 mM phosphate buffer at pH 7.5; then dialyzed extensively against 2 mM Tris-HCl buffer at pH 7.5. Aliquots of 1 mL, each containing 6 mg of protein, were freeze-dried to be used for SSNMR analysis.

S3
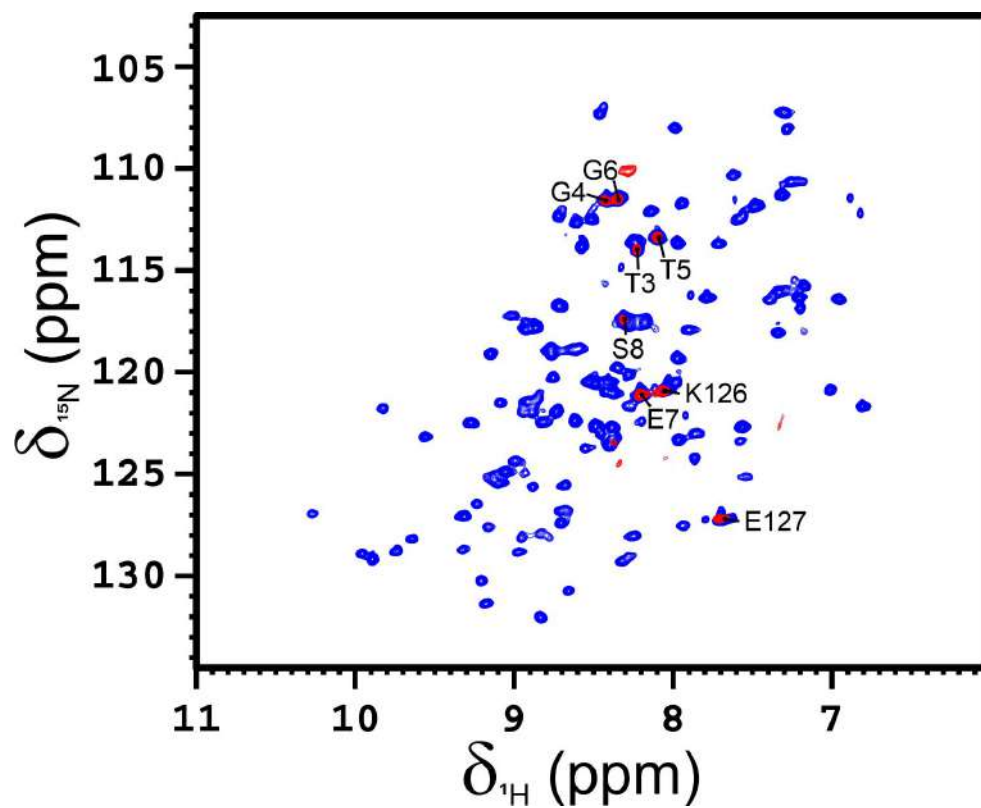
Figure S1. 2D ^{1}H-^{15}N TROSY-HSQC spectrum of TTR (blue) collected on a solution of the protein at the concentration of 100 µM superimposed with the same spectrum collected on TTR (100 µM) encapsulated in alginate/gelatine hydrogel (red). The spectra were recorded on a 950 MHz spectrometer at 310 K.

S4
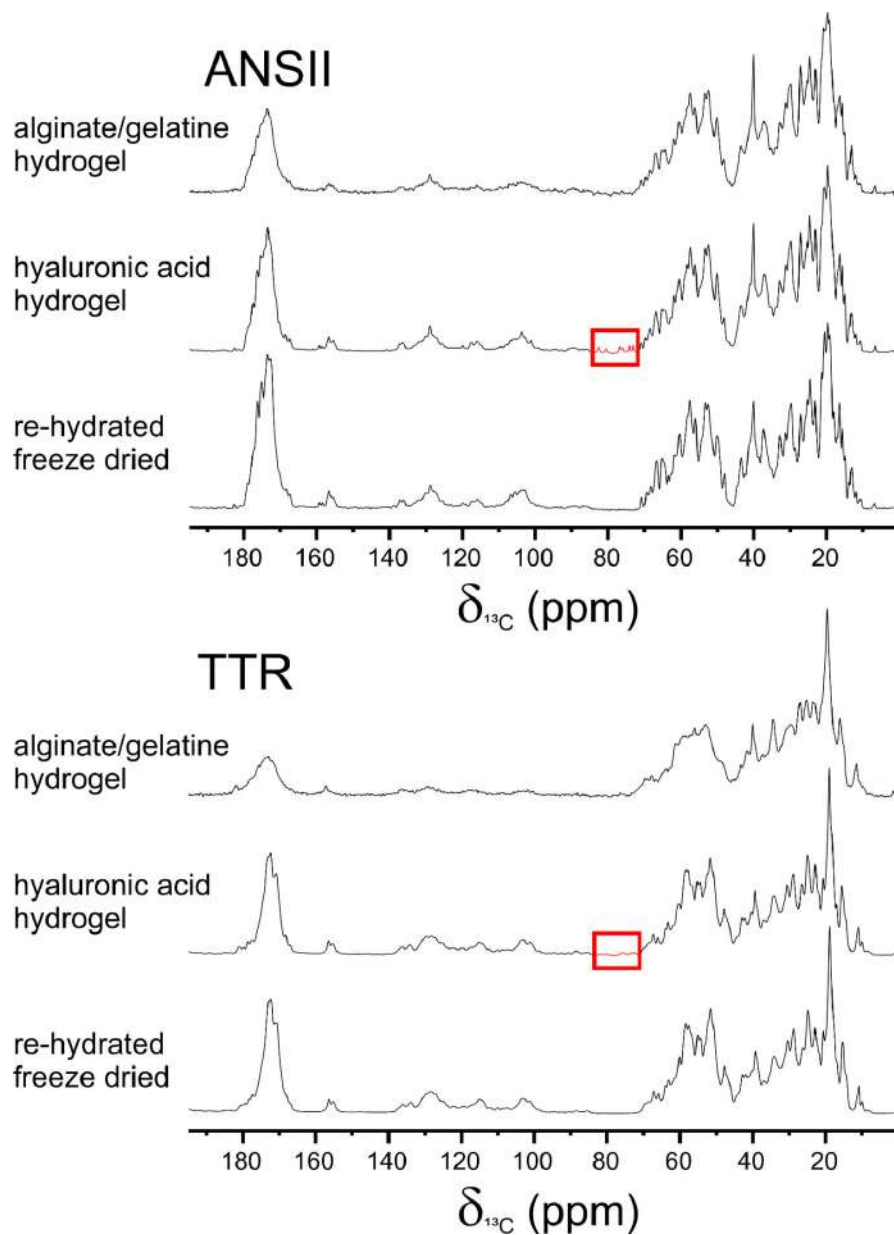
Figure S2. 1D {[1]H}[13]C cross-polarization spectra acquired on the re-hydrated freeze-dried proteins, on the proteins embedded in the hyaluronic acid hydrogels, and in the alginate/gelatine hydrogels (ANSII, top, and TTR, bottom). The signals of the hyaluronic acid are highlighted by a red box. The spectra were acquired at ~290 K, MAS 14 kHz and 800 MHz (number of scans: 512, recycle delay: 3 sec).
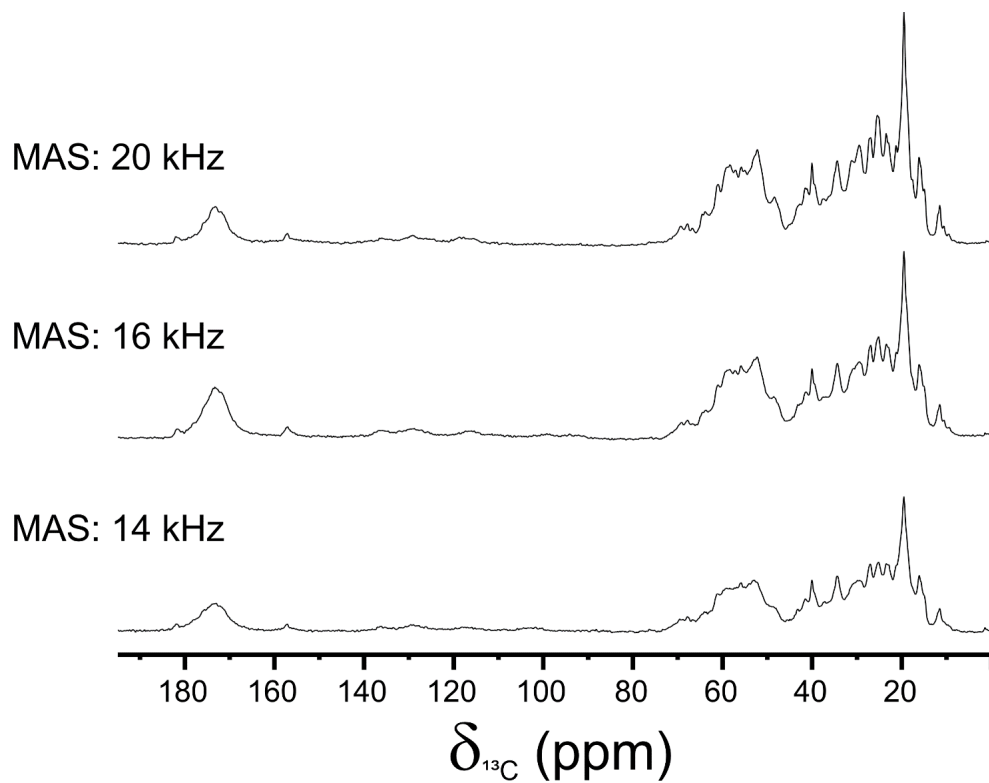
Figure S3. 1D {^{1}H} ^{13}C cross-polarization spectra acquired on the TTR-AG at the different MAS speeds indicated in the figure. The spectra were acquired at ~290 K and 800 MHz (number of scans: 512, recycle delay: 3 sec).
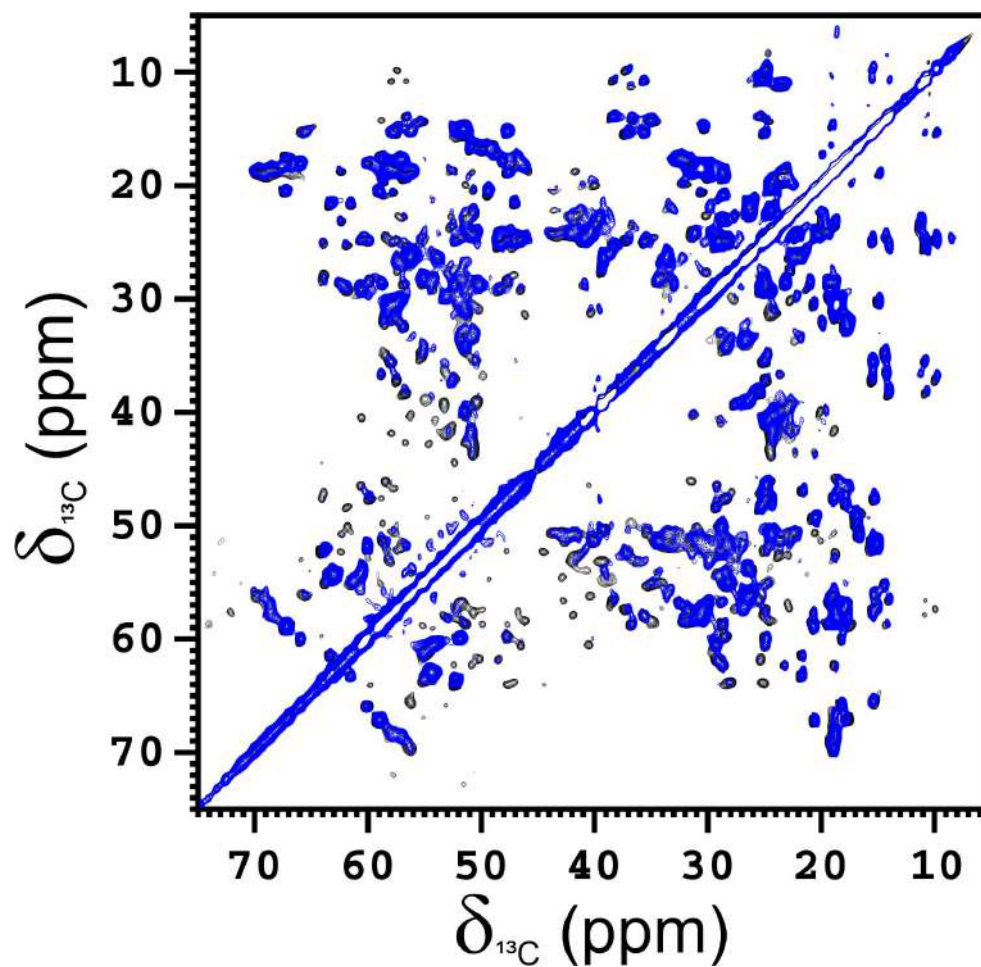
Figure S4. Aliphatic region of the 2D ^{13}C-^{13}C CORDxy4 recorded on TTR-AG hydrogel (blue) superimposed with the CORDxy4 recorded on the re-hydrated freeze-dried TTR (black). The spectra were acquired at ~290 K, MAS 20 kHz and 800 MHz.

3.3 CSF lipoproteins inhibit the aggregation of α-synuclein in seeding aggregation assays by interacting with oligomeric species (Submitted)

The aim of this work is to characterize the interaction of α-synuclein with human biofluid components for the development of promising diagnostic tools for the diagnosis of synucleinopathies. My contribution to this project was to produce recombinant α-synuclein and recombinant Transthyretin with very high purity level, to perform seeding aggregation assays (SAAs), CSF pooling and fractionation and NMR experiment in solution on isotopically enriched samples of these protein.

Giovanni Bellomo[1*], Silvia Paciotti[1], **Domenico Rizzo[2,3]**, Leonardo Gatticchi[4], Linda Cerofolini[2,5], Stefano Giuntini[2], Chiara Maria Giulia De Luca[6,7], Giuseppe Pieraccini[8], Sara Bologna[2], Marta Filidei[1], Enrico Ravera[2,3,5], Moreno Lelli[2,3,5], Fabio Moda[6], Marco Fragai[2,3,5], Lucilla Parnetti[1] and Claudio Luchinat[2,3,5*].

[1]Laboratory of Clinical Neurochemistry, Section of Neurology, Department of Medicine and Surgery, University of Perugia; Piazzale Lucio Severi 1/8, Perugia, 06132, Italy.

[2]Magnetic Resonance Center (CERM), University of Florence, Via Luigi Sacconi 6, Sesto Fiorentino, 50019, Italy

[3]Department of Chemistry "Ugo Schiff", University of Florence, Via della Lastruccia 3, Sesto Fiorentino, 50019, Italy

[4]Section of Physiology and Biochemistry, Department of Medicine and Surgery, University of Perugia, Perugia, Piazzale Lucio Severi 1/8, Perugia, 06132, Italy.

[5]Consorzio Interuniversitario Risonanze Magnetiche MetalloProteine (CIRMMP), Via Luigi Sacconi 6, Sesto Fiorentino, 50019, Italy

[6]Fondazione IRCCS Istituto Neurologico Carlo Besta, Division of Neurology 5 and Neuropathology, Via Celoria 11, Milano, 20133, Italy

[7]Scuola Internazionale Superiore di Studi Avanzati (SISSA), Department of Neuroscience, Via Bonomea 265, Trieste, 34136 Italy

[8]CISM Mass Spectrometry Centre, Department of Health Sciences, University of Florence, Viale Gaetano Pieraccini 6, Firenze, 50139 Italy

Abstract

Aggregation of α-synuclein (α-syn) is a prominent feature of synucleinopathies, including Parkinson's disease. In these diseases, the extracellular spreading of misfolded α-syn significantly contributes to the cell-to-cell propagation of the α-syn misfolding pathology in a prion-like fashion. Therefore, extracellular α-syn aggregates are considered primary targets both for diagnostics and for novel disease modifying therapies. α-Syn seeding aggregation assays (SAAs) in cerebrospinal fluid (CSF) represent the most promising diagnostic tools for the diagnosis of synucleinopathies. However, CSF itself contains several compounds that are able to modulate the aggregation of α-syn and significantly alter the performances of SAAs. Indeed, human CSF exerts an inhibitory effect on α-syn aggregation both in the presence and in absence of preformed α-syn aggregates. In our work, we focused on the inhibitory effect of CSF on α-syn aggregation in SAAs. After having assessed that the inhibitory effect is mainly produced by the CSF high-molecular weight fraction, we selected some candidate inhibitors by considering the most abundant compounds determined by mass-spectrometry. Among the tested compounds, lipoproteins produced the most marked effects on α-syn aggregation. Although a direct interaction between lipoproteins and monomeric α-syn was not detected by solution nuclear magnetic resonance spectroscopy, lipoprotein-α-syn complexes were detected by transmission electron microscopy, suggesting that the interaction may not involve monomeric but rather oligomeric/proto-fibrillary intermediates. The identification of compounds able to modulate α-syn aggregation in CSF may not only improve the development of SAAs but may also indicate novel chaperones able to inhibit the amyloidogenic potential of extracellular α-syn aggregates.

Significance Statement

Among the constituents of human cerebrospinal fluid, we identified lipoproteins as major responsible for the delay/inhibition of α-synuclein aggregation in diagnostic aggregation assays. Both high-density and low-density lipoproteins inhibited or significantly delayed α-synuclein aggregation, even at levels lower than the ones physiologically present in human cerebrospinal fluid. The interaction between lipoproteins and α-synuclein did not involve α-synuclein monomers while involved α-synuclein protofibrillary/oligomeric intermediates. The identification of endogenous compounds able to modulate α-syn aggregation may not only improve the

development of seeding aggregation assays by identifying possible confounders but may also indicate novel chaperones able to inhibit the amyloidogenic potential of extracellular α-syn aggregates that may be of interest for the development of novel disease modifying agents.

Introduction

Accumulation, misfolding and aggregation of α-synuclein (α-syn) are prominent biochemical features of Parkinson's disease (PD), dementia with Lewy bodies (DLB) and multiple system atrophy (MSA). These neurodegenerative diseases, pathologically characterized by the presence of cytoplasmic and axonal inclusions in selectively vulnerable brain regions, are commonly referred to as synucleinopathies. Apart from rare familial monogenic forms[71], the sporadic accumulation and consequent misfolding of this protein in synucleinopathies may result from an impairment of protein degradation pathways, such as the autophagic lysosomal pathway [72], as well as exposure to environmental factors [73]. In physiological conditions, α-syn is mainly located in the intracellular environment, prevalently in synaptic terminals, where it participates in maintaining the structural integrity of membranes and in the formation of SNARE complexes [74]. Conversely, pathologically aggregated α-syn species are able to move from the intracellular to the extracellular environment and *vice versa* [75–77]. In particular, oligomeric and protofibrillary α-syn species have been found to spread from cell to cell either via exosomal pathways or by passive diffusion through extracellular milieu and/or cerebrospinal fluid (CSF) [75,77]. The extracellular spreading of misfolded α-syn eventually results in the propagation of the α-syn misfolding pathology from an initial site to the whole CNS in a prion-like fashion. This is why extracellular α-syn aggregates are being considered primary targets both for diagnostic assays as well as for novel disease modifying therapies. In particular, the detection of cerebrospinal fluid (CSF) α-syn oligomers by immunoassays showed good performance in differentiating patients affected by synucleinopathies from patients affected by other neurodegenerative diseases and from controls [77,78]. More recently, the development of seeding aggregation assays (SAAs), among which protein cycling misfolding amplification (PMCA)[79] and real-time quaking-induced conversion (RT-QuIC)[80], significantly improved the diagnosis of synucleinopathies. These assays, initially developed in the field of prion diseases, enabled efficient detection of prions in peripheral tissues of diseased patients, including urine, blood, CSF, skin and olfactory

mucosa [82,83]. SAAs are currently being adapted for the detection of α-syn aggregates in biological specimens of patients affected by synucleinopathies. SAAs is based on the amplification of a small amount of prone-to-aggregation prion-like protein (α-synuclein in this case) present in a biological fluid by recruiting recombinant monomers that are provided in the reaction mixture, through cycles of incubation and sonication/shaking [81]. Usually, monomeric recombinant α-syn is used as a reaction substrate and the aggregation process is monitored in real-time using thioflavin-T (ThT), a fluorescent dye that binds with high affinity to the cross-β-sheet motifs of amyloid aggregates. SAAs have been recently tested in different biological matrices, such as olfactory mucosa [84] and skin biopsies [85,86], with good sensitivity and specificity in detecting synucleinopathies. Notably, α-syn aggregation assays similar to SAAs are commonly used also to discover novel therapeutical agents against α-syn misfolding/aggregation [87]. The most reliable results have been obtained in cerebrospinal fluid (CSF), where the reaction is thought to be "seeded" by extracellular oligomeric/fibrillary α-syn aggregates [79,80,88,89]. However, the proteostasis of α-syn in this extracellular fluid has been poorly characterized. Indeed, in some works applying α-syn PMCA/RT-QuIC on human CSF, it was observed that, CSF exerts an inhibitory effect on α-syn aggregation with respect to the sole buffer, independently of the presence of a synucleinopathy [79,90,91], and that efficient seeding can be obtained only after determining an optimal CSF dilutions [80,91]. This effect has been repeatedly observed but, surprisingly, not yet characterized, in spite of the opportunities arising from improving SAAs and of the relevance of the autoprotective effect of CSF. This is thus the topic of the present work. Here, we tested the inhibitory effect of CSF on α-syn aggregation in SAAs, and specifically characterized its interactions with α-syn. After having assessed that the effect is mainly produced by the CSF high-molecular weight fraction (HMW), we have selected some candidate inhibitors by considering the most abundant compounds in the HMW CSF fraction and the ones that were previously reported to have an effect on Aβ aggregation/clearance [92,93], and specifically analyzed their interactions with monomeric α-syn and their effect on α-syn aggregation. Understanding the role of α-syn interactions with CSF can provide useful information for development and standardization of CSF SAAs. Thus, the fact that CSF modulates α-syn aggregation in SAA may lead to the identification of novel endogenous anti-aggregation agents that could be of interest for the development of novel disease modifying therapies targeting α-syn aggregation.

Results

CSF abolishes the fibrillization of α-syn in SAAs

To evaluate the ability of human CSF in modulating α-syn aggregation in SAAs, we tested the effect of adding human CSF (from a pool of CSF samples belonging to cognitively unimpaired neurological non-neurodegenerative controls) to a physiological buffer (phosphate buffer saline, PBS) containing recombinant α-syn at a concentration of 0.7 mg/mL, in a 1:5 volume ratio (40 μL CSF in 200 μL total reaction volume). We chose to test the inhibitory effect of CSF in PBS to see if the inhibitory effect of CSF observed in previous works [79,90,91] could be observed also in physiological pH and ionic strength values. Our results showed that the addition of CSF to the reaction substrate drastically reduced α-syn aggregation (Fig.1A). The same effect was observed also with other reaction buffers/experimental conditions (*SI Appendix* Fig. S1).

The experiment was then repeated by adding preformed α-syn aggregates to wells containing and not containing CSF (Fig. 1B) to analyze the effect in "seeded" conditions. By looking at Fig 1B and Fig. S2 in the *SI Appendix*, it can be noticed that α-syn aggregation was efficiently seeded in wells without CSF (*SI Appendix* Fig. S2) while the inhibition effect of CSF was enough to impede a consistent aggregation even in the presence of preformed aggregates.

To quantitatively analyze the α-syn aggregation kinetics we fitted thioflavin-T (ThT) fluorescence profiles with a sigmoidal function. Since we repeatedly observed a two-phase growth in fluorescence, (i.e., a small increase in fluorescence, followed by a plateau, followed by an exponential fluorescence increase, followed by a second plateau) we decided to use a double sigmoid to fit our data. The exact fitting function and the analytical meaning of fitted parameters are displayed in Fig. 1C. In Fig. 1D the average fitted A2 parameters are representative of the value of the final fluorescence plateau, the average maximum fluorescence values (MAX) are also displayed in the same bar plot. The parameters A2 and MAX provide similar information, however, we decided to display both since, whereas A2 may be a more robust estimate of the final fluorescence plateau, it is not measurable when fitting is not possible (i.e., in the absence of an appreciable increase in ThT fluorescence).

α-syn aggregation is inhibited by high-molecular weight constituents of CSF

We proceeded with our analysis by investigating which components of CSF were most responsible for the inhibitory effect. Thus, we fractionated the CSF pool used for the experiments as shown in *SI Appendix* Fig. S3. Further details about the fractionation procedure and the characteristics of the CSF fractions are described in the *SI Appendix* Materials & Methods section (CSF pools and fractionation) and Table S1. After the fractionation procedure, we obtained 6 samples, relative to: whole CSF, CSF constituents of molecular weight (MW) above 100 kDa, CSF constituents of MW between 100 and 50 kDa, CSF constituents of MW between 50 and 10 kDa, CSF constituents of MW between 10 and 3 kDa, and CSF constituents of MW below 3 kDa. To characterize the protein content of the CSF fractions, we performed a nanoLiquidChromatography coupled to high resolution mass spectrometry equipped with a nanoelectrospray interface (nLC-nESI HRMS/MS). Among the detected protein constituents in whole CSF, the most abundant were human serum albumin (HSA), apolipoproteins, transthyretin (TTR) and prostaglandin-D synthase (PGDS, also known as β-trace protein). Interestingly, all of these compounds previously showed antiaggregatory properties on Aβ [92,93] or α-syn [94,95]. Considering that the measured exponentially modified protein abundance index (emPAI) score (see *SI Appendix* Materials and Methods: nLC-nESI HRMS/MS) can be considered approximately proportional to the amount concentration of the compound, in order to make comparisons among fractions, we multiplied the emPAI score with the MW in kDa to obtain a value proportional to the mass/volume concentration. The average of this value on 3 runs in each sample is plotted in the bar graph in Fig. 2A (in logarithmic scale) while raw values are shown in *SI Appendix* Table S2. Almost no measurable quantities of these proteins or other relevant peptides were measured in the 10-3 kDa and <3 kDa fractions (just very low levels of albumin). Among apolipoproteins, ApoA-I and ApoE were the most abundant, representing ~80% of the relative apolipoprotein weight in the >100 kDa fraction, with ApoJ and ApoD contributing by a ~6% each. We subsequently tested the CSF fractions with SAAs to test their inhibitory effect on α-syn aggregation. The measured kinetic parameters of this experiment are shown in Fig. 2B and Fig. 2C, while the average ThT fluorescence intensity profiles are shown in *SI Appendix* Fig. S4. Except for whole CSF and the >100 kDa fraction (in which we did not detect any relevant increase in fluorescence), we were able to efficiently fit the ThT fluorescence profiles with the double sigmoid function described in Fig 1C. Samples

relative to fractions 50-100 kDa and 10-50 kDa showed a reduced final fluorescence (~2000 a. u.) but it was still possible to identify and fit the typical α-syn aggregation profile. The fraction that exhibited the most similar effect compared to whole CSF was the >100 kDa fraction, the fraction in which apolipoproteins (and lipoproteins) were most abundant (*SI Appendix* Table S1). On passing, we note that α-syn aggregation is slightly reduced also by the <3 kDa CSF fraction. However, this effect is related to a change in the pH of this sample and better described in *SI Appendix* Solution NMR experiments on CSF fractions. In summary, we observed a complete inhibition of α-syn aggregation in the presence of the >100 kDa CSF fraction, the fraction in which we measured the highest concentration of apolipoproteins. An appreciable inhibition was also observed in the presence of the 100-50 kDa and 50-10 kDa fractions. As another confirmation of the relevance of HMW CSF constituents on the inhibition of α-syn aggregation, we applied a slightly modified version of the diagnostic protocol of Shahnawaz *et al.* [79] (see *SI Appendix* Materials and Methods: SAA protocols) on two CSF samples belonging to two cognitively unimpaired normal-pressure hydrocephalic (NPH) patients who produced very different SAA outcomes. As can be seen from the averaged ThT profiles (Fig. 3A), and from the average maximum fluorescence values and averaged fitted A2 (Fig. 3B), t1 and t2 parameters (Fig. 3C), NPH1 produced a much stronger inhibitory effect compared to NPH2. Since these patients were not affected by clinical synucleinopathies, we hypothesized that the marked difference in the aggregation inhibition could be produced by different concentrations of compounds present in the two samples due to different CSF dilution effects, which are commonly observed in NPH patients [96]. To qualitatively test this hypothesis, we analyzed the content of these two CSF samples by high-field NMR spectroscopy.

A portion of 1D ^{1}H solution NMR spectra is shown in Fig. 3D. The most apparent differences between the two spectra were detectable between 1.5 and 0 ppm, where methyl resonances are usually observed. Interestingly, some species seems more concentrated in the CSF of NPH1 with respect to NPH2. Most of the difference between the spectra is due to the different amplitudes of the broad peaks underlying the methyl peaks of smaller metabolites. From metabolomics studies, fatty acids-rich lipoproteins and/or other HMW proteins are known to produce similar broad peaks in ^{1}H solution NMR spectra [97,98]. By summarizing the results obtained on CSF fractions and the observations on CSF samples from NPH, lipoproteins are likely the species most contributing for the inhibitory effect, and these are found, to a lesser extent, also in the

100-50 kDa and 50-10 kDa fractions. It is therefore relevant to understand if lipoproteins can exert their inhibitory effect also at the concentrations that are likely present in these fractions (as it will be shown later), and that the inhibitory effect of these fractions is not related to other CSF macromolecular constituents abundant in these fractions. To test these hypotheses, we proceeded by analyzing the individual effects of the most abundant compounds present in the >100 kDa fraction on α-syn aggregation, namely lipoproteins, HSA and TTR.

Lipoproteins inhibits α-syn fibrillization in SAAs already at sub-physiological CSF concentrations

We differentially tested the effect of serum-purified lipoproteins, serum-purified HSA and recombinant TTR on α-syn aggregation by SAAs. In a previous work, we described the effect of HSA on α-syn aggregation [95]. HSA significantly reduced α-syn fibrillization at typical plasma concentrations but was poorly effective at CSF concentrations. In a first experiment, in addition to HSA, we also tested the effect of serum-purified human high-density lipoproteins (HDL) (LP3, Sigma-Aldrich) at two different concentrations (0.12 mg/mL and 0.57 mg/mL), comparable to HDL plasma levels, on α-syn aggregation with the same SAA protocol of those published results. The results of this experiment are shown in Fig. 4A, while average maximum fluorescence values and average fitted A2 are shown in Fig. 4B for all the tested conditions. By looking at Fig. 4, the lowest tested concentration of HDL (0.12 mg/mL) produced a stronger inhibitory effect compared to the highest tested concentration of HSA (43 mg/mL comparable to HSA concentration in blood). It is possible that the presence of HDL might have favored the formation of recombinant α-syn aggregates that were not efficiently detectable by ThT, thus explaining the negative results observed in SAAs. To exclude this hypothesis, we performed a dot-blot assay by using A11 and OC conformational antibodies, which are specific for amorphous and fibrillary oligomeric aggregates, respectively [99]. The inverted, window-level adjusted image of the dot-blot is shown in Fig 4C (the native image is shown in *SI Appendix* Fig. S7), and the intensity profile over a rectangle containing the dots is shown in Fig. 4D.

The dot-blot assay confirmed the results of the ThT assay, since much less oligomeric and fibrillary aggregates were detected in α-syn + HDL compared to α-syn + HSA samples. Of importance, neither OC antibody nor A11 antibody showed affinity for HSA and HDL.

We therefore tested more HDL concentrations (1, 0.3, 0.03 and 0.003 mg/mL). The results of this experiment are shown in Fig. 5. Indeed, the concentrations of the two most abundant CSF apolipoproteins, ApoE and ApoA1, are approximately 0.01 mg/mL and 0.004 mg/mL, respectively [100]. Thus, considering that these proteins constitutes about 50-60% of CSF HDL [100], total CSF HDL concentration is approximately 0.03 mg/mL. By looking at the average ThT fluorescence profiles in Fig. 5A and at the kinetic parameters shown in *SI Appendix* Table S3, it can be noticed that even at concentrations lower than the ones of CSF, HDL exerts a marked antiaggregatory action on α-syn. For further confirmation, we monitored monomer depletion for samples containing α-syn alone during the time course of the SAA and the remaining monomer for all the samples at the end of the experiment by Western-blot (WB). These experiments produced results in agreement with the ThT fluorescence profiles. As time increased, fibrils started to form at the expense of the free α-syn monomer in solution (Fig. 5B). At increasing HDL concentrations, higher levels of monomeric α-syn were found at the end of the experiment (Fig. 5C).

By looking at the zoom shown in Fig. 5A and by the fitted kinetic parameters shown in *SI Appendix* Table S3, it can be noticed that, in samples where α-syn aggregation was detectable (0, 0.003 and 0.03 mg/mL HDL), increasing HDL concentrations were accompanied by longer t2 parameters and by lower ThT intensities at the first plateau (quantified by A1 parameters).

Recalling that CNS HDL has an intermediate size between serum HDL and serum LDL [100–102], we also tested the effect of serum-purified LDL (LP2, Sigma-Aldrich) on α-syn aggregation; in parallel, the effect of adding recombinant TTR was also analyzed. Since in the previous experiments the antiaggregatory effects at HDL concentrations above 0.3 were too strong to observe an appreciable aggregation, in the subsequent experiment we doubled the shaking time in the SAA protocol (from 14 min rest and 1 min shaking at 500 rpm to 13 min rest and 2 min shaking at 500 rpm) to further assist α-syn aggregation. In these conditions we were able to obtain a detectable fluorescence increase even in the presence of HDL 0.3 mg/mL. Considering the high number of ThT profiles obtained, only the fitted kinetic parameters are shown in Fig. 6A and Fig. 6B, while the average ThT profiles of α-syn in the presence of LDL are shown in *SI Appendix* Fig. S8. By looking at maximum fluorescence levels and fitted A2 parameters (Fig. 6A), it can be noticed that TTR produced a significantly less marked inhibitory effect compared to human serum HDL and LDL, even at very high

concentrations of TTR (1.0 mg/mL), similar to those in plasma (44). However, longer t2 parameters were found for TTR 1.0 mg/mL and 0.3 mg/mL with respect to α-syn alone. Between the tested lipoproteins, serum LDL seemed to have comparable or even stronger antiaggregatory properties compared to serum HDL. The final reaction mixtures of these experiments belonging to samples with α-syn alone, LDL alone and α-syn + LDL, were subsequently analyzed by transmission electron-microscopy (TEM). Some representative images of this analysis are shown in Fig. 6C-D-E. By looking at these images, in agreement with the fitted parameters of Fig. 6A and Fig. 6B, it can be noticed that less α-syn fibrils are formed in the presence of LDL. Interestingly, the formed fibrils were intertwined with lipoproteins, which probably prevented them from interacting with other monomers and/or oligomers of α-syn. Similar images, obtained by incubating α-syn with HDL and human CSF, are shown in *SI Appendix* Fig. S9. For CSF we assumed that the observed globular structures were lipoproteins, due to their relatively high concentration in CSF and because no lipid bilayers (found in vesicles) were observed.

Solution NMR experiments on HDL, LDL and TTR

Solution NMR experiments were performed to assess whether the tested compounds were able to significantly interact with monomeric α-syn. In a previous work we already demonstrated the interaction between monomeric α-syn and HSA [95]: the most interacting residues were in agreement to the ones found by Theillet *et al.* [104]. At the tested HDL concentrations (0.57 mg/mL and 0.12 mg/mL), no significant interactions were observed by 2D ^{1}H-^{15}N HSQC experiments (*SI Appendix* Fig. S9A). As we did for HDL, we tested the interaction between monomeric α-syn and LDL by solution NMR, to test whether the strong inhibitory effect of LDL on α-syn aggregation could be due to a monomer-lipoprotein interaction. The amplitude ratios of the peaks of the 2D ^{1}H-^{15}N HSQC experiments performed on ^{15}N-labelled monomeric α-syn, before and after the addition of LDL, are shown in *SI Appendix* Fig. S9B. No relevant intensity decreases were observed, even by adding 1 mg/mL of LDL into the NMR tube. However, though not significant, a slight trend toward lower amplitude ratios can be noticed at the N-terminus and NAC region of α-syn compared to residues 105-140 (C-terminus). This is in line with the fact that, at physiological pH, the C-terminus of α-syn is negatively charged, while the N-terminus and the NAC region are lipophilic and confer apolipoprotein-like properties to α-syn [105,106]. Interestingly, a similar pattern was

observed for the >100 kDa CSF fraction rich in lipoproteins (*SI Appendix* Fig. S4C). Similar results (lack of evident interaction) were obtained also for TTR (*SI Appendix* Fig. S10C) except that the slight trend toward lower amplitude ratios was observed at the C-terminus of α-syn.

Discussion

The repeated observation that human CSF naturally inhibits α-syn aggregation [79,90,91] prompted us to characterize the interaction between CSF constituents and α-syn. A multi-technique integrative approach (SAA, nLC-nESI HRMS/MS, solution NMR, dot-blot assays and TEM) was applied for this purpose. In the cases in which an increase of ThT fluorescence could be detected, quantitative analysis of SAA kinetic traces was also performed. We initially confirmed that human CSF naturally inhibits α-syn aggregation in different experimental conditions, even when supplemented with α-syn preformed aggregates. After the fractionation of human CSF, we noticed that CSF fractions of different MW differently modulated α-syn aggregation. The low MW fraction (MW <3 kDa) slightly inhibited α-syn aggregation and produced a quite different 2D ^{1}H-^{15}N HSQC pattern on monomeric ^{15}N-labelled α-syn with respect to the other fractions, but similar to the one of whole CSF in PBS. These effects were probably due to a pH drift of CSF, and not further analyzed here. It is worth mentioning that in our experiments normal PBS was not able to fully counteract this pH drift, which is reported to be a result of air exposure and the consequent loss of carbon dioxide [107–109].

The strongest inhibitory effect on α-syn aggregation was observed for the CSF fraction relative to high MW compounds (>100 kDa). In this fraction (where the lower MW components of the CSF result diluted by the repeated washing with PBS) we did not find any relevant alteration in the 2D ^{1}H-^{15}N HSQC spectra of monomeric ^{15}N-labelled α-syn (*SI Appendix* Fig. S5C). In order to characterize the biospecimens contained in it and responsible of such inhibitory effect, nLC-nESI HRMS/MS experiments were performed. We observed that the most abundant macromolecular constituents in unfractionated pooled human CSF were albumin, TTR, apolipoproteins and PGDS. All of these compounds were previously investigated as modulators of Aβ aggregation/toxicity [92], but only albumin was previously studied as an α-syn chaperone [95]. Among these, apolipoproteins (in particular, ApoA1 and ApoE) were mostly present in the >100 kDa fraction. Considering the MW of these apolipoproteins (28.3 kDa and 34 kDa for ApoA1 and ApoE, respectively) we can assume that their lipidated versions

(HDL and LDL) were likely present in that fraction. We subsequently tested the effect of the three most abundant constituents of the >100 kDa CSF fraction. We observed a strong antiaggregatory effect for HDL with respect to HSA by SAA. These results were confirmed by WB and dot-blot analyses of the SAA final products with OC and A11 conformational antibodies. Moreover, while the effect of HSA on α-syn aggregation was shown to be negligible at its physiological concentrations in CSF [95], the inhibitory effect of HDL on α-syn aggregation was detectable even at sub-physiological levels (Fig. 5). In the SAA experiments presented in Fig. 5A, the kinetics of α-syn aggregation, mirrored by ThT fluorescence, showed a double sigmoidal behavior. This peculiar behavior, probably caused by the transient formation of protofibrillary/oligomeric species, was previously observed for Aβ [110]. The main effect of HDL on α-syn aggregation consisted in the lowering of the intensity of first plateau, that consequently slowed or blocked the formation of the second. Since no relevant interactions were detected by solution NMR between HDL and monomeric α-syn, we hypothesize that HDL interacted with oligomeric species present during the lag-phase of the aggregation process prior to or during the formation of the first fluorescence plateau. These effects were observed at HDL levels lower than the physiological HDL content of CSF. Since CSF HDL are bigger in size than blood HDL and smaller than LDL [101,102], in subsequent experiments the effects of HDL on α-syn aggregation were compared to those produced by LDL and TTR. TTR did not generate significant effects at physiological CSF levels (~0.03 mg/mL), while a delayed α-syn aggregation was observed at higher TTR concentrations with respect to PBS (Fig. 6 A and B). Much stronger effects were observed for HDL and LDL, with LDL producing the most marked inhibition of α-syn aggregation (Fig. 6A and B). The TEM analysis of the final reaction products revealed a decreased number of formed fibrillary aggregates in α-syn + LDL with respect to α-syn alone, with the few aggregates formed being interlaced to lipoparticles. Similar structures have been observed by co-incubating α-syn with CSF and serum-derived HDL (*SI Appendix* Fig. S9). Of note, the globular structures observed in CSF resembled those observed in serum-derived LDL more than serum-derived HDL (smaller in size). Similar structures have been previously observed by TEM by incubating prion aggregates (PrP^Sc) with LDL [111]. Interestingly, PrP^Sc was shown to bind to LDL with an apparent dissociation constant (Kd) of ~30 pM.

In conclusion, we described a drastic reduction of α-syn aggregation in the presence of human CSF by SAAs. CSF lipoproteins are the main responsible of this inhibitory

effect, although it cannot be excluded that other less abundant constituents may also contribute. These findings are in line with previous studies which demonstrated an interaction between α-syn and lipoproteins both in plasma [105] and CSF [112] by coimmunoprecipitation. Our data provide strong support for this interaction by complementary techniques, demonstrating that the interaction may be relevant in diagnostic SAA protocols and that it does not involve α-syn in its monomeric state. Together with α-syn-lipoprotein interaction, CSF pH drift can be another confounder in SAAs. The use of reaction buffers more concentrated than PBS or using smaller CSF volumes can mitigate these effects in RT-QuIC and PMCA diagnostic applications. The fact that lipoproteins can target extracellular α-syn aggregates blocking their amyloidogenic potential may be clinically meaningful, especially in the view of identifying novel disease modifying drugs for synucleinopathies. Intravenous injections of ApoA1 or ApoA1-Milano, a genetic variant expressed by centenarians inhabitants of *Limone sul Garda, Italy* [113], have been already tested for human safety [114,115] showing interesting therapeutic potential for the treatment of arteriosclerosis [115]. More recently, promising results have been obtained in transgenic mouse model of AD, in which the peripheral administration of recombinant ApoA1-Milano lipoproteins resulted in a lower Aβ plaques load and in a lower inflammatory response [116]. Thus, considering the high tolerability of its intravenous administration in humans [115], the fact that it is able to cross bidirectionally the BBB [105,117] and the results obtained in AD animal models [116], our results also support the idea that ApoA1 isoforms should be further investigated as therapeutic candidates for synucleinopathies.

Figures and Tables
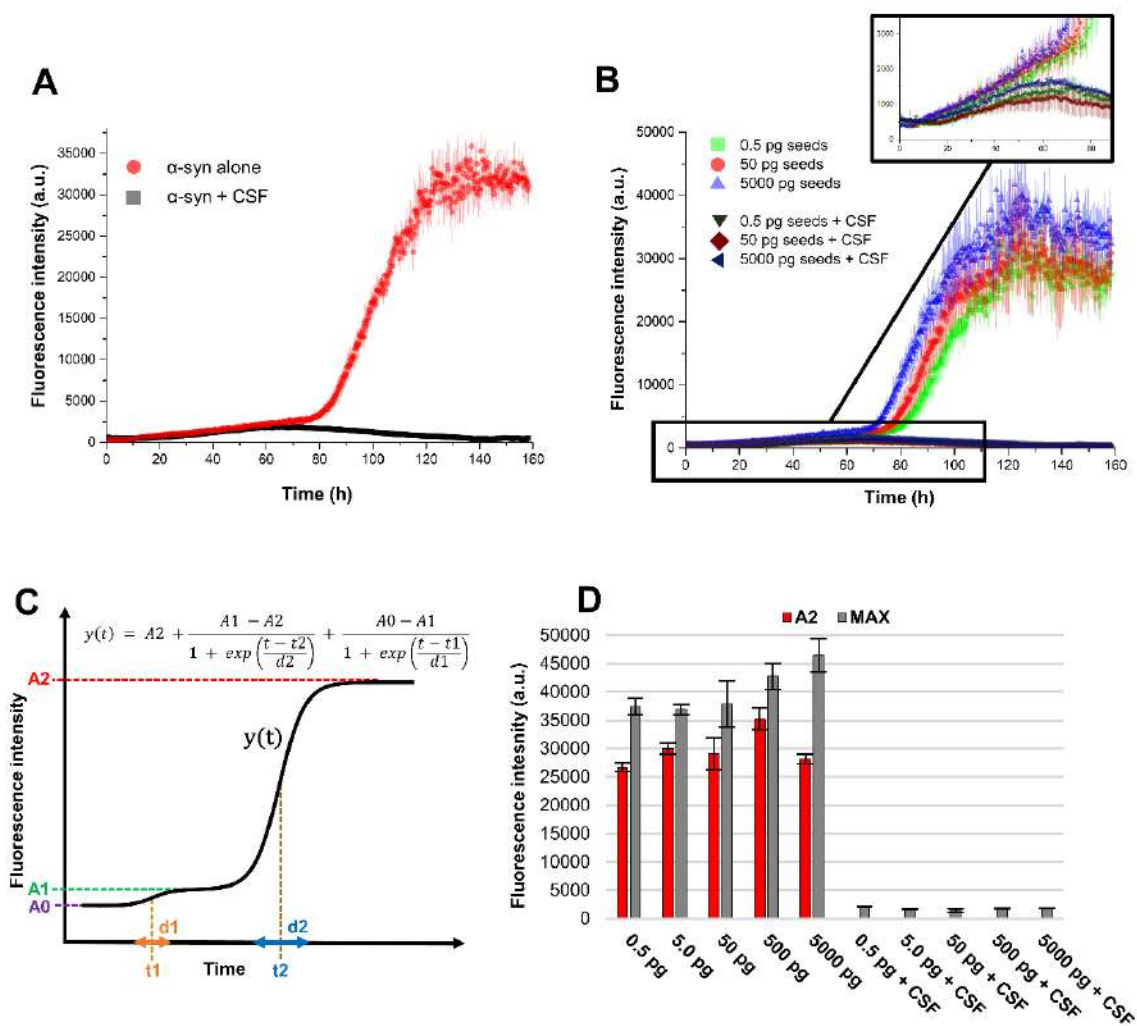
Fig. 1. CSF inhibit α-syn aggregation in unseeded and seeded conditions. A) SAA performed using 0.7 mg/mL (50 μM) of recombinant α-syn in PBS with (black) and without (red) 40 μl of human pooled CSF (final volume of 200 μL). B) The experiment was repeated by adding to the α-syn substrate 0.5, 5, 50, 500 and 5000 pg of preformed α-syn fibrils (seeds). The data shown in A) and B) represent the average fluorescence of three replicates with error bars representing the standard error of the mean value (SEM). Only the ThT profiles relative to samples with 0.5, 50 and 5000 pg seeds are shown for the sake of viewing. C) Graphical description of the fitting function used. A2 fits the fluorescence value of the second plateau, A1 fits the fluorescence value of the first plateau and A0 fits the baseline fluorescence. The time parameters t1 and t2 fit the first and the second inflection points, respectively, while d1 and d2 represent the slopes of the sigmoids. D) The fitted A2 plateau parameters and maximum fluorescence values (MAX) for the seeded experiment with and without 40 μL of pooled CSF. Both A2 and MAX values result from the average of three replicates, error bars reflect the SEM. Fitting with sigmoids was not possible for samples with CSF.
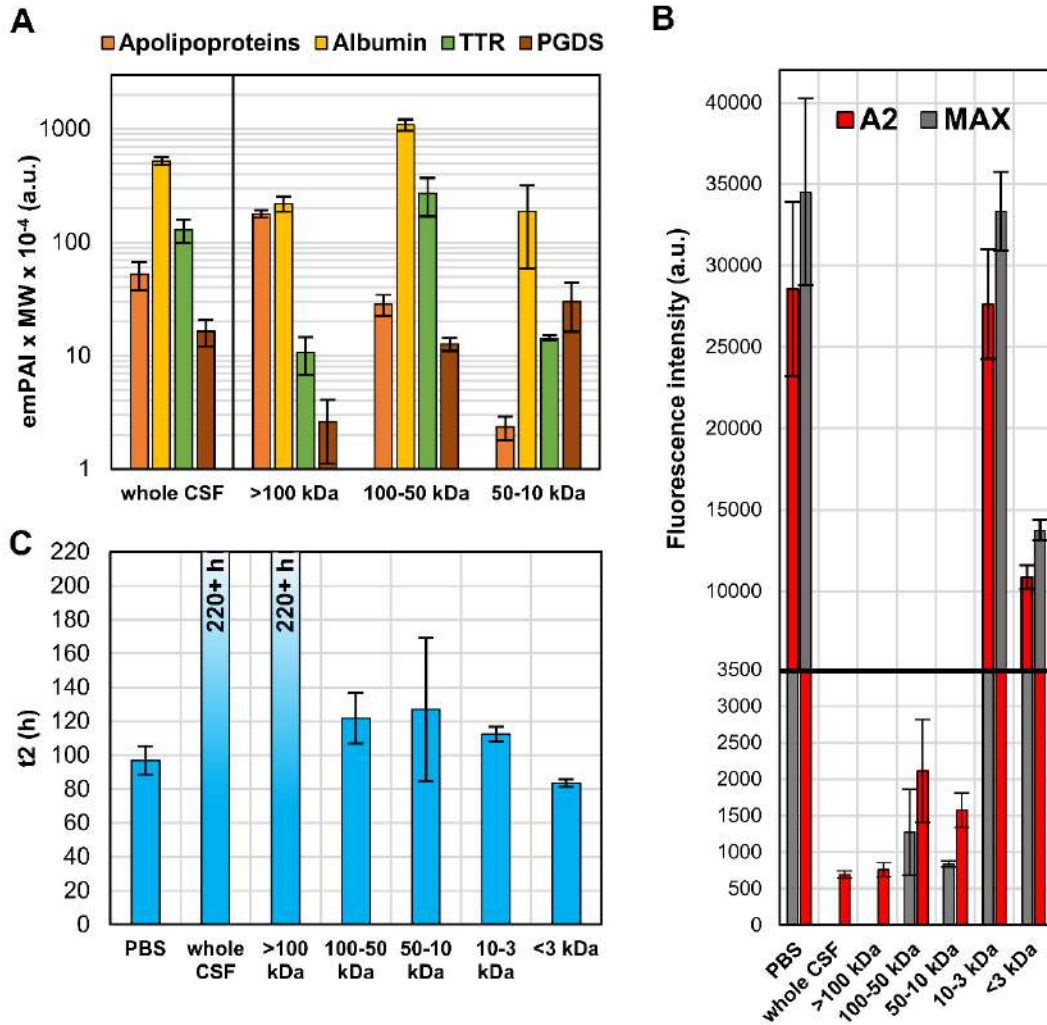
Fig. 2. Different CSF fractions differently affect α-syn aggregation. A) Relative concentration (emPAI score multiplied by protein molecular weight) of the most abundant protein constituents measured by nLC-nESI HRMS/MS. Apolipoproteins scores were summed together, with ApoA-I and ApoE being the most abundant. Scores for fractions 3-10 and <3 kDa are not shown since the protein content of these fractions was negligible with respect to the others. Due to the fractionation procedure, macromolecular constituents of the CSF fractions (>100, 50-100, 10-50 and 3-10) were more concentrated (by a theoretical factor of 5) compared to whole CSF and to the <3 kDa fraction. B-C) SAAs performed using 0.7 mg/mL (50 μM) of recombinant α-syn in PBS with 40 μl of PBS/human pooled CSF fractions (final volume of 200 μl). Six glass beads with a diameter of 1 mm were added in each well. The SAA protocol consisted in 14 min rest at 37°C and 1 min shaking at 500 rpm. To remove the background fluorescence, the average fluorescence of three replicates containing PBS, whole CSF and CSF fractions without α-syn was subtracted prior to the analysis. B) Mean fitted A2 parameters (fitting was not possible for samples with whole CSF and the >100 kDa fraction) and maximum fluorescence values (MAX) of samples with 40 μl of PBS/CSF fractions. Two scales of fluorescence intensity were used to better compare the results. C) Mean fitted t2 parameters. All the values displayed in the bar-plots of panels A, B and C result from the average of three replicates with error bars reflecting the SEM.
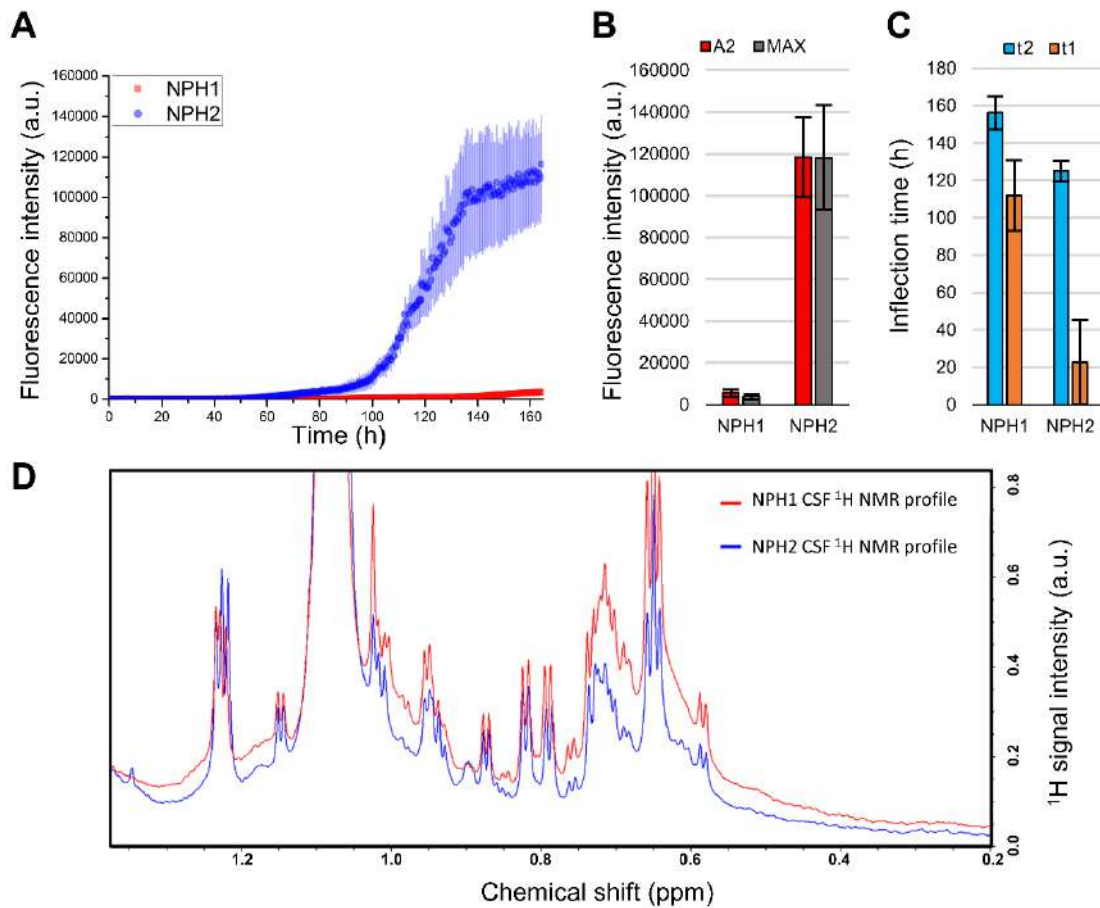
Fig. 3. CSF aggregation inhibition may differ from a subject to another. A) SAAs performed using 0.1 mg/mL of recombinant α-syn in PIPES pH 6.5 and 500 mM NaCl with 40 μL of human CSF (final volume of 200 μL) obtained from two NPH patients. The data shown represent the average fluorescence of three replicates with error bars representing the SEM. B) C) Average (3 replicates) of maximum fluorescence values, fitted A2, t1 and t2 parameters for the two tested CSF samples. NPH2 showed a weaker aggregation inhibition capability compared to NPH1. D) Portion of 1D ^{1}H NMR spectra relative to the two NPH CSF samples analyzed with SAAs.
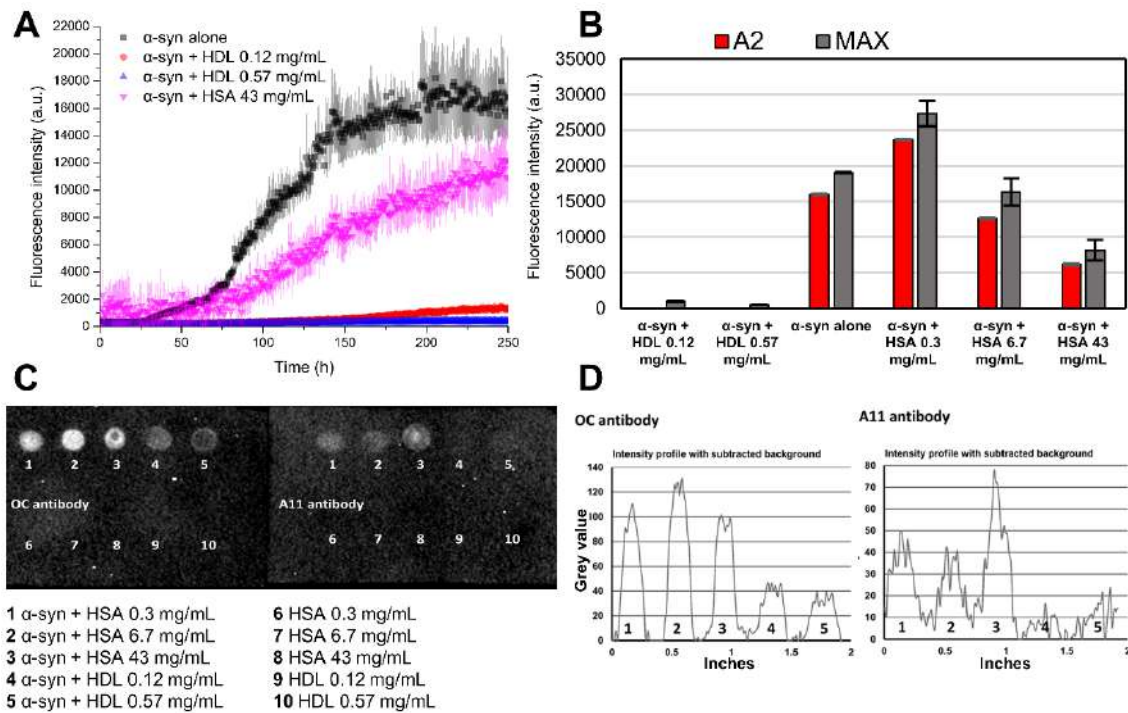
Fig. 4. HDL reduce α-syn aggregation more efficiently than HSA. A) average SAA performed using 0.7 mg/mL of recombinant α-syn (50 μM) in PBS pH 7.4 in the presence of different concentrations of HSA (0, 0.3, 6.7 and 43 mg/mL) and HDL (0, 0.12 and 0.57 mg/mL). For the sake of viewing the fluorescence profiles of samples containing HSA at 0.3 and 6.7 mg/mL were not shown. To remove the background fluorescence, the average fluorescence of three replicates containing the same amount of HSA and HDL without α-syn was subtracted prior to the analysis. The data represent the average fluorescence of three replicates with error bars representing the SEM. The addition of HDL or HSA reduced the efficiency of α-syn aggregation with HDL producing a much stronger effect. B) Maximum fluorescence values (MAX) and fitted A2 parameters averaged on the three replicates are shown. C) Inverted and window/level-adjusted image of the dot-blot assay performed on the HSA and HDL containing samples with OC (detection of fibrillary oligomers) and A11 (detection of amorphous oligomers) conformational antibodies. D) Intensity profile (gray level) over a rectangle containing the dots (samples 1-5).
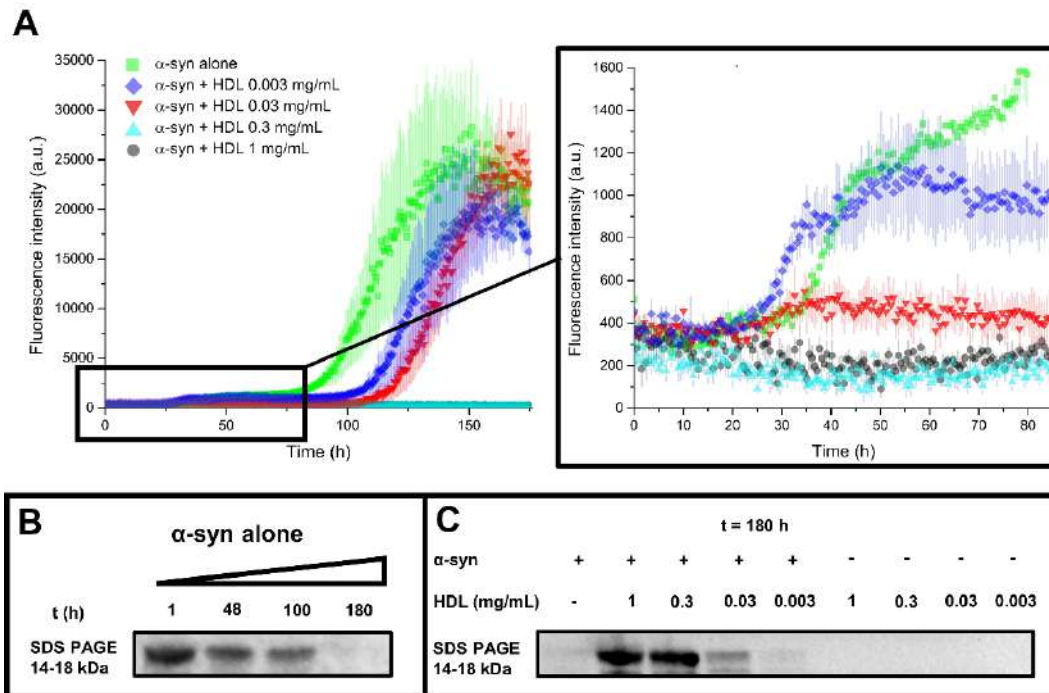
Fig. 5. HDL reduce α-syn aggregation even at CSF physiological (ca. 0.03 mg/mL) and sub-physiological levels by preventing the formation of transient oligomeric/protofibrillary species. A) SAA performed using 0.7 mg/mL (50 μM) of recombinant α-syn in PBS with 0, 0.003, 0.03, 0.3 and 1 mg/mL of added human serum HDL. To remove the background fluorescence, the average fluorescence of three replicates containing the same amounts of HDL without α-syn was subtracted prior to the analysis. B) The presence of monomeric α-syn (14-18 kDa) was monitored during SAA by WB. Samples derive from replicate wells containing α-syn alone recovered at different timepoints of the SAA protocol. With reference to panel A and C, monomeric α-syn decreases as t increases due to the formation of HMW fibrils.
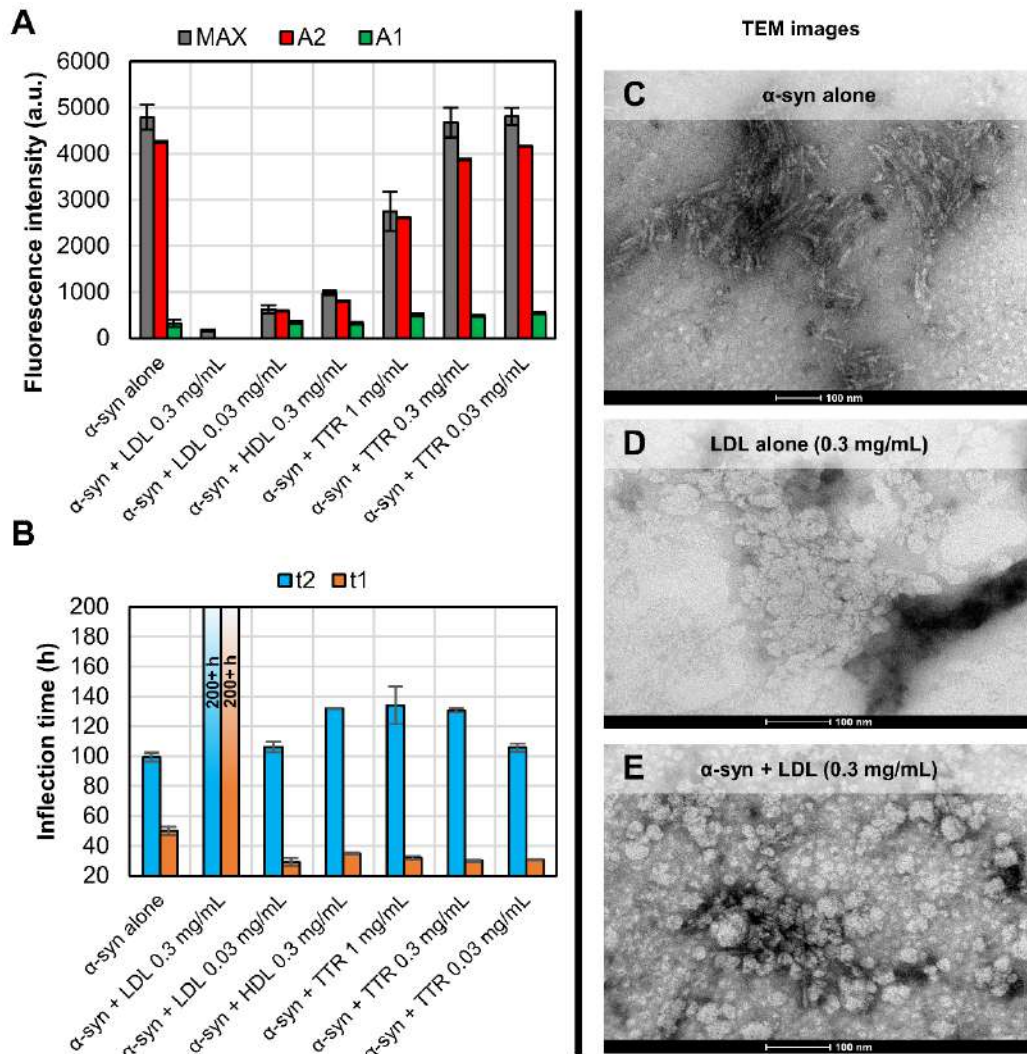
Fig. 6. HDL and LDL impede α-syn aggregation more efficiently than TTR. Lipoproteins exert their anti-aggregation properties by interlacing to early protofibrillary/oligomeric species. A-B) Fitted kinetic parameters of a SAA performed using 0.7 mg/mL (50 μM) of recombinant α-syn in PBS with different concentrations of LDL, HDL and TTR. The average fluorescence of three replicates containing the same amounts of LDL, HDL and TTR without α-syn was subtracted prior to the analysis. C-E) TEM images relative to the final products obtained in SAA reactions performed using (C) α-syn alone (0.7 mg/mL), (D) LDL 0.3 mg/mL alone and (E) a combination of both α-syn 0.7 mg/mL + LDL 0.3 mg/mL. This last condition indicates that the LDL are able to reduce the aggregation of α-syn and probably by interlacing to early protofibrillary/oligomeric species, thus impairing their "seeding" effect.

Supplementary Information

Supplementary Results

Solution NMR experiments on CSF fractions

To clarify the molecular basis of the inhibition of α-syn aggregation by CSF, we titrated ^{15}N isotopically enriched monomeric α-syn (144 mg/mL, 100 μM) with all the CSF fractions and evaluated the intensity changes in α-syn amide resonances by 2D ^{1}H-^{15}N HSQC solution NMR spectra. Relevant intensity decreases were observed by titrating α-syn with whole CSF and with the <3 kDa fraction (Fig. S5A and S5B), while no relevant intensity decreases were detected for the other fractions (as an example, the results for the >100 kDa fraction are shown in Fig. S5C). However, the intensity decreases observed by titrating α-syn with whole CSF and with the <3 kDa fraction were accompanied by a shift in the position of the amide-proton of histidine-50 (for whole CSF $\Delta^1H = 0.042$ ppm, $\Delta^{15}N = 0.26$ ppm). The resonance frequency of histidine-50 amide protons of α-syn is known to be particularly sensitive to pH changes, which also affect the chemical exchange between bulk water protons and amide protons, which in turn modulates the intensity of peaks in 2D ^{1}H-^{15}N HSQC solution NMR spectra. To test whether CSF could produce such a pH change also in the presence of PBS, we performed pH measurements over-time on the whole CSF fraction (2/3 CSF + 1/3 PBS 3x) and in undiluted CSF. The results of these experiments are shown in Fig. S6: exposing CSF to air upon vigorous shaking caused a significant increase in pH both in the presence and absence of PBS. This effect had been reported previously [107,108] and is produced by the loss of carbon dioxide from CSF (and the consequent displacement of the CO_2/HCO_3^- equilibrium). This effect is likely responsible for the intensity decreases observed in HSQC spectra while titrating α-syn with whole CSF and with the <3 kDa fraction. It is also well known that the aggregation propensity of α-syn is strongly dependent on pH [118]. For this reason, we interpreted the slight decrease in the maximum fluorescence signal observed for the <3 kDa fraction (main text Fig. 2B), as a possible effect of the pH increase due to the loss of CO_2, which could be significantly present both in this fraction and in the whole CSF sample (the other fractions were washed multiple times with PBS).

Materials and Methods

Protein expression and purification

Recombinant α-synuclein (α-syn) expression and purification

Escherichia coli BL21 (DE3) Gold were transformed with a pT7-7 vector cloned with the gene encoding α-synuclein. The overnight preculture of transformed cells was diluted 100-fold in LB medium and induced at an OD_{600} value of 0.6–0.8 with 1 mM isopropyl-β-d-thiogalactoside; after 5 h of incubation at 37 °C, the cells were harvested at 4000 rpm (JA-10, Beckman Coulter). The extraction was carried out through osmotic shock using 100 mL of the buffer Tris 30 mM, ethylenediaminetetraacetic acid (EDTA) 2 mM, and sucrose 40%, at pH 7.2, according to Shevchik et al.[65] and Huang et al.[66]. The suspension was then ultra-centrifuged at 20 000 rpm (Type 70 Ti rotor, Beckman Coulter) for 25 min, and the pellet was collected and resuspended with 90 mL precooled ultrapure water containing 38 µL of 1 M $MgCl_2$ and then ultra-centrifuged a second time. Supernatants derived from these two centrifugation steps were combined and dialyzed against 4 L of 20 mM Tris/HCl buffer at pH 8.0. The protein was then loaded in the fast protein liquid chromatography system, and anion-exchange chromatography was carried out with 0–50% linear gradient 1 M NaCl (GE Healthcare HiPrep Q HP 16/10 Column). The collected fractions were lyophilized and resuspended in 10 mM Tris/HCl, 1 mM EDTA, and 8 M urea at pH 8.0 for chemical denaturation. To eliminate all of the protein that formed aggregates, two size-exclusion chromatographies (HiLoad 16/600 Superdex 75 pg Column) were performed with 20 mM phosphate and 0.5 mM EDTA at pH 8.0 as the elution buffer. Purified α-synuclein (α-syn) was dialyzed against Milli-Q water and lyophilized in batches for long-term storage. The Roche complete protease inhibitor cocktail was added only during the extraction step in the quantity suggested by the producer.

[15]N-labeled wild-type α-syn was expressed in *Escherichia coli* grown in M9 minimal medium supplemented with [15]NH_4Cl and purified as started for E. coli in LB medium.

For ^{15}N-labelled and unlabelled α-syn, protein expression and purification was performed as previously described [95]. An extended description of the methodologies used is present in the Supplementary Material.

Recombinant transthyretin (TTR) expression and purification

For TTR, Escherichia coli BL21(DE3) RIPL PLysS cells were transformed with pET-28a(+) plasmid encoding TTR gene. The cells were cultured in LB Medium containing 0.1 mg/mL of Kanamycin, grown at 37 °C, until OD_{600} reached 0.6–0.8, then induced with 1 mM isopropyl β-D-1-thiogalactopyranoside. They were further grown at 37°C overnight and then harvested by centrifugation at 6500 rpm (JA-10 Beckman Coulter) for 15 min at 4°C. The pellet was suspended in 20 mM Tris-HCl, pH 8.5 (60 mL per liter of culture) and sonicated at 4°C for 40 min. The suspension was centrifuged at 40,000 rpm (F15-6x100y Thermo Scientific) for 40 min and the pellet discarded. TTR was purified by anionic-exchange chromatography using a HiPrep Q FF 16/10 column (GE Healthcare Life Science). The protein was eluted in 20 mM Tris-HCl buffer at pH 8.6 with a linear 0–1 M NaCl gradient. Fractions containing pure TTR were identified by Coomassie staining SDS-PAGE gels, then joined and purified by Size Exclusion Chromatography using HiLoad Superdex 26/60 75pg in 50 mM phosphate buffer at pH 7.5.

Cerebrospinal fluid (CSF) pools and fractionation

CSF from neurological OND (Other Neurological Diseases) control subjects were collected in order to perform a fractionation to discover the molecular weight range of the compounds responsible for the interaction effects.

CSF from 19 different subjects (10 females and 9 males, average age = 70 y, standard deviation= 8 y) were collected reaching a total volume of 8 mL that was split in 2 aliquots of 3 mL and 10 aliquots of 200 μL.

An aliquot of 3 mL was resuspended in 1.5 mL of PBS 3x in order to have 4.5 mL of human pooled CSF in PBS 1x. This volume was then subjected to a series of filtrations using Centricon® filters of different molecular weight cut-offs. We did not performed size-exclusion chromatography since the concentration of the constituents [119] was too low to see a chromatogram and we did not want to start our analysis from an ultra-concentrated CSF (e.g. 40:1, as it was done in the work of Padayachee et al.[120]). The procedure used to fractionate human CSF is schematized in Fig. S3. The aliquots collected in this way contained the different constituents of the starting 4.5 mL of CSF in PBS with different concentration factors, the volume and the relative concentration factors (with respect to fraction 1) of the aliquots depicted in Fig. S3 are summarized in Table S1. Aliquots 2, 3, 4 and 5 were washed 2 times with PBS before the storage,

to dilute as much as possible compounds smaller than the cutoff value. The ability to interact with α-syn monomers was then tested for all the CSF fractions. for seeding aggregation assays (SAAs) and nLC-nESI HRMS/MS experiments, concentration factors of samples 2, 3 and 4 were brought to the same concentration factor of fraction 5 by diluting them with PBS. We chose to bring these concentrations to a factor of 5 (with respect to whole CSF) in order to take into account possible loss of protein due to the not perfect recovery efficiency of centrifugal filters.

Generation of preformed α-syn aggregates

Preformed α-syn aggregates were generated by incubating 1 mg/mL of α-syn in PBS for one week at 37°C under vigorous double orbital shaking (500 rpm) in a sealed 1.5 mL polypropylene vial. The final products were subjected to cycles of sonication (20 sec tip sonication, 20 sec rest) with an amplitude of 12 μm. The polypropylene vial had been immersed in ice for the whole duration of the sonication procedure. The aggregates were then diluted at 0.25, 2.5, 25, 250 and 2500 pg/μL, considering the initial monomer concentration as reference. The generated α-syn aggregates were then aliquoted and stored at -80°C.

SAA protocols

All the SAA experiments were performed with a programmable BMG LABTECH ClarioStar® fluorimeter in Greiner clear-bottom 96-well plates. The ThT fluorescence was read from the bottom using excitation and emission wavelengths of 450 and 480 nm, respectively. An incubation temperature of 37°C was used for all the experiments. A ThT concentration of 10 μM was used for all the experiments, 0.1% NaN$_3$ was also present in all the tested conditions to avoid bacterial contamination.

Testing of the inhibitory effect of CSF

Lyophilized recombinant α-syn was thawed in NaOH 3 mM at the concentration of 3.5 mg/mL. The solution was brought to physiological pH by diluting it with four-times concentrated phosphate-buffered saline (PBS) and distilled water, reaching a concentration of PBS 1.27x, 0.89 mg/mL α-syn, 12.7 μM ThT and 0.127% NaN$_3$. 158 μL of the solution containing monomeric α-syn was then poured in wells, each of them containing 6 glass beads of 1 mm diameter. In half of the wells 40 μL of human pooled CSF were added, while in the others, 40 μL of PBS were added instead. Subsequently,

2 µL of PBS containing 0, 0.25, 2.5, 25, 250 and 2500 pg/µL of α-syn aggregates were added to the wells. Each concentration of α-syn aggregated was replicated in 3 distinct wells. The plate was then sealed, put inside the fluorimeter at 37°C and subjected to cycles of shaking (14 min rest at 37 °C, 1 min double-orbital shaking at 500 rpm). At the end of each cycle the fluorescence of ThT was read from the bottom using excitation and emission wavelengths of 450 and 480 nm, respectively.

SAA on NPH CSF

Lyophilized recombinant α-syn was thawed in NaOH 3 mM at the concentration of 3.5 mg/mL. The solution was brought to physiological pH by diluting it with concentrated buffer and distilled water, reaching the final condition of PIPES pH 6.5, 500 mM NaCl, 0.125 mg/mL α-syn, 12.5 µM ThT and 0.125% NaN$_3$. 160 µL of the reaction buffer when then poured in 6 wells, each of them containing 21 glass beads of 0.5 mm diameter; 40 µL of CSF belonging to two hydrocephalus patients were then added in 3 wells, respectively. The plate was then sealed, put inside the fluorimeter at 37°C and subjected to cycles of shaking (29 min rest at 37°C, 1 min double-orbital shaking at 500 rpm). At the end of each cycle the fluorescence of ThT was read from the bottom using excitation and emission wavelengths of 450 and 480 nm, respectively.

Testing of the inhibitory effect of CSF fractions

Lyophilized recombinant α-syn was thawed in NaOH 3 mM at the concentration of 3.5 mg/mL. The solution was brought to physiological pH by diluting it with concentrated PBS (4x) and distilled water, reaching a concentration of PBS 1.25x, 0.75 mg/mL α-syn, 12.5 µM ThT and 0.125% NaN$_3$. 160 µL of the solution containing monomeric α-syn was then poured in wells, each of them containing 6 glass beads of 1 mm diameter. 40 µL CSF fractions were added. Each condition was replicated in 3 distinct wells. The plate was then sealed, put inside the fluorimeter at 37°C and subjected to cycles of shaking (14 min rest at 37 °C, 1 min double-orbital shaking at 500 rpm). At the end of each cycle the fluorescence of ThT was read from the bottom using excitation and emission wavelengths of 450 and 480 nm, respectively.

SAA with human serum albumin (HSA) and high-density lipoproteins (HDL)

The experiment was performed in the same exact way as it is described in Bellomo et al. (2019)[95]. Briefly, 0.7 mg/mL of recombinant α-syn (50 µM) in PBS pH 7.4 was used.

Six glass beads with a diameter of 1.0 mm were added in each well, the shaking/incubation protocol consisted in 29 min rest at 37°C and 1 min shaking at 500 rpm (double-orbital shaking). In addition to HSA, wells containing 0.12 mg/mL and 0.57 mg/mL human serum HDL (Sigma Aldrich, LP3) with and without α-syn were also analyzed (3 replicates for each condition).

SAA with HDL, low-density lipoproteins (LDL) and TTR

Lyophilized recombinant α-syn was thawed in NaOH 3 mM at the concentration of 3.5 mg/mL. The solution was brought to physiological pH by diluting it with concentrated PBS (4x) and distilled water, reaching a concentration of PBS 1.25x, 0.75 mg/mL α-syn, 12.5 μM thioflavin-T (ThT) and 0.125% NaN_3. 160 μL of the solution containing monomeric α-syn was then poured in wells, each of them containing 6 glass beads of 1 mm diameter. Subsequently, 40 μL of solutions containing different dilutions (all the products were diluted with distilled H_2O) of human serum HDL (Sigma-Aldrich LP3), human serum LDL (Sigma-Aldrich LP2), recombinant TTR were added (final condition: 0.7 mg/mL of recombinant α-syn in PBS 1x, final volume of 200 μL). Each condition was replicated in 3 distinct wells in the presence and absence of α-syn. The plate was then sealed, put inside the fluorimeter at 37°C. For the experiments in which we tested the effect of different concentrations of human serum HDL (0, 0.003, 0.03, 0.3 and 1 mg/mL) the plate was subjected to cycles of shaking (14 min rest, 1 min double-orbital shaking at 500 rpm).

For the experiments in which we tested the effect of different concentrations of human serum HDL (0.3 mg/mL), LDL (0.03 and 0.3 mg/mL) and TTR (1.0, 0.3 and 0.03 mg/mL) the plate was subjected to cycles of shaking (13 min rest, 2 min double-orbital shaking at 500 rpm). At the end of each cycle the fluorescence of ThT was read from the bottom using excitation and emission wavelengths of 450 and 480 nm, respectively.

SAA data analysis

The average background fluorescence produced by three wells containing the analyte without α-syn was subtracted prior to the analysis to the ThT intensity profiles relative to the same analyte in the presence of α-syn. While analyzing data relative to the sole α-syn the background fluorescence from well containing only the reaction buffer were subtracted. Each ThT kinetic trace was then fitted with the double sigmoid function

described in Fig. 1C (main text) by using Origin Pro v9.0. In the fitting model, A2 fits the fluorescence value of the second plateau, A1 fits the fluorescence value of the first plateau and A0 fits the baseline fluorescence. The time parameters t1 and t2 fit the first and the second inflection points, respectively, while d1 and d2 represent the slopes of the sigmoids. In the non-linear fitting procedure used, the following bounds were applied: $0 < A0 < 1000$, $500 < A1 < 5000$, $A2 > 2000$, $0 < t1 < 100$ h and $t2 > 0$. For some kinetic traces, a decrease in fluorescence was observed after reaching the second plateau. This known phenomenon is caused by the sequestration of ThT molecules by mature HMW fibrillary aggregates and by the sedimentation of HMW insoluble aggregates [121]. In these cases, the last descending part of the ThT profile was removed prior to fitting. Fitting was rejected when the adjusted determination coefficient R^2 was below 0.3.

Western blot and dot-blot assays

Equal amounts of SAAs products (volumes containing an initial α-syn concentration of 2 µg) were added with Laemmli's sample buffer without sodium dodecyl sulfate (SDS), without boiling them to prevent solubilization of SDS-sensitive aggregates. Samples were separated through SDS-PAGE on 4-20% polyacrylamide gels (Bio-Rad) and transferred into PVDF membranes (0.45 µm, Bio-Rad) by wet transfer at 100 V constant for 90 min using a 25 mM Tris-HCl, 192 mM glycine, 20% methanol added with 0.015% SDS. Membranes were fixed with 4% PFA for 30 min prior to blocking with 5% non-fat milk in TBS-T (TBS with 0.1% Tween 20) for 1 hour at RT. After blocking, filters were incubated with primary antibody against α-syn (211, sc-12767, Santa Cruz Biotechnology) O/N at 4°C. The membranes were further incubated with a goat-anti-mouse IgG-HRP conjugate (Bio-Rad, 1706516; 1:5000) secondary antibody for 1 hour at RT, and signals were visualized using an ECL reaction.

For dot blotting aliquots of products obtained in SAAs corresponding to 300 ng of monomeric α-syn in the initial reaction mixtures were spotted (2 µL/spot) on nitrocellulose membrane pre-equilibrated with TBS-T. Samples were dried at RT and fixed with PFA (0.4% in PBS) for 30 min, and then filters were blocked with 2% non-fat milk (in TBS-T). The membranes were incubated overnight at 4 °C with OC (1:1000) or A11 (1:1000) antibodies followed by incubation with goat-anti-rabbit IgG-HRP conjugate (1:5000; 1706515 Bio-Rad) secondary antibody for 1 hour at RT. Membranes were developed with an ECL reaction and images were acquired through

a ChemiDoc™ imaging system. Densitometric analysis was performed with ImageJ software (National Institute of Health). Dot-blot images were inverted, and window/level adjusted prior to the analysis. The gray level profile was extracted from a rectangle containing all the α-syn containing samples. The intensity profile of an adjacent rectangle not containing any dot was subtracted to remove the background intensity. No significant gray level fluctuations were found while repeating the same procedure for control samples not containing α-syn.

Solution nuclear magnetic resonance (NMR) experiments

All the NMR spectra were acquired at 283 K with a Bruker Avance III HD NMR spectrometer operating at 950 MHz ^{1}H Larmor frequency, equipped with a cryogenically cooled probe. For all the measurements performed, samples were analyzed in 3 mm diameter NMR tubes. Spectra were initially processed with the Bruker TOPSPIN 4.0 software tools.

Solution NMR experiments on NPH CSF

1D NMR experiments (Bruker sequence: zgesgp, number of scans = 128) on NPH CSF were performed by analyzing 170 µL of CSF samples + 10 µL D$_2$O (5.6%).

Solution NMR titrations with monomeric α-syn

2D ^{1}H-^{15}N HSQC spectra (Bruker sequence: hsqcetfpf3gp, number of scans = 16) were performed to test possible interactions between monomeric α-syn and CSF fractions/HDL/LDL/TTR.

Solution NMR titration experiments were carried out starting from 200 µL of a solution containing 100 µM of recombinant ^{15}N labelled α-syn in PBS buffer and 10% D$_2$O.

For CSF fractions titration experiments, the added volumes were 100 µL for fraction 1, 5 and 6, while 62.5 µL, 71 µL and 83 µL were added for fraction 2, 3 and 4 respectively to compensate for the different concentration factor with respect to fraction 5.

For HDL titration experiments 2 and 10 µL of a solution containing 11.97 mg/mL of human serum HDL (Sigma Aldrich, LP3) were added to the solution containing monomeric α-syn.

For LDL titration experiments 2, 10 and 40 µL of a solution containing 6.27 mg/mL of human serum LDL (Sigma Aldrich, LP2) were added to the solution containing monomeric α-syn.

For TTR titration experiments 20 and 40 µL of a solution containing 30 mg/mL of recombinant human TTR were added to the solution containing monomeric α-syn.

In order to compute amplitude ratios and/or evaluate chemical shifts perturbations, 2D ^1H-^{15}N HSQC spectra were further analyzed by the program Computer Aided Resonance Assignment [122].

nLC-nESI HRMS/MS

The analyses of proteins contained in CSF and in each CSF fractions were performed by nanoLiquidChromatography coupled to High Resolution Mass Spectrometry equipped with a nanoelectrospray interface (nLC-nESI HRMS/MS). From each CSF fraction a 10 µL volume was taken in triplicate and reduced with DTT (1 µL of a 0.5 mg/mL solution in ultrapure water) for 30 min at room temperature (RT) in the dark and then alkylated adding 1 µL of a 2.5 mg/mL iodoacetamide solution in ultrapure water and left for 20 min at RT in the dark. The samples were diluted with four volumes of 50 mM NH_4HCO_3 pH 8. Protein digestion was started adding 1 µL of 0.4 mg/mL LysC solution and incubated for 3 h at 37 °C, then adding 1 µL of 0.5 mg/mL sequencing grade trypsin (Promega) solution and incubated at 37 °C overnight. The reaction was stopped adding 1 µL 10% trifluoroacetic acid to reach a <2.5 pH value. C18 Empore (3M) Stage tips were prepared in-house and sequentially conditioned with 50 µL methanol, 50 µL 80% acetonitrile, 19.5% ultrapure water, 0.5% acetic acid and then with 50 µL 0.5% acetic acid. The digested samples were loaded into the stage tips, washed with 50 µL 0.5% acetic acid, then dried and peptides eluted with 50 µL methanol, 50 µL 80% acetonitrile, 19.5% ultrapure water, 0.5% acetic acid. The samples were then concentrated to less than 10 µL and bring to a final volume of 20 µL with 0.5% acetic acid; a 1 µL volume was injected into the nLC-nESI HRMS/MS system; this was composed of a nanoLC system EASY-nLC 1200 coupled to a LTQ Orbitrap hybrid mass spectrometer (Thermo Scientific). The nESI spray potential was 1.7 kV, capillary and tube lens voltages were 42 and 120 V, respectively. The chromatographic column was an Acclaim® PepMap 100 C18, 3 µm, 100 Å, 75 µm x 150 mm, operating at 300 nL/min flow rate. Solvent A was 100 % water and solvent B was 80% acetonitrile/20% water, both containing 0.1% formic acid; solvents were of LC-MS grade from Sigma (Sigma Italy, Merck). Elution was done by gradient starting from 2% B for 5 min, then to 40% B in 340 min, to 90% B in 5 min and returning to initial conditions. Data were acquired in data dependent manner, performing a survey

HRMS full scan from 350 to 2000 m/z at 60000 nominal resolution (at m/z 400) in the Orbitrap, using a 1×10^6 target value. Precursors were isolated from the seven most intense signals above 500 a.u. threshold with an isolation window of 2 Da. Normalized collision energy of 35% and an activation time of 20 ms were used. Precursor ions with no charge state assigned and singly charged did not trigger MS/MS experiments. Precursor masses already selected were dynamically excluded for 30 s with an exclusion window of 20 ppm (repeat count 2, repeat duration 15 s).

The acquired data were searched with Mascot 2.4 search engine (Matrix Science Ltd., London, UK) against a human database created from NCBI. Searches were performed allowing: (i) trypsin as enzyme, (ii) up to two missed cleavage sites, (iii) 10 ppm of tolerance for the monoisotopic precursor ion and 0.5 mass unit for monoisotopic fragment ions, (iv) carbamidomethylation of cysteine and oxidation of methionine as variable modifications. A target-decoy search was used: a false discovery rate (FDR) of 1% was imposed and the criterion used to accept protein identification included probabilistic score sorted by the software. The exponentially modified PAI (emPAI) values were used to estimate protein abundances [123,124].

<u>TEM</u>

The final reaction products of SAA for samples containing α-syn 0.7 mg/mL, LDL 0.3 mg/mL, α-syn 0.7 mg/mL + LDL 0.3 mg/mL, α-syn 0.7 mg/mL + HDL 0.3 mg/mL and α-syn 0.7 mg/mL + pooled human CSF (1:5 ratio) were diluted 3-fold in water. Ten µL of each dilution was adsorbed onto 200-mesh Formvar-carbon coated nickel grids, at room temperature. After 30 minutes, the remaining drop was dried using filter paper and the grids were stained with 25% Uranyl Acetate Replacement (negative staining) for 10 min and air-dried for 15 minutes. Images were taken using a FEI Tecnai Spirit electron microscope (120kV), equipped with an Olimpus Megaview G2camera.
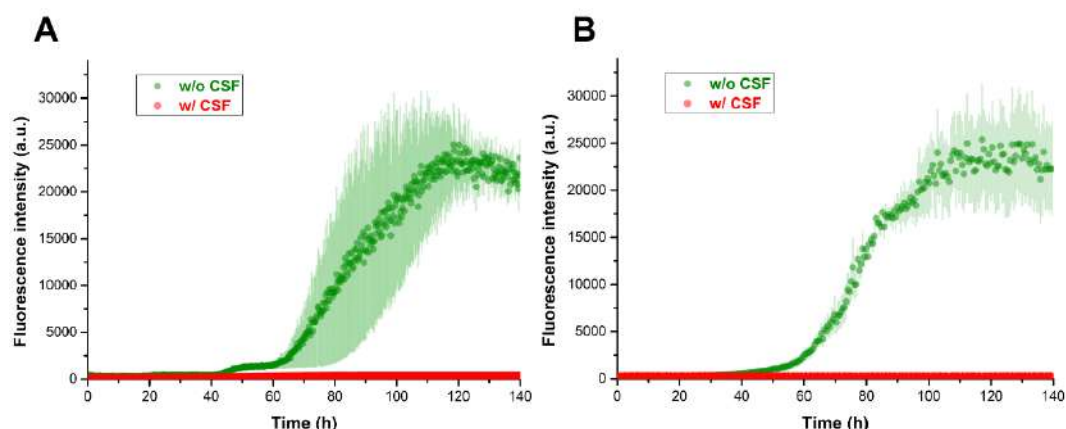
Fig. S1. CSF inhibit α-syn aggregation in different experimental conditions. A) SAA performed using 0.1 mg/mL of recombinant α-syn in PBS pH 7.4 + 137 mM NaCl with (red) and without (green) 40 µl of human CSF (final volume of 200 µl). Six glass beads with a diameter of 1.0 mm were added in each well (14 min rest, 1 min shaking at 500 rpm). B) SAA performed using 0.08 mg/mL of recombinant α-syn in PIPES pH 6.5 + 500 mM NaCl with (red) and without (green) 40 µl of human CSF (final volume of 200 µl). 21 glass beads with a diameter of 0.5 mm were added in each well (29 min rest, 1 min shaking at 500 rpm). The data shown are the averages of three replicates on a 96-well plate.
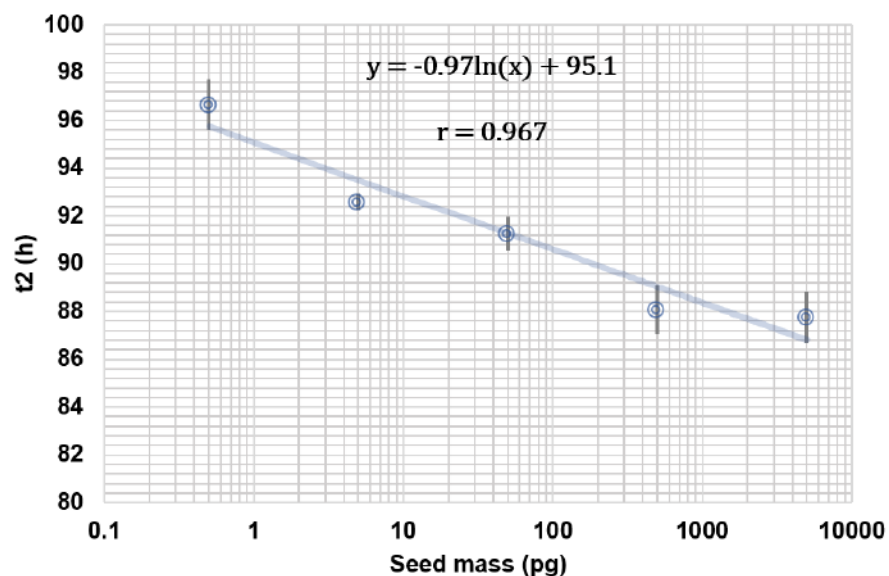
Fig. S2. Quantitative regression analysis of the seeded SAA in the absence of human CSF. Measured t2 parameters (in hours) for the seeded experiment vs the quantity of seeds added; the horizontal axis is displayed in log10 scale. The t2 values displayed result from the average of three replicates, error bars reflect the standard deviation of the mean value. The data were fitted with a natural logarithm function, the correlation between t2 and the added seed masses was assessed by means of Pearson's correlation coefficient (r).
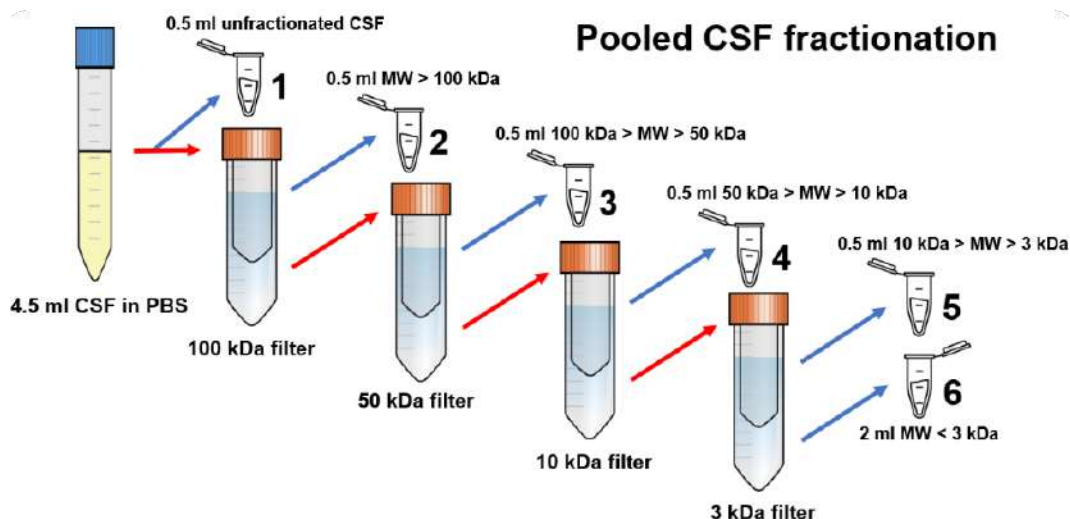
Fig. S3. Scheme of the CSF fractionation procedure. From a starting aliquot of 4.5 mL of CSF in PBS 1x, we collected 6 aliquots containing compounds of different molecular weight and froze them in liquid nitrogen. After every filtration with centrifugal filters, the flow-through of the filtered fraction was passed to a filter with smaller cutoff. Aliquots 2, 3, 4 and 5 were washed 2 times with PBS before storage, to dilute as much as possible compounds smaller than the cutoff value. The aliquots collected in this way contained the different constituents of the starting 4.5 mL of CSF in PBS with different concentration factors. The volume and the relative concentration factors (with respect to sample 1) of the aliquots depicted are summarized in Table S1.
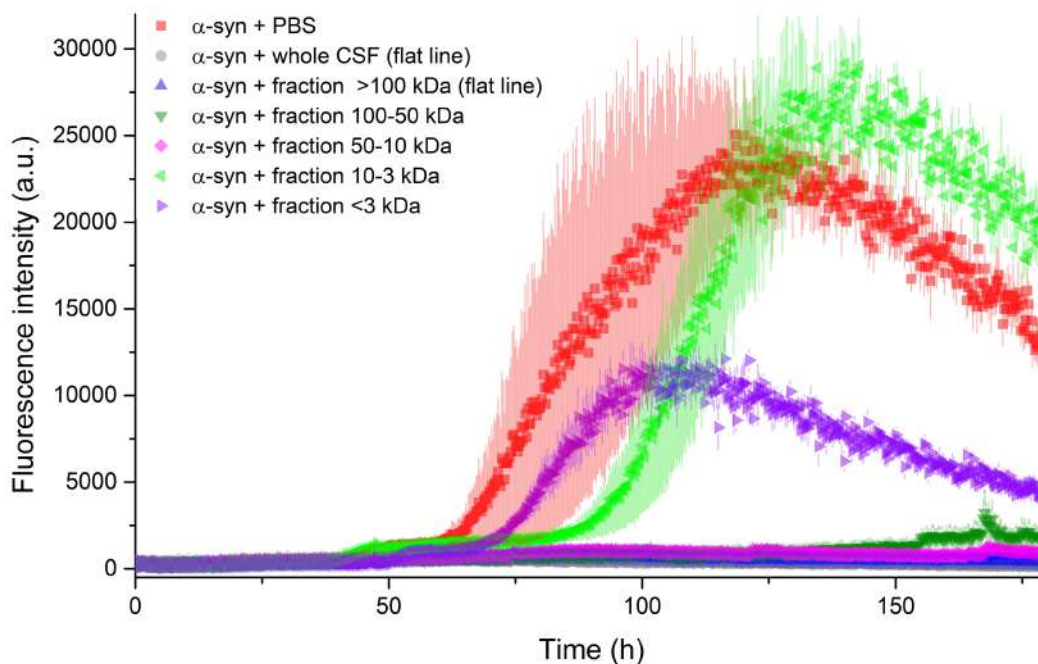
Fig. S4. Average α-syn aggregation profiles in the presence of CSF fractions. Average ThT fluoresce intensities relative to SAAs performed using 0.7 mg/mL (50 µM) of recombinant α-syn in PBS with 40 µl of PBS/human pooled CSF fractions (final volume of 200 µl). Six glass beads with a diameter of 1 mm were added in each well. The SAA protocol consisted in 14 min rest at 37 °C and 1 min shaking at 500 rpm. To remove the background fluorescence, the average fluorescence of three replicates containing PBS, whole CSF, and CSF fractions without α-syn was subtracted prior to the analysis.
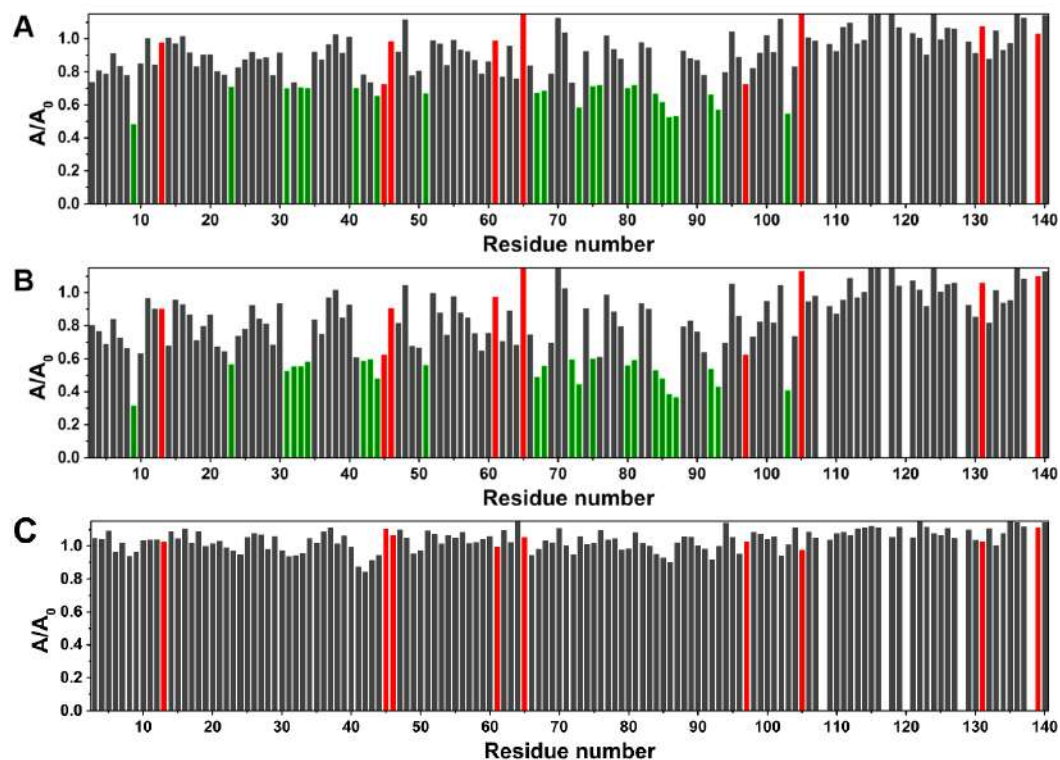
Fig. S5. NMR titrations of α-syn with CSF fractions. Intensity decreases of the signals of two-dimensional (2D) ^{15}N–^{1}H HSQC experiments acquired at 950 MHz at T = 283 K on ^{15}N labelled α-syn (100 µM) in PBS after the addition of: (A) whole pooled CSF in PBS, (B) < 3 kDa CSF fraction in PBS and (C) > 100 kDa CSF fraction in PBS. The residues experiencing the largest decreases in signal intensity (smaller by one or more standard deviations with respect to the average value) are highlighted in green. The intensity ratios corresponding to overlapping peaks are highlighted in red (their values were not considered in the calculation of the average decreases and standard deviations).
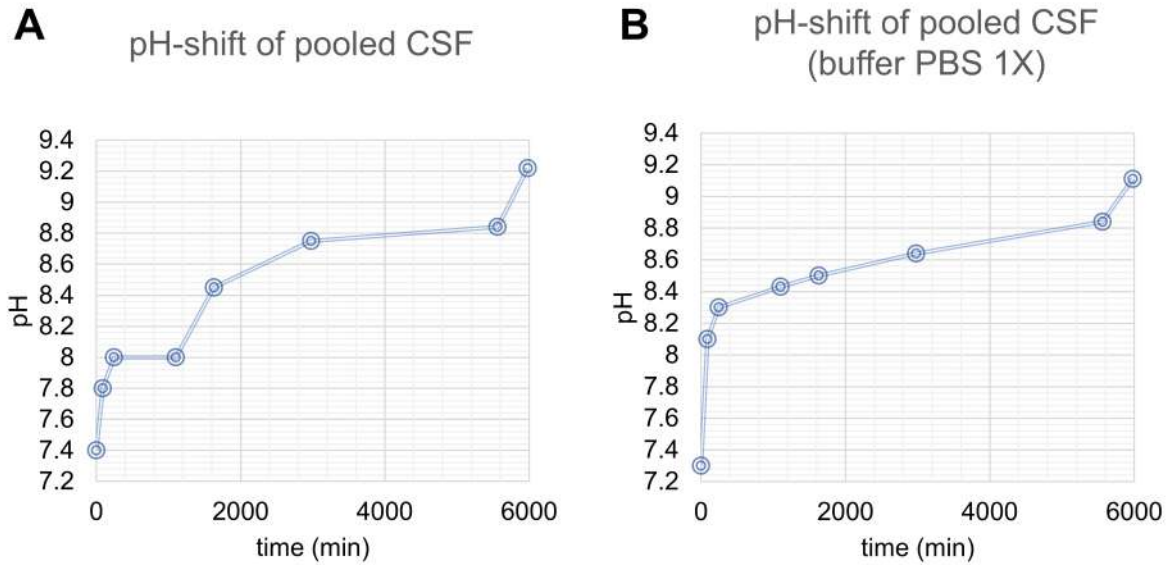
Fig. S6. CSF pH drift. The pH change due to the exposure of CSF to air was monitored over time in 500 µL of undiluted pooled CSF (A) and in the presence of PBS (400 µL CSF + 200 µL PBS 3x) in polypropylene vials with a Thermo Scientific Orion pH-meter equipped with a glass 6 mm diameter pHenomenal MIC 220 Micro electrode. Right before each measurement, the sample was vortexed for 20 sec and left open to air for another 20 sec.

1 α-syn + HSA 4.5 µM (0.3 mg/mL) **5** α-syn + HDL 0.57 mg/mL **9** HDL 0.12 mg/mL
2 α-syn + HSA 100 µM (6.7 mg/mL) **6** HSA 4.5 µM (0.3 mg/mL) **10** HDL 0.57 mg/mL
3 α-syn + HSA 640 µM (43 mg/mL) **7** HSA 100 µM (6.7 mg/mL)
4 α-syn + HDL 0.12 mg/mL **8** HSA 640 µM (43 mg/mL)
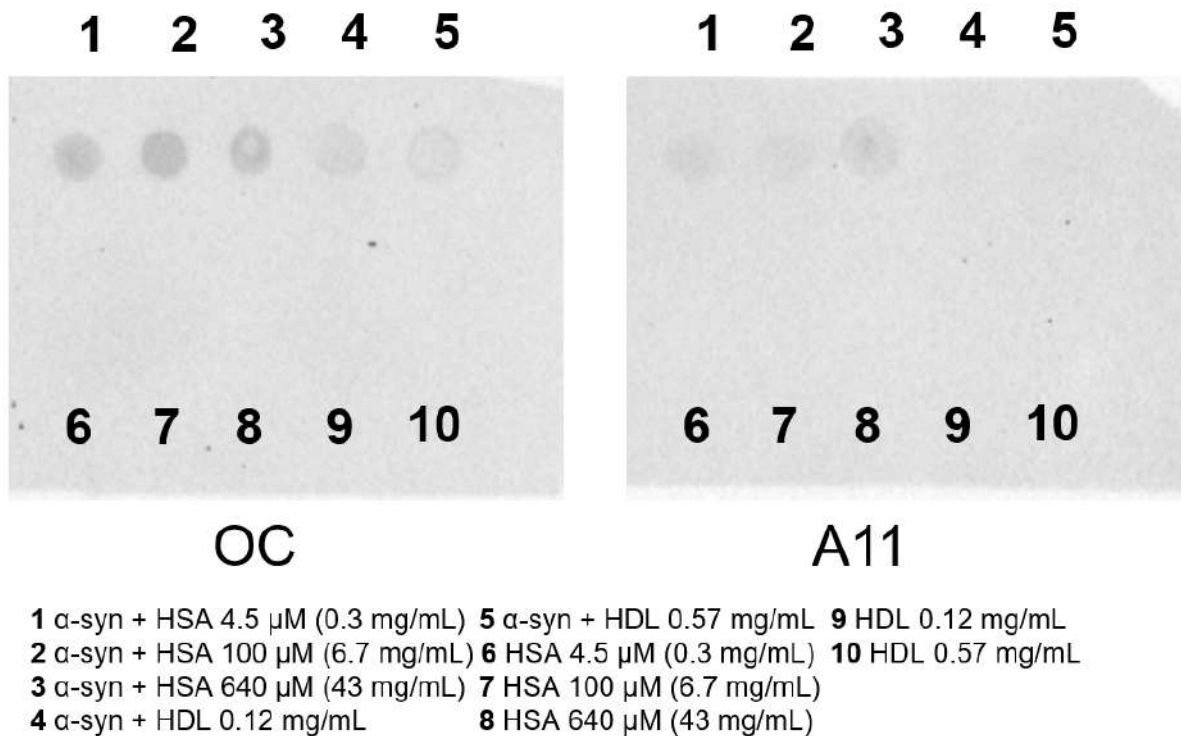
Fig. S7. Native image of the dot-blot assay. Native image of the dot-blot assay performed on the HSA and HDL containing samples with OC (detection of fibrillary oligomers) and A11 (detection of amorphous oligomers) conformational antibodies.
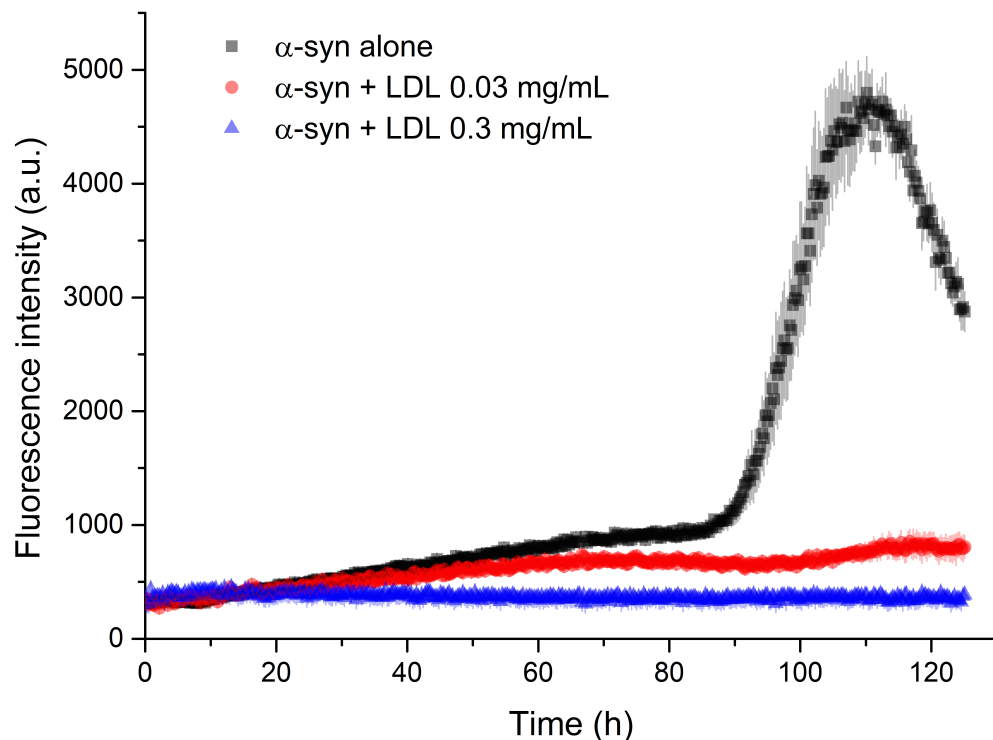
Fig. S8. Average α-syn aggregation profiles in the presence of human LDL. ThT aggregation profile relative to a SAA performed using 0.7 mg/mL (50 µM) of recombinant α-syn in PBS with 0, 0.03 and 0.3 mg/mL of added human serum LDL. Six glass beads with a diameter of 1 mm were added in each well. The SAA protocol consisted in 13 min rest at 37 °C and 2 min shaking at 500 rpm. For some kinetic traces, a decrease in fluorescence was observed after reaching the second plateau. This known phenomenon is caused by the sequestration of ThT molecules by mature HMW fibrillary aggregates and by the sedimentation of HMW insoluble aggregates [121].
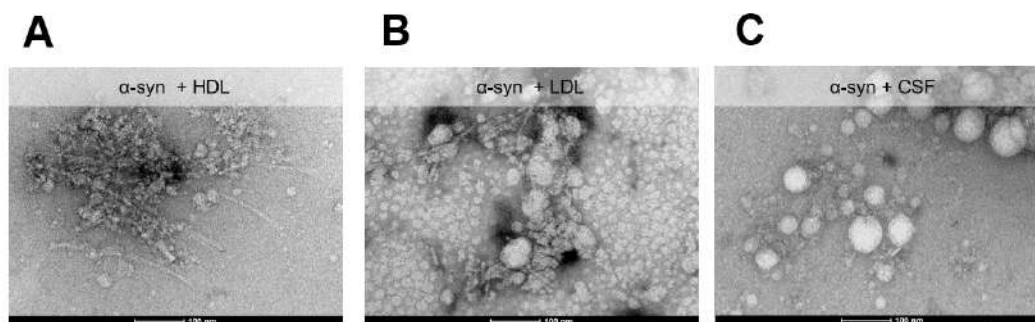
Fig. S9. TEM images of α-syn incubated with HDL, LDL and CSF. Representative TEM images obtained by analyzing samples obtained by the co-incubation of α-syn 0.7 mg/mL at 37 °C with (A) HDL 0.3 mg/mL, (B) LDL 0.3 mg/mL and (C) pooled human CSF (1:5 ratio with respect to total reaction volume). Samples were subjected to cycles of incubation (13 min) and shaking (double-orbital, 2 min) at 500 rpm.
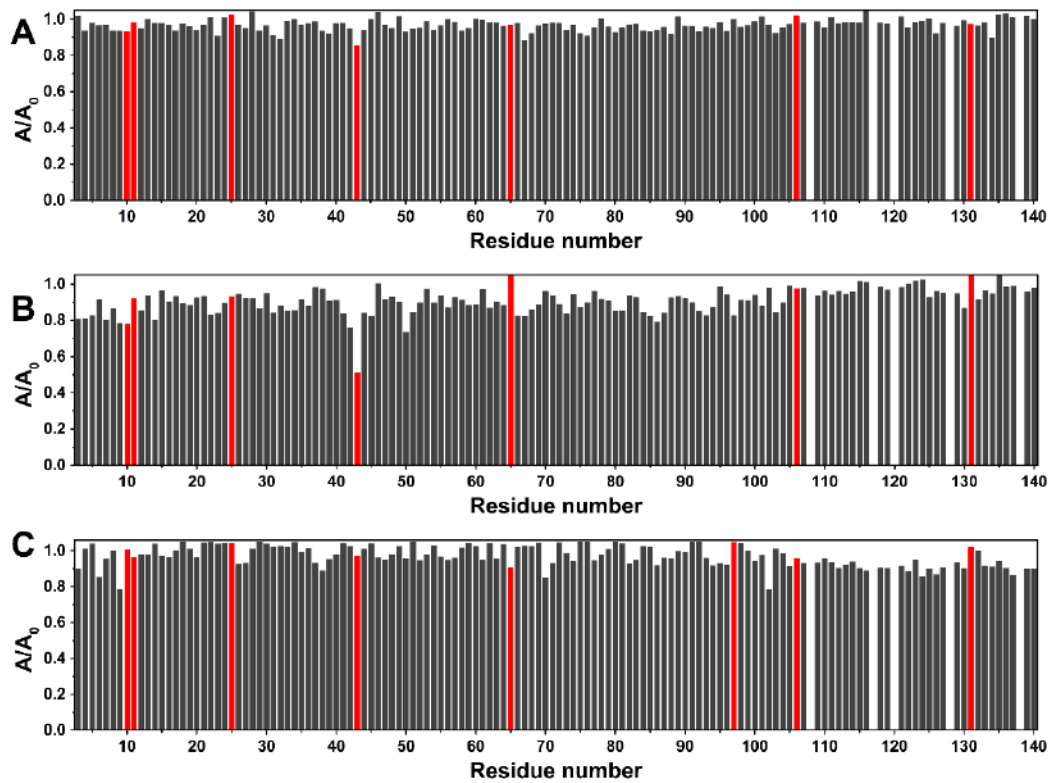
Fig. S10. **NMR titrations of α-syn with HDL, LDL and TTR.** A) Intensity decreases of the signals of two-dimensional (2D) ^{15}N–^{1}H HSQC experiments acquired at 950 MHz at T = 283 K on ^{15}N labelled α-syn (100 µM) in PBS after the addition of 0.57 mg/mL serum-derived HDL. The intensity ratios corresponding to overlapping peaks are highlighted in red. B) Intensity decreases of the signals of two-dimensional (2D) ^{15}N–^{1}H HSQC experiments acquired at 950 MHz at T = 283 K on ^{15}N labelled α-syn (100 µM) in PBS after the addition of 1 mg/mL serum-derived LDL. C) Intensity decreases of the signals of two-dimensional (2D) ^{15}N–^{1}H HSQC experiments acquired at 950 MHz at T = 283 K on ^{15}N labelled α-syn (100 µM) in PBS after the addition of 3 mg/mL TTR.

Supplementary Tables

Table S1. Concentration factors and final volumes of the CSF fractions.

Sample number	MW range	Volume (mL)	Native concentration factor	Experimental concentration factor
1	whole CSF	0.5	1	1
2	>100 kDa	0.5	8	5
3	50-100 kDa	0.5	7	5
4	10-50 kDa	0.5	6	5
5	3-10 kDa	0.5	5	5
6	<3 kDa	2	1	1

Table S2. Measured levels of the most abundant macromolecular CSF constituents by nLC-nESI HRMS/MS. Albumin was the most abundant protein in whole CSF at its native concentration and in all concentrated fractions, although its level was similar to the one of apolipoproteins (apolip.) in the > 100 kDA fraction. TTR was abundant in the 100-50 kDa fraction. Apolipoproteins were mostly present in the >100 kDa fraction but relevant quantities were also detected in the 100-50 kDa and 50-10 kDa fractions while PGSD was mostly present in the 50-10 kDa fraction. Table cells are colored according to the relative concentration (emPAI x MW, proportional to the protein concentration in mg/mL) of each analyte in each concentrated CSF fraction, from blue (most abundant), to white (low levels or not detected, n.d.), the highest value of each analyte is highlighted in bold. The overall dilution/concentration factors (with respect to whole CSF) of the samples depicted are summarized in Table 3 in the Materials and Methods section.

Sample	whole CSF	>100 kDa	50-100 kDa	50-10 kDa	10-3 kDa	<3kDa
Albumin (MW x emPAI)	$(520 \pm 40) \cdot 10^4$	$(220 \pm 30) \cdot 10^4$	$(1090 \pm 130) \cdot 10^4$	$(180 \pm 130) \cdot 10^4$	$(1.4 \pm 0.4) \cdot 10^4$	n.d.
TTR (MW x emPAI)	$(130 \pm 40) \cdot 10^4$	$(11 \pm 4) \cdot 10^4$	$(270 \pm 100) \cdot 10^4$	$(14 \pm 1) \cdot 10^4$	n.d.	n.d.
apolip. (MW x emPAI)	$(52 \pm 15) \cdot 10^4$	$(180 \pm 10) \cdot 10^4$	$(28 \pm 6) \cdot 10^4$	$(2.4 \pm 0.6) \cdot 10^4$	n.d.	n.d.
PGSD (MW x emPAI)	$(16 \pm 4) \cdot 10^4$	$(2.6 \pm 1.6) \cdot 10^4$	$(13 \pm 2) \cdot 10^4$	$(30 \pm 14) \cdot 10^4$	n.d.	n.d.

Table S3. Mean fitted kinetic parameters and maximum fluorescence values (MAX) of the analyzed samples. Fitting was not possible for samples containing 0.3 and 1 mg/mL of HDL. Data are represented as mean ± SEM.

HDL (mg/mL)	MAX (a.u.)	2nd plateau A2 (a.u.)	1st plateau A1 (a.u.)	2nd inflection t2 (h)	1st inflection t1 (h)
0	$(31 \pm 6) \cdot 10^3$	$(27 \pm 5) \cdot 10^3$	$(12 \pm 1.2) \cdot 10^2$	120 ± 11	39.1 ± 0.3
0.003	$(27 \pm 4) \cdot 10^3$	$(22 \pm 4) \cdot 10^3$	$(9.4 \pm 1.7) \cdot 10^2$	135 ± 9	29.6 ± 1.3
0.03	$(35 \pm 3) \cdot 10^3$	$(28 \pm 2) \cdot 10^3$	$(3.3 \pm 0.7) \cdot 10^2$	139 ± 7	30.2 ± 0.3
0.3	$(50 \pm 2) \cdot 10$	n.d.	n.d.	> 215	> 215
1	$(49 \pm 3) \cdot 10$	n.d.	n.d.	> 215	> 215

During my PhD project I was also involved in a line of research aimed to investigate the origins of the relaxivity in fruit juice used as oral contrast agents for magnetic resonance imaging of the gastrointestinal tract. These natural products contain high concentrations of the paramagnetic Mn(II) ion but the observed relaxivity is modulated by the other components of the juice and can be increased by the addition of hydrogels. The results of this research activity are reported in two following papers.

3.4 Origin of the MRI Contrast in Natural and Hydrogel Formulation of Pineapple Juice

Research Article

Origin of the MRI Contrast in Natural and Hydrogel Formulation of Pineapple Juice

Domenico Rizzo [ID],[1,2] **Enrico Ravera** [ID],[1,2] **Marco Fragai** [ID],[1,2]
Giacomo Parigi [ID],[1,2] **and Claudio Luchinat** [ID][1,2]

[1]*Magnetic Resonance Center (CERM), Department of Chemistry, University of Florence, Via Sacconi 6, Sesto Fiorentino, Florence, Italy*
[2]*Consorzio Interuniversitario Risonanze Magnetiche di Metalloproteine (CIRMMP), Sesto Fiorentino, Florence, Italy*

Correspondence should be addressed to Marco Fragai; fragai@cerm.unifi.it and Giacomo Parigi; parigi@cerm.unifi.it

Magnetic resonance imaging (MRI) often requires contrast agents to improve the visualization in some tissues and organs, including the gastrointestinal tract. In this latter case, instead of intravascular administration, oral agents can be used. Natural oral contrast agents, such as fruit juice, have the advantages of better taste, tolerability, and lower price with respect to the artificial agents. We have characterized the relaxometry profiles of pineapple juice in order to understand the origin of the increase in relaxation rates (and thus of the MRI contrast) in reference to its content of manganese ions. Furthermore, we have characterized the relaxometry profiles of pineapple juice in the presence of alginate in different amounts; the interaction of the manganese ions with alginate slows down their reorientation time to some extent, with a subsequent increase in the relaxation rates. The relaxometry profiles were also compared with those of manganese(II) solutions in 50 mmol/dm^3 sodium acetate solution (same pH of pineapple juice), which revealed sizable differences, mostly in the number of water molecules coordinated to the metal ion, their lifetimes, and in the constant of the Fermi-contact interaction. Finally, the fit of the transverse relaxivity shows that the increased viscosity in the hydrogel formulations can improve significantly the negative contrast of pineapple juice at the magnetic fields relevant for clinical MRI.

1. Introduction

Fruit juice rich in manganese ions is increasingly used in clinical MRI as oral contrast agent for imaging of the gastrointestinal tract [1]. Magnetic resonance cholangiopancreatography images are in fact frequently degraded by the high signal due to the fluid collecting in stomach and duodenum. Oral contrast agents can greatly improve the visualization of both biliary tree and pancreatic ducts, facilitating the evaluation of distal ducts, and of the stomach and small bowel. Oral manganese ions were also shown to provide good MRI contrast for the imaging of peripheral nerves involved in pain perception, thanks to the ability of Mn^{2+} to enter neurons via calcium channels [2].

The ideal oral agent must be nontoxic, increase the contrast homogeneously even when diluted through the gastrointestinal tract, and have good digestive acceptance, absence of collateral effects, minimum peristaltic stimulation, and an accessible price [3]. Several natural substances have been tried because of their content of Mn^{2+} ions [4–9]. Natural commercially available manganese-rich fruits include pineapple, blueberry, raspberry, blackberry, medlar, plum, and the Amazonian fruit pulp from Euterpe oleracea (popularly named Açaí) [10–12]. Pineapple juice is the most promising natural food for higher content of Mn^{2+} ions [13, 14], providing image contrast of a degree similar to commercially available negative contrast agents [6]. Since Mn^{2+} ions can largely increase both the longitudinal and the transverse relaxation rate of water protons, it can be used as

114

both T1 and T2 contrast agent. For instance, as T2 agent, it was shown to suppress the signal from bowel fluid in pediatric magnetic resonance cholangiopancreatography, while as T1 agent, it can delineate the gut [13].

Pineapple juice has been shown effective as an oral contrast agent in magnetic resonance images, and, more recently, concentrated juices added with hydrogels [15] have been proposed to further enhance the contrast. However, so far, no detailed studies were performed on natural juices or on their derivatives to characterize the relaxation properties in detail. Field-dependent relaxometry [16, 17], which consists in the measurement of the nuclear relaxation rates as a function of the applied magnetic field, is a technique of choice in this respect. In fact, it provides access to a number of physicochemical parameters upon which the relaxation rates depend [18–20]. In the presence of paramagnetic systems, they are structural parameters, such as the number and distance of water molecules coordinated to the paramagnetic metal ions, and motional parameters, such as the reorientation time of the system, the lifetimes of the water molecules coordinated to the metal, the electron relaxation parameters, and the unpaired electron spin density delocalized onto the water protons [17]. From the values of these parameters, it is possible to infer on the occurring interactions of the paramagnetic metal with its environment and to monitor how they change upon changing the experimental conditions. Furthermore, the analysis of the relaxometry profiles permits to evaluate the different contributions to relaxation arising from the modulation of different types of metal-proton interactions and from the different motional regimes.

In this study, we characterize the relaxometry profile of pineapple juice in order to describe the relevance of the different parameters determining the experimental rates. We also analyze the effect of alginate added to pineapple juice as a natural food able to slower the dynamics of the paramagnetic ions present in the juice and thus to increase the nuclear relaxation rates. As manganese ions represent the major actors driving the relaxation properties of pineapple juice, the relaxation rates of solutions of manganese ions in conditions similar to those of the juice are also investigated, in order to evaluate the effects that other components than these ions have on the relaxation rates of the juice.

2. Materials and Methods

2.1. Sample Preparation. Samples were prepared by dissolving sodium alginate (Sigma-Aldrich, A1112) in pineapple juice (Coop, 100%, pineapple juice) or in a simulated pineapple juice to obtain hydrogels at 5% and 15% (w/w) of polysaccharide. The simulated pineapple juice containing the same concentration of inorganic salts (4 mmol/dm^3 Ca^{2+}; 6 mmol/dm^3 Mg^{2+}; 0.437 mmol/dm^3 Mn^{2+}) and the same pH (3.6) of the natural product were prepared by dissolving stock solutions of $MgCl_2$, $CaCl_2$, and $MnCl_2$ in 50 mmol/dm^3 of sodium acetate. Sodium acetate solution was prepared by dissolving pure acetic acid in water and then by adding a concentrated solution of sodium hydroxide until pH 3.6 is reached. Water was then added to match the

desired concentration. The hydrogels were homogenized by several steps of sonication.

2.2. ^1H NMRD Measurements. Water relaxation profiles were acquired with a Stelar Spinmaster FFC2000-1T relaxometer by measuring the water proton relaxation rates as a function of the applied magnetic field (0.01–40 MHz proton Larmor frequency). The relaxation measurements, obtained from the fit of the magnetization decay/recovery curves against a monoexponential function, were affected by an error of about ±1%. The relaxivity profiles were obtained by normalization of the measured relaxation data, subtraction of the diamagnetic relaxation rate contribution, to the Mn^{2+} concentration (in mmol/dm^3). The measurements were performed at 25 and 37°C.

2.3. High-Field NMR Measurements. R_1 and R_2 at high field were measured on a Bruker Avance III spectrometer operating at 400 MHz ^1H Larmor frequency (9.4 T) to mitigate the effects of relaxation, using a 5 mm BBO probehead. To mitigate the effect of radiation damping, the samples were put in a single capillary coaxial to the 5 mm tube, and the probehead was detuned by 1 MHz.

2.4. Model Used to Analyze the Data. The experimental water proton relaxation rates $R_1 = R_{1dia} + R_{1p}$ and $R_2 = R_{2dia} + R_{2p}$ are composed of diamagnetic and paramagnetic contributions. The paramagnetic contributions are related to the presence of paramagnetic metal ions in solution, which increase the relaxation rates of the water protons coordinated to the metal ions through hyperfine coupling. These paramagnetic relaxation enhancements (R_{1M} and R_{2M}) are then transferred to bulk water protons through chemical exchange so that

$$R_{1p} = f_M \left(R_{1M}^{-1} + \tau_M \right)^{-1} + R_{1\text{out}}, \tag{1}$$

$$R_{2p} = \frac{f_M}{\tau_M} \frac{R_{2M}^2 + R_{2M}\tau_M^{-1} + (\Delta\omega_M)^2}{\left(R_{2M} + \tau_M^{-1} \right)^2 + (\Delta\omega_M)^2} + R_{2\text{out}}$$
$$\cong f_M \left(R_{2M}^{-1} + \tau_M \right)^{-1} + R_{2\text{out}}, \tag{2}$$

being the difference in chemical shift $\Delta\omega_M$ between the paramagnetic and the diamagnetic species much smaller than R_{2M}, where

$$f_M = \frac{q \left[Mn^{2+} \right]}{55.5}. \tag{3}$$

The lifetime τ_M is the inverse of the exchange rate, q is the number of water molecules coordinated to the metal ion, and $R_{1\text{out}}$ and $R_{2\text{out}}$ indicate the paramagnetic relaxation enhancements due to longitudinal and transverse translational diffusion (also called outer sphere relaxation), i.e., due to the dipole-dipole interaction between the paramagnetic metal ion and the water molecules freely diffusing around it up to a distance of closest approach d.

R_{1M} and R_{2M} can be described by the Solomon–Bloembergen–Morgan (SBM) model [21, 22] and are composed of the Fermi-contact and dipolar contributions:

$$R_{1M} = \frac{2S(S+1)}{3}\left(\frac{A^{\text{FC}}}{\hbar}\right)^2\left[\frac{\tau_{\text{FC}}}{1+\omega_S^2\tau_{\text{FC}}^2}\right] + \frac{2}{15}\left(\frac{\mu_0}{4\pi}\frac{\gamma_I g_{\text{iso}}\mu_B}{r^3}\right)^2$$

$$\cdot S(S+1)\left\{S_{LS}^2\left[\frac{7\tau_c}{1+\omega_s^2\tau_c^2}+\frac{3\tau_c}{1+\omega_I^2\tau_c^2}\right]\right.$$

$$\left.+\left(1-S_{LS}^2\right)\left[\frac{7\tau_f}{1+\omega_s^2\tau_f^2}+\frac{3\tau_f}{1+\omega_I^2\tau_f^2}\right]\right\}, \tag{4}$$

$$R_{2M} = \frac{S(S+1)}{3}\left(\frac{A^{\text{FC}}}{h}\right)^2\left[\tau^{\text{FC}}+\frac{\tau_{\text{FC}}}{1+\omega_S^2\tau_{\text{FC}}^2}\right]$$

$$+\frac{1}{15}\left(\frac{\mu_0}{4\pi}\frac{\gamma_I g_{\text{iso}}\mu_B}{r^3}\right)^2 S(S+1)$$

$$\cdot\left\{S_{LS}^2\left[4\tau_c+\frac{13\tau_c}{1+\omega_s^2\tau_c^2}+\frac{3\tau_c}{1+\omega_I^2\tau_c^2}\right]+\left(1-S_{LS}^2\right)\right.$$

$$\left.\cdot\left[4\tau_f+\frac{13\tau_f}{1+\omega_s^2\tau_f^2}+\frac{3\tau_f}{1+\omega_I^2\tau_f^2}\right]\right\}, \tag{5}$$

where (A^{FC}/h) is the contact coupling constant, r is the distance between metal ion and coordinated protons, S is the electron spin quantum number (5/2 in the case of Mn^{2+}), τ_{FC} is the correlation time for the Fermi-contact interaction:

$$\tau_{\text{FC}}^{-1} = \tau_e^{-1} + \tau_M^{-1}, \tag{6}$$

and τ_c is the correlation time for the dipole-dipole interaction, given by

$$\tau_c^{-1} = \tau_r^{-1} + \tau_e^{-1} + \tau_M^{-1}, \tag{7}$$

where τ_r is the tumbling time of the paramagnetic system and τ_e is the electron relaxation time, and

$$\tau_e^{-1} = \frac{2\Delta_t^2}{50}\left[4S(S+1)-3\right]\left[\frac{\tau_v}{1+\omega_S^2\tau_v^2}+\frac{4\tau_v}{1+4\omega_S^2\tau_v^2}\right], \tag{8}$$

described in the pseudorotation model by the parameters Δ_t and τ_v, which correspond to the transient zero-field splitting and the correlation time for electron relaxation, respectively. Using the Lipari and Szabo model-free approach [23], in equations (4) and (5), a squared order parameter S_{LS}^2 is also introduced to account for contributions arising in the presence of nonrigid molecular reorientations. In this case, in fact, the dipole-dipole interaction is partially modulated with a further correlation time (τ_f) which is also determined by the internal faster mobility, with correlation time τ_i:

$$\tau_f^{-1} = \tau_r^{-1} + \tau_e^{-1} + \tau_M^{-1} + \tau_i^{-1}. \tag{9}$$

Other symbols in equations (4) and (5) have the usual meaning [17]. The outer sphere relaxation can be described using the Freed model [24]:

$$R_1^{\text{out}} = \frac{32\pi}{405}\left(\frac{\mu_0}{4\pi}\right)^2\frac{1000N_A\left[Mn^{2+}\right]\left(\gamma_I\mu_B g_e\right)^2 S(S+1)}{d\,D}$$

$$\cdot\left[7J^F\left(\omega_S,\tau_D\right)+3J^F\left(\omega_I,\tau_D\right)\right], \tag{10}$$

$$R_2^{\text{out}} = \frac{16\pi}{405}\left(\frac{\mu_0}{4\pi}\right)^2\frac{1000N_A\left[Mn^{2+}\right]\left(\gamma_I\mu_B g_e\right)^2 S(S+1)}{d\,D}$$

$$\cdot\left[4+13J^F\left(\omega_S,\tau_D\right)+3J^F\left(\omega_I,\tau_D\right)\right], \tag{11}$$

where

$$J^F(\omega,\tau_D) = \frac{1+(5z/8)+\left(z^2/8\right)}{1+z+\left(z^2/2\right)+\left(z^3/6\right)+\left(4z^4/81\right)+\left(z^5/81\right)+\left(z^6/648\right)}, \tag{12}$$

$$z = \left(2\omega\tau_D\right)^{1/2}, \tag{13}$$

$$\tau_D = \frac{d^2}{D}, \tag{14}$$

and D is the sum of the diffusion coefficients of the water molecule and of the paramagnetic complex.

The paramagnetic longitudinal and transverse relaxivities correspond to R_{1p} and R_{2p}, respectively, when the concentration of the paramagnetic ion is 1 mmol/dm^3.

3. Results and Discussion

3.1. Metal Content of Pineapple Juice.
The amount of copper, iron, and manganese ions in pineapple juice was evaluated through ICP-AES. The resulting concentrations of the three ions were 0.002–0.007 mmol/dm^3, 0.027–0.031 mmol/dm^3, and 0.42–0.46 mmol/dm^3, respectively. The ranges refer to the variability observed for four samples taken from different fruit juice batches. The concentration of Mn^{2+} is more than one order of magnitude larger than that of iron and copper so that the relaxation properties of the juice are largely dictated by the presence of this ion.

3.2. ^1H NMRD Profiles of Pineapple Juice.
The ^1H longitudinal relaxation profiles measured for pineapple juice at 25 and 37°C are shown in Figure 1. As expected, for water solutions of Mn^{2+} ions, there are two dispersions, one at the lowest frequency corresponding to the Fermi-contact dispersion and the other to the dipolar ω_S dispersion. In order to evaluate the paramagnetic relaxivity due to Mn^{2+}, we should estimate the diamagnetic contribution and the contributions from the other paramagnetic ions. The contribution from copper ions should be negligible, due to the low concentration and low relaxivity of this $S = 1/2$ ion [17] and also with respect to the diamagnetic relaxation rate which is expected to be about $0.4\,s^{-1}$. We can figure out the relaxation contribution of iron from the relaxivity of Fe^{3+} aqua ion and its concentration in pineapple juice [25]. Once added to the diamagnetic contribution, we obtain an estimate of the relaxation rates not ascribable to the hyperfine interaction of the water protons
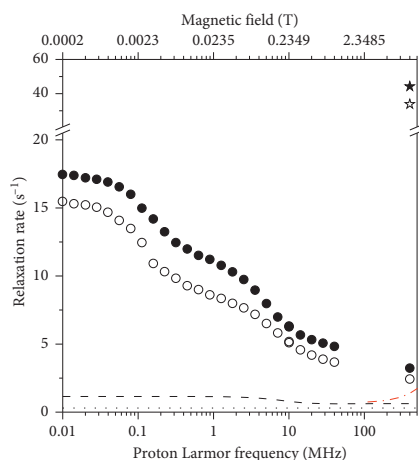
Figure 1: Experimental ^{1}H R_1 profiles (circles) and ^{1}H R_2 at 400 MHz (stars) of pineapple juice at 25°C (solid symbols) and 37°C (empty symbols). The dotted and dashed lines represent estimates of the diamagnetic contribution and of the latter summed to the R_1 contribution from iron ions at 37°C, respectively; the dotted-dashed red line provides an estimate of the contributions to R_2 from diamagnetic relaxation and from transverse relaxation of iron ions at 37°C.

Figure 2: ^{1}H longitudinal relaxivity profiles (circles) and transverse relaxivity at 400 MHz (stars) of Mn^{2+} ions in pineapple juice at 25°C (solid symbols) and 37°C (empty symbols). The solid and dotted lines represent the best fit profiles of the longitudinal and transverse relaxivities, respectively. The thin lines refer to the fit without inclusion of the order parameter S_{LS}^2.

with the Mn^{2+} ions, which should amount to the values indicated by the dashed line in Figure 1 (at 37°C). Since these contributions are one order of magnitude smaller than the experimental rates of pineapple juice, we are confident that some inaccuracies in these estimates do not affect the following analysis appreciably. Once subtracted from the measured relaxation rates and normalized to the Mn^{2+} concentration, we obtain the relaxivity of Mn^{2+} ions in pineapple juice, as shown in Figure 2.

The transverse relaxation rates of pineapple juice at 400 MHz and 25 and 37°C were also measured (shown as star symbols in Figure 1). Again, the rates are more than one order of magnitude larger than the expected contribution from iron ions [25] and diamagnetic terms (dotted-dashed line in Figure 1). The calculated R_2 relaxivity of Mn^{2+} ions in pineapple juice results as large as 100 and 75 $s^{-1} \cdot mM^{-1}$ at 25 and 37°C, respectively (star symbols in Figure 2).

The longitudinal and transverse relaxivity data of Mn^{2+} ions in pineapple juice were fit to the model described by equations (1)–(13). In the fit, the Mn-water proton distances r were fixed to 2.85 Å, the distance of closest approach d to 3.6 Å, and the diffusion coefficients at 25 and 37°C to 3.0×10^{-9} and 3.9×10^{-9} m^2/s, respectively. As a first step, the number of coordinated water molecules q, the reorientation correlation time τ_r, the water proton lifetime τ_M, the electronic parameters Δ_t and τ_v, and the constant of contact coupling (A^{FC}/h) were left free to be adjusted, with $S_{LS}^2 = 1$. The resulting best fit is of low quality, as shown in Figure 2 as thin lines (we checked that the quality of the fit does not improve even if the parameters indicated as fixed are left free to adjust). Therefore, a squared order parameter S_{LS}^2 was introduced to
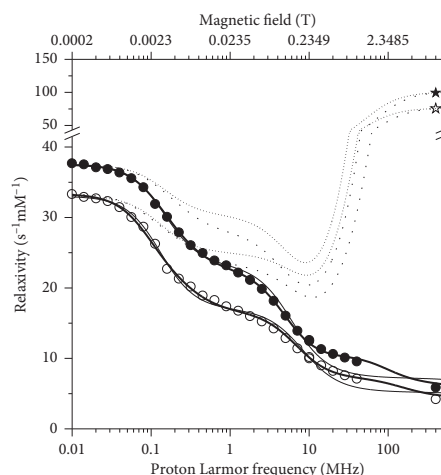
account for the presence of contributions arising from two different reorientation correlation times, namely, τ_r and τ_ι, where τ_ι is much smaller than τ_r. Using this model-free approach, it is thus possible to consider the relaxation contributions from water molecules experiencing overall and local dynamics occurring on quite different time scales. In this way, the fit was very good (thick lines in Figure 2). The best fit values of the parameters are reported in Table 1. The value of Δ_t is completely covariant with the values of τ_v and τ_M, and it can thus be fixed (in Table 1, it was fixed to the value obtained from the analysis of the profiles collected in the presence of alginate). The contributions from the dipolar interaction modulated by slow mobility and by fast mobility, from the Fermi-contact interaction as well as from outer sphere relaxation, are shown in Figure 3. The figure shows that the largest contribution to longitudinal relaxation originates from the metal-proton dipole-dipole interactions modulated by reorientation motions with correlation times of about 40–50 ps. The proton lifetime is relatively small, of the order of tens of nanoseconds. A Fermi-contact contribution is present with a contact coupling constant of 0.55 MHz. Fermi-contact relaxation is responsible of the first inflection in the longitudinal relaxation profile and is basically responsible (together with the water proton lifetime and field-dependent electron relaxation time) for the very high transverse relaxation at 400 MHz. The need for minor contributions (2%) from dynamics in the nanosecond regime, required for achieving a good fit of the data, suggests that the manganese ions interact with some macromolecules present in the juice. Consistently, the occurrence of these interactions decreases the number of water molecules coordinated to Mn^{2+} (q) from 6 to 4.

TABLE 1: Best fit parameters for pineapple juice without and with addition of alginate 5% or 15% w/w.

	Pineapple				+5% alginate		+15% alginate		
	25°C	37°C	25°C	37°C	25°C	37°C	25°C	37°C	
r (*)					2.85				Å
q	5.3 ± 0.3		4.0 ± 0.1		4.5 ± 0.3		4.3 ± 0.4		
Δ_t					0.015 ± 0.001				cm^{-1}
τ_r	42 ± 3	30 ± 2	1700 ± 300	1000 ± 200	4700 ± 1100	2900 ± 800	4700 ± 1200	2700 ± 800	ps
τ_v	11 ± 1	9 ± 1	9 ± 1	7 ± 1	16 ± 1	16 ± 1	16 ± 3	16 ± 3	ps
τ_M	22 ± 2	16 ± 2	39 ± 3	29 ± 2	200 ± 90	91 ± 60	140 ± 80	92 ± 60	ns
S^2_{LS}	—		0.021 ± 0.003		0.05 ± 0.01		0.10 ± 0.01		
τ_l	—	—	51 ± 2	36 ± 2	74 ± 8	49 ± 6	83 ± 15	54 ± 11	ps
A^{FC}/h	0.63 ± 0.02		0.55 ± 0.02		0.37 ± 0.02		0.38 ± 0.05		MHz

Outer sphere relaxation was also included with $d = 3.6$ Å and $D = 3.0 \cdot 10^{-5}$ and $3.9 \cdot 10^{-5}$ cm^2/s at 25°C and 37°C, respectively. (*) fixed.


(a)

(b)
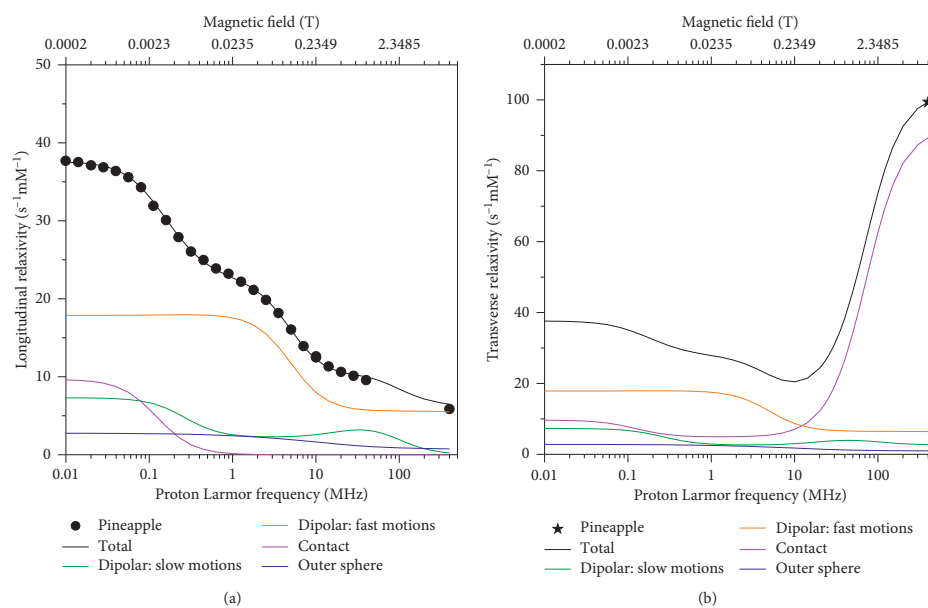
FIGURE 3: Continued.
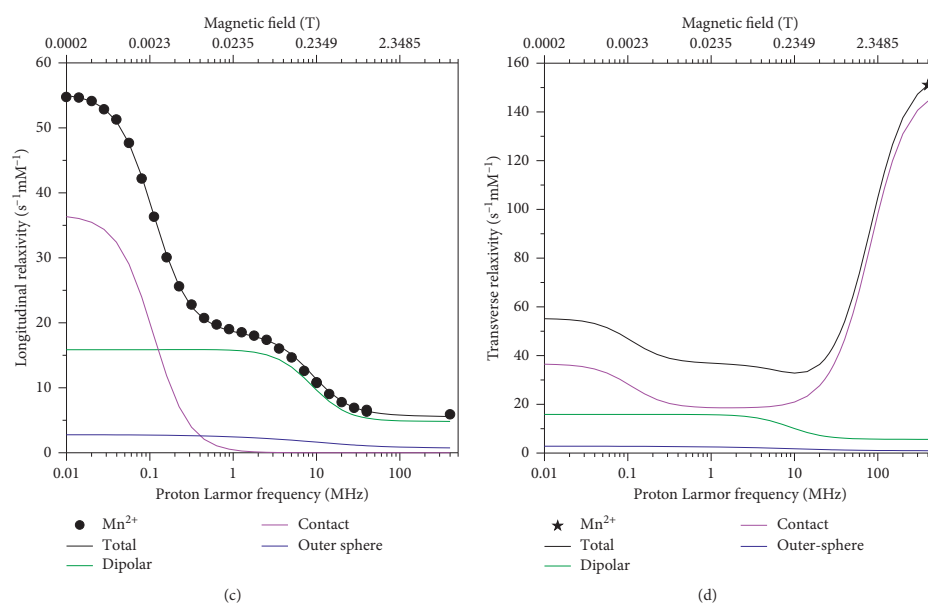
FIGURE 3: ^{1}H longitudinal relaxivity (a, c) and transverse relaxivity (b, d) at 25°C and their dipolar, Fermi-contact, and outer sphere contributions in pineapple juice (a, b) and in Mn^{2+} solution (c, d).

3.3. ^{1}H NMRD Profiles of Mn^{2+} Solution. In order to check whether the relaxivity profiles of pineapple juice is only determined by the relaxivity of the manganese ions in water solution, or whether there are effects from the other components of the juice, the relaxivity profiles of a Mn^{2+} solution at the same pH (3.6) and salt concentrations of pineapple juice were obtained (Figure 4). The low-field relaxivity in this case is larger, and the Fermi-contact (low field) dispersion is higher in Mn^{2+} solution than in pineapple juice, whereas the high-field relaxivity is smaller. This suggests that the contact coupling constant in Mn^{2+} solution is larger than in pineapple juice. The position of the dipolar (high field) dispersion is at larger frequency in Mn^{2+} solution than in pineapple juice, thus indicating a shorter reorientation correlation time for dipolar relaxation. The R_2 values of Mn^{2+} at 400 MHz are somewhat larger than those of pineapple juice. In this case, the fit obtained assuming six water molecules regularly coordinated to the manganese ion was excellent (solid lines in Figure 4). The best fit parameters are reported in Table 2 and are in good agreement with previous results obtained for Mn^{2+} aqua ions [26]. The relative contributions of Fermi-contact and dipolar inner sphere and outer sphere relaxation are shown in Figure 3. Different from pineapple juice, the complex is free to reorient with correlation times of 20–30 ps, as expected for an aqua ion. The contact coupling constant is 0.82 MHz. This value is significantly larger in Mn^{2+} solution than in pineapple juice likely because in the latter, water coordination is somewhat hampered by macromolecular interactions. Clearly, Fermi-contact relaxation provides the

major contribution to the longitudinal relaxivity at low fields, whereas dipolar relaxation provides the major contribution at high fields. However, the Fermi-contact interaction represents by far the largest source for transverse relaxation at 400 MHz. The lifetime of the coordinated water protons is similar to that of pineapple juice.

3.4. ^{1}H NMRD Profiles of Pineapple Juice in the Presence of Alginate. As a general strategy to increase the relaxation rates at high fields, the molecular dynamics of the paramagnetic complex can be slowed down by promoting transient interactions between the paramagnetic complex and macromolecules [1, 27, 28]. The relaxivity of Gd^{3+} contrast agents, for instance, has a peak at fields of about 1 T when the Gd^{3+} complex binds proteins [29–31], is coordinated to nanoparticles [32–37], or is entrapped into hydrogels [38, 39]. In this case, we aim at introducing a food stuff containing large macromolecules with which the Mn^{2+} ion can transiently interact or which may cause its confinement in a restricted environment, in such a way as to reduce its mobility. Alginate, a polysaccharide which is a commercially available natural food, was used for this purpose. Since sodium alginate increases dramatically the viscosity of the solution, the relaxometric analysis can provide crucial data to optimize the amount of polysaccharide in order to obtain a high contrast and suitable rheological properties. After a preliminary screening of sodium alginate concentrations, solutions at 5% and 15% in weight were investigated to determine the physicochemical parameters
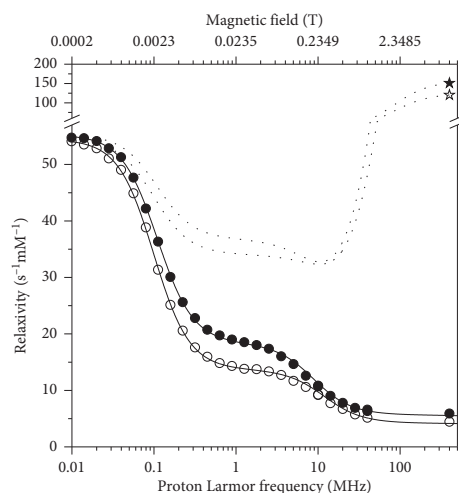
FIGURE 4: [1]H longitudinal relaxivity profiles (circles) and transverse relaxivity at 400 MHz (stars) of Mn^{2+} solutions (pH 3.6) at 25°C (solid symbols) and 37°C (empty symbols). The solid and dotted lines represent the best fit profiles of the longitudinal and transverse relaxivities, respectively.

TABLE 2: Best fit parameters for Mn^{2+} solution without and with addition of alginate 5% or 15% w/w.

	Mn^{2+} solution		+5% alginate		+15% alginate		
	25°C	37°C	25°C	37°C	25°C	37°C	
r (*)			2.85				Å
q			6				
Δ_t			0.018 ± 0.001				cm^{-1}
τ_r	28 ± 1	20 ± 1	4200 ± 1400	3100 ± 1200	3800 ± 600	2700 ± 500	ps
τ_v	5.3 ± 0.1	4.5 ± 0.1	17 ± 2	16 ± 2	18 ± 1	18 ± 1	Ps
τ_M	18 ± 1	14 ± 1	44 ± 16	29 ± 11	220 ± 100	100 ± 70	ns
S_{LS}^2	—		0.03 ± 0.01		0.06 ± 0.01		
τ_l	—	—	39 ± 1	29 ± 1	51 ± 3	36 ± 2	ps
A^{FC}/h	0.82 ± 0.01		0.48 ± 0.08		0.29 ± 0.02		MHz

Outer sphere relaxation was also included with $d = 3.6$ Å and $D = 3.0·10^{-5}$ and $3.9·10^{-5} cm^2/s$ at 25°C and 37°C, respectively. (*) fixed.

influencing the relaxation rates of these hydrogels. While solutions at 5% in weight of sodium alginate are still viscous liquids, solutions at 15% appear to be thick pastes.

The diamagnetic relaxation rates of alginate solutions at 5% and 15% in weight are shown in Figure 5(a). These solutions were prepared in sodium acetate, in order to have the same pH of pineapple juice and by addition of 4 mmol/ dm^3 (150 mg/L) concentration of Ca^{2+} ions, as present in the commercial juice, which promotes the formation of a hydrogel [40]. The large increase in the relaxation rates, which can be observed by decreasing the magnetic field, actually indicates cross-linking of alginate polymers [41–43]. Alginate in the same concentration was also added to pineapple juice, and the relaxation profiles were measured (Figure 5(a)). At all fields, the relaxation rates in this case are sizably larger than those measured for the pristine pineapple juice (Figure 1); the steep decrease in relaxation at low fields parallels the decrease seen for the alginate sample and is thus ascribed to the diamagnetic contribution, whereas the relaxivity peak observed at about 1 T originates from the restricted mobility of the paramagnetic ion and the field dependence of the electron relaxation rates.

Figure 6 shows the relaxivity data for the samples of pineapple juice with addition of alginate, obtained after subtraction of the diamagnetic relaxation rates of alginate and of the paramagnetic contribution from iron ions, and subsequent normalization to 1 mmol/dm^3 Mn^{2+} concentration. The paramagnetic contribution from iron ions is assumed similar to that considered in the absence of alginate because of the polymer chelation of the Fe(III) ions at this pH [44], with subsequent increase in the reorientation time and decrease in the number of bound water molecules. The relaxivity profiles of pristine pineapple juice are also reported in Figure 6 for an easier comparison, as well as the transverse relaxivity of all samples at 400 MHz. The data were fit using equations (1)–(13), including an order
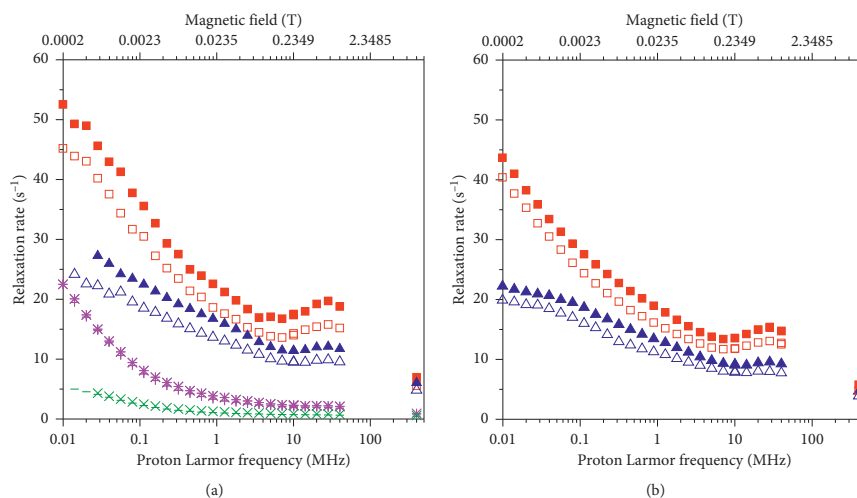
FIGURE 5: (a) Experimental ^1H R1 profiles of pineapple juice with alginate (red squares: 15%, and blue triangles: 5% w/w) at 25°C (solid symbols) and 37°C (empty symbols), and of alginate solutions (pink symbols: 15%, and green symbols: 5% w/w; ∗ and ×: 25 °C, + and -: 37 °C). (b). Experimental 1H R1 profiles of the Mn^{2+} solutions with alginate (red squares: 15%, and blue triangles: 5% w/w) at 25°C (solid symbols) and 37°C (empty symbols).
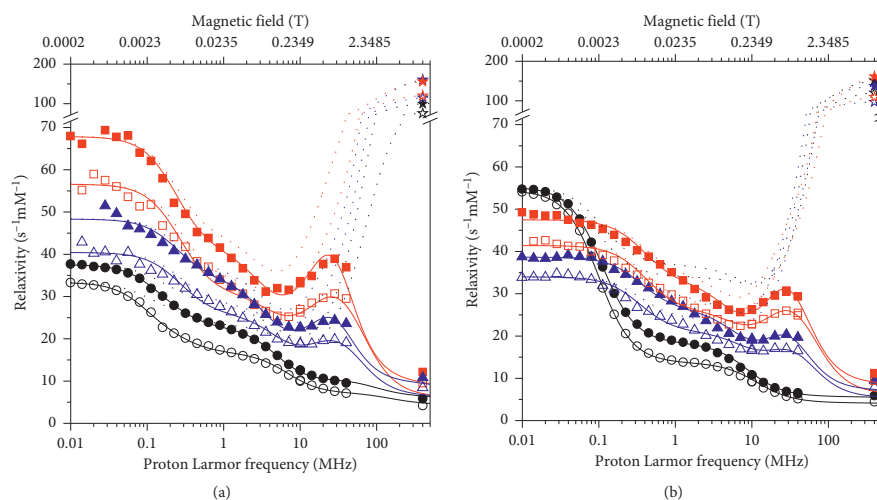
FIGURE 6: (a) ^1H longitudinal relaxivity profiles and transverse relaxivity at 400 MHz (stars) of Mn^{2+} ions in pineapple juice without (black symbols) and with alginate (5%: blue symbols; 15%: red symbols) at 25°C (solid symbols) and 37°C (empty symbols). (b) ^1H longitudinal relaxivity profiles and transverse relaxivity at 400 MHz (stars) of Mn^{2+} solutions without (black symbols) and with alginate (5%: blue symbols; 15%: red symbols) at 25°C (solid symbols) and 37°C (empty symbols). The solid and dotted lines represent the best fit profiles of the longitudinal and transverse relaxivities, respectively.

parameter, and the best fit parameters are shown in Table 1. The contributions from the dipolar interaction modulated by slow mobility and fast mobility, from the Fermi-contact interaction as well as from outer sphere relaxation, are shown in Figures 7(a) and 7(b) for the sample with 15% alginate at 25°C.

121

(a)

(b)

(c)

(d)
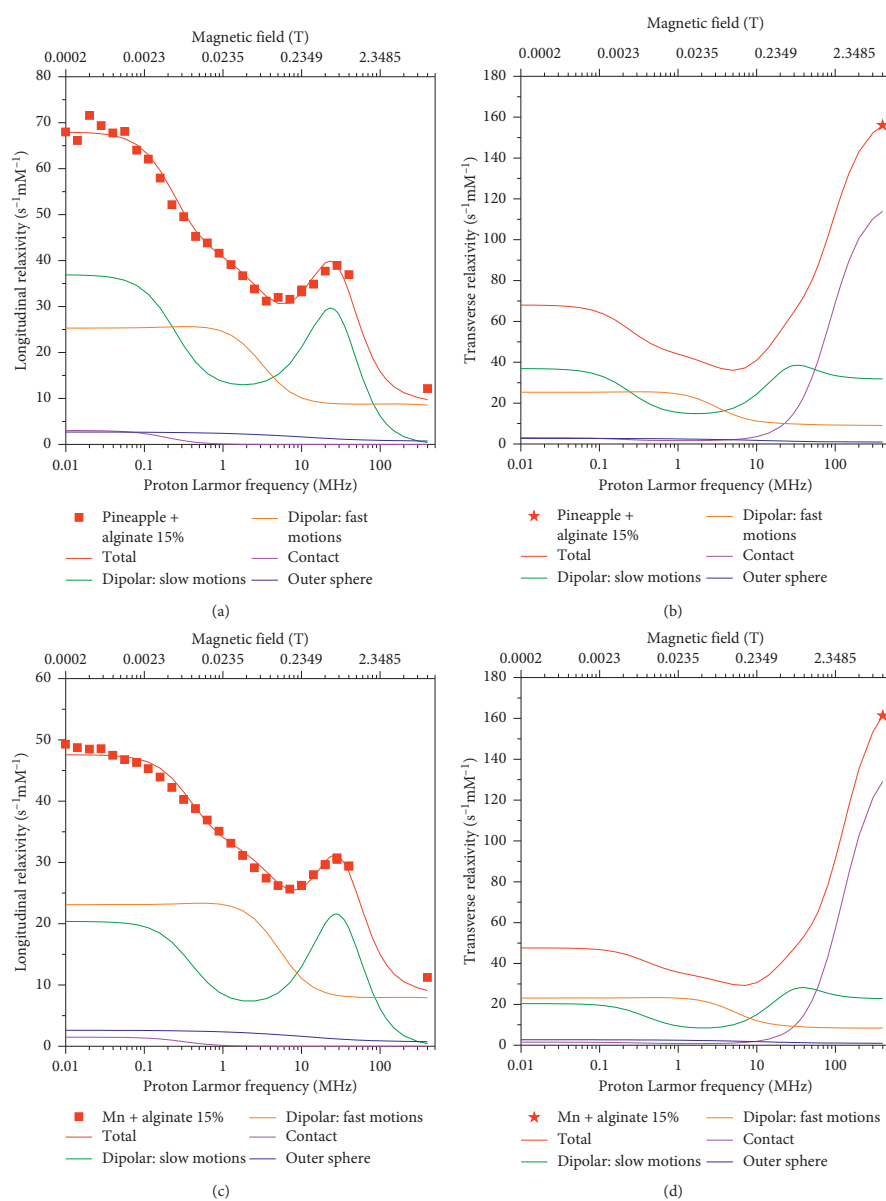
FIGURE 7: ^{1}H longitudinal relaxivity (a, c) and transverse relaxivity (b, d) at 25 °C and their dipolar, Fermi-contact, and outer-sphere contributions in the pineapple juice (a, b) and in the Mn^{2+} solution (c, d) upon addition of 15% w/w alginate.

The fit indicates a similar number of water molecules coordinated to the Mn^{2+} ions upon alginate addition (the small increase in the best fit value of q may just reflect larger outer and/or second sphere contributions arising from the higher viscosity of the system, which may decrease the microscopic diffusion constant and slower the lifetime of
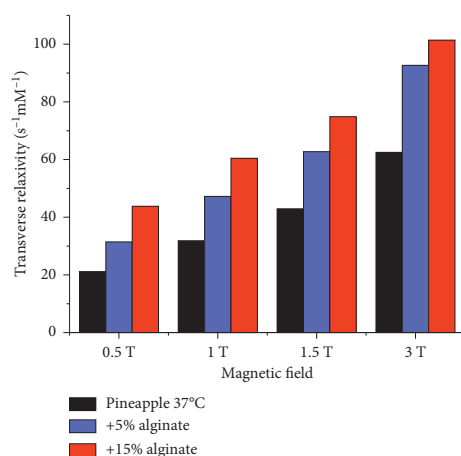
Figure 8: Transverse relaxivity of pineapple juice without and with alginate at 37°C.

Table 3: Relaxation rates (s^{-1}) at 37°C measured for pineapple juice and Mn^{2+} solutions without and with alginate.

	R_1 at 0.94 T	R_1 at 9.4 T	R_2 at 9.4 T
Pineapple juice	3.7	2.4	33.9
Pineapple juice + 5% alginate	9.6	4.8	58.4
Pineapple juice + 15% alginate	15.2	5.6	73.7
Mn^{2+} solution 0.43 mmol/dm^3, pH 3.6	2.5	2.2	52.1
Mn^{2+} solution 0.43 mmol/dm^3 + 5% alginate	7.7	3.9	49.5
Mn^{2+} solution 0.43 mmol/dm^3 + 15% alginate	12.6	4.8	68.0

second sphere water molecules). The analysis indicates a decrease in the value of the contact coupling constant in the presence of alginate and a sizable increase of the lifetime of the coordinated water molecules and of the value of S_{LS}^2.

3.5. ^{1}H NMRD Profiles of Mn2+ Solution in the Presence of Alginate. Finally, the relaxation profiles were measured for Mn^{2+} solution in the presence of alginate (Figure 5(b)). The shapes of the profiles are very similar to those observed for pineapple juice although the rates are in this case somewhat smaller. The corresponding relaxivity profiles are shown in Figure 6(b). Like in the previous cases, the data were fit using equations (1)–(13), and the best fit parameters are reported in Table 2. Figures 7(c) and 7(d) show the contributions from the dipolar interaction modulated by slow mobility and by fast mobility, from the Fermi-contact interaction, as well as from outer sphere relaxation for the sample with 15% alginate at 25°C. Also, in this case, there is a reduction in the value of the contact coupling constant with respect to the pristine Mn^{2+} solution and a large increase in the lifetime of the coordinated water molecules. As for pineapple juice, there are contributions from dipolar relaxation with reorientation times of the order of nanoseconds, which originate the relaxation peak at about 1 T.

A lower order parameter is obtained for Mn^{2+} solution than for pineapple juice (in the presence of alginate), and this causes the observed smaller relaxivity measured for the Mn^{2+} solutions, despite that the opposite trend was measured in the absence of alginate. Overall, the analysis indicates a lower restriction in the mobility of the Mn^{2+} complex caused by alginate in this solution with respect to pineapple juice.

3.6. Contribution of Hydrogel to the Negative Contrast. The profiles of the transverse relaxivity in the range 0.01–400 MHz, generated from the fit of the experimental

data, allow for a detailed evaluation of the contrast enhancement of pineapple juice in the hydrogel formulations, at the magnetic fields used in clinical MRI (Figure 8). It is interesting to observe that the hydrogel formulations exhibit sizable larger transverse relaxivities than the pristine pineapple juice, proportional to the alginate concentration. On the contrary, the transverse relaxivities of Mn^{2+} solutions are almost unaffected by the presence of alginate (Figure 6(b)).

4. Conclusions

The acquired ^{1}H NMRD profiles confirm that the relaxation rates measured for pineapple juice are mostly determined by the large relaxivity of the Mn^{2+} ions, as expected. However, the analysis of the profiles indicates that the number of water molecules coordinated to the Mn^{2+} ions is about 4, instead of 6, as in the aqua ions, the Fermi-contact coupling constant is smaller than for the Mn^{2+} aqua ion, and the tumbling time of the Mn^{2+} complex has components in the nanosecond time scale, likely due to a fraction of metal ions with mobility restricted by interactions with macromolecules present in the juice. The presence of alginate can further slower the tumbling time, and thus the relaxation rates, the effect being larger for pineapple juice than for Mn^{2+} solution. This makes the values of R_1 at 0.94 T higher for pineapple juice than for Mn^{2+} solution with the same ion concentration, both in the absence and in the presence of alginate (Table 3). At 9.4 T, the longitudinal relaxation rates are somewhat smaller than at 0.94 T, especially for the samples in the presence of alginate. However, the high transverse relaxation rates of pineapple juice are largely increased upon addition of alginate (of about a factor 2). The R_2 measured at 9.4 T for Mn^{2+} solution is somewhat larger than for pineapple juice due to the larger contact coupling constant, but in this case, the increase in the rate is minor upon addition of alginate, due to the lifetime of the water molecules coordinated to the metal ions which is limiting the increase in the transverse relaxation.

Collectively, these data provide new hints for the possible use of a hydrogel prepared from pineapple juice, as negative oral contrast agent in magnetic resonance imaging. It should be noted that the profiles of the transverse relaxivity as a function of the applied magnetic field strength show that the increased viscosity can improve significantly the negative

contrast at physiological temperature and MRI fields of 0.5–1 T (and at lower magnetic fields, see Figures 6 and 8). Conversely, at any magnetic field values, the increase of the viscosity does not enhance significantly the transverse relaxivity of solutions obtained by dissolving Mn^{2+} salts. These results suggest that the macromolecular components that are present in pineapple juice play a pivotal role in the observed relaxivity enhancement, most likely by immobilizing the Mn^{2+} ions of the solution to a larger extent.

Data Availability

The data used to support the findings of this study are available upon request to Giacomo Parigi and Marco Fragai.

Conflicts of Interest

The authors declare that they have no conflicts of interest.

Acknowledgments

References

[1] J. Wahsner, E. M. Gale, A. Rodríguez-Rodríguez, and P. Caravan, "Chemistry of MRI contrast agents: current challenges and new frontiers," *Chemical Reviews*, vol. 119, no. 2, pp. 957–1057, 2019.

[2] K. E. Jacobs, D. Behera, J. Rosenberg et al., "Oral manganese as an MRI contrast agent for the detection of nociceptive activity," *NMR in Biomedicine*, vol. 25, no. 4, pp. 563–569, 2012.

[3] A. Giovagnoni, A. Fabbri, and F. Maccioni, "Oral contrast agents in MRI of the gastrointestinal tract," *Abdominal Imaging*, vol. 27, no. 4, pp. 367–375, 2002.

[4] Y. C. Hung, V. M. Sava, C. L. Juang, T. C. Yeh, W. C. Shen, and G. S. Huang, "Gastrointestinal enhancement of MRI with melanin derived from tea leaves (Thea sinensis Linn.)," *Journal of Ethnopharmacology*, vol. 79, no. 1, pp. 75–79, 2002.

[5] A. H. Karantanas, N. Papanikolaou, J. Kalef-Ezra, A. Challa, and N. Gourtsoyiannis, "Blueberry juice used per os in upper abdominal MR imaging: composition and initial clinical data," *European Radiology*, vol. 10, no. 6, pp. 909–913, 2000.

[6] R. D. Riordan, M. Khonsari, J. Jeffries, G. F. Maskell, and P. G. Cook, "Pineapple juice as a negative oral contrast agent in magnetic resonance cholangiopancreatography: a preliminary evaluation," *The British Journal of Radiology*, vol. 77, no. 924, pp. 991–999, 2004.

[7] K. Hiraishi, I. Narabayashi, O. Fujita et al., "Blueberry juice: preliminary evaluation as an oral contrast agent in gastrointestinal MR imaging," *Radiology*, vol. 194, no. 1, pp. 119–123, 1995.

[8] Y. Mino, K. Yamada, T. Takeda, and O. Nagasawa, "Metal-containing components in medicinal plants. III. Manganese-containing components in Theae folium as oral magnetic resonance imaging contrast materials," *Chemical and Pharmaceutical Bulletin*, vol. 44, no. 12, pp. 2305–2308, 1996.

[9] M. Zarrini, F. Seilanian Toosi, B. Davachi, and S. Nekooei, "Natural oral contrast agents for gastrointestinal magnetic resonance imaging," *Reviews in Clinical Medicine*, vol. 2, pp. 200–204, 2015.

[10] M. G. Espinosa, M. Sosa, L. M. De León-Rodríguez et al., "Blackberry (Rubus spp.): a pH-dependent oral contrast medium for gastrointestinal tract images by magnetic resonance imaging," *Magnetic Resonance Imaging*, vol. 24, no. 2, pp. 195–200, 2006.

[11] T. A. Sanchez, J. Elias, L. A. Colnago et al., "Clinical feasibility of Açai (Euterpe olerácea) pulp as an oral contrast agent for magnetic resonance cholangiopancreatography," *Journal of Computer Assisted Tomography*, vol. 33, no. 5, pp. 666–671, 2009.

[12] T. Córdova-Fraga, D. B. de Araujo, T. A. Sanchez et al., "Euterpe olerácea (Açaí) as an alternative oral contrast agent in MRI of the gastrointestinal system: preliminary results," *Magnetic Resonance Imaging*, vol. 22, no. 3, pp. 389–393, 2004.

[13] O. J. Arthurs, M. J. Graves, A. D. Edwards, I. Joubert, P. A. Set, and D. J. Lomas, "Interactive neonatal gastrointestinal magnetic resonance imaging using fruit juice as an oral contrast media," *BMC Medical Imaging*, vol. 14, p. 33, 2014.

[14] J. K. Beattie and T. N. Quoc, "Manganese in pineapple juices," *Food Chemistry*, vol. 68, no. 1, pp. 37–39, 2000.

[15] R. Faletti, M. Gatti, A. Di Chio et al., "Concentrated pineapple juice for visualisation of the oesophagus during magnetic resonance angiography before atrial fibrillation radiofrequency catheter ablation," *European Radiology Experimental*, vol. 2, p. 39, 2018.

[16] G. Ferrante and S. Sykora, "Technical aspects of fast field cycling," *Advances in Inorganic Chemistry*, vol. 57, pp. 405–470, 2005.

[17] I. Bertini, C. Luchinat, G. Parigi, and E. Ravera, "NMR of paramagnetic molecules," *Applications to Metallobiomolecules and Models*, vol. 2, 2017.

[18] I. Bertini, C. Luchinat, and G. Parigi, "^{1}H NMRD profiles of paramagnetic complexes and metalloproteins," *Advances in Inorganic Chemistry*, vol. 57, pp. 105–172, 2005.

[19] E. Ravera, P. G. Takis, M. Fragai, G. Parigi, and C. Luchinat, "NMR spectroscopy and metal ions in life sciences," *European Journal of Inorganic Chemistry*, vol. 2018, no. 44, pp. 4752–4770, 2018.

[20] S. Aime, E. Gianolio, and A. Viale, "Chapter 7. Relaxometry and contrast agents," in *New Developments in NMR*, C. Luchinat, G. Parigi, and E. Ravera, Eds., Royal Society of Chemistry, Cambridge, UK, pp. 189–218, 2018.

[21] N. Bloembergen and L. O. Morgan, "Proton relaxation times in paramagnetic solutions. Effects of electron spin relaxation," *The Journal of Chemical Physics*, vol. 34, no. 3, pp. 842–850, 1961.

[22] I. Solomon, "Relaxation processes in a system of two spins," *Physical Review*, vol. 99, no. 2, pp. 559–565, 1955.

[23] G. Lipari and A. Szabo, "Model-free approach to the interpretation of nuclear magnetic resonance relaxation in macromolecules. 1. Theory and range of validity," *Journal of the American Chemical Society*, vol. 104, no. 17, pp. 4546–4559, 1982.

[24] J. H. Freed, "Dynamic effects of pair correlation functions on spin relaxation by translational diffusion in liquids. II. Finite

jumps and independent T1 processes," *The Journal of Chemical Physics*, vol. 68, no. 9, pp. 4034–4037, 1978.

[25] I. Bertini, F. Capozzi, C. Luchinat, and Z. Xia, "Nuclear and electron relaxation of hexaaquairon(3+)," *The Journal of Physical Chemistry*, vol. 97, no. 6, pp. 1134–1137, 1993.

[26] I. Bertini, F. Briganti, Z. C. Xia, and C. Luchinat, "Nuclear magnetic relaxation dispersion studies of hexaaquo Mn(II) ions in water-glycerol mixtures," *Journal of Magnetic Resonance, Series A*, vol. 101, no. 2, pp. 198–201, 1993.

[27] M. Botta and L. Tei, "Relaxivity enhancement in macromolecular and nanosized GdIII-based MRI contrast agents," *European Journal of Inorganic Chemistry*, vol. 2012, pp. 1945–1960, 2012.

[28] E. Terreno, D. D. Castelli, A. Viale, and S. Aime, "Challenges for molecular magnetic resonance imaging," *Chemical Reviews*, vol. 110, no. 5, pp. 3019–3042, 2010.

[29] P. Caravan, G. Parigi, J. M. Chasse et al., "Albumin binding, relaxivity, and water exchange kinetics of the diastereoisomers of MS-325, a gadolinium(III)-based magnetic resonance angiography contrast agent," *Inorganic Chemistry*, vol. 46, no. 16, pp. 6632–6639, 2007.

[30] P. L. Anelli, I. Bertini, M. Fragai, L. Lattuada, C. Luchinat, and G. Parigi, "Sulfonamide-functionalized gadolinium DTPA complexes as possible contrast agents for MRI: a relaxometric investigation," *European Journal of Inorganic Chemistry*, vol. 2000, no. 4, pp. 625–630, 2000.

[31] E. Gianolio, G. B. Giovenzana, D. Longo, I. Longo, I. Menegotto, and S. Aime, "Relaxometric and modelling studies of the binding of a lipophilic Gd-aazta complex to fatted and defatted human serum albumin," *Chemistry—A European Journal*, vol. 13, no. 20, pp. 5785–5797, 2007.

[32] F. Alhaique, I. Bertini, M. Fragai, M. Carafa, C. Luchinat, and G. Parigi, "Solvent ^{1}H NMRD study of biotinylated paramagnetic liposomes containing Gd-bis-SDA-DTPA or Gd-DMPE-DTPA," *Inorganica Chimica Acta*, vol. 331, no. 1, pp. 151–157, 2002.

[33] A. T. Preslar, G. Parigi, M. T. McClendon et al., "Peptide nanofibers for reporting on biomaterial localization in vivo," *ACS Nano*, vol. 8, pp. 7325–7332, 2014.

[34] N. Rammohan, K. W. MacRenaris, L. K. Moore et al., "Nanodiamond-Gadolinium(III) aggregates for tracking cancer growth in vivo at high field," *Nano Letters*, vol. 16, pp. 7551–7564, 2016.

[35] M. W. Rotz, K. S. B. Culver, G. Parigi et al., "High relaxivity Gd(III)-DNA gold nanostars: investigation of shape effects on proton relaxation," *ACS Nano*, vol. 9, pp. 3385–3396, 2015.

[36] D. Delli Castelli, E. Gianolio, S. Geninatti Crich, E. Terreno, and S. Aime, "Metal containing nanosized systems for MR-molecular imaging applications," *Coordination Chemistry Reviews*, vol. 252, pp. 2424–2443, 2008.

[37] F. Carniato, M. Muñoz-Úbeda, L. Tei, and M. Botta, "Selective functionalization of mesoporous silica nanoparticles with ibuprofen and Gd(III) chelates: a new probe for potential theranostic applications," *Dalton Transactions*, vol. 44, no. 41, pp. 17927–17931, 2015.

[38] T. Courant, V. G. Roullin, C. Cadiou et al., "Hydrogels incorporating GdDOTA: towards highly efficient dual T1/T2 MRI contrast agents," *Angewandte Chemie International Edition*, vol. 51, no. 36, pp. 9119–9122, 2012.

[39] M. Callewaert, V. G. Roullin, C. Cadiou et al., "Tuning the composition of biocompatible Gd nanohydrogels to achieve hypersensitive dual T1/T2 MRI contrast agents," *Journal of Materials Chemistry B*, vol. 2, no. 37, pp. 6397–6405, 2014.

[40] K. Y. Lee and D. J. Mooney, "Alginate: properties and biomedical applications," *Progress in Polymer Science*, vol. 37, no. 1, pp. 106–126, 2012.

[41] M. Fragai, E. Ravera, F. Tedoldi, C. Luchinat, and G. Parigi, "Relaxivity of Gd-based MRI contrast agents in crosslinked hyaluronic acid as a model for tissues," *ChemPhysChem*, vol. 20, no. 17, pp. 2204–2209, 2019.

[42] S. H. Koenig and R. D. Brown, "Field-cycling relaxometry of protein solutions and tissue: implications for MRI," *Progress in Nuclear Magnetic Resonance Spectroscopy*, vol. 22, no. 6, pp. 487–567, 1990.

[43] E. Ravera, G. Parigi, A. Mainz, T. L. Religa, B. Reif, and C. Luchinat, "Experimental determination of microsecond reorientation correlation times in protein solutions," *The Journal of Physical Chemistry B*, vol. 117, no. 13, pp. 3548–3553, 2013.

[44] R. D. Horniblow, M. Dowle, T. H. Iqbal et al., "Alginate-iron speciation and its effect on in vitro cellular iron metabolism," *PLoS One*, vol. 10, Article ID e0138240, 2015.

3.5 Not only manganese, but fruit component effects dictate the efficiency of fruit juice as oral MRI contrast agent (NMR in Biomedicine, accepted in data 07/09/21 DOI: 10.1002/nbm.4623)

Giulia Licciardi, **Domenico Rizzo**, Enrico Ravera, Marco Fragai*, Giacomo Parigi*, Claudio Luchinat

Magnetic Resonance Center (CERM), University of Florence, via Sacconi 6, Sesto Fiorentino, 50019 Italy; Department of Chemistry "Ugo Schiff", University of Florence, via della Lastruccia 3, Sesto Fiorentino, 50019 Italy; and Consorzio Interuniversitario Risonanze Magnetiche Metallo Proteine (CIRMMP), via Sacconi 6, Sesto Fiorentino, 50019 Italy.

E-mail: fragai@cerm.unifi.it, parigi@cerm.unifi.it

Abstract

Several fruit juices are used as oral contrast agents to improve the quality of images in magnetic resonance cholangiopancreatography. They are often preferred to conventional synthetic contrast agents because of very low cost, their natural origin, intrinsic safety and comparable image qualities. Pineapple and blueberry juices are the most employed in clinical practice due to their higher content of manganese(II) ions. The interest of pharmaceutical companies for these products is testified by the appearance in the market of fruit-juice derivatives with improved contrast efficacy. We here investigate the origin of the contrast of blueberry juice, analyze the parameters that can effect it, and elucidate the differences with pineapple juice and manganese(II) solutions. It appears that, although manganese(II) is the paramagnetic ion responsible for the contrast, it is the interaction of manganese(II) with other juice components that modulates the efficiency of the juice as magnetic resonance contrast agent. On these grounds, we can conclude that blueberry juice concentrated to the same manganese concentration of pineapple juice would prove a more efficient contrast agent than pineapple juice.

Keywords: manganese in fruit juice, nuclear magnetic relaxation dispersion (NMRD), relaxometry, paramagnetic molecules

Abbreviations:

NMRD   Nuclear Magnetic Relaxation Dispersion

ICP-AES   Inductively Coupled Plasma-Atomic Emission Spectroscopy

Introduction

Oral contrast agents are used in magnetic resonance cholangiopancreatography because they can greatly improve the visualization of biliary tree and pancreatic ducts, the images of which are frequently degraded by the high signal due to the fluid collecting in stomach and duodenum[125]. Ideal oral contrast agents must increase the contrast homogeneously through the gastrointestinal tract, must be non-toxic and easily digestible, palatable, not stimulate peristalsis, with no side effects, and with a low cost[126]. Fruit juices that are rich in manganese ions fulfill most of the above requirements, and therefore they are conveniently used in magnetic resonance cholangiopancreatography[127–131]. Similarly to gadolinium(III), whose complexes with multidentate ligands are used as intravenous MRI contrast agents, manganese(II) is a paramagnetic ion which can increase the longitudinal relaxation rate (R_1) of the neighboring water protons, thus increasing their signal intensity in T1-weighted MRI images[127,132–134]. This causes a higher contrast between tissues where the paramagnetic ions are absorbed and those where they are not present. Manganese(II) is also a T2-agent because, similarly to iron oxides, can increase the transverse relaxation rate (R_2) of the neighboring water protons, thus decreasing their signal intensity in T2-weighted MRI scans. Intravenous administration of contrast agents is a routine method in neurologic and musculoskeletal T1-weighted MRI images; oral contrast agents are mostly used for gastrointestinal and hepatobiliary T2-weighted MRI images[131]. Since manganese(II) ions can largely increase both R_1 and R_2, manganese oral contrast agents can be used either as T2-agent to suppress the signal from bowel fluid, or as T1-agent to better delineate the gut[135].

The most promising and clinically employed juices are pineapple and blueberry juices, due to their relatively high content of manganese(II) ions[136]. These fruit juices have been shown effective as oral contrast agents in magnetic resonance images. More

recently, concentrated juices added with hydrogels[137] and semiliquid preparations of concentrates from pineapple, organic agave syrup, blackcurrant, guar gum (thickening agent), and defoamers[138,139] have been proposed to further enhance the contrast.

A field-cycling relaxometric analysis of pineapple juice was recently performed to characterize its relaxation properties in detail, without and with the addition of hydrogels[140]. The field-cycling relaxometric characterization is based on the analysis of the magnetic field dependence of water proton relaxation rates, called Nuclear Magnetic Relaxation Dispersion (NMRD) profile[141,142]. Water ^{1}H longitudinal relaxation rates are measured with a fast-field cycling relaxometer, ranging from ca. 0.0002 T to 1 T[143]. Longitudinal and transverse relaxation rates can then be measured at higher magnetic fields using high-resolution NMR spectrometers. The decrease in the relaxation rates with increasing magnetic fields, called dispersion, informs on the timescales of the dynamic processes occurring in the system and causing nuclear relaxation[142,144–146], whereas the magnitude of the rates can provide information on structural parameters, such as the number and distance of water molecules coordinated to the paramagnetic metal ions, and on the unpaired electron spin density delocalized onto the water protons[141]. The analysis of the NMRD profiles of pineapple juice permitted to evaluate the contributions to relaxation arising from the modulation of different types of metal-proton interactions, and to analyze the effects of the addition of alginate, a natural food able to slow down the dynamics of the paramagnetic ions present in the juice and thus to increase the relaxation rates.

In this contribution, we analyze the NMRD profiles of blueberry juice, the second fruit juice mostly employed in oral MRI, and compare its relaxation properties with those of the pineapple juice and of a solution containing $[Mn(H_2O)_6]^{2+}$. A commercially available blueberry nectar was used, in order to investigate the relaxation properties of a readily

obtainable product, which can be repeatable and immediately available for clinical administration.

Materials and methods

Sample preparation

The analyzed juice was Viviverde Coop organic blueberry nectar (fruit 40% minimum), with ingredients: water, blueberry puree (40%), brown sugar, citric acid. The centrifuged blueberry juice was prepared by collecting the supernatant after centrifugation of the blueberry nectar at 20000 rpm at 4 °C for 15 minutes.

^{1}H NMRD measurements

Water ^{1}H NMRD were acquired with a Stelar Spinmaster FFC2000-1T relaxometer by measuring the water proton relaxation rates as a function of the applied magnetic field (0.01–40 MHz proton Larmor frequency). The relaxation measurements, obtained from the fit of the magnetization decay/recovery curves against a monoexponential function, were affected by an error of about ±1%.

High field NMR measurements

R_1 and R_2 at high field were measured on a Bruker Avance III spectrometer operating at 400 MHz ^{1}H Larmor frequency (9.4 T), using a 5 mm, BBO probehead. To mitigate the effect of radiation damping, the samples were placed into a capillary tube, coaxial to the 5 mm NMR tube filled with D_2O.

Results and Discussion

The ^{1}H NMRD profiles of the blueberry juice were collected at 25 and 37 °C. The profiles, reported in Figure 1 as red symbols, show two dispersions, as typical of

solutions containing manganese(II) aqua ions[147]. Figure 1 also shows the relaxation rates measured for pineapple juice (black symbols), which was determined to contain 0.45 mmol/dm^3 of manganese[140]. The shape of the profiles for the two fruit juice are similar, as a result of the leading contribution from this paramagnetic ion. The lower relaxation rates measured for the blueberry juice are in agreement with a lower manganese concentration expected in this juice[135], where water was added to the blueberry puree, with respect to that of the pineapple juice.

The amounts of paramagnetic metals present in the juice were evaluated through ICP-AES. The concentration of manganese in the blueberry juice was measured equal to 0.116 mmol/dm^3. The relaxation efficiency of a paramagnetic metal is expressed by its longitudinal and transverse relaxivities, r_1 and r_2, defined as the longitudinal and transverse relaxation enhancements due to the presence of 1 mmol/dm^3 of paramagnetic metal ions in the investigated system. Therefore, since manganese concentration in the blueberry juice is four times smaller than that in the pineapple juice, whereas the relaxation rates at low fields are only about 2/3 smaller, the relaxivities of manganese in the blueberry juice are expected significantly larger than in pineapple juice.

In order to evaluate the contribution to the relaxation rates from the manganese(II) ions, the diamagnetic relaxation rates as well as the contributions from other paramagnetic ions present in the blueberry juice should be estimated. The appearance of the juice was not that of a clear solution, but rather a fine suspension, so that the presence of some aggregated material is expected. This may largely affect the diamagnetic contribution to the observed relaxation rates, especially at low fields. The juice was thus centrifuged and the NMRD profiles of the centrifuged juice were acquired (shown in Figure 1 as blue symbols). Water ^{1}H longitudinal and transverse relaxation rates were also measured at 400 MHz. The concentrations of manganese

in the centrifuged blueberry juice was measured equal to 0.109 mmol/dm^3 (very close to that of the intact juice, 0.116 mmol/dm^3). Consistently, the rates measured for the centrifuged juice are only slightly smaller than those measured for the intact juice at all frequencies larger than 0.1 MHz. However, at lower frequencies the disagreement becomes relevant. This expected disagreement increases with decreasing the magnetic field, and is thus ascribable to the increasing diamagnetic relaxation rates, due to the presence of aggregated material, which yields a typical power-law dependence.
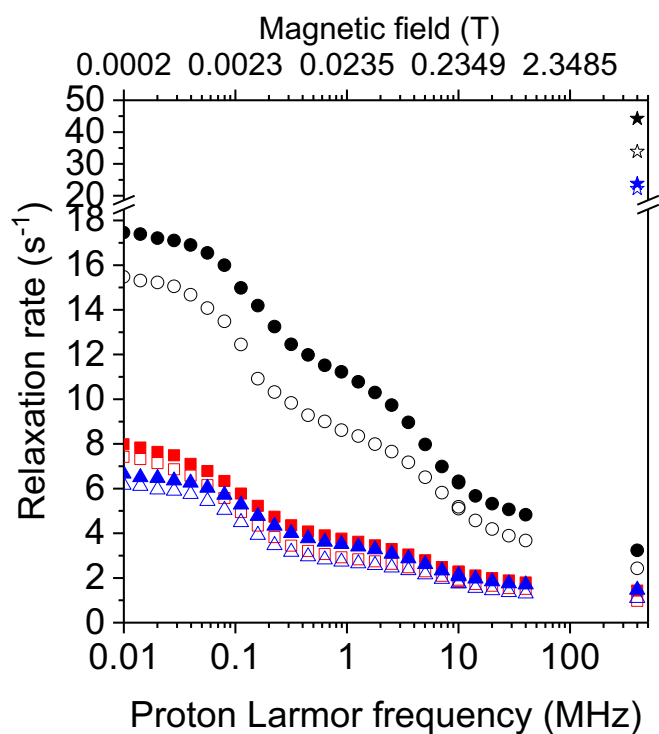

Figure 1. Experimental ^{1}H R_1 profiles of intact blueberry juice (red squares) and of centrifuged blueberry juice (blue triangles) at 25 (solid symbols) and 37 (empty symbols) °C. The profiles previously collected for the pineapple juice are also reported[140]. ^{1}H R_2 at 400 MHz in the centrifuged blueberry juice (blue stars) and pineapple juice (black stars) are also shown.

The concentrations of iron in both the intact and centrifuged blueberry juices were 0.040 mmol/dm^3. The concentrations of copper, nickel and cobalt were below 0.002 mmol/dm^3. The concentration of manganese is thus sizably higher than that of the other paramagnetic metals, so that this metal ion is largely determining the relaxation profile of the juice. The concentration of iron is however not negligible with respect to that of manganese, and thus also this metal ion may contribute significantly to the observed relaxation rates. The contribution from iron ions largely depends on the oxidation state of this metal and on the pH. In fact, the relaxivity of high spin iron(III) is expected to be large at very low pH (close to 0), and to decrease markedly above pH 3 as a result of the formation and precipitation of a variety of hydroxides[148]. On the other hand, the relaxivity of iron(II) is very low even at very low pH[141]. The pH of the investigated blueberry juice was measured to be 3.2. It is not thus easy to predict the contributions to relaxation from iron ions at this pH, and experimental information is needed.

In order to separate the contribution of manganese(II) species to the paramagnetic relaxivity from those of iron species, the contribution from iron ions was estimated using two different approaches. In the first approach, $Fe(NO_3)_3$ was dissolved at a concentration of 0.040 mmol/dm^3 in a citrate buffer solution (pH 3.2) containing 0.1 mmol/dm^3 oxalate. Citrate buffer was used because the investigated juice contains citric acid (see materials and methods), and oxalate was added because the juice was estimated to contain it in the used concentration[149]. Basically identical profiles were anyway obtained also in the absence of oxalate (Figure S1). The relaxation rates have very little dependence on the magnetic field, ranging from 0.50 to 0.43 s^{-1} on passing from low fields to 1 T, at 25 °C. The water proton relaxivity due to manganese(II) ions in the centrifuged blueberry juice was then calculated from the differences between the relaxation rates of the juice and those of the $Fe(NO_3)_3$ solution, normalized to 1

mmol/dm^3 manganese concentration (Figure 2). In the second approach, Fe(NO$_3$)$_3$ was added in known concentrations (0.020, 0.040 and 0.120 mmol/dm^3, corresponding to 50%, 100% and 300% of the iron amount concentration originally present in the juice) to the centrifuged blueberry juice, so that the relaxation rates in the absence of iron could be extrapolated (see Figure S2B). Both approaches provided basically the same relaxivity profiles (see Figure S2B) for manganese in the centrifuged blueberry juice.

Figure 2 shows the longitudinal and transverse relaxivity data for manganese in the centrifuged blueberry juice and in the pineapple juice, as well as the relaxivity data of the manganese(II) aqua ion at pH 3.6. As expected, the relaxivity of the blueberry juice is much higher than that of the pineapple juice. Interestingly, at intermediate fields (around 1 MHz) the relaxivity is smallest for the manganese aqua ion, and increases on passing to the pineapple and then to the blueberry juice. This suggests that the reorientation correlation times should increase on passing from the aqua ion to the juices, and thus that the manganese ions partially interact with other molecules in the pineapple juice and possibly even more in the blueberry juice; a larger relaxivity in blueberry than in pineapple juice may also be due to a higher number of water molecules coordinated to the manganese(II) ion and/or to a slightly higher fraction of manganese(II) bound to macromolecules.
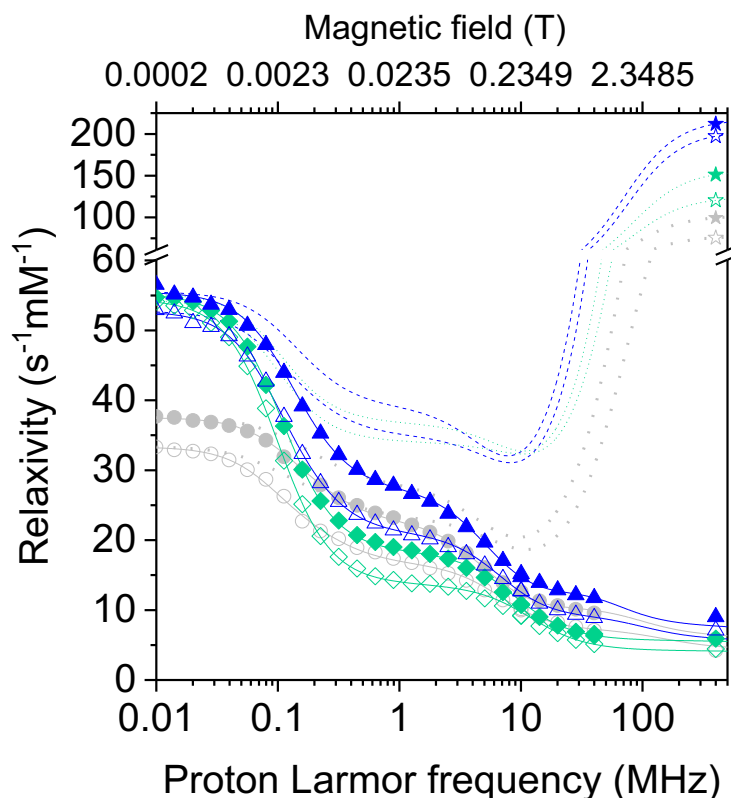
Figure 2. ^1H longitudinal relaxivity profiles (blue triangles) and transverse relaxivity at 400 MHz (blue stars) of Mn^{2+} ions in centrifuged blueberry juice at 25 (solid symbols) and 37 (empty symbols) °C. The same data for pineapple juice (grey symbols) and Mn^{2+} aqua ions (green symbols) are also shown. The solid and dotted lines represent the best fit profiles of the longitudinal and transverse relaxivities, respectively.

The low field relaxivity is largely determined by the Fermi-contact relaxation. The low field relaxivity in the blueberry juice, similar to that of the manganese aqua ion, indicates a greater fraction of manganese aqua ions, or a larger Fermi-contact coupling constant, than that in pineapple juice (the difference in relaxivity before and after the first dispersion being however significantly smaller in the blueberry juice than in the manganese aqua ions). Together with a higher (low field) Fermi-contact longitudinal relaxivity, also the transverse relaxivity at high field is consistently higher in the blueberry juice than in the pineapple juice.

The relaxivity profiles were fitted using the Solomon-Bloembergen-Morgan model[150–153] (see Supporting Information) and the best fit parameters are reported in Table 1 together with those previously obtained for the pineapple juice and the manganese aqua ion[140]. The best fit profiles are shown in Figure 2, and the different contributions to the relaxivity (inner-sphere dipole-dipole relaxation modulated by slow mobility and by fast mobility, Fermi-contact relaxation and outer-sphere relaxation) in Figure 3. Clearly, Fermi-contact relaxation provides a very large contribution to the longitudinal relaxivity at low fields, whereas at high fields the longitudinal relaxivity is determined by dipole-dipole interactions. However, the Fermi-contact interaction represents by far the largest source for transverse relaxation at 400 MHz.
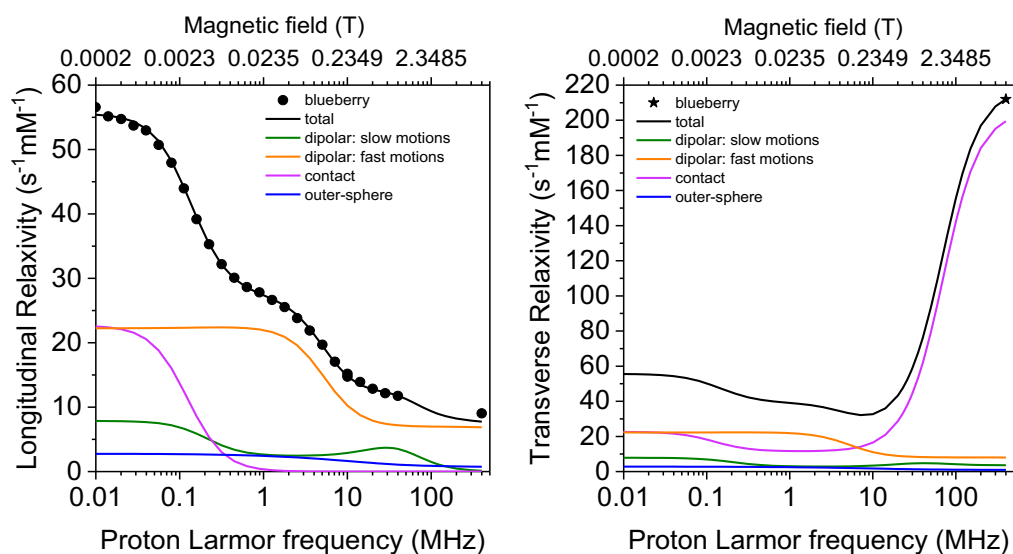
Figure 3. [1]H longitudinal relaxivity (left panel) and transverse relaxivity (right panel) of Mn^{2+} ions at 25 °C and their dipolar, Fermi-contact and outer-sphere contributions in the centrifuged blueberry juice.

The best fit parameters indicate that, as expected from the inspection of the profiles, the reorientation time increases on passing from the aqua ion to the juices (from 28 ps to ca. 50 ps, at 25 °C), with a minor component present only in the juices (with weight

136

1.4% in the blueberry juice) experiencing a reorientation times of few nanoseconds. This points to the presence of some large manganese complexes in the juices, with molecular weight of at least 5000.[154] The best fit value of hydration water molecules can result from the averaging between those in aqua ions and in other complexes. This value in blueberry juice is higher than that in pineapple juice, possibly due to a lower concentration of polydentate ligands that naturally occur in the juice[155].

The higher r_1 relaxivity and, most importantly, the higher r_2 relaxivity, of blueberry juice than of the pineapple juice suggests a higher efficiency of the former, if concentrated in such a way that manganese ions have the same concentration than in the pineapple juice. This assumes that by concentrating the blueberry juice there are no significant changes in the parameters on which its relaxation properties depend (aggregation, lifetimes of water molecules coordinated to manganese(II), tumbling times, metal ion coordination environment). To verify this higher efficiency of the concentrated blueberry juice, 10.0 ml of the juice were freeze-dried and then redissolved in 2.50 ml of H_2O in order to achieve a manganese(II) concentration of 0.45 mmol/dm^3, i.e. the same concentration of the pineapple juice. The acquired NMRD profiles are shown in Figure 4 as pink triangles, whereas the profiles calculated from the original blueberry juice rescaled to account for the increased metal ions concentrations are shown as red squares. Interestingly, there is a very good agreement at the intermediate magnetic fields, whereas the longitudinal relaxation rates are smaller than expected at low magnetic fields and higher at high magnetic fields. These effects were observed also for pineapple juice upon addition of alginate, and are ascribed to the larger viscosity of the solution resulting from juice concentration and to transient interactions of manganese(II) ions, with possible confinement in a restricted environment, in such a way as to reduce their mobility [140]. This is confirmed by the appearance of a small relaxivity peak at about 25 MHz. The increase in the tumbling time is paralleled by a

reduction of Fermi-contact relaxation (due to a smaller fraction of manganese aqua ions, a smaller electron relaxation time at low fields and/or a smaller contact coupling constant), which is also causing a decrease in the observed transverse relaxation rate at 400 MHz with respect to the prediction from the intact blueberry juice data. Nevertheless, both the longitudinal and transverse relaxation rates of the concentrated blueberry juice are sizably larger than those of the pineapple juice, despite the same Mn^{2+} concentration.
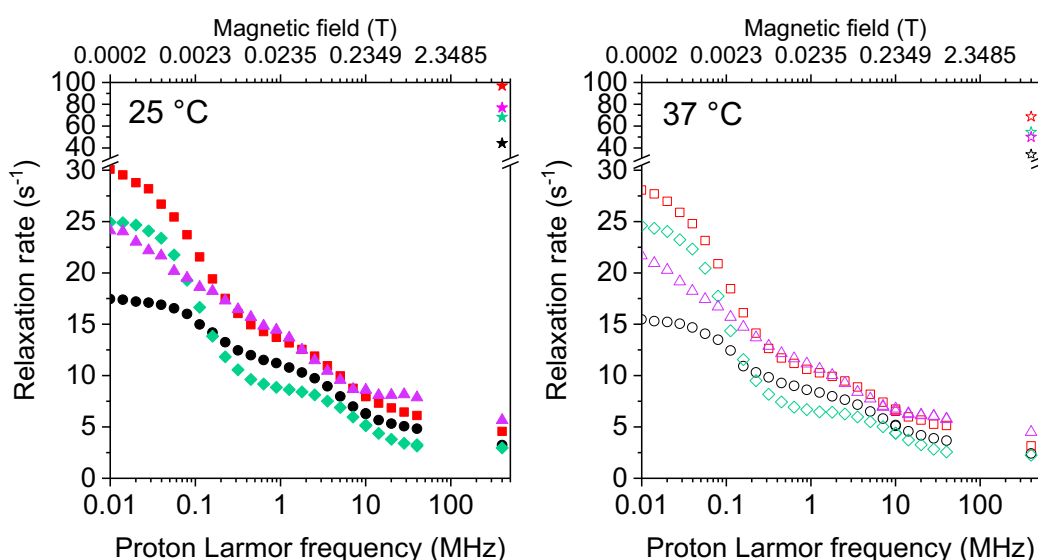
Figure 4. Longitudinal relaxation rates (triangles and circles) and transverse relaxation rates at 400 MHz (stars) of the blueberry juice concentrated 4.1 times (pink symbols) and of the pineapple juice (black symbols). The relaxation rates of these samples, containing Mn^{2+} with concentration 0.45 mmol/dm^3, are also compared to those of Mn^{2+} aqua ions (green symbols) and those obtained with rescaling the data collected for intact blueberry juice (red symbols) at the same Mn^{2+} concentration. Solid symbols indicate data at 25 °C (left panel), empty symbols at 37 °C (right panel).

Table 1. Best fit parameters for the centrifuged blueberry juice and for the pineapple juice and the Mn^{2+} solution. The corresponding best fit profiles are shown in Figures 2 and 3.

	Blueberry juice		Pineapple juice		Mn^{2+} aqua ion		
	25 °C	37 °C	25 °C	37 °C	25 °C	37 °C	
r (*)	2.85						Å
q	5.2 ± 0.2		4.0 ± 0.1		6 (*)		
Δ_t (*)	0.015				0.018		cm^{-1}
w	0.014 ± 0.003		0.021 ± 0.003		1		
τ_r	2800 ± 900	1600 ± 600	1700 ± 300	1000 ± 200	28 ± 1	20 ± 1	ps
τ_v	9 ± 1	8 ± 1	9 ± 1	7 ± 1	5.3 ± 0.1	4.5 ± 0.1	ps
τ_M	38 ± 2	36 ± 2	39 ± 3	29 ± 2	18 ± 1	14 ± 1	ns
τ_l	48 ± 2	36 ± 1	51 ± 2	36 ± 2	-	-	ps
A^{FC}/h	0.74 ± 0.02		0.55 ± 0.02		0.82 ± 0.01		MHz

Outer-sphere relaxation was also included with d = 3.6 Å and D = 3.0 and 3.9 cm^2/s at 25 °C and 37 °C, respectively.

(*) fixed

Conclusions

The relaxometric analysis performed for blueberry juice indicates that the manganese ions in this juice have a higher relaxivity than those in pineapple juice. Therefore, the water proton relaxation rates in the blueberry juice are increased to a larger extent than

in the pineapple juice when manganese(II) ions are contained in the same concentration (Figure 4). On the other hand, this implies that a lower quantity of manganese(II) contained in blueberry juice is enough to achieve the same relaxation enhancement, and thus the same contrast in the MRI images, obtainable with a larger quantity of manganese(II) contained in pineapple juice.

Very importantly, the transverse relaxation rate at high fields is sizably larger (almost double) in blueberry juice than in pineapple juice when both juices contain the same concentration of manganese(II). This points to a higher efficiency as T2-agent of the concentrated blueberry juice, similar to that of Mn^{2+} aqua ions, than of pineapple juice. The analysis of the relaxivity profiles shows that this higher efficacy is determined by a larger Fermi-contact contribution to relaxation. This larger transverse relaxation rate is however somewhat smaller than expected without considering in the concentrated solution the presence of a larger fraction of metal ions interacting with other molecules/macromolecules contained in the juice. In conclusion, although manganese(II) is the paramagnetic ion responsible for the relaxation enhancements caused by the juices, its interaction with other molecules present in the juices can sizably affect its efficiency as MRI contrast agent.

specifically the CERM/CIRMMP Italy center, and the support of the University of Florence CERM-TT, *Recombinant Proteins JOYNLAB*.

Supporting Information

Theoretical model used for the fit of the relaxivity data

The relaxivity profiles were fitted using the Solomon-Bloembergen-Morgan model[150–153], considering the contributions from Fermi-contact and dipole-dipole relaxation, and the presence of two components, with weights w and $(1-w)$, with a fast (τ_l) and a slow (τ_r) reorientation correlation times, respectively:

$$r_i = \frac{q[\text{Mn}^{2+}]}{55.5}(R_{iM}^{-1} + \tau_M)^{-1} + R_{i\text{out}} \tag{1}$$

$$R_{1M} = \frac{2S(S+1)}{3}\left(\frac{A^{FC}}{\hbar}\right)^2\left[\frac{\tau_{FC}}{1+\omega_S^2\tau_{FC}^2}\right] + \frac{2}{15}\left(\frac{\mu_0}{4\pi}\frac{\gamma_I g_{\text{iso}}\mu_B}{r^3}\right)^2 S(S+1)\left\{w\left[\frac{7\tau_c}{1+\omega_s^2\tau_c^2}+\frac{3\tau_c}{1+\omega_I^2\tau_c^2}\right]+(1-$$

$$w)\left[\frac{7\tau_f}{1+\omega_s^2\tau_f^2}+\frac{3\tau_f}{1+\omega_I^2\tau_f^2}\right]\right\} \tag{2}$$

$$R_{2M} = \frac{S(S+1)}{3}\left(\frac{A^{FC}}{\hbar}\right)^2\left[\tau_{c1}^{FC}+\frac{\tau_{c2}^{FC}}{1+\omega_S^2(\tau_{c2}^{FC})^2}\right]+\frac{1}{15}\left(\frac{\mu_0}{4\pi}\frac{\gamma_I g_{\text{iso}}\mu_B}{r^3}\right)^2 S(S+1)\left\{w\left[4\tau_c +\frac{13\tau_c}{1+\omega_s^2\tau_c^2}+\right.\right.$$

$$\left.\left.\frac{3\tau_c}{1+\omega_I^2\tau_c^2}\right]+(1-w)\left[4\tau_f +\frac{13\tau_f}{1+\omega_s^2\tau_f^2}+\frac{3\tau_f}{1+\omega_I^2\tau_f^2}\right]\right\} \tag{3}$$

where i = 1 or 2, q is the number of water molecules coordinated to the manganese ion, τ_M is their lifetimes, $\frac{A^{FC}}{h}$ is the Fermi-contact coupling constant, r the distance between metal ion and coordinated protons, S the electron spin quantum number (5/2 in the case of Mn^{2+}), τ_{FC} the correlation time for the Fermi-contact interaction

$$\tau_{FC}^{-1} = \tau_e^{-1} + \tau_M^{-1} \tag{4}$$

τ_c and τ_f are the correlation times for the dipole-dipole interaction

$$\tau_c^{-1} = \tau_r^{-1} + \tau_e^{-1} + \tau_M^{-1} \tag{5}$$

$$\tau_f^{-1} = \tau_l^{-1} + \tau_e^{-1} + \tau_M^{-1} \tag{6}$$

and τ_e is the electron relaxation time,

$$\tau_e^{-1} = \frac{2\Delta_t^2}{50}[4S(S+1)-3]\left[\frac{\tau_v}{1+\omega_S^2\tau_v^2} + \frac{4\tau_v}{1+4\omega_S^2\tau_v^2}\right] \tag{7}$$

described in the pseudorotation model by the parameters Δ_t and τ_v, which correspond to the transient zero-field splitting and to the correlation time for electron relaxation, respectively. $R_{i\text{out}}$ (in Eq. 1) indicate the paramagnetic relaxation enhancements due to the dipole-dipole interaction between the manganese ion and the water molecules freely diffusing around. This contribution has been described using the Freed model[156] and standard parameters. Other symbols have their usual meaning[157].

A fit of the longitudinal relaxivity profiles of the blueberry juice was first tried using a single reorientation correlation time ($w = 1$). After checking that the best fit profiles thus obtained were unsatisfactory, the fit was performed by allowing w to be smaller than 1; the best fit parameters are reported in Table 1 together with those previously obtained for the pineapple juice and the manganese aqua ion[140]. In the fit, the distance r of the protons in the q fast exchanging water molecules coordinated to the manganese ion was fixed to 2.85 Å, and Δ_t was fixed to the value obtained from the fit of the relaxivity of pineapple juice with addition of alginate[140], to remove the strong covariance of this parameter with τ_v, and facilitate the comparison of the obtained parameters.

The number of hydration water molecules (5.2 ± 0.2) in the blueberry juice is somewhat smaller than 6, but significantly larger than in the pineapple juice. Also the constant of Fermi-contact interaction is somewhat smaller than for the manganese aqua ion, but significantly larger than in pineapple juice, likely because water coordination is less hampered by interactions between the metal and other molecules/macromolecules

contained in the juice. This significantly larger constant of the Fermi-contact interaction, causing a high low-field longitudinal relaxivity, is also responsible of a transverse relaxivity at 400 MHz much larger for the blueberry juice than for the pineapple juice.

Figure S1. NMRD profiles of $Fe(NO_3)_3$ at a concentration of 0.040 mmol/dm^3 in a citrate buffer solution (pH 3.2) without (blue symbols) and with (black symbols) oxalate (0.1 mmol/dm^3).
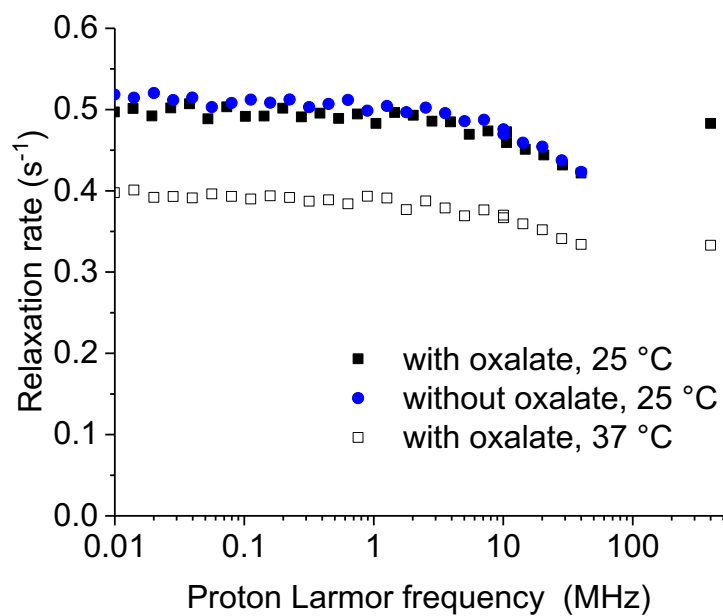
Figure S2. (A) Relaxation rates of centrifuged blueberry juice with addition of 0.020, 0.040 and 0.120 mmol/dm^3 Fe(NO$_3$)$_3$ (corresponding to 50%, 100% and 300% of the iron originally present in the juice), at 25 °C. The relaxation rates in the absence of iron could be extrapolated from a linear ft. The different lines correspond to the fits obtained for the data collected at the different proton Larmor frequencies. (B) ^{1}H longitudinal relaxivity of manganese(II) ions in the centrifuged blueberry juice, calculated from extrapolation of the rates in the absence of iron (blue symbols), and by subtracting the rates of Fe(NO$_3$)$_3$ reported in Fig. S1 (red symbols).
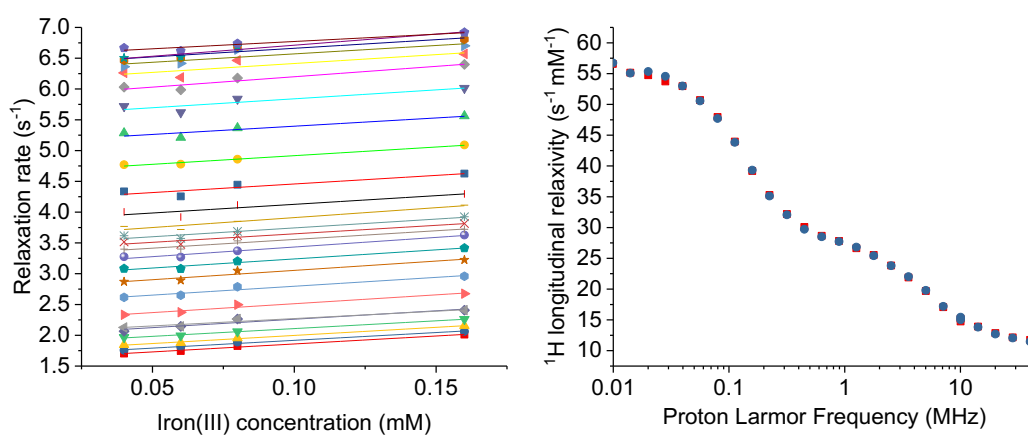
4. Conclusion and Perspectives

This PhD research project was focused on the application of molecular biology techniques and development of experimental protocols to express and purify several proteins.

At first human α-synuclein and Aβ peptides were expressed and characterized by NMR for their importance and correlation in neurodegenerative disorders. These two proteins, expressed during my research activity, have been used to design and carry out experiments aimed to investigate i) the structural features of Aβ mixed fibrils assembly, ii) the interaction of α-synuclein with human biofluid components. The quality of the proteins in terms of purity from contaminant proteases was crucial to obtain reliability and reproducibility in the experimental data. At this regard, two important results of my research activity have been: i) the development of protocols to prevent/remove the contamination by bacteria proteases and ii) the purification of monomeric form of Aβ peptides and α-synuclein from pre-formed aggregates. These protocols have been crucial to provide a structural model of interlaced mixed fibrils of Aβ1-40 and Aβ1-42 peptides, and to clarify the origins of the modulation of α-synuclein aggregation by CSF components.

Concurrently, proteins with potential biotherapeutic applications were expressed and characterized. These proteins have been used to develop new strategies based on the use of solid-state NMR spectroscopy to investigate the preservation of the higher order structure (HOS) in heterogeneous materials. Our results prove that SSNMR can be efficiently employed to evaluate the preservation of protein folding by a simple and direct comparison of bidimensional spectra collected on the protein before and after encapsulation in a matrix. In particular, interesting results were obtained investigating hydrogels encapsulating the therapeutic protein ANSII and the potential drug carrier TTR. These proteins were embedded in hydrogel matrices, that can be used for bioprinting or controlled drug release purposes. The analysis of the solid-state NMR spectra revealed that encapsulation did not affect the HOS of the two proteins.

The simplicity of the procedures for sample preparation, the sensitivity of magnetic resonance to structural perturbations and the possibility to obtain a full structural analysis are important features of this approach that be extended also to other industrial applications.

5. References

1.   Kovacs, G. G. Concepts and classification of neurodegenerative diseases. in *Handbook of Clinical Neurology* vol. 145 301–307 (Elsevier, 2018).

2.   Bayer, T. A. Proteinopathies, a core concept for understanding and ultimately treating degenerative disorders? *Eur. Neuropsychopharmacol. J. Eur. Coll. Neuropsychopharmacol.* **25**, 713–724 (2015).

3.   Nijholt, D. a. T., De Kimpe, L., Elfrink, H. L., Hoozemans, J. J. M. & Scheper, W. Removing protein aggregates: the role of proteolysis in neurodegeneration. *Curr. Med. Chem.* **18**, 2459–2476 (2011).

4.   Sweeney, P. *et al.* Protein misfolding in neurodegenerative diseases: implications and strategies. *Transl. Neurodegener.* **6**, 6 (2017).

5.   Brettschneider, J., Del Tredici, K., Lee, V. M.-Y. & Trojanowski, J. Q. Spreading of pathology in neurodegenerative diseases: a focus on human studies. *Nat. Rev. Neurosci.* **16**, 109–120 (2015).

6.   Stelzmann, R. A., Norman Schnitzlein, H. & Reed Murtagh, F. An english translation of alzheimer's 1907 paper, ?   ber eine eigenartige erkankung der hirnrinde? *Clin. Anat.* **8**, 429–431 (1995).

7.   Eghiaian, F. *et al.* Insight into the PrPC-->PrPSc conversion from the structures of antibody-bound ovine prion scrapie-susceptibility variants. *Proc. Natl. Acad. Sci. U. S. A.* **101**, 10254–10259 (2004).

8.   Alyenbaawi, H., Allison, W. T. & Mok, S.-A. Prion-Like Propagation Mechanisms in Tauopathies and Traumatic Brain Injury: Challenges and Prospects. *Biomolecules* **10**, E1487 (2020).

9.   Scekic-Zahirovic, J. *et al.* Motor neuron intrinsic and extrinsic mechanisms contribute to the pathogenesis of FUS-associated amyotrophic lateral sclerosis. *Acta Neuropathol. (Berl.)* **133**, 887–906 (2017).

10.   Hawkins, P. N. *et al.* Evolving landscape in the management of transthyretin amyloidosis. *Ann. Med.* **47**, 625–638 (2015).

11.   Spillantini, M. G. *et al.* α-Synuclein in Lewy bodies. *Nature* **388**, 839–840 (1997).

12.   Klein, A. D. & Mazzulli, J. R. Is Parkinson's disease a lysosomal disorder? *Brain* **141**, 2255–2262 (2018).

13.   Parnetti, L. *et al.* Cerebrospinal fluid lysosomal enzymes and alpha-synuclein in Parkinson's disease. *Mov. Disord.* **29**, 1019–1027 (2014).

14.   Sidransky, E. & Lopez, G. The link between the GBA gene and parkinsonism. *Lancet Neurol.* **11**, 986–998 (2012).

15.   Li, J.-Q., Tan, L. & Yu, J.-T. The role of the LRRK2 gene in Parkinsonism. *Mol. Neurodegener.* **9**, (2014).

16.   Hoffmann, A.-C. *et al.* Extracellular aggregated alpha synuclein primarily triggers lysosomal dysfunction in neural cells prevented by trehalose. *Sci. Rep.* **9**, 544 (2019).

17.   Noyce, A. J., Lees, A. J. & Schrag, A.-E. The prediagnostic phase of Parkinson's disease. *J Neurol Neurosurg Psychiatry* **87**, 871–878 (2016).

18.   Eusebi, P. *et al.* Diagnostic utility of cerebrospinal fluid α-synuclein in Parkinson's disease: A systematic review and meta-analysis. *Mov. Disord.* **32**, 1389–1400 (2017).

19.   Majbour, N. K. *et al.* Oligomeric and phosphorylated alpha-synuclein as potential CSF biomarkers for Parkinson's disease. *Mol. Neurodegener.* **11**, 7 (2016).

20.   Parnetti, L. *et al.* Cerebrospinal fluid biomarkers in Parkinson disease. *Nat. Rev. Neurol.* **9**, 131–140 (2013).

21.   Majbour, N. K. *et al.* Increased levels of CSF total but not oligomeric or phosphorylated forms of alpha-synuclein in patients diagnosed with probable Alzheimer's

disease. *Sci. Rep.* **7**, (2017).

22.   Steiner, J. A., Angot, E. & Brundin, P. A deadly spread: cellular mechanisms of α-synuclein transfer. *Cell Death Differ.* **18**, 1425–1433 (2011).

23.   Tokuda, T. *et al.* Detection of elevated levels of α-synuclein oligomers in CSF from patients with Parkinson disease. *Neurology* **75**, 1766–1772 (2010).

24.   Danzer, K. M. *et al.* Exosomal cell-to-cell transmission of alpha synuclein oligomers. *Mol. Neurodegener.* **7**, 42 (2012).

25.   Lavedan, C. The synuclein family. *Genome Res.* **8**, 871–880 (1998).

26.   Venda, L. L., Cragg, S. J., Buchman, V. L. & Wade-Martins, R. α-Synuclein and dopamine at the crossroads of Parkinson's disease. *Trends Neurosci.* **33**, 559–568 (2010).

27.   Hashimoto, M. *et al.* Oxidative stress induces amyloid-like aggregate formation of NACP/alpha-synuclein in vitro. *Neuroreport* **10**, 717–721 (1999).

28.   Fusco, G. *et al.* Direct observation of the three regions in α-synuclein that determine its membrane-bound behaviour. *Nat. Commun.* **5**, 3827 (2014).

29.   Calderon-Garciadueñas, A. L. & Duyckaerts, C. Alzheimer disease. in *Handbook of Clinical Neurology* vol. 145 325–337 (Elsevier, 2018).

30.   Bateman, R. J. *et al.* Human amyloid-β synthesis and clearance rates as measured in cerebrospinal fluid in vivo. *Nat. Med.* **12**, 856–861 (2006).

31.   Thal, D. R. *et al.* [^{18} F]flutemetamol amyloid positron emission tomography in preclinical and symptomatic Alzheimer's disease: Specific detection of advanced phases of amyloid-β pathology. *Alzheimers Dement.* **11**, 975–985 (2015).

32.   Kuperstein, I. *et al.* Neurotoxicity of Alzheimer's disease Aβ peptides is induced by small changes in the Aβ42 to Aβ40 ratio. *EMBO J.* **29**, 3408–3420 (2010).

33.   Kim, J. *et al.* Abeta40 inhibits amyloid deposition in vivo. *J. Neurosci. Off. J. Soc. Neurosci.* **27**, 627–633 (2007).

34.   Linse, S. Monomer-dependent secondary nucleation in amyloid formation. *Biophys. Rev.* **9**, 329–338 (2017).

35.   Cukalevski, R. *et al.* The Aβ40 and Aβ42 peptides self-assemble into separate homomolecular fibrils in binary mixtures but cross-react during primary nucleation. *Chem. Sci.* **6**, 4215–4233 (2015).

36.   Bertini, I., Gonnelli, L., Luchinat, C., Mao, J. & Nesi, A. A new structural model of Aβ40 fibrils. *J. Am. Chem. Soc.* **133**, 16013–16022 (2011).

37.   Wälti, M. A. *et al.* Atomic-resolution structure of a disease-relevant Aβ(1–42) amyloid fibril. *Proc. Natl. Acad. Sci.* **113**, E4976–E4984 (2016).

38.   Saborio, G. P., Permanne, B. & Soto, C. Sensitive detection of pathological prion protein by cyclic amplification of protein misfolding. *Nature* **411**, 810 (2001).

39.   Atarashi, R., Sano, K., Satoh, K. & Nishida, N. Real-time quaking-induced conversion: a highly sensitive assay for prion detection. *Prion* **5**, 150–153 (2011).

40.   Shahnawaz, M. *et al.* Development of a Biochemical Diagnosis of Parkinson Disease by Detection of α-Synuclein Misfolded Aggregates in Cerebrospinal Fluid. *JAMA Neurol.* **74**, 163–172 (2017).

41.   Fairfoul, G. *et al.* Alpha-synuclein RT-QuIC in the CSF of patients with alpha-synucleinopathies. *Ann. Clin. Transl. Neurol.* **3**, 812–818 (2016).

42.   Groveman, B. R. *et al.* Rapid and ultra-sensitive quantitation of disease-associated α-synuclein seeds in brain and cerebrospinal fluid by αSyn RT-QuIC. *Acta Neuropathol. Commun.* **6**, 7 (2018).

43.   Sano, K. *et al.* Prion-Like Seeding of Misfolded α-Synuclein in the Brains of Dementia with Lewy Body Patients in RT-QUIC. *Mol. Neurobiol.* **55**, 3916–3930 (2018).

44.   Salvadores, N., Shahnawaz, M., Scarpini, E., Tagliavini, F. & Soto, C. Detection of misfolded Aβ oligomers for sensitive biochemical diagnosis of Alzheimer's disease. *Cell Rep.* **7**, 261–268 (2014).

45.   Blennow, K. A Review of Fluid Biomarkers for Alzheimer's Disease: Moving from CSF to Blood. *Neurol. Ther.* **6**, 15–24 (2017).

46.   Blennow, K. & Zetterberg, H. Biomarkers for Alzheimer's disease: current status and prospects for the future. *J. Intern. Med.* **0**,.

47.   Blennow, K. & Zetterberg, H. Cerebrospinal fluid biomarkers for Alzheimer's disease. *J. Alzheimers Dis. JAD* **18**, 413–417 (2009).

48.   Rumund, A. van *et al.* α-Synuclein real-time quaking-induced conversion in the cerebrospinal fluid of uncertain cases of parkinsonism. *Ann. Neurol.* **85**, 777–781 (2019).

49.   Li, P., Dai, Y.-N., Zhang, J.-P., Wang, A.-Q. & Wei, Q. Chitosan-alginate nanoparticles as a novel drug delivery system for nifedipine. *Int. J. Biomed. Sci. IJBS* **4**, 221–228 (2008).

50.   Li, N., Wang, J., Yang, X. & Li, L. Novel nanogels as drug delivery systems for poorly soluble anticancer drugs. *Colloids Surf. B Biointerfaces* **83**, 237–244 (2011).

51.   Buwalda, S. J., Vermonden, T. & Hennink, W. E. Hydrogels for Therapeutic Delivery: Current Developments and Future Directions. *Biomacromolecules* **18**, 316–330 (2017).

52.   Dolowy, W. C., Henson, D., Cornet, J. & Sellin, H. Toxic and antineoplastic effects of L-asparaginase. Study of mice with lymphoma and normal monkeys and report on a child with leukemia. *Cancer* **19**, 1813–1819 (1966).

53.   Broome, J. D. STUDIES ON THE MECHANISM OF TUMOR INHIBITION BY L-ASPARAGINASE. *J. Exp. Med.* **127**, 1055–1072 (1968).

54.   Yokoyama, T., Kosaka, Y. & Mizuguchi, M. Crystal Structures of Human Transthyretin Complexed with Glabridin. *J. Med. Chem.* **57**, 1090–1096 (2014).

55.   Walker, K. W. *et al.* The serum protein transthyretin as a platform for dimerization and tetramerization of antibodies and Fab fragments to enable target clustering. *J. Biol. Chem.* **295**, 10446–10455 (2020).

56.   Demain, A. L. & Vaishnav, P. Production of recombinant proteins by microbes and higher organisms. *Biotechnol. Adv.* **27**, 297–306 (2009).

57.   Sezonov, G., Joseleau-Petit, D. & D'Ari, R. *Escherichia coli* Physiology in Luria-Bertani Broth. *J. Bacteriol.* **189**, 8746–8749 (2007).

58.   Shiloach, J. & Fass, R. Growing E. coli to high cell density—A historical perspective on method development. *Biotechnol. Adv.* **23**, 345–357 (2005).

59.   Sivashanmugam, A. *et al.* Practical protocols for production of very high yields of recombinant proteins using *Escherichia coli*. *Protein Sci.* **18**, 936–948 (2009).

60.   Andersen, K. R., Leksa, N. C. & Schwartz, T. U. Optimized *E. coli* expression strain LOBSTR eliminates common contaminants from His-tag purification. *Proteins Struct. Funct. Bioinforma.* **81**, 1857–1861 (2013).

61.   Mondal, S., Shet, D., Prasanna, C. & Atreya, H. S. High yield expression of proteins in <i>E. coli</i> for NMR studies. *Adv. Biosci. Biotechnol.* **04**, 751–767 (2013).

62.   Chen, B. P. C. & Hai, T. Expression vectors for affinity purification and radiolabeling of proteins using Escherichia coli as host. *Gene* **139**, 73–75 (1994).

63.   Li, Z., Nimtz, M. & Rinas, U. Optimized procedure to generate heavy isotope and selenomethionine-labeled proteins for structure determination using Escherichia coli-based expression systems. *Appl. Microbiol. Biotechnol.* **92**, 823–833 (2011).

64.   Ki, M.-R. & Pack, S. P. Fusion tags to enhance heterologous protein expression. *Appl. Microbiol. Biotechnol.* **104**, 2411–2425 (2020).

65.   Shevchik, V. E., Condemine, G. & Robert-Baudouy, J. Characterization of DsbC, a periplasmic protein of Erwinia chrysanthemi and Escherichia coli with disulfide isomerase activity. *EMBO J.* **13**, 2007–2012 (1994).

66.   Huang, C., Ren, G., Zhou, H. & Wang, C. A new method for purification of recombinant human α-synuclein in Escherichia coli. *Protein Expr. Purif.* **42**, 173–177 (2005).

67.   Lakowicz, J. R. *Principles of fluorescence spectroscopy*. (Springer, 2010).

68.   Bertini, I., Luchinat, C., Parigi, G. & Ravera, E. SedNMR: On the Edge between Solution and Solid-State NMR. *Acc. Chem. Res.* **46**, 2059–2069 (2013).

69.   Bertini, I. *et al.* Solid-state NMR of proteins sedimented by ultracentrifugation. *Proc. Natl. Acad. Sci.* **108**, 10396–10399 (2011).

70.   Ravera, E. *et al.* NMR of sedimented, fibrillized, silica-entrapped and microcrystalline (metallo)proteins. *J. Magn. Reson. San Diego Calif 1997* **253**, 60–70 (2015).

71.   Schneider, S. A. & Alcalay, R. N. Neuropathology of genetic synucleinopathies with parkinsonism: Review of the literature. *Mov. Disord. Off. J. Mov. Disord. Soc.* **32**, 1504–1523 (2017).

72.   Bellomo, G., Paciotti, S., Gatticchi, L. & Parnetti, L. The vicious cycle between α-synuclein aggregation and autophagic-lysosomal dysfunction. *Mov. Disord.* **35**, 34–44 (2020).

73.   Villar-Piqué, A. *et al.* Environmental and genetic factors support the dissociation between α-synuclein aggregation and toxicity. *Proc. Natl. Acad. Sci.* **113**, E6506–E6515 (2016).

74.   Sulzer, D. & Edwards, R. H. The physiological role of α-synuclein and its relationship to Parkinson's Disease. *J. Neurochem.* **150**, 475–486 (2019).

75.   Steiner, J. A., Angot, E. & Brundin, P. A deadly spread: cellular mechanisms of α-synuclein transfer. *Cell Death Differ.* **18**, 1425–1433 (2011).

76.   Ingelsson, M. Alpha-Synuclein Oligomers-Neurotoxic Molecules in Parkinson's Disease and Other Lewy Body Disorders. *Front. Neurosci.* **10**, 408 (2016).

77.   Tokuda, T. *et al.* Detection of elevated levels of α-synuclein oligomers in CSF from patients with Parkinson disease. *Neurology* **75**, 1766–1772 (2010).

78.   Hansson, O. *et al.* Levels of cerebrospinal fluid α-synuclein oligomers are increased in Parkinson's disease with dementia and dementia with Lewy bodies compared to Alzheimer's disease. *Alzheimers Res. Ther.* **6**, 25 (2014).

79.   Shahnawaz, M. *et al.* Development of a Biochemical Diagnosis of Parkinson Disease by Detection of α-Synuclein Misfolded Aggregates in Cerebrospinal Fluid. *JAMA Neurol.* **74**, 163–172 (2017).

80.   Fairfoul, G. *et al.* Alpha-synuclein RT-QuIC in the CSF of patients with alpha-synucleinopathies. *Ann. Clin. Transl. Neurol.* **3**, 812–818 (2016).

81.   Paciotti, S., Bellomo, G., Gatticchi, L. & Parnetti, L. Are We Ready for Detecting α-Synuclein Prone to Aggregation in Patients? The Case of 'Protein-Misfolding Cyclic Amplification' and 'Real-Time Quaking-Induced Conversion' as Diagnostic Tools. *Front. Neurol.* **9**, 415 (2018).

82.   Saborio, G. P., Permanne, B. & Soto, C. Sensitive detection of pathological prion protein by cyclic amplification of protein misfolding. *Nature* **411**, 810–813 (2001).

83.   Atarashi, R., Sano, K., Satoh, K. & Nishida, N. Real-time quaking-induced conversion. *Prion* **5**, 150–153 (2011).

84.   De Luca, C. M. G. *et al.* Efficient RT-QuIC seeding activity for α-synuclein in olfactory mucosa samples of patients with Parkinson's disease and multiple system atrophy. *Transl. Neurodegener.* **8**, 24 (2019).

85.   Manne, S. *et al.* Blinded RT-QuIC Analysis of α-Synuclein Biomarker in Skin Tissue From Parkinson's Disease Patients. *Mov. Disord.* **35**, 2230–2239 (2020).

86.   Wang, Z. *et al.* Skin α-Synuclein Aggregation Seeding Activity as a Novel Biomarker for Parkinson Disease. *JAMA Neurol.* (2020) doi:10.1001/jamaneurol.2020.3311.

87.   Pujols, J. *et al.* Small molecule inhibits α-synuclein aggregation, disrupts amyloid fibrils, and prevents degeneration of dopaminergic neurons. *Proc. Natl. Acad. Sci. U. S. A.* **115**, 10481–10486 (2018).

88.   Kang, U. J. *et al.* Comparative study of cerebrospinal fluid α-synuclein seeding aggregation assays for diagnosis of Parkinson's disease. *Mov. Disord.* **34**, 536–544 (2019).

89.   Rossi, M. *et al.* Ultrasensitive RT-QuIC assay with high sensitivity and specificity for

Lewy body-associated synucleinopathies. *Acta Neuropathol. (Berl.)* **140**, 49–62 (2020).

90.   Concha-Marambio, L., Shahnawaz, M. & Soto, C. Detection of Misfolded α-Synuclein Aggregates in Cerebrospinal Fluid by the Protein Misfolding Cyclic Amplification Platform. *Methods Mol. Biol. Clifton NJ* **1948**, 35–44 (2019).

91.   Bargar, C. *et al.* Streamlined alpha-synuclein RT-QuIC assay for various biospecimens in Parkinson's disease and dementia with Lewy bodies. *Acta Neuropathol. Commun.* **9**, 62 (2021).

92.   Pate, K. M. & Murphy, R. M. Cerebrospinal Fluid Proteins as Regulators of Beta-amyloid Aggregation and Toxicity. *Isr. J. Chem.* **57**, 602–612 (2017).

93.   Padayachee, E. R. *et al.* Cerebrospinal fluid-induced retardation of amyloid β aggregation correlates with Alzheimer's disease and the APOE ε4 allele. *Brain Res.* **1651**, 11–16 (2016).

94.   Yerbury, J. J. *et al.* The extracellular chaperone clusterin influences amyloid formation and toxicity by interacting with prefibrillar structures. *FASEB J. Off. Publ. Fed. Am. Soc. Exp. Biol.* **21**, 2312–2322 (2007).

95.   Bellomo, G. *et al.* Dissecting the Interactions between Human Serum Albumin and α-Synuclein: New Insights on the Factors Influencing α-Synuclein Aggregation in Biological Fluids. *J. Phys. Chem. B* **123**, 4380–4386 (2019).

96.   Taghdiri, F. *et al.* Association Between Cerebrospinal Fluid Biomarkers and Age-related Brain Changes in Patients with Normal Pressure Hydrocephalus. *Sci. Rep.* **10**, 9106 (2020).

97.   Aru, V. *et al.* Quantification of lipoprotein profiles by nuclear magnetic resonance spectroscopy and multivariate data analysis. *TrAC Trends Anal. Chem.* **94**, 210–219 (2017).

98.   Jiménez, B. *et al.* Quantitative Lipoprotein Subclass and Low Molecular Weight Metabolite Analysis in Human Serum and Plasma by 1H NMR Spectroscopy in a Multilaboratory Trial. *Anal. Chem.* **90**, 11962–11971 (2018).

99.   Kayed, R. & Glabe, C. G. Conformation-Dependent Anti-Amyloid Oligomer Antibodies. in *Methods in Enzymology* vol. 413 326–344 (Academic Press, 2006).

100.   Mahley, R. W. Central Nervous System Lipoproteins. *Arterioscler. Thromb. Vasc. Biol.* **36**, 1305–1315 (2016).

101.   Pitas, R. E., Boyles, J. K., Lee, S. H., Hui, D. & Weisgraber, K. H. Lipoproteins and their receptors in the central nervous system. Characterization of the lipoproteins in cerebrospinal fluid and identification of apolipoprotein B,E(LDL) receptors in the brain. *J. Biol. Chem.* **262**, 14352–14360 (1987).

102.   Orth, M. & Bellosta, S. Cholesterol: Its Regulation and Role in Central Nervous System Disorders. *Cholesterol* https://www.hindawi.com/journals/cholesterol/2012/292598/ (2012) doi:10.1155/2012/292598.

103.   Ingenbleek, Y. Plasma Transthyretin as A Biomarker of Sarcopenia in Elderly Subjects. *Nutrients* **11**, 895 (2019).

104.   Theillet, F.-X. *et al.* Structural disorder of monomeric α-synuclein persists in mammalian cells. *Nature* **530**, 45–50 (2016).

105.   Emamzadeh, F. N. & Allsop, D. α-Synuclein Interacts with Lipoproteins in Plasma. *J. Mol. Neurosci.* **63**, 165–172 (2017).

106.   Sharon, R. *et al.* alpha-Synuclein occurs in lipid-rich high molecular weight complexes, binds fatty acids, and shows homology to the fatty acid-binding proteins. *Proc. Natl. Acad. Sci. U. S. A.* **98**, 9110–9115 (2001).

107.   Cunniffe, J. G., Whitby-Strevens, S. & Wilcox, M. H. Effect of pH changes in cerebrospinal fluid specimens on bacterial survival and antigen test results. *J. Clin. Pathol.* **49**, 249–253 (1996).

108.   Fura, A., Harper, T. W., Zhang, H., Fung, L. & Shyu, W. C. Shift in pH of biological fluids during storage and processing: effect on bioanalysis. *J. Pharm. Biomed. Anal.* **32**, 513–

522 (2003).

109.   Siesjö, B. K. The regulation of cerebrospinal fluid pH. *Kidney Int.* **1**, 360–374 (1972).

110.   Bellomo, G. *et al.* Aggregation kinetics of the Aβ1–40 peptide monitored by NMR. *Chem. Commun.* **54**, 7601–7604 (2018).

111.   Safar, J. G. *et al.* Human prions and plasma lipoproteins. *Proc. Natl. Acad. Sci. U. S. A.* **103**, 11312–11317 (2006).

112.   Paslawski, W. *et al.* α-synuclein−lipoprotein interactions and elevated ApoE level in cerebrospinal fluid from Parkinson's disease patients. *Proc. Natl. Acad. Sci.* **116**, 15226–15235 (2019).

113.   Gualandri, V. *et al.* AIMilano apoprotein identification of the complete kindred and evidence of a dominant genetic transmission. *Am. J. Hum. Genet.* **37**, 1083–1097 (1985).

114.   Nanjee, M. N., Doran, J. E., Lerch, P. G. & Miller, N. E. Acute effects of intravenous infusion of ApoA1/phosphatidylcholine discs on plasma lipoproteins in humans. *Arterioscler. Thromb. Vasc. Biol.* **19**, 979–989 (1999).

115.   Kallend, D. G. *et al.* A single infusion of MDCO-216 (ApoA-1 Milano/POPC) increases ABCA1-mediated cholesterol efflux and pre-beta 1 HDL in healthy volunteers and patients with stable coronary artery disease. *Eur. Heart J. Cardiovasc. Pharmacother.* **2**, 23–29 (2016).

116.   Fernández-de Retana, S. *et al.* Intravenous treatment with human recombinant ApoA-I Milano reduces beta amyloid cerebral deposition in the APP23-transgenic mouse model of Alzheimer's disease. *Neurobiol. Aging* **60**, 116–128 (2017).

117.   Zhou, A. L. *et al.* Apolipoprotein A-I Crosses the Blood-Brain Barrier through Clathrin-Independent and Cholesterol-Mediated Endocytosis. *J. Pharmacol. Exp. Ther.* **369**, 481–488 (2019).

118.   Uversky, V. N., Li, J. & Fink, A. L. Evidence for a Partially Folded Intermediate in α-Synuclein Fibril Formation *. *J. Biol. Chem.* **276**, 10737–10744 (2001).

119.   Pate, K. M. & Murphy, R. M. Cerebrospinal Fluid Proteins as Regulators of Beta-amyloid Aggregation and Toxicity. *Isr. J. Chem.* **57**, 602–612 (2017).

120.   Padayachee, E. R. *et al.* Cerebrospinal fluid-induced retardation of amyloid β aggregation correlates with Alzheimer's disease and the APOE ε4 allele. *Brain Res.* **1651**, 11–16 (2016).

121.   Adler, J., Scheidt, H. A., Lemmnitzer, K., Krueger, M. & Huster, D. N-terminal lipid conjugation of amyloid β(1–40) leads to the formation of highly ordered N-terminally extended fibrils. *Phys. Chem. Chem. Phys.* **19**, 1839–1846 (2017).

122.   Morris, R. G., Evenden, J. L., Sahakian, B. J. & Robbins, T. W. Computer-aided assessment of dementia: Comparative studies of neuropsychological deficits in Alzheimer-type dementia and Parkinson's disease. in *Cognitive neurochemistry* 21–36 (Oxford University Press, 1987).

123.   Ishihama, Y. *et al.* Exponentially modified protein abundance index (emPAI) for estimation of absolute protein amount in proteomics by the number of sequenced peptides per protein. *Mol. Cell. Proteomics MCP* **4**, 1265–1272 (2005).

124.   Shinoda, K., Tomita, M. & Ishihama, Y. emPAI Calc--for the estimation of protein abundance from large-scale identification data by liquid chromatography-tandem mass spectrometry. *Bioinforma. Oxf. Engl.* **26**, 576–577 (2010).

125.   Frisch, A., Walter, T. C., Hamm, B. & Denecke, T. Efficacy of oral contrast agents for upper gastrointestinal signal suppression in MRCP: A systematic review of the literature. *Acta Radiol. Open* **6**, 2058460117727315 (2017).

126.   Giovagnoni, A., Fabbri, A. & Maccioni, F. Oral contrast agents in MRI of the gastrointestinal tract. *Abdom. Imaging* **27**, 367–375 (2002).

127.   Wahsner, J., Gale, E. M., Rodríguez-Rodríguez, A. & Caravan, P. Chemistry of MRI Contrast Agents: Current Challenges and New Frontiers. *Chem. Rev.* **119**, 957–1057 (2019).

128.   Karantanas, A. H., Papanikolaou, N., Kalef-Ezra, J., Challa, A. & Gourtsoyiannis, N. Blueberry juice used per os in upper abdominal MR imaging: composition and initial clinical data. *Eur. Radiol.* **10**, 909–913 (2000).

129.   Riordan, R. D., Khonsari, M., Jeffries, J., Maskell, G. F. & Cook, P. G. Pineapple juice as a negative oral contrast agent in magnetic resonance cholangiopancreatography: a preliminary evaluation. *Br. J. Radiol.* **77**, 991–999 (2004).

130.   Hiraishi, K. *et al.* Blueberry juice: preliminary evaluation as an oral contrast agent in gastrointestinal MR imaging. *Radiology* **194**, 119–123 (1995).

131.   Zarrini, M., Seilanian Toosi, F., Davachi, B. & Nekooei, S. Natural oral contrast agents for gastrointestinal magnetic resonance imaging. *Rev. Clin. Med.* **2**, 200–204 (2015).

132.   Uzal-Varela, R. *et al.* Mn2+ Complexes Containing Sulfonamide Groups with pH-Responsive Relaxivity. *Inorg. Chem.* **59**, 14306–14317 (2020).

133.   Terreno, E., Castelli, D. D., Viale, A. & Aime, S. Challenges for Molecular Magnetic Resonance Imaging. *Chem. Rev.* **110**, 3019–3042 (2010).

134.   Li, H., Parigi, G., Luchinat, C. & Meade, T. J. Bimodal Fluorescence-Magnetic Resonance Contrast Agent for Apoptosis Imaging. *J. Am. Chem. Soc.* **141**, 6224–6233 (2019).

135.   Arthurs, O. J. *et al.* Interactive neonatal gastrointestinal magnetic resonance imaging using fruit juice as an oral contrast media. *BMC Med. Imaging* **14**, 33 (2014).

136.   Renzulli, M. *et al.* What is the best fruit juice to use as a negative oral contrast agent in magnetic resonance cholangiopancreatography? *Clin. Radiol.* **74**, 220–227 (2019).

137.   Faletti, R. *et al.* Concentrated pineapple juice for visualisation of the oesophagus during magnetic resonance angiography before atrial fibrillation radiofrequency catheter ablation. *Eur. Radiol. Exp.* **2**, 39 (2018).

138.   Kulinna-Cosentini, C. *et al.* Performance of a new natural oral contrast agent (LumiVision®) in dynamic MR swallowing. *Eur. Radiol.* (2021) doi:10.1007/s00330-021-07927-5.

139.   Frisch, A. *et al.* Performance survey on a new standardized formula for oral signal suppression in MRCP. *Eur. J. Radiol. Open* **5**, 1–5 (2018).

140.   Rizzo, D., Ravera, E., Fragai, M., Parigi, G. & Luchinat, C. Origin of the MRI Contrast in Natural and Hydrogel Formulation of Pineapple Juice. *Bioinorganic Chemistry and Applications* https://www.hindawi.com/journals/bca/2021/6666018/ (2021) doi:https://doi.org/10.1155/2021/6666018.

141.   Bertini, I., Luchinat, C., Parigi, G. & Ravera, E. *NMR of paramagnetic molecules: applications to metallobiomolecules and models*. (2017).

142.   Parigi, G., Ravera, E., Fragai, M. & Luchinat, C. Unveiling protein dynamics in solution with field-cycling NMR relaxometry. *Prog. Nucl. Magn. Reson. Spectrosc.* **124–125**, 85–98 (2021).

143.   Ferrante, G. & Sykora, S. Technical aspects of fast field cycling. *Adv.Inorg.Chem.* **57**, 405–470 (2005).

144.   Bertini, I., Luchinat, C. & Parigi, G. 1H NMRD profiles of paramagnetic complexes and metalloproteins. *Adv.Inorg.Chem.* **57**, 105–172 (2005).

145.   Ravera, E., Takis, P. G., Fragai, M., Parigi, G. & Luchinat, C. NMR Spectroscopy and Metal Ions in Life Sciences: NMR Spectroscopy and Metal Ions in Life Sciences. *Eur. J. Inorg. Chem.* **2018**, 4752–4770 (2018).

146.   Fragai, M., Ravera, E., Tedoldi, F., Luchinat, C. & Parigi, G. Relaxivity of Gd-Based MRI Contrast Agents in Crosslinked Hyaluronic Acid as a Model for Tissues. *ChemPhysChem* **20**, 2204–2209 (2019).

147.   Esteban-Gómez, D., Cassino, C., Botta, M. & Platas-Iglesias, C. ^{17}O and ^1H relaxometric and DFT study of hyperfine coupling constants in $[Mn(H_2O)_6]^{2+}$. *RSC Adv.* **4**, 7094–7103 (2014).

148.   Bertini, I., Capozzi, F., Luchinat, C. & Xia, Z. Nuclear and electron relaxation of

Fe(OH2)63+. *J.Phys.Chem.* **97**, 1134–1137 (1993).

149. Nguyễn, H. V. H. & Savage, G. P. Oxalate content of New Zealand grown and imported fruits. *J. Food Compos. Anal.* **31**, 180–184 (2013).

150. Bloembergen, N. & Morgan, L. O. Proton relaxation times in paramagnetic solutions. Effects of electron spin relaxation. *J.Chem.Phys.* **34**, 842–850 (1961).

151. Solomon, I. Relaxation Processes in a System of Two Spins. *Phys. Rev.* **99**, 559–565 (1955).

152. Bloembergen, N. Proton relaxation times in paramagnetic solutions. *J.Chem.Phys.* **27**, 572–573 (1957).

153. Parigi, G., Ravera, E. & Luchinat, C. Magnetic susceptibility and paramagnetism-based NMR. *Prog. Nucl. Magn. Reson. Spectrosc.* **114–115**, 211–236 (2019).

154. Bertini, I., Fragai, M., Luchinat, C. & Parigi, G. 1H NMRD profiles of diamagnetic proteins: a model-free analysis. *Magn. Reson. Chem.* **38**, 543–550 (2000).

155. Wojcieszek, J., Kwiatkowski, P. & Ruzik, L. Speciation analysis and bioaccessibility evaluation of trace elements in goji berries (Lycium Barbarum, L.). *J. Chromatogr. A* **1492**, 70–78 (2017).

156. Freed, J. H. Dynamic effects of pair correlation functions on spin relaxation by translational diffusion in liquids. II. Finite jumps and independent T1 processes. *J.Chem.Phys.* **68**, 4034–4037 (1978).

157. Bertini, I., Luchinat, C., Parigi, G. & Ravera, E. *NMR of paramagnetic molecules: applications to metallobiomolecules and models*. (Elsevier, 2017).